Electro-catalytic reactions at charged solid/liquid interface - a DFT study

Tripkovic, Vladimir

Publication date:
2010

Document Version
Publisher's PDF, also known as Version of record

Ph.D Thesis

Electro-catalytic reactions at charged solid/liquid interface - a DFT study

Vladimir Tripković

Center for Atomic-scale Materials Design
Department of Physics
Technical University of Denmark

Thesis submitted for the degree of
Ph.D in Physics
July 2010

Preface

This dissertation is submitted in candidacy for the Ph. D. degree from the Technical University of Denmark (DTU). The work presented here has been carried out at the Center for Atomic-scale Materials Design (CAMD), Department of Physics from August 2007 to July 2010 under supervision of Assistant Professor Jan Rossmeisl and Professor Jens K. Nørskov. Financial support was provided by DTU.

Lyngby, July, 2010

Vladimir Tripković

Acknowledgements

First of all I would like to thank my supervisors Jan Rossmeisl and Jens K. Nørskov for their excellent guidance during the course of my study. Their huge knowledge and expertise in the field of atomic-scale modeling have greatly inspired me in my work. Besides they set an example for me of how excellent results can be achieved by working in a relaxing atmosphere.

I would also like to acknowledge the “superusers” Ole H. Nielsen, Jens J. Mortensen and Marcin Dulak for keeping all the bites and bits of niflheim in place and for helping me out with all the hardware and software issues.

I show huge appreciation for the “people behind the curtains” Marianne Ærsøe, Helle W. Wellejus, Stavroula G. Nielsen and Henning B. Nicolajsen for taking care of all administrative work and for keeping the wheel of CAMD turning smoothly.

I am extremely grateful to Mårten Björketun who proofread major part of the thesis and Ifan Stephens, Marco Vanin, Egill Skúllason and George Tritsaris for proofreading parts of the thesis.

Besides, I would also like to express special thanks to my office mates in the past three years. I thank Anca Paduraru for keeping the atmosphere vibrant. I thank Mikkel Strange for giving me a good deal for his bike. I thank Egill Skúllason for helping me to get started with the research and for helping me to better understand the atomic scale universe. I thank Marco Vanin for generously sharing his knowledge about both the first principles and the barbecuing methods. I thank George Tritsaris for sharing all the booze from his bar. I thank Jón Bergmann for bringing all the funny stuff and Jón Myrdal for giving me a nice tour of Iceland. The last but not the least I thank Jakob Howalt for making me always laugh.

During three years I spent at CAMD I was privileged to work and share corridor and coffee/tea cups with a number of extraordinary people. Here I would like to acknowledge

them all for all the help they gave me, for the time we spent together and for all the scientific and non-scientific discussions we have had. Guys, you have created a unique scientific environment in which it was always a pleasure to work.

I am especially thankful to Tijana and my family for their endless love and for giving me strength whenever I was feeling down.

In the end I am also very glad I came to Denmark and Copenhagen because this is indeed a wonderful place to be.

Abstract

The main goal of my thesis was to elucidate reaction mechanisms of the hydrogen oxidation reaction (HOR), hydrogen evolution reaction (HER) and oxygen reduction reaction (ORR). These reactions take place at the electrodes of energy converting devices such as fuel cells and photo-electrolyzers that are envisaged to replace carbon burning engines in a foreseeable future. Albeit the reactions seem quite simple, there is still no conclusive evidence as through which reaction pathway they proceed, which are the main reaction intermediates and which step is rate determining. DFT is a perfect tool to address these issues because it can give an atomic level insight into surface processes that is often hard to obtain with experimental techniques.

The HER, HOR and ORR are electrochemical reactions and to be able to study them at different biases we had to develop a scheme to control the surface charge within our simulated cell. The bias was introduced by explicitly adding hydrogen atoms in the water bilayer. These spontaneously split into protons and electrons which resulted in charging of the electrode/water interface. The charge (potential) was subsequently tuned by changing the proton concentration in the cell. Since these set up the potential and the electric field; problems appeared when protons were allowed to react in order to probe a charge transfer reaction. Namely, the potential changed along the reaction path, which was not a genuine physical effect but an artifact of the very restricted size of the unit cell we were able to model. To workaround this problem we have devised an “extrapolation scheme” which enabled us to alleviate the finite size effect and to approach the limit of a real electrochemical cell, where the electrode potential does not change during a charge transfer reaction. All the potentials were reported versus an internal absolute standard hydrogen electrode (ASHE) scale. We show that the ASHE potential, though in reality material independent, will in practice vary with a metal electrode owing to the limited amount of water afforded in the calculations.

There are two viable routes for hydrogen to oxidize. The first one is the so-called Volmer-Heyrovski pathway where both steps involve charge transfer reactions and the second one is the Volmer-Tafel mechanism where the Tafel step represents a typical Langmuir-Hinshelwood-type reaction. We concentrated our research efforts on Pt(111) since Pt is the state-of-the-art catalyst for the HER/HOR reaction and the (111) surface its dominant facet. We have also analyzed other low index Pt surfaces, different transition metals and facets and concluded that the Volmer-Tafel mechanism will prevail on all of them. Using a simple kinetic model with all inputs coming from DFT calculations, we reproduced remarkably well the experimentally measured activities and we confirmed that the H adsorption energy is indeed a unique descriptor for the HOR/HER activity.

We have also investigated the reaction mechanism of the ORR. The novelty of the approach we used was that the water environment was explicitly taken into account and its influence on the kinetics of the ORR was subsequently quantified. In that perspective we have found out that a half dissociated water layer is the relevant water structure at the potentials of interest for the ORR and subsequently we have modeled all reaction intermediates integrated inside this water network. We have deconvoluted the reaction mechanisms in three sequences - proton transfer, surface diffusion and oxygen species reduction - and we have shown that there are essentially very small kinetic barriers associated with each step. From the DFT data we have constructed a free energy diagram, which corroborates the previous finding that the potential determining step is OH removal from the surface.

Finally, we have also shown the versatility of DFT to simulate dissolution processes by emulating dissolution of zinc anode in zinc/air batteries.

Resume

Hovedformålet med min afhandling var at klarlægge reaktionsmekanismerne for brintoxideringsreaktionen (HOR), brintudviklingsreaktionen (HER) og iltreduceringsreaktionen (ORR). Disse reaktioner finder sted ved elektroderne i apparater til energiomdannelse såsom brændselsceller og fotoelektrolyseapparater, som er udset til at erstatte kuludledende motorer i den nærmeste fremtid. Selvom reaktionerne virker simple, er der stadig ikke noget endeligt bevis for hvilke reaktionsveje de gennemgår, hvilke reaktionsmellemprodukter er de vigtigste og hvilke trin er hastighedsbegrænsende. Tæthedfunktionalteori (DFT) er et velegnet instrument til at undersøge disse spørgsmål, da det kan give indsigt i processer på overflader på atomart niveau, som ofte er vanskelig at få med eksperimentelle teknikker.

HER, HOR og ORR er elektrokemiske reaktioner, så for at kunne undersøge dem ved forskellige spændinger, blev vi nødt til at udvikle et system til at kontrollere overfladeladningen i vores simuleringscelle. Spændingen blev indført ved at tilsætte brintatomer i vandlaget. Det elektriske potentiale blev indført ved at tilføje hydrogen atomer i vandets bilayer. Disse hydrogen atomer splittes spontant i protoner og elektroner, som resulterede i en opladning af elektrode/vand grænsefladen. Ladningen (potentialet) blev efterfølgende justeret ved at ændre proton koncentrationen i cellen. Ved at introducere potentialet og det elektriske felt på denne måde, opstår der problemer når protonerne får lov at reagerer for at undersøge en ladnings overførsels reaktion. Specielt ændres potentialet langs reaktions vejen, hvilket ikke er en reel fysisk effekt, men en konsekvens af den meget begrænsede størrelse for enhedscellen vi var i stand til at modellere. Som løsning til dette problem har vi udviklet en "ekstrapolations metode", som gav os mulighed for at afhjælpe de problemer som opstår når man benytter en begrænset størrelse af enhedscellen og vi kan derfor nærme os grænsen for en reel elektrokemisk celle, hvor elektrodens potentiale ikke ændrer sig under en ladnings

overførsels reaktion. Alle potentialerne blev rapporteret versus en intern absolut standard hydrogen elektrode (ASHE) skala. Vi viser, at ASHE potentialet, som i virkeligheden er materiale uafhængig, i praksis vil varierer fra metal elektrode til metal elektrode på grund af den begrænsede antal lag af vand der er benyttet i beregningerne. Hydrogen kan oxideres via to mulige reaktionsruter. Den første er den såkaldte Volmer-Heyrovski rute, hvor begge trin indebærer ladningsoverførselsreaktioner, og den anden er Volmer-Tafel mekanismen, hvor Tafel trinnet udgør en typisk Langmuir-Hinshelwood reaktion. Vi har koncentreret vores forskningsarbejde om Pt(111), da Pt er den bedste kendte katalyst for HOR/HER reaktionen, og (111) overfladen dens dominerende facet. Vi har endvidere analyseret andre Pt overflader med lave indeks, samt forskellige overgangsmetaller og facet, og konkluderet at Volmer-Tafel mekanismen fungerer bedst uanset overfladen. Ved hjælp af en simpel kinetisk model, hvor alle parametre kommer fra DFT beregninger, har vi opnået overraskende god overensstemmelse med eksperimentelt målte aktiviteter, og vi har bekræftet at H-adsorptionsenergien er en unik indikator for HOR/HER aktiviteten.

Vi har også undersøgt reaktionsmekanismen for ORR. Det nye ved den brugte metode er, at vandets struktur ved reaktionsoverfladen er blevet studeret og dens indflydelse på kinetikken af ORR blev efterfølgende kvantificeret. I det perspektiv har vi fundet ud af, at et halvt dissocieret vandlag udgør vandets struktur ved overfladerne ved de interessante anvendte potentialer for ORR og efterfølgende har vi modelleret alle mellemprodukter reaktionsmekanismen ved brug af denne struktur for vandet. Vi kan opdele reaktions mekanismerne i tre sekvenser - proton overførsel, overflade diffusion og reduktionen af oxygenholdige molekyler - og vi har vist, at der eksistere meget små kinetiske barrierer forbundet med hvert trin. Fra DFT data, har vi konstrueret et fri energi diagram, hvilket bekræfter den tidligere konstatering af, at det afgørende reaktions skridt er fjernelsen af OH fra overfladen.

Endelig, har vi også vist alsidigheden af DFT, ved at simulere opløsningsprocesser ved at efterligne opløsningen af en zink anode i zink / luft batterier.

List of Included Papers

PAPER I
Modeling the electrified solid-liquid interface
J. Rossmeisl, E. Skúlason, M. E. Björketun, V. Tripković, J. K. Nørskov
Chemical Physics Letters, **466** (2008) 68

PAPER II
Modeling the electrochemical hydrogen oxidation and evolution reactions on the basis of density functional theory calculations
E. Skúlason, V. Tripković, M. E. Björketun, S. Guðmundsdóttir, G. Karlberg, J. Rossmeisl, T. Bligaard, H. Jónsson, J. K. Nørskov
The Journal of Physical Chemistry C

PAPER III
The computational standard hydrogen electrode
V. Tripković, M. Björketun, E. Skúlason, J. K. Nørskov, J. Rossmeisl
In preparation

PAPER IV
The oxygen reduction reaction mechanism on Pt(111) from density functional theory calculations
V. Tripković, E. Skúlason, S. Siahrostami, J. K. Nørskov, J. Rossmeisl
Electrochimica Acta, doi:10.1016/j.electacta.2010.02.056

PAPER V
First principle investigation of zinc-anode dissolution in zinc/air battery
V. Tripković, S. Siahrostami, K. T. Lundgård, K. E. Jensen, H. A. Hansen, J. S. Hummelshøj, J. S. Garðarsson, T. Vegge, J. K. Nørskov, J. Rossmeisl
To be submitted

Other Publications

PAPER I

Density functional theory based screening of ternary alkali-transition metal borohydrides: A computational materials design project

J. S. Hummelshøj, D. D. Landis, J. Voss, T. Jiang, A. Tekin, N. Bork, M. Dułak, J. J. Mortensen, ...V. Tripković,…

Journal of Chemical Physics **131** (2009) 014101.

PAPER II

Trends for methane oxidation at solid oxide fuel cell conditions

J. Kleis, G. Jones, F. Abild-Pedersen, V.Tripković, Thomas Bligaard, J. Rossmeisl

Journal of The Electrochemical Society **156** (2009) B1447.

PAPER III

Electro-catalysis of oxygen reduction reaction

J. Rossmeisl, V. Tripković, G. Tritsaris, F. Calle-Vallejo.

Submitted to The Electrochemical Society Transactions

PAPER IV

The Pt(111)|electrolyte interface under oxygen reduction reaction conditions: an electrochemical impedance spectroscopy study

A. S. Bondarenko, I. E. L. Stephens, V. Tripković, H. A. Hansen, T. P. Johansson, F. J. Pérez-Alonso, J. Rossmeisl, J. K. Nørskov, I. Chorkendorff

In preparation

Contents

1 Introduction

As the world is becoming more advanced in technology, more energy is consumed to keep up with our changing requirements. Naturally, the question that arises is for how long we can continue like this. Quality of life is strongly correlated with energy consumption and 90% of today's energy is produced by burning carbon based fuels (oil, coal and gas) [1]. This comes with a high price, that is, the emission of CO_2 from the combustion processes into the atmosphere. The outcome of this is the huge environmental and climate changes we have witnessed over the past years. Unfortunately for our existence, natural resources are limited and what nature took million of years to produce we will have spent in just a few decades. The severity of the problem we are facing is best illustrated in **Fig. 1.1**.

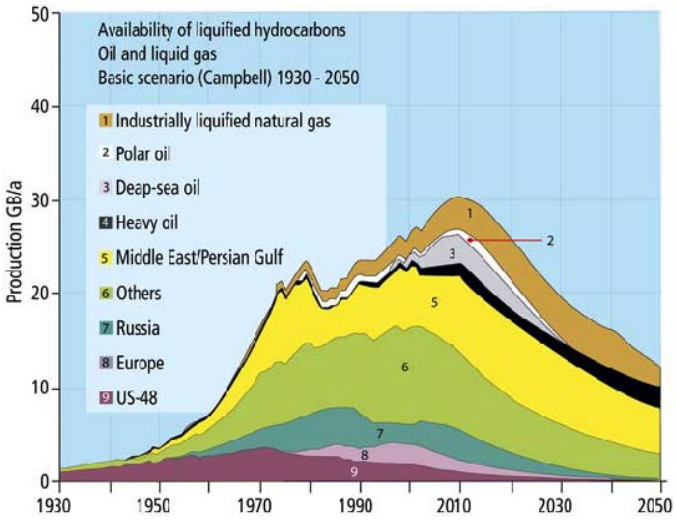

Fig. 1.1: *World Peak of Liquid Hydrocarbon Production. Taken from ref. [2]*

Evidently seen that we have already reached the climax of oil production and henceforth the production will begin to contract. To maintain the premises of the modern life and to meet future energy requirements, new alternative energy sources have to be

brought to market. Solar energy is the most abundant and ubiquitous energy source. The amount of energy adsorbed by the atmosphere, landmass and sea, is astonishing, equivalent to 89 PW [3]. To give an impression of how large this amount is, it is sufficient to say that more energy is adsorbed in an hour than annually consumed worldwide. The amount of solar energy absorbed in six months would exceed the energy that could be obtained from all the fossil and nuclear reserves on Earth. The future challenge is to find an efficient way to store solar energy in the form of chemicals such as hydrogen, ammonia, methanol, ethanol or other hydrocarbons that could be subsequently used to produce electricity.

Three different ways of harnessing the solar energy are shown in **Fig. 1.2**.The indirect way to achieve this is to grow biomass. The downside is that the process is not really efficient and diverting crops to biomass production is not politically justified. Another indirect approach is to use photovoltaics and wind generators to harness solar energy and afterwards convert it electro catalytically into chemical energy. The use of these necessitates infrastructure and the overall efficiency would be lower since the two processes (harnessing and conversion) are connected in series. The highest efficiency is attained if solar energy is converted into chemical in a single process. This could be achieved in a photo-electrochemical cell by utilizing light to split water into H_2 and O_2. Ideally these could then be converted to electrical energy in a Fuel Cell (FC) device [4,5,6].

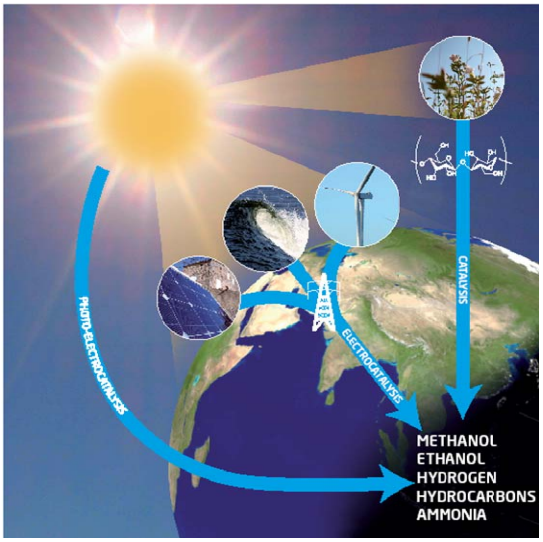

Fig. 1.2: *Different ways of harnessing the solar energy. Taken from ref. [7]*

The ultimate challenge is to construct a device that would combine the two processes. Such a dream device would be capable of producing hydrogen in one operating regime and then converting it into electrical energy upon need in the other operating regime. An unlimited energy could be thus generated under zero emission costs. A prototype of such a device is shown in **Fig. 1.3**. A catalyst is coated on the silicon rods which are used to increase the surface area. The rods have a cylindrical cross-section which have a very small diameter so that the electrons can easily reach the electrode surface where they do the chemistry. Cathode and anode material should be capable of performing both ORR/OER and HER/HOR depending on the operating regime of the cell.

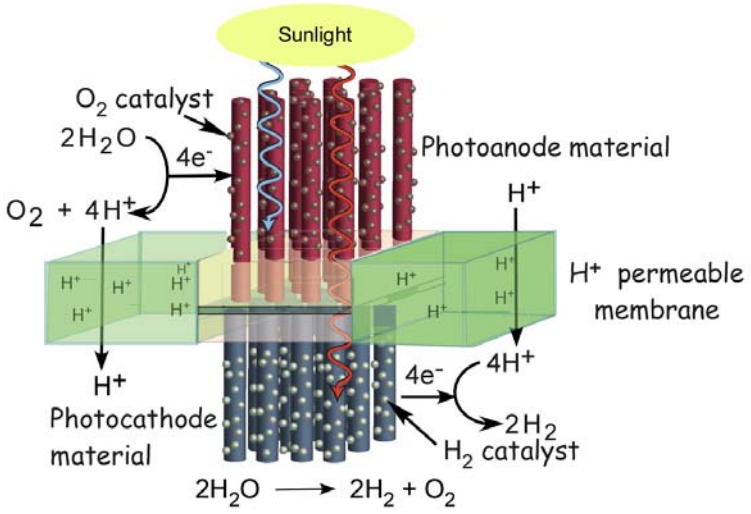

Fig. 1.3: *Combined photo-electrochemical and Fuel Cell device. Taken from ref. [8]*

In this thesis I have studied three reactions, the Hydrogen Oxidation Reaction (HOR), the Hydrogen Evolution Reaction (HER) and the Oxygen Reduction Reaction (ORR), pertaining to the anode and the cathode of such a dream device. The goal was to obtain an atomic level understanding of the electrochemical processes and to disclose the prevalent reaction mechanism, using Density Functional Theory (DFT). To be able to study electrochemical reactions within DFT in the first place we had to develop the method for explicitly controlling the surface charge and hence the bias in our simulation cell.

1.1 Outline of the thesis

Chapter 2 Here, I will define basic equations and quantities in electrochemistry. Furthermore I will address the Fuel Cell technology, stress its advantages, limitations and challenges and finally I will show how DFT calculations can be used to pinpoint promising catalytic materials.

Chapter 3 In this Chapter I will outline the formalism behind the DFT and introduce approximations to make the method feasible in practice. In addition, I will demonstrate how reaction energies and activation barriers are calculated and corrected for different effects. I will also show how a simple model for accounting the bias based on definition of a normal hydrogen electrode, is used to shift free energy levels to desired potentials.

Chapter 4 In this chapter I will introduce the method we developed to control the surface charge (potential) within the simulated unit cell. In addition, I will show that our method captures perfectly features of a Helmholtz electrical double layer model. This work refers to Papers I and II in the thesis.

Chapter 5 Here, I will benchmark the strength and accuracy of the developed method, using the example of the HOR and HER. This work refers to Paper II in the thesis.

Chapter 6 Here, I will demonstrate the importance of having an internal measure of the absolute standard hydrogen electrode potential (ASHEP) when deducing potentials from system workfunctions. Furthermore I will show that the ASHEP value is not universal but explicitly dependent on the chosen water structure. This work refers to Paper III in the thesis.

Chapter 7 In this Chapter I will present an overall free energy diagram for the oxygen reduction reaction obtained on the basis of thermodynamic and kinetic analyses. This work refers to Paper IV in the thesis.

Chapter 8 I will model bulk dissolution of zinc that takes place at the anode of a zinc/air battery. This work refers to Paper V in the thesis.

2 Background

The key to modeling surface reactions is to establish a tight link between experiments and theory. DFT is an indispensible tool because it provides information on a molecular level. For instance, it can distinguish the dominant reaction mechanism and the identity of the reaction intermediates. DFT serves as a valuable compliment to experiments because it can provide explanations to experimental observations. However, it follows that theoretical electrochemists should also be familiar with the phenomenology used by experimental electrochemists. For that reason, I will start this Chapter by reviewing some of the most commonly used equations and quantities in electrochemistry. In the second part of this chapter I will stress the versatility of DFT in modeling surface reactions and its predictive strength in screening for new catalyst materials.

2.1 Basic electrochemistry

Most of the information in this section is taken from the textbooks in ref. [9,10].

2.1.1 Butler-Volmer equation

The Butler-Volmer equation is one of the most fundamental relationships in electrochemistry which expresses the current density as a function of the overpotential. It is valid only in the potential range where the reaction kinetics is a rate limiting step.

$$j = j_a + j_k = j_0 \left\{ \exp\left(\frac{(1-\alpha)F\eta}{RT} \right) - \exp\left(-\frac{\alpha F\eta}{RT} \right) \right\} \qquad (2.1)$$

where j and j_0 are total and the exchange current density, α transfer coefficient and η the overpotential. The total current density is expressed as a sum of anodic and cathodic

current densities represented by the two terms in the brackets. A graphic illustration of the Eq. (2.1) is shown in **Fig. 2.1a**.

The exchange current density is an intrinsic property of material and in principle it shows how good catalyst a material is for a certain reaction. Its value can be increased by using more effective catalyst, increasing an active surface area, reactant concentration/pressure or raising the temperature. Influence of the exchange on the total current density is illustrated in **Fig. 2.1b**.

$$j_0 = Fk_a c_R \left(\frac{(1-\alpha)FE_r}{RT} \right) = Fk_c c_O \exp\left(-\frac{\alpha FE_r}{RT} \right) \tag{2.2}$$

where c_R, c_O, k_a and k_c are the concentrations of the reactant and product and the rate constants in the anodic and cathodic direction respectively. At low overpotentials (micropolarization region) the Eq. (2.2) collapses to a much simpler form

$$j = j_0 \frac{F\eta}{RT} \tag{2.3}$$

This linear approximation is only valid for a small potential window around equilibrium where still both of the currents contribute to the overall current density. The width of this region depends on the rate of a reaction. Eq. (2.3) can be used to extract exchange current density for the reactions characterized with very fast kinetics such as e.g. HER/HOR [11]

.

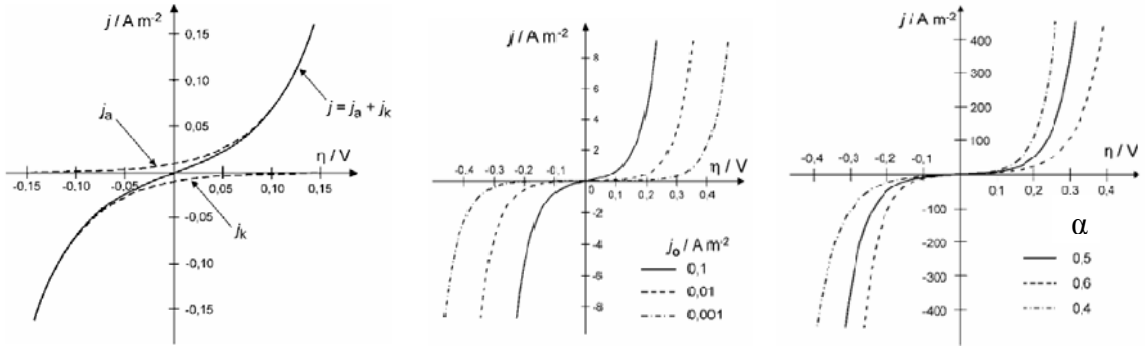

Fig. 2.1: *Graphic illustration of a) the Butler Volmer equation b) influence of the exchange current density on the total current density c) influence of transfer coefficient on the total current density. Adapter from ref. [10].*

Another form of the Butler-Volmer equation is valid for large cathodic/anodic overpotentials where anodic/cathodic currents can be neglected.

$$j = j_a = j_0 \exp\left(\frac{(1-\alpha)F\eta}{RT}\right) \text{ or} \tag{2.4}$$

$$j = j_c = -j_0 \exp\left(-\frac{\alpha F\eta}{RT}\right), \tag{2.5}$$

The minus sign in Eq. (2.5) arises because of the convention that the anodic current should always be positive whereas the cathodic should always be negative.

2.1.2 Tafel equation

Rearranging the Butler-Volmer equation by expressing the overpotential as a function of a logarithm of the current density leads to another very important equation in electrochemistry called Tafel equation.

$$\eta = a_1 \log j_0 + b_1 \log j_a = a_2 \log j_0 + b_2 \log j_c \tag{2.6}$$

where a_1, a_2, b_1, b_2 are coefficients dependent on the transfer coefficient. The exchange current density and the transfer coefficient can be obtained from the intercept and slope of a Tafel plot. The Tafel equations (Eq. (2.6)) were used intensively in the past to obtain transfer coefficients for simple reactions and to derive reaction mechanisms for complex reactions comprised of more than one electron transfer step. The problem is that it is extremely difficult to interpret Tafel slopes because they are a macroscopic property. Thus they give a picture of many processes that are simultaneously occurring on the surface of an electrode. In recent years, the use of DFT to resolve reaction mechanisms has become more widespread, as it is a more reliable tool for this purpose than the more traditional methods.

2.1.3 Transfer coefficient

This is yet another very important quantity in electrochemistry. With the help of **Fig. 2.2** I will try to explain its physical meaning. I shall assume that the potential energy profile in **Fig. 2.2** corresponds to the simplest electrochemical reaction $H^+ + e^- \rightarrow H^*$. At U=0 (full line) electrochemical potential by definition is equal to chemical potential and the transition state is located in the intersection of the potential energy curve of the reactant and the product. Activation energies (Ea_1 and Ea_2) in this case are equal in both directions. At some finite positive potential U the initial state will be stabilized by the amount ($\Delta G=eU$) and hence its energy level will shift downwards (broken line). Since the final state is potential independent, its energy will remain constant. At the same time the transition state will also move downwards but only for a fraction (α) of eU. This fraction of change is termed the transfer coefficient and how large this fraction is depends on whether the transition state resembles more the initial or the final state. Consequently at some finite U, activation energy in the oxidation direction (Ea_2) will be lowered by ($\alpha\Delta G$), whereas in the reduction direction (Ea_1) it will be increased for $(1-\alpha)\Delta G$. α thus shows how much does the activation energy change if the reaction energy is changed by ΔG. The influence of the transfer coefficient on the Butler-Volmer equation is illustrated in **Fig. 2.1c**.

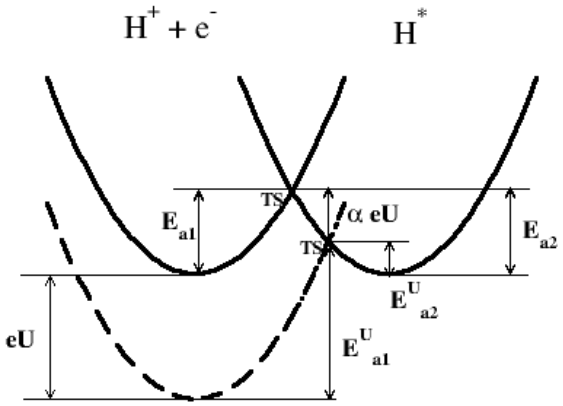

Fig. 2.2: *The free energy change during the electrochemical reaction.*

$$E_{a_1}^{U} = E_{a_1} + \alpha eU \tag{2.7}$$

$$E_{a_2}^{U} = E_{a_2} - (1-\alpha)eU \tag{2.8}$$

2.1.4 Nernst equation

The ultimate test for any kinetic reaction is that it should coincide with the equation derived from thermodynamic principles at equilibrium conditions. At equilibrium, cathodic and anodic current densities are equal and there is no net current flowing in the system. The Nernst equation can be easily derived from Eq. (2.2) if E_r is expressed as a dependent variable

$$E_r = \frac{RT}{F}\ln K - \frac{RT}{F}\ln\frac{c_R}{c_O} \tag{2.9}$$

where $K = k_k / k_a$ is the equilibrium constant and $E_r^\theta = RT/F \ln K$ is the equilibrium potential at standard conditions.

2.1.5 Cyclic voltammetry

Cyclic voltammetry (CV) is the most widely used method for studying electrochemical reactions. It can provide a significant amount of information about the investigated system. For instance, it can reveal the potential at which a reaction starts or where certain species adsorb [1], to determine the electrical double layer capacitance, the reversibility of a reaction, how many electrons are exchanged and much more. All of this makes CV and an indispensible tool in studying electrochemical reactions. I will address some of the features of CVs on the example of Pt(111) in a oxygen free $HClO_4$ solution shown in **Fig. 2.3**. Three distinct regions are clearly discernable: hydrogen adsorption (H_{upd}) region at 0-0.4 V, Double Layer (DL) region at 0.4-0.6 V and OH adsorption region (>0.6 V). Symmetry about x-axis points to a high degree of reversibility of the reaction in the reported potential window. In the H_{upd} region, H adsorbs in the fcc positions on the surface. In the DL region there are no specifically adsorbed ions and the capacitance of the charged interface can thus be easily calculated from the width of the CV. In the OH adsorption region we see two features. The first one is the shoulder attributed to a reversible OH formation, whereas the origin of the second feature is a matter of debate. It is either attributed to concurrent chloride adsorption or ordered-disordered phase transition taking place at these potentials. At even higher potentials than 0.8 V the irreversible feature relater to the oxide formation will appear.

[1] This is not always the case. For example CV cannot resolve where H^* initially adsorbs on the reconstructed Pt(110) surface.

The CV measures only the amount of charge transferred to the surface, otherwise it does not give any qualitative information as to which species is discharging. In these situations, DFT can provide improved molecular insight of the surface phenomena.

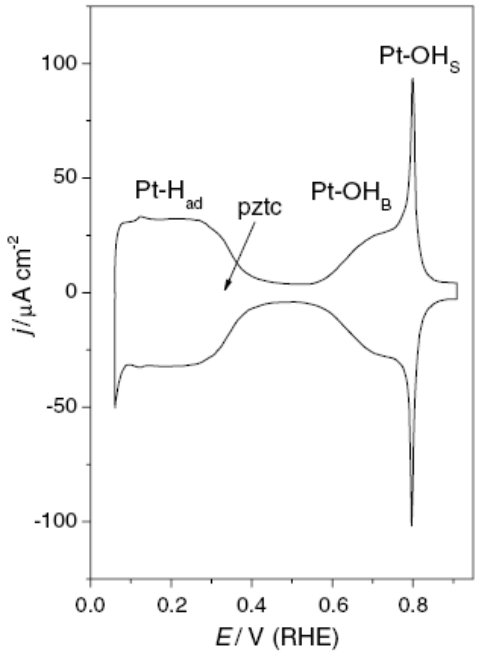

Fig. 2.3: *Cyclic voltammogram on Pt(111) in oxygen free argon-purged 0.1 M $HClO_4$ solution at 298 K and 20 mV s^{-1} sweep rate. Adapted from ref. [12].*

2.1.6 Arrhenius equation

The Arrhenius equation is a simple but astonishingly accurate empirical equation that describes temperature dependence of a rate constant. It was first proposed by Swedish scientist Svante Arrhenius in 1889. The equation is usually written in the form

$$k = \nu \cdot e^{-\frac{E_a}{RT}} \tag{2.10}$$

where k is the rate constant and ν is the pre-exponential factor or equally an attempt frequency. The Arrhenius equation can be also explained in terms of collisions. In that interpretation, k is the number of successful collisions that result in a reaction, ν is the total number of collision and the exponential factor is the probability that a certain collision will result in a reaction. Taking the natural logarithm of the Arrhenius equation yields another form of the equation:

$$\ln k = -\frac{E_a}{R}\frac{1}{T} + \ln(\nu) \qquad (2.11)$$

Eq. (2.11) can be plotted as lnk vs T. For a reaction obeying the Arrhenius equation this would give a straight line whose slope and intercept yield activation energy and pre-exponential factor for that reaction. In **Fig. 2.4** such a plot is presented for the ORR on three low index single crystal platinum surfaces at the equilibrium potential [12]. However, the reaction environment is complex and there might be several processes occurring concurrently on the surface. Similar to the Tafel slope, the rate constant is a macroscopic quantity and therefore it gives information on all of these processes[2]. Consequently it is hard to probe reaction rates at the molecular level and to extract activation energy and rate constants in the rate experiments.

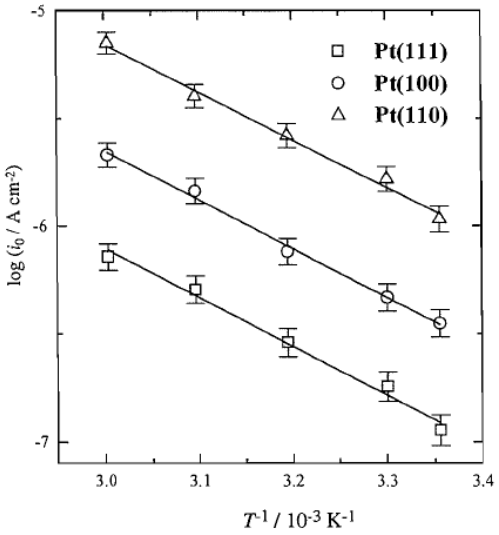

Fig. 2.4: *Arrhenius plots on three low indexed platinum monocrystals at the equilibrium potential for the ORR in H_2SO_4. Adapted from ref. [13].*

[2] For the same reason it is hard to interpret Tafel slopes.

2.2 Proton exchange membrane fuel cell

We have seen in the Introduction that in order to solve future energy requirements one would ideally need a device capable of converting solar energy to chemical fuels and then upon need chemical fuels to electrical energy. Here we will address in more detail the second part of such a device, the fuel cell. Notably, the fuel cell has been studied intensively for several decades.

It was first demonstrated by Sir William Grove in 1839 [14] that running current through electrodes immersed in an electrolyte solution, through which H_2 and O_2 is bubbled produces electricity. This simple device was named the "gas voltaic battery" and it was the forerunner of a modern proton exchange membrane fuel cell (PEMFC). The core of the PEMFC is the membrane electrode assembly (MEA, cf. **Fig. 2.5**) which comprises of proton conducting electrolyte sandwiched by two electrodes, anode and cathode respectively. The hydrogen oxidation reaction (Eq. (2.12)) on the cathode produces 2 proton and electron pairs per each hydrogen molecule. Protons move internally through a proton exchange membrane (usually made of Nafion) and the electrolyte to arrive at the cathode on the opposite side of the cell. Since the membrane is impermeable for electrons, they have to pass through an external circuit to reach the cathode where they recombine with protons and reduce oxygen to water. The flow of electrons creates a current that can be used to supply external consumers. Adding the half reactions pertaining to each electrode and their potentials together gives the overall reaction and potential of the system.

Anode:	$H_2(g) \rightarrow 2H^+ + e^-$	$E^\theta = 0$ V	(2.12)
Cathode:	$O_2 + 4H^+ + 4e^- \rightarrow H_2O(g,l)$	$E^\theta = 1.23$ V	(2.13)

Overall:	$2H_2(g) + O_2(g) \rightarrow 2H_2O(g,l)$	$E^\theta = 1.23$ V	(2.14)

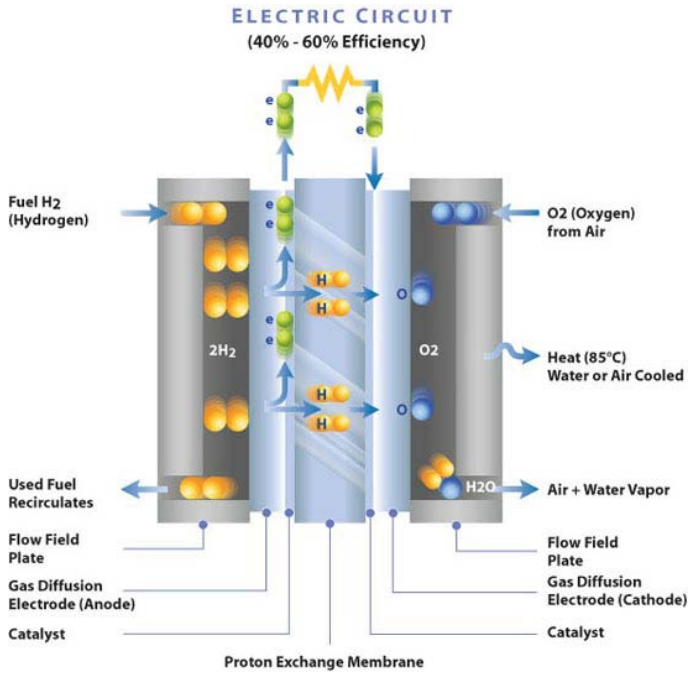

Fig. 2.5: *Schematics of the MEA. Taken from [15].*

The overall reaction is exorgonic by 241/286 kJ/mol, or 1.23/1.48eV per hydrogen molecule at standard conditions, depending on whether water is in the gas or liquid phase. This value is also known as the reversible open circuit voltage (OCV) and it corresponds to the condition where there is no load in the system or thermodynamically to the maximum work that can be extracted out of a system. The value is temperature sensitive and it decreases with increasing temperature.

The goal behind the FC technology is to try to convert major part of the reversible potential into electrical energy. In the next section I will show the basics of the PEMFC and what are the crucial factors limiting its performance.

Even tough the theoretical efficiency of the PEMFC is very high (83%), its practical value is much lower (40-60%) [16]. Nevertheless it is still more than in the engines with the internal combustion, which are limited by Carnot's efficiency to less than 40%. Losses can be quantified in terms of overvoltage or the voltage superimposed over the reversible voltage. There are in principle 3 major causes of irreversibility. They are quantified in **Fig. 2.6**, using the example of the state-of-the-art PEMFC [17].

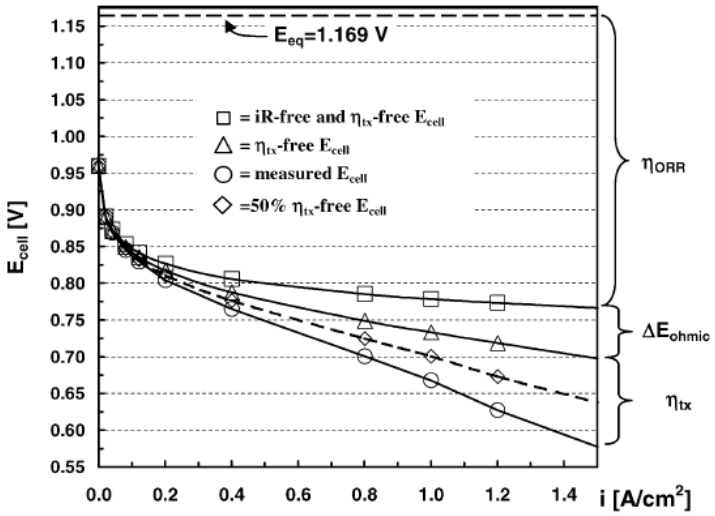

Fig. 2.6: *Influence of different irreversibilities on the voltage drop in the state-of-the-art PEMFC at 80 C and 100% relative humidity, with Pt/C nanoparticulate catalysts. The equilibrium potential at these conditions is 1.169 V. (a) squares: activation losses (b) triangles: activation and ohmic losses (c) circles: activation, ohmic and mass transport losses (d) diamonds: activation, ohmic and 50% of mass transport losses. Adapted from ref. [17].*

Activation losses (squares) originate from the slow reaction kinetics on an electrode. Certainly they are material dependent.

Ohmic losses arise as a consequence of electric resistance of the electrodes and the electrolyte. They are linearly dependent on the current.

Mass transport losses arise when rate of a reaction is sufficiently high that one of the reactants is immediately consumed when supplied to the surface of an electrode. When the mass transport losses become rate limiting, which usually occurs at high overpotentials, the current density reaches a plateau (diffusion limited current).

As one can infer from **Fig. 2.6**, activation losses constitute the largest part of the voltage drop (ca. 0.4 V) and there are primarily related to the sluggishness of the ORR at the cathode. Furthermore platinum, a very scarce and expensive metal, is found to be the best catalyst for this reaction. Research efforts are therefore concentrated in eliminating platinum or at least significantly reducing its amount without affecting the PEMFC performance to meet future automotive demands [18].

We get an impression of how much platinum presently limits the FC technology by performing a simple “gedanken experiment”. The annual supply of platinum is about 130

tones. The state of the art FC demands around 1g of Pt per kW of power [17]. For a normal city car of around 80 kW this implies ~80 g of platinum per FC stack. If we divide the annual production of Pt by the amount needed to make the single FC stack we would get that only ~1.6 million cars can be annually built with the present FC technology.

$$N_{cars} = \frac{\text{annual Pt production}}{\text{amount of Pt per car}} \approx 1.6 \text{ million} \qquad (2.15)$$

Moreover this is under constraint that all the platinum mined is used only for this purpose. Cost wisely with the present Pt price of 1550 $/oz (~55 $/g) [19] this translates to 4400 $ for Pt content without considering other parts of the MEA. The short term goal is therefore to reduce the amount of platinum by at least factor of 4-8 [17,18].

Besides, considerable efforts have to be devoted to FC design, especially concerning heat and water management, although this is more of a problem of the technical nature than fundamental.

2.3 Catalysis from first principles

Catalysis is a large field that encompasses all the chemical reactions that are fostered by use of specific substances called catalysts. Unlike other reagents, catalysts speed up reaction rates by lowering transition state energies, hence increasing a probability of reactants to undergo change. Besides, catalysts are not self consumed in a reaction. The production of most industrially important chemicals involves catalysis. For instance, catalysis plays a key role in the production of ammonia which is the main feedstock in production of fertilizers. The ammonia is produced via the so-called Haber-Bosch (HB) process which is boosted by many orders of magnitude if catalysts are used. The use of fertilizers is essential in agriculture and for this reason they are one of the major contributors to the world's population boom. The Earth houses more than 6 billion people today or 6 times more than the amount, prior to the discovery of the HB process [20]. Besides, catalysts are inevitable factor in petrochemical, pharmaceutical, automotive and many other industries [21]. Hence it would be hard to conceive a modern society without catalysts.

The largest drawback in catalysis is that usually transition metals and their compounds are found to be the best catalyst materials. Unfortunately some of these are also the scarcest metals and most expensive to produce. Our future goal and the ultimate aim of the present research would be to find suitable replacements made of earth abundant materials.

Modern world faces many other challenges and problems that should be resolved. We are closing to the end of a fossil fuel era and before draining the last drop of oil we should have new alternative energy sources ready to take over the job. One of the options on this path is to e.g. reduce carbon dioxide to hydrocarbons (artificial photosynthesis) which can be then used to synthesize fuels or alternatively to produce electricity from the solar energy by means of photo-electrocatalysis [22,4]. In this way both environmental and energetic issues would be solved for good. Adoption of new technologies and processes and the improvement of the present ones call for new, more active and selective catalysts. Large part in this field is still uncharted and it is on scientific community and individuals to demonstrate they can rise to the challenge.

Significant steps have been made in the past in understanding the connection between a catalytic behavior and electronic structure. It is a common fact that the electronic structure is intimately related to material structure and composition. Based on this insight we have shown why particular materials are good catalysts for almost all vital reactions. Furthermore it has been demonstrated in dozen of cases how one can promote catalytic activity by modifying surface composition. Ultimately with technological progress it should be possible to desirably tune catalytic behavior of a material by tailoring its composition atom by atom [23].

Naturally question arises as to where density functional theory (DFT) fits in this picture? DFT is a powerful and accurate enough tool to enable large scale screening studies targeted to discover new catalytic materials. The advantage of DFT is that it can promptly analyze hundreds of structures and pinpoint the best catalyst candidates which enabled the possibility of computer based catalyst design. This in contrast to the present experimental tools where sometimes days, maybe even months are needed to perform a single experiment correctly.

2.3.1 Trends and activity descriptors

DFT is usually considered to perform semi-quantitatively although there have been some cases where complete kinetics of a catalytic reaction have been assessed via DFT [24,25,26,27]. In such instances, experiment and theory agreed surprisingly well, taken into account the level of accuracy of DFT. In the thesis I will present another case where the kinetic model based exclusively on the inputs from DFT agreed exceptionally well with the experimental measured activities. On the other hand, it is well established that DFT can provide the interaction energies of molecules and atoms with metal surfaces with sufficient accuracy to describe trends in reactivity for transition metals and alloys.

The origin of the trends can be traced back to the changes in the electronic structure of material induced by adsorption. Deviations from the trends arise because species sometimes bind to different adsorption sites depending on the metal substrate. This "geometrical effect"[3] can be best viewed as a difference in trends among sites with different atomic coordination. In that sense adsorption energies on terraces, steps, kinks and other defects scale linearly with the same slope whereas the strength of adsorption (the intercept) varies substantially [28,29,30,31]. Trends give rise to volcano plots which can be rationalized in terms of a Sabatier principle [32] which states that the optimal catalyst is the one that has binds moderately. If it binds too weakly adsorbents will fail to react on the surface and if it binds to strongly products will fail to desorb. Different classes of material obey different trends, hence they fall on different volcano plots, e.g. metals and alloys follow one trend [33], whereas metal oxides follow another trend [34]. Trends are not a new phenomenon; they have been perceived ca. 50 years ago and studied ever since. The activity was first correlated to the metal work function [35,36,37,38], but, since the work functions were not precisely known, latter authors decided to choose metal-adsorbate bond strength as the activity descriptor [39,40,41]. These early studies showed there a unique physical quantity can be identified, that determines the macroscopic activity.

A number of these *descriptors* have been identified for different chemical reactions. For instance, in the case of the HER/HOR, ORR and the electrochemical ammonia

[3] The Geometrical effect is also caused by the changes in the electronic structure. It has been simply given different name to distinguish it from the "true electronic effect" associated with differences seen across metal substrates.

synthesis reaction, oxygen [42], hydrogen [43] and nitrogen [44] binding energies were found to be universal descriptors of activity. For some other reactions, where splitting of the chemical bond is a rate determining step (methanation reaction, NO decomposition reaction), dissociation barriers were found to be good descriptors of activity (CO and NO dissociation energy) [45,46]. In some cases (methane oxidation) two descriptors were required (C and O binding energy) [47,48,49] to describe the activity. Using the example of the ORR, I will explain how activity can be predicted from simple scaling relations and why is platinum the best single element catalyst for this reactions.

Even though the ORR appears to be a simple reaction, in reality it is a very complicated reaction that involves 4 electron transfer steps and many reaction intermediates. It has been shown that the binding energies of the intermediates which bind to the surface via the same kind of atom scale linearly with each other [28]. This is a simple consequence of number of bonds they make to the surface, *viz.*, O makes 2 bonds, OOH and OH one bond, while HOOH and H_2O[4] make 0 bonds to the surface. When these are scaled against e.g. O binding energy this simple bond counting will manifest as 0.5 slope for OOH and OH species and 0 slope for HOOH and H_2O. The scaling relations will give rise to a volcano plot with the oxygen binding energy being the unique descriptor of activity [42]. For a detailed procedure of how to construct a volcano plot from scaling relationships I refer to ref. [34]. In the case of ORR, activity is limited by two rate determining steps (the OOH formation and OH removal). Which one prevails depends on the strength of the metal-oxygen bond. This can be better illustrated with a potential energy diagram shown in **Fig. 2.7** for ORR on Pt(111). The best catalyst for this reaction would be the one where all the reaction steps are downhill in free energy at the potential slightly below the equilibrium potential. This corresponds to the dashed line in **Fig. 2.7** where all the steps have the same change in free energy at U=0V. At equilibrium potential every step will be shifted by integral multiplies of nU where n is the number of electrons involved in the reaction. Pt(111) deviates from the optimal catalyst in a way that it binds OH too strongly and OOH too weakly.

[4] These are the closed shell molecules hence they do not bind strongly to the surface

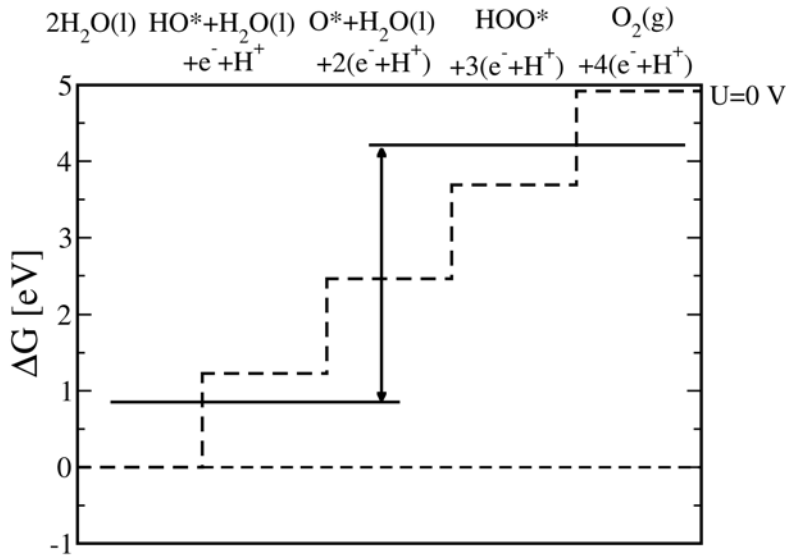

Fig. 2.7: *The free energy diagram for ORR. Free energy steps of a perfect catalyst are shown with dashed lines. The linear relation between HOO* and HO* implies that for any catalyst the two intermediates are separated by ~3.2 eV-2eU. At equilibrium (U=1.23 V) this gives ½(3.2 eV-2.46 eV)/e ~0.4 V.*

From the above analysis we have seen that the binding energies of OOH and OH are linearly correlated. Consequently it is impossible to change one independently of the other. Moreover because of the same sign of the slope in scaling relations, this change always needs to be in the same direction. The free energy difference between OH and OOH scaling relations is ~3.2 eV [50]. For a catalyst with no overpotential the difference should equal two times the equilibrium potential or 2.46 eV. This implies that even the best catalyst, the one at the volcano peak, will still feature ~0.4 V voltage drop (overpotential). The most one can do is to place the OOH and OH free energy levels symmetrically with respect to the ideal OOH and OH positions (black arrow in **Fig. 2.7**). This can be achieved by slightly tuning the oxygen binding energy of Pt by means of alloying it with some other transition metals. The activities of the best catalyst materials are compared in a volcano plot in **Fig. 2.8**.

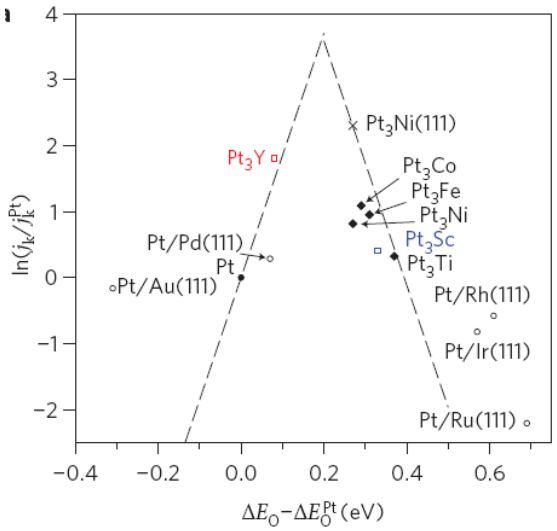

Fig. 2.8: *Volcano plot of exchange current density versus oxygen binding energy for the catalytically active alloy catalysts for the ORR. Both axes are normalized with respect to Pt(111). Adapted from ref. [51].*

2.3.2 Stability

Sometimes, working conditions demand very durable and resistant catalysts. Cathode materials in acidic PEMFC are exposed to very harsh environment (high potentials and strong acidic conditions) under which conditions only few pristine metal electrodes are stable. The harsh operating environment of the PEMFC is not even sufficiently benign to prevent the corrosion of Pt at the equilibrium potential, 1.23 V. Nevertheless, the operating voltage is always lower at ca. 0.65-0.9V. One of the approaches to reduce amount of platinum is to alloy it with some non-precious metal catalyst such as V, Cr, Fe, Ni, Co, Cu [52,53,54,55,56]. These alloys are coated with platinum in order to prevent dissolution of a less noble component. Since most of the compounds do not form stable alloys, the less noble component will tend to segregate to the surface and leach over time. More stable Pt alloy catalysts, with an activity an order of magnitude higher than Pt have recently been reported [51]. However, their performance under PEMFC operating conditions still remains to be tested. From the above analysis it is evident that stability criterion is as important as activity criterion. A promising means of identifiyng a new catalyst material is to plot the two descriptors against each other as shown in **Fig. 2.9**. The oxygen binding energy is the activity criterion in this case (cf. **Fig. 2.8**).

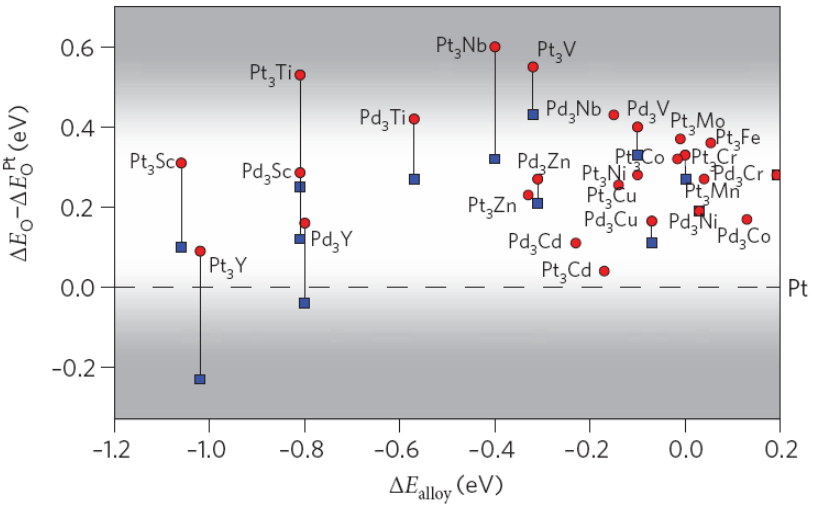

Fig. 2.9: *Activity of a rangeof alloy catalysts for the ORR plotted against its stability. Both axis are normalized to Pt. The solute content in the second layer is denoted by the blue square (25%) and the red circles (50%). The range of the interesting oxygen binding energies is highlighted in brighter tone of a grayscale gradient. Adapted from ref. [51].*

2.3.3 Selectivity

Selectivity implies favoring specific reaction pathway among several others. Selectivity is of a major interest, particularly in the petrochemical industry where many products can be formed, depending on the catalyst and reaction conditions. The aim of a selective catalyst is to increase yield of main reaction products and suppress yield of unwanted side-products. To desirably tune the selectivity, one should first determine the overall reaction pathway and use that knowledge to gain insight as to which barrier should be increased/decreased to eliminate/maximize yield of specific reaction products. Several successful examples of promoting selectivity with the help of DFT can be found in the literature [57,58].

2.3.4 Cost and supply

Supply is associated with the abundance of material in the earth's crust whereas the cost depends on the processing cost to produce metal from its ore. However, the cost and supply are usually correlated, meaning that the more abundant the metal cheaper it is to produce and vice versa. The problem is that the catalytic behavior scales in the exact reverse way. Consequently, transition metals are usually found to be the best catalytic materials. The main research efforts in the future should be thus directed toward design

of new catalyst made of earth abundant materials. Some steps have already been made in this direction [6,59].

Activities should always be scaled to price since market is, after all an ultimate test of any catalyst quality. For this purpose, activity and price are often scaled in the so-called Pareto plots where the best catalyst materials are connected with a Pareto-optimal line. The outcome of a large scale screening study of different metals and alloys for the methanation reaction is shown in the form of a Pareto plot in **Fig. 2.10**. The activity descriptor (x-axis) in this case is the CO dissociation energy. The closer the descriptor lies to the optimum value, the better the predicted catalytic activity. The Pareto optimal set of solutions is connected by a solid line, which defines the best compromise between price and catalytic performance.

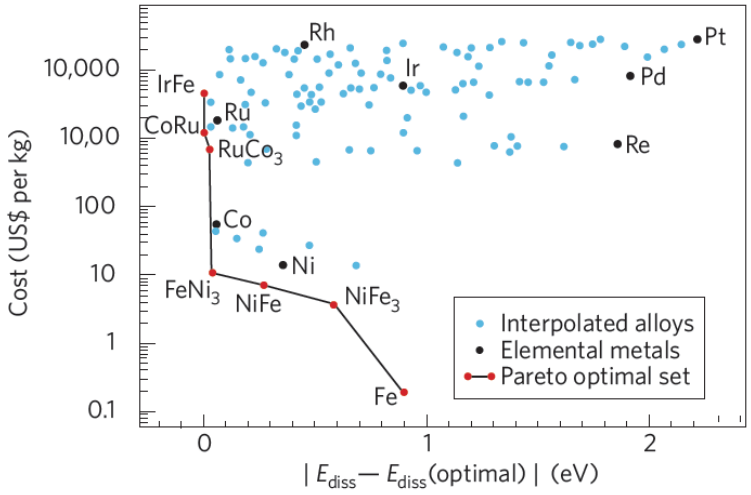

Fig. 2.10 *Pareto optimal plot - cost as a function of the normalized CO dissociation energy. The best set of solutions is connected with a Pareto optimal line. Adapted from ref. [60].*

2.4 Summary

In this chapter I have outlined some of the basic equations and quantities in the electrochemistry. Many of these will be summoned in the later chapters especially when we compare the level of agreement between theory and experiments. Additionally, I have shown the strength of DFT and in which way it can assist to the quest of finding better, cheaper and more durable catalysts.

3 Theoretical methods and tools

All results in this thesis are obtained from Density Functional Theory (DFT) calculations. In this chapter basic concepts behind the DFT will be introduced and its limitations and advantages will be contemplated. Methodology behind new Van der Waals density functional will be also briefly addressed. Second part of this Chapter is devoted to implementing DFT and which approximations have to be made to make DFT feasible in practice. At the end important theoretical tools such as standard hydrogen electrode will be presented and discussed.

3.1 Density functional theory

Density functional theory is an extremely successful quantum mechanical approach to matter. DFT became a leading method for investigation of the ground state electronic structure of many-body systems and it is now widely applied in chemistry, solid state physics and it also becomes increasingly popular in biology. This high popularity DFT owes to simplicity of its fundamental concepts and the flexibility one has in implementing them. Versatility of DFT allows one to calculate binding energies, lattice constants, bulk moduli, cohesive energies, band structures and other material properties with reasonable accuracy. On the other hand it substantially and systematically underestimates band gaps and it fails to describe the strong correlated systems such as transition metal oxides.

Advantage of DFT compared to other quantum computational methods is that it is much less computationally demanding without it reflecting dramatically on the accuracy of physical observables. Unlike other methods such as Coupled Cluster, Møller-Plesset or Configuration Interaction which work with wave functions, DFT relies solely on the electron density. Hence solving many-body problem in 3N (N-number of quantum particles) vector space can be mapped to a much simpler problem of solving for only 3

independent variables. The impact the DFT made on modern chemistry and physics was acknowledged by awarding its founding father Walter Kohn with the Noble Prize in Chemistry. Noble prize was co-shared with John People who worked on implementing DFT in chemistry. In the following I will present the transition between the classical quantum-mechanical to the DFT formalism. Naturally Schrodinger equation is the best place to start with.

3.1.1 Schrödinger equation

The time dependent Schrödinger equation (SE) describes the evolution of any quantum mechanical state in time. It was derived by German physicist Erwin Schrödinger in 1926. This is a central equation in quantum mechanics and in a macroscopical limit it reduces to Newton's second law. In its full form SE is written as

$$i\hbar\frac{\partial}{\partial t}\Psi(R_1,R_2,...R_N,r_1,r_2,...,r_n)=\hat{H}\Psi(R_1,R_2,...R_N,r_1,r_2,...,r_n). \quad (3.1)$$

where $\Psi(R_1,R_2,...R_N,r_1,r_2,...,r_n)$ is the wavefunction depending on nuclear and electron coordinates. For a stationary system this equation simplifies to

$$E\Psi=\hat{H}\Psi. \quad (3.2)$$

where the energy operator $\hat{H}$ or the Hamiltonian reads

$$\hat{H}=\hat{T}_n+\hat{T}_e+\hat{U}_{nn}+\hat{U}_{ee}+\hat{V}_{ext}. \quad (3.3)$$

The operators on the right hand side are defined as:

$\hat{T}_n+\hat{T}_e$ - nuclear and the electronic kinetic energy

$\hat{U}_{nn}+\hat{U}_{ee}$ - nuclear-nuclear and electron-electron interaction energy

$\hat{V}_{ext}$ - external potential

We note here that relativistic effects are not taken into account in Eq. (3.2). SE is a tremendously complex partial differential equation. It is dependent on 3N nuclear and 3n electron coordinates. To be able to solve it we have to introduce some approximations.

First in line is the Born-Oppenheimer (BO) approximation which states that total wave function can be broken into the product of its nuclear and electronic component.

$$\Psi(\mathrm{r},\mathrm{R}) = \Psi_{\mathrm{e}}(\mathrm{r},\mathrm{R})\Psi_{\mathrm{n}}(\mathrm{R}) \tag{3.4}$$

The Born-Oppenheimer approximation rests on the fact that the nuclei are much more massive than the electrons, which allows us to say that they are nearly fixed with respect to electron motion (kinetic energy is negligible). We can fix R, the nuclear configuration, at some value Ra, and solve for the electronic wavefunction ψ(r,Ra). If we do this for a range of R, we obtain the potential energy curve along which the nuclei move. After applying BO approximation Hamiltonian simplifies to

$$\hat{\mathrm{H}} = \hat{\mathrm{T}}_{\mathrm{e}} + \hat{\mathrm{U}}_{\mathrm{ee}} + \hat{\mathrm{V}}_{\mathrm{ext}}. \tag{3.5}$$

Here the kinetic energy operator is defined as

$$\hat{\mathrm{T}}_{\mathrm{e}} = -\frac{\hbar^2}{2\mathrm{m}}\sum_{\mathrm{i}}\nabla_{\mathrm{i}}^2. \tag{3.6}$$

where *i* extends over all electrons in the system. Second term represents the electron-electron interaction and it is analogous to its classical counterpart-Coulomb potential. This term separates single-body from the many-body quantum mechanics.

$$\hat{\mathrm{U}}_{\mathrm{H}} = \sum_{\mathrm{i<j}} \mathrm{U}(\mathrm{r}_{\mathrm{i}},\mathrm{r}_{\mathrm{j}}) = \sum_{\mathrm{i<j}} \frac{\mathrm{q}^2}{\left|\mathrm{r}_{\mathrm{i}} - \mathrm{r}_{\mathrm{j}}\right|} \tag{3.7}$$

What distinguishes system from being an atom, bulk or solid is contained in $\hat{V}_{ext}$. This term is called external potential, since the lattice potential energy is external to the electron system. An external potential acting on the system will be also contained in this term.

$$\hat{V}_{ext} = \sum_{ik} \frac{Q_k q}{|r_i - R_k|} \tag{3.8}$$

where sum on k extends over all nuclei and the sum on i over all electrons in the system.

Procedure for solving SE is to first specify the external potential by choosing the system. Solution of this equation yields electronic wave functions. Taking expectation values of operators with respect to these wavefunctions yields all other physical observables. One among others is the electron density.

$$n(r) = N\int d^3r_2 \int d^3r_3 ... \int d^3r_N \Psi^*(r, r_2, ..., r_N) N\Psi(r, r_2, ..., r_N) \tag{3.9}$$

The complexity of using wavefunction could be alleviated if one could find a suitable way of inverting the problem and use the electron density instead. It looks rather infeasible at first sight, that a variable dependent on 3 parameters can contain the same information as the one dependent on 3n parameters. It will be shown later that this kind of mapping is indeed possible. The formalism of the transition from electron wavefunction to electron density constitutes the basis of the Hohenberg Kohn theory.

3.1.2 Hohenberg-Kohn theorem

In the center of DFT lies the Hohenberg-Kohn (HK) theory. This theorem is composed of two statements [61].

1. The first one states that a nondegenerate ground-state (GS) wavefunction is a unique functional of the GS density. In other words there is no other density that reproduces the same wavefunction. This one to one mapping between the electron density and the wavefunction constitutes the heart of DFT. Consequently all other physical observables (O) are also unique functionals of electron density.

$$\Psi_0(r_1, r_2, ..., r_n) = \Psi[n_0(r)] \tag{3.10}$$

$$O_0 = O[n_0] = \left\langle \Psi[n_0] \middle| \hat{H} \middle| \Psi[n_0] \right\rangle \tag{3.11}$$

2. Second statement says that minimization of GS wavefunction yields the GS energy. Hence no other density can yield energy below the true GS energy.

   If the ground state is degenerate, several of the degenerate GS wave functions may produce the same density, so that unique functional of Ψ[n] does not exist; however by definition of Eq. (3.11) they will still yield the same ground state energy.

$$E_0 = E[n_0] = \left\langle \Psi[n_0] \middle| \hat{H} \middle| \Psi[n_0] \right\rangle \tag{3.12}$$

$$E[n_0] \leq E\ [n'] \tag{3.13}$$

   where n' is some density other than GS density.

3.1.3 Kohn-Sham equations

Hamiltonian can be divided into three terms Eq. (3.5) Here we will closely examine each one of them. The kinetic energy operator can be written as a sum of two terms:

$$T_e[n] = T_s[n] + T_c[n] \tag{3.14}$$

where $T_s[n]$ stands for the kinetic energy operator of non interacting electrons and $T_c[n]$ is a remainder that accounts for the electron interactions.

The first term is easy to calculate since the total electron kinetic energy is just a sum of individual electron kinetic energies. This term can be expressed as a function of single particle orbitals.

$$T_s = -\frac{\hbar^2}{2m} \sum_i^N \int d^3 r \varphi_i^*(r) \nabla^2 \varphi_i(r) \tag{3.15}$$

Neglecting the $T_c[n]$ term in Eq. (3.14) yields Thomas Fermi (TF) theory which was a forerunner of modern DFT. A major defect of the TF theory is that it did not produce any binding. Energy of isolated atoms was systematically lower than the energy of the same atoms bound in a molecule. This defect clearly stresses the importance of explicitly including the interactions.

In a similar fashion electron interaction energy term can be also expressed as a sum

$$U[n] = U_H[n] + U_c[n]. \tag{3.16}$$

where U_H is the classical Hartree potential introduced at the beginning of this chapter and U_c accounts again for a non-Coulomb interaction. Since T_c and U_c both describe the interactions and are not exactly known, they can be lumped together in a common term called exchange-correlation energy.

$$E_{xc} = U_c + T_c \tag{3.17}$$

In the next section I will address nature of this functional and introduce some simple approximations to account for it. After defining all the terms we can finally write the total energy as

$$E[n] = T_e[n] + U_H[n] + V_{ext}[n] = T_S\left[\left(\varphi[n]\right)\right] + U_H[n] + E_{xc}[n] + V[n]. \tag{3.18}$$

Since T_S in Eq. (3.15) is written as a functional of the orbitals, it cannot be directly minimized with respect to n. Fortunately Kohn and Sham devised a method of how to workaround this problem [62]. After minimization Eq. (3.18) can be written as

$$\frac{\delta E[n]}{\delta n(r)} = \frac{\delta T_S}{\delta n(r)} + \frac{\delta V_{ext}[n]}{\delta n(r)} + \frac{\delta U_H[n]}{\delta n(r)} + \frac{\delta E_{xc}[n]}{\delta n(r)} = \frac{\delta T_S}{\delta n(r)} + \nu_{ext}(r) + \nu_H(r) + \nu_{xc}(r). \tag{3.19}$$

The last three terms on the right hand side are known as external, Hartree and exchange-correlation potential. Similarly the minimization in the case of non-interacting system yields

$$0 = \frac{\delta E_S[n]}{\delta n(r)} = \frac{\delta T_S}{\delta n(r)} + \frac{\delta V_S[n]}{\delta n(r)} = \frac{\delta T_S}{\delta n(r)} + \nu_S(r). \tag{3.20}$$

where subscript S stands for non-interacting system. Hartree and XC terms are absent because there are no interactions. Comparison of the two last equations gives

$$\nu_S(r) = \nu_{ext}(r) + \nu_H(r) + \nu_{xc}(r). \tag{3.21}$$

The beauty of this theory is that one can now replace the external, Hartree and XC potential of interacting system with the noninteracting $\nu_S(r)$ which is much easier to deal with. In this way it is possible to solve the non-interacting SE and to get the wave functions or the KS orbitals of the new system.

$$\left[-\frac{\hbar^2 \nabla^2}{2m} + \nu_S(r) \right] \varphi_i(r) = \varepsilon_i \varphi_i(r) \tag{3.22}$$

It is noteworthy to stress that the KS orbitals are eigenstates of an auxiliary single-body equation. Hence they do not posses any physical meaning and therefore they are not to be trusted quantitatively. The only exception to this rule are the eigenvalues corresponding to the highest occupied and the lowest unoccupied molecular orbitals or HOMO and LUMO respectively. However, this holds just for the exact XC functional that is in principle not known. KS orbitals produce the electron density of the system via

$$n(r) = n_S(r) = \Sigma_i^N f_i \left| \varphi_i(r) \right|^2 . \tag{3.23}$$

where f_i is the occupation of the i^{th} orbital.

KS equations, Eq (3.21) and (3.22) have to be solved self consistently, since ν_H and ν_{xc} are both dependent on the electron density and electron density is itself dependent on the wavefunctions. The usual way of solving these problems is to start with an initial guess for the electron density; then calculate the Hartree and the XC potential and then solve the SE for φ_i. From those a new electron density can be calculated (Eq. (3.23)) that becomes a starting guess for the next iteration. This process is repeated until convergence with respect to density, energy and occupancy is reached. The converged solution will give the GS electron density that is used to calculate the total energy of the system from

$$E_0 = \Sigma_i^N \varepsilon_i - \frac{1}{2}\iint \frac{n_0(r)n_0(r')}{|r-r'|}drdr' - \int \nu_{xc}(r)n_0(r)dr + E_{xc}\left[n_0(r)\right]. \qquad (3.24)$$

where the first term on the right hand side represents the sum of the single particle energies and the rest accounts for the energy reduction due to the electron interactions. As HK theorem replaced the problem of solving the interacting SE by performing minimization of energy functional; KS equations replaced that problem by solving the noninteracting SE. By means of both HK and KS theory initial problem of solving interacting SE was ultimately replaced by much easier problem of solving the noninteracting SE.

3.1.4 Exchange-correlation functional

Here I return back to the problem pertaining to the XC energy. This is the only term that is not explicitly known in DFT and therefore it entails a special attention. The name originates from its two constituents, viz., exchange and correlation.

$$E_{xc}\left[n\right] = E_x\left[n\right] + E_c\left[n\right] \qquad (3.25)$$

The exchange component E_x describes the energy lowering due to the tendency of like-spin electrons to avoid each other (antisymmetrazation). It can be expressed in terms of KS or equally Hartree-Fock orbitals.

$$E_x\left[\left(\varphi_i[n]\right)\right] = -\frac{q^2}{2}\Sigma_{jk}\int d^3r\int d^3r'\frac{\varphi_j^*(r)\varphi_k^*(r')\varphi_j(r')\varphi_k(r)}{|r-r'|} \tag{3.26}$$

This is a genuine quantum phenomenon without an analogue in classical physics.

Correlation is a well-known mathematical concept that describes the fact that certain events are not independent. If they were independent then the probability of the composed event would be equal to the product of the probabilities of individual events. Translated to quantum mechanics, the wavefunction of the many-body system does not equal the product of single particle wave functions. Due to the correlation effect even the electrons with the opposite spin would like to avoid each other. As a contrast to exchange energy there is no explicit expression for the correlation energy. Hence it has to be approximated in some manner. This renders DFT an approximate tool in practice, even tough the theory behind it is exact.

Functionals that rely on Eq. (3.26) are called exact exchange functionals. The problem is that the correct description of exchange does not warrant more accurate results. Au contrary, it proves much easier to find approximations for both terms. Although, in order to get more accurate results, it is sometimes instructive to include a fraction of exchange like it was done in construction of PBE0 functional where ¼ of exact exchange was included [63]. This particular functional gives much better results for band gaps owing to this fraction of exchange.

There are certain rules to be obeyed when developing new exchange-correlation energy function but this is beyond this simple introduction about DFT. In the following I will introduce two most common approximations for the XC energy, viz., Local Density Approximation (LDA) and General Gradient Approximation (GGA).

LDA is the most simple and successful approximation. It is based on the homogenous electron gas model. In this approach the density is considered to be constant and equal to the density of a homogeneous electron gas within small unit volumes and the integration over the whole space gives the total electron density.

$$E_{xc}[n] \approx E_{xc}^{LDA}[n] = \int d^3r\, e_{xc}^{hom}(n(r)) \tag{3.27}$$

$$e_{xc}^{hom} = e_x^{hom} + e_c^{hom}, \quad e_x^{hom}(n) = -\frac{3q^2}{4}\left(\frac{3}{\pi}\right)^{1/3} n^{4/3} \tag{3.28}$$

where e_x^{hom} is the exchange energy per volume of the homogenous electron gas and e_c^{hom} is its correlation counterpart that is now known exactly. The reason LDA gives remarkable good results, even for the systems with varying electron density such as solids and molecules, is due to the systematical error cancelation between exchange and correlation. This is another reason that methods where exchange is treated separately do not necessary perform better than this simple approximation. One can build on LDA by inclusion of another term that depends on the spatial variation of the electron density. This gives better results for inhomogeneous systems such as transition metals.

Functionals that depend locally on the electron density and its gradient are known generalized-gradient approximations (GGAs). They have the general form

$$E_{xc}^{GGA}[n] = \int d^3r\, f(n(r), \nabla n(r)). \tag{3.29}$$

where $\nabla n(r)$ is the electron density gradient.

In the thesis I used RPBE-GGA functional which was developed on the basis of popular PBE functional [64]. This functional gave better adsorption energies for small atoms and molecules on metal surfaces [65].

3.1.5 Van der Waals functional

We have seen that LDA functional performs well for homogenous systems, while GGA functionals perform better for inhomogenous systems such as transition metals. Problem with those functionals is that they are locally and semi-locally dependent on the electron density, therefore they cannot directly take into account long-ranged non-local interactions such as Van der Waals (VdW) forces. For weak interacting systems they are sometimes the only forces responsible for bonding. This calls for development of new XC functional that will take these effects into account.

In chapter 7 we have performed VdW calculations to determine water bilayer stabilization on Pt(111) surface. For this purpose we have used VdW XC density

functional proposed by Dion et al. [66]. The formalism behind it will be briefly summarized here. In this scheme the XC energy can be written as a sum

$$E_{xc}^{VdW}[n] = E_x^{revPBE}[n] + E_c^0[n] + E_c^{nl}[n]. \tag{3.30}$$

where $E_x^{revPBE}[n]$ is the exchange term from revPBE functional [67], while $E_c^0[n]$ and $E_c^{nl}[n]$ are two terms that account for short and long range correlation effects. In our case $E_x^{RPBE}[n]$ has been used instead, but the choice of the exchange functional should not matter as long as its exchange is similar to the exact exchange from Hartree-Fock. $E_c^0[n]$ is a short range nonlocal term and it can be approximated by the LDA correlation. The $E_c^{nl}[n]$ term is more difficult to deal with and in ref. [66] the authors have proposed an exact term at long distances to account for it.

$$E_c^{nl} = \int_0^\infty \frac{du}{2\pi} \mathrm{tr}\left[\ln\left(1 - V\tilde{\chi}\right) - \ln\varepsilon\right] \tag{3.31}$$

where $\tilde{\chi}$ is the density response to a fully self-consistent potential, V is the interelectronic Coulomb interaction, ε the approximated dielectric function and “u” is the imaginary frequency.

Performance of this XC functional has been tested on a few typical VdW dominant systems. One of them is benzene dimmer. Results for few chosen quantum methods for this system are presented in **Fig. 3.1a**. It is obvious that VdW XC functional outperforms other standard GGA functionals and gives results similar to the ones obtained from the wave function based calculations. Recently, new XC functionals , with a parameterized enhancement factor have been reported to give better interaction energies for dispersion and hydrogen bonded systems of weakly interacting dimmers and water clusters (cf. **Fig. 3.1b**) [68].

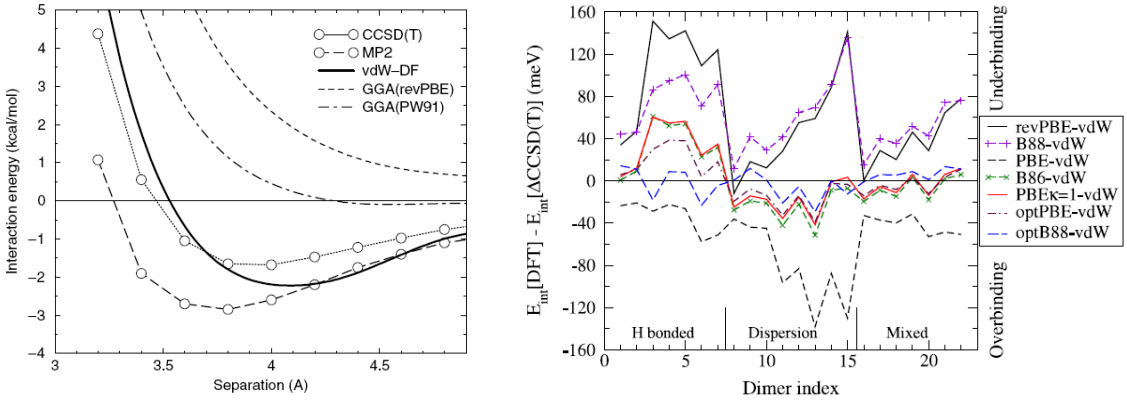

Fig. 3.1: *a) Interaction energy between two benzene molecules in a-top configuration. The VdW functional is compared to two wave function methods, CCSD(T) and MP2 and two popular GGA functionals, revPBE and PW91. b) Differences in interaction energies for vdW-DF with various exchange functionals. Figures are adapted from refs. [66,68]*

3.2 Implementation of DFT

In this section I will go over tools used to successfully implement DFT within quantum chemical codes. I will talk about basis sets, periodic systems, pseudopotentials and other approximations. The construction of appropriate basis functions is a major enterprise within electronic-structure calculations. Selection usually falls either on plane waves, which are delocalized and extend over all space or atomic orbitals that are localized and centered on atoms. The choice of the former ones implies the use of periodic boundary conditions. In the thesis all the electronic structure calculations, except for the ones in Chapter 8, were performed using planewaves as the basis set. Therefore in the following I will explain how these are used in practice.

Using periodic boundary conditions implies repeating slab infinitely in all directions. Such a crystal will have an infinite number of electrons which will extend over all space. This would entail an infinite number of one electron orbitals that would demand an infinite basis set. To workaround this problem one calls Bloch's theorem (BT) in help [69]. Since ions in a crystal are arranged in a regular periodic way, external potential felt by electrons will also be periodic. Periodicity is exploited in BT to reduce the infinite number of electrons to just its number in the single unit cell of a crystal. BT states that the wavefunction can be broken into a periodic and a wavelike part.

$$\psi_i(r) = \exp(ikr) f_i(r) \tag{3.32}$$

where k is the wave vector and $f_i(r)$ is the wavelike part defined by the envelope function

$$f_i(r) = \sum_G c_{i,G} \exp(iGr) \tag{3.33}$$

where G stands for reciprocal lattice vectors. Substituting Eq. (3.33) into Eq. (3.32) yields

$$\psi_i(r) = \sum_G c_{i,k+G} \exp(i(k+G)r) \tag{3.34}$$

The number of plane waves representing each wavefunction is in principle infinite. Fortunately plane waves with a smaller kinetic energy are generally more important than those with higher kinetic energy. This enables us to truncate the expansion in Eq. (3.34) to a certain cutoff and reduce the basis set to a finite size.

BT does not fully remedy the problem, since there are still an infinite number of k-points in the Brillouin zone at which wavefunctions should be evaluated. It is possible to represent the electronic wavefunction over a region of reciprocal space at a single k-point. Here one exploits the fact that wavefunctions very close together in k-space will be almost identical. This approximation allows the electronic potential to be calculated at a finite number of k-points.

To summarize, problem of solving SE for an infinite number of electrons at an infinite number of points in an infinite basis set is reduced to solving the same problem with finite number of electrons, whose wave functions are expanded in a finite basis set evaluated at finite number of k-points in space.

To further ease computational load one has to call for more approximations. One of these is to use pseudopotential (PP) instead of all electron potential. Here the fact that valence electrons are mainly responsible for chemical bonding in molecules and solids is vastly exploited. The inner electrons retain the same configuration and their orbitals do

not change much if the atom is put in a different environment. In addition, the core electrons demand much higher kinetic energy cutoff because their wave functions oscillate rapidly to keep all the states orthogonal due to the Pauli Exclusion Principle. In this approach the Hartree and XC terms are evaluated only for the valence density and the core electrons are accounted for by replacing the external potential with the pseudopotential. Hence the total potential reads

$$v_S^{PP}[n_v] = v_{ext}^{PP}[n_v] + v_H[n_v] + v_{xc}[n_v]. \tag{3.35}$$

Reduction of a basis set size and number of electrons are both accomplished with the use of pseudopotentials. There are certain rules that PPs have to fulfill. One of them is the norm conservation condition which implies that beyond certain cutoff radius, pseudo and all-electron valence wavefunctions, should have the same energy and amplitude (cf. **Fig. 3.2**). Relaxation of this condition leads to ultrasoft pseudopotentials.

Another technical approximation is to use small electronic temperature for numerical reasons. Electrons are fermions and hence they populate energy states according to the Fermi-Dirac distribution function. At 0 K this distribution has a shape of a step function where the highest populated state is at the Fermi level. Since step function produces numerical difficulties one has to specify some small electronic temperature (0.1 k_BT) that smoothness this distribution. Once the calculation has converged, the total energy is extrapolated to 0 K. Electronic temperature specified is a tradeoff between faster convergence at higher values and higher accuracy at lower values.

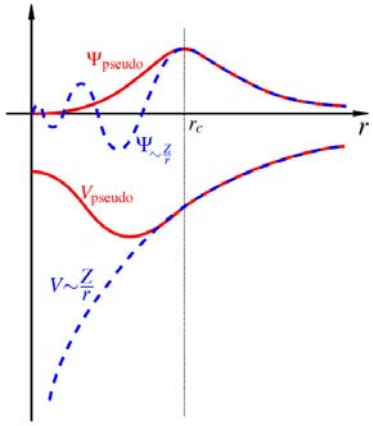

Fig. 3.2: *Comparison of all electron (blue) and pseudo (red) wavefunction and potential.*

3.3 Adsorption and activation energies

Reaction energy is defined as a difference in energies between initial and final state. In DFT it can be easily computed by reading off total energies of both states.

$$\Delta E = E_{FS} - E_{IS} \tag{3.36}$$

where ΔE is the enthalpy of a given reaction and subscripts IS and FS stand for initial and final state. Usually it is more instructive to use free energies since these are final measures of how much work a system can produce. Free energies are obtained by adding zero point energy and entropy contributions to the enthalpy. We note here that these are the main contributors, but as we shall see in the next section, there are also other terms depending on the conditions of a given reaction.

$$\Delta G = \Delta E + \Delta ZPE - T\Delta S \tag{3.37}$$

where ΔZPE and $T\Delta S$ are changes in ZPE and entropy from initial to final state. Here it is assumed that adsorbed atoms have no rotational and translational degrees of freedom. Hence only vibration modes contribute to the ZPE and these can be readily calculated from DFT normal mode analysis (NMA).

$$\nu_i = \frac{1}{2\pi}\sqrt{\frac{k_i}{m_i}}\,,\; k_i = \frac{d^2V}{dx^2} \tag{3.38}$$

where k_i is the force constant and m_i is the mass of an atom or a molecule. The curvature of the second derivative of potential energy gives the force constant and thereof vibration frequencies. If a molecule behaves as an ideal harmonic oscillator expression for ZPE reads

$$ZPE = \frac{\hbar\nu}{2} \tag{3.39}$$

As far as the entropy is concerned, it is assumed to be 0 for adsorbed species and for molecules in the gas phase it is taken from standard molecular tables [70].

A configuration entropy term can be also added to Eq.. This term is related to the number of ways in which all the particles of the system can be arranged while keeping the energy constant. Constant energy condition implies no interaction between the adsorbent particles. If this condition is not fulfilled, Eq. (3.40) does not hold any longer.

$$\frac{dS_{conf}}{d\theta_{H^*}} = k_B T \ln\left(\frac{1-\theta_{H^*}}{\theta_{H^*}}\right) \tag{3.40}$$

Thermodynamics offers just a partial insight into the chemical reaction. It shows how much stable is a certain state compared to another, but it does not tell anything about how quickly the species react. This information is given by the energy barrier between reaction intermediates which can be readily obtained with the help of Nudged Elastic Band (NEB) method [71,72]. This method is very simple to use. One just needs to specify initial and final state, number of images on the path and the strength of a spring potential. The spring potential is set between the images to prevent them of sliding on either sides of potential energy surface (PES).

$$F(R_1, R_2, ..., R_{P-1}) = \sum_{i=1}^{P-1} V(R_i) + \sum_{i=1}^{P-1} \frac{k_{sp}}{2}(R_i - R_{i+1})^2 \tag{3.41}$$

where the first term represents the potential energy of individual images and the second term the spring energy that connects them. The transition state is located after system relaxation and free activation energies can be computed by adding the ZPE[5] and entropy corrections.

$$E_a = E_{TS} - E_{IS} \tag{3.42}$$

$$G_a = E_a + \Delta ZPE - T\Delta S \tag{3.43}$$

[5] If the saddle point is flat, transition state cannot be approximated by an ideal harmonic oscillator.

where subscript TS stands for transition state.

3.3.1 Theoretical standard hydrogen electrode

In this section I will introduce the concepts behind the theoretical standard hydrogen electrode (TSHE). TSHE became the state-of-the art tool in mapping potential energy diagrams for electrochemical reactions that in some stage involve proton and electron transfers. This method has been used throughout this thesis to get the free adsorption energies of reaction intermediates at different potentials. The beauty of this tool is that one can now calculate relative stability of two states by taking that the energy of proton and electron equals half of the energy of a hydrogen molecule.

$$\frac{1}{2}\mathrm{H_2(g)} \rightarrow \mathrm{H^+ + e^-} \tag{3.44}$$

Eq. (3.44) is defined at the standard conditions ($p_{H_2} = 1\,\mathrm{bar}$, $T = 298\,\mathrm{K}$, $c = 1\,\mathrm{M}$, $pH = 0$). At some other conditions new equilibrium is established and it is related to the one at standard conditions via Nernst equation.

$$\Delta G = \Delta G^{\theta} + kT \ln\left(\frac{a_{H^+}}{\left(p_{H_2}/p^{\theta}\right)}\right) \tag{3.45}$$

where a_{H^+} is the activity of protons and the denominator in the bracket stands for the relative content of hydrogen in the influent. If pure hydrogen is supplied at the anode, which is usually the case in PEMFC ($p_{H_2} = p^{\theta}$) second term simply becomes – 0.059*kTpH.

I will demonstrate how TSHE is implemented in practice on the example of the ORR.

$$\mathrm{O_2 + H^+ + e^- \rightarrow OOH} \tag{3.46}$$

$$\mathrm{OOH + H^+ + e^- \rightarrow O^* + H_2O} \tag{3.47}$$

$$\mathrm{O^* + H^+ + e^- \rightarrow HO^*} \tag{3.48}$$

$$HO^{*} + H^{+} + e^{-} \rightarrow H_2O \tag{3.49}$$

Herein, we will assume that the ORR proceeds through the associative mechanism. Adsorption energies of O, OH and OOH can be calculated by using the definition of the TSHE via

$$\Delta E_{HOO^{*}} = E_{HOO^{*}} + 3E_{H^{+}} + 3E_{e^{-}} - 2E_{H_2O} = E_{HO^{*}} + \frac{3}{2}E_{H_2} - 2E_{H_2O} \tag{3.50}$$

$$\Delta E_{HO^{*}} = E_{HO^{*}} + E_{H^{+}} + E_{e^{-}} - E_{H_2O} = E_{HO^{*}} + \frac{1}{2}E_{H_2} - E_{H_2O} \tag{3.51}$$

$$\Delta E_{O^{*}} = E_{O^{*}} + 2E_{H^{+}} + 2E_{e^{-}} - E_{H_2O} = E_{O^{*}} + E_{H_2} - E_{H_2O} \tag{3.52}$$

The free adsorption energies of all intermediates can be obtained from DFT calculations and standard molecular tables as explained in the previous section. If some finite bias is turned on, then all the states involving an electron will be stabilized by nU, where n is the number of electrons. The potential drop at the interface gives rise to an electric field. The electric field exerts as well, the influence on adsorption and transition state energies of reaction intermediates.

Since many electrochemical reactions occur in the presence of an aqueous solvent it is essential to include the water induced stabilization of the reactive species. This term depends on the nature of the species and how much they are stabilized by hydrogen bonding to water. It was found that H^{*} and O^{*} binding energies are minimally affected by the presence of water [43]. Conversely water exhibits huge stabilization effect (0.6 & 0.2 eV) on the OH and OOH species [34,43].

Now we can write the overall free adsorption energy, including all aforementioned corrections as

$$\Delta G = \Delta E + \Delta ZPE - T\Delta S - T\frac{dS_{conf}}{d\theta_{H^{*}}} - 0.059kT \cdot pH - nU + \Delta E_{w,water} + \Delta E(\varepsilon). \tag{3.53}$$

where the terms $-0.059kT \cdot pH$ and $-nU$ account for the chemical potential of protons (pH) and electrons respectively, $\Delta E_{w,water}$ accounts for water induced stabilization and

$\Delta E(\varepsilon)$ for the change in the adsorption energy induced by the presence of an electric field. For more details about this methodology I refer to ref. [43,73,74].

3.4 System setup and calculation details

Most of the electronic structure calculations presented in this thesis have been carried out using DFT, with the RPBE functional chosen for exchange and correlation [65]. This functional gives somewhat better adsorption energies than the state-of-the art PBE functional [64]. Lattice constants used were optimized for metals in bulk. Metal slabs were represented by periodically repeated 3 layer slabs separated by 10-12 Å of vacuum. This amount of vacuum ensured convergence of workfunctions and total energies. Various unit cell areas 3x2, 3x3, 3x4, 6x3 and (6x6) sampled with (4,6,1), (4x4x1), (3x2x1 & 4x3x1), (2x4x1) and (2x2x1)) Monkhorst-Pack k-point sampling grid [75] were used throughout this work. In all cases symmetry has been applied to further reduce number of k-points. The dipole correction was used as well to decouple the electrostatic interaction between the periodically repeated images. The Kohn-Sham equations were solved using a plane wave basis set with a plane wave and density cutoff of 26 Ry. Ionic cores were described with Vanderbilt ultrasoft pseudopotentials [76]. Fermi smearing was set to 0.1 eV and at end of relaxation; the energies were extrapolated to an electronic temperature of 0 K. All the structure optimizations were performed with a Quasi-Newton (QN) algorithm, until the sum of the absolute forces on the atoms was less than 0.01-0.05 eV $Å^{-1}$ depending on the unit cell size. The two bottom layers of the slab were fixed in their bulk positions, while the top layer together with adsorbates was allowed to relax. Transition states were located using NEB method [71,72]. In addition to the standard RPBE calculations, in Chapter 6 we also used the vdW-DF to investigate the effect of including van der Waals interaction on the stability of the water layer covering the Pt(111) surface [66,77]. All calculations were performed using Dacapo [78] code, except for the ones in Chapter 8 where the newly developed GPAW code was used instead [79]. The calculation details in the latter case will be presented in Chapter 8. Both codes were integrated with the Atomic Simulation Environment (ASE) [80].

4 Modeling electro-catalytic reactions

In the introduction Chapter we have witnessed the impact of the electrochemical reactions on every day's life and why future needs call for better, cheaper and more selective catalysts. Furthermore I have also emphasized the strength of DFT as a predictive tool in the quest for new catalyst materials. To get an overall picture about a reaction, one needs to consider both thermodynamics and kinetics. To study these at different biases, we have implemented a new computation scheme to explicitly include how the potential in our calculations. In the past, the potential was accounted for posteriori, by shifting the free energy levels of the states involving electrons by the chemical potential of those electrons. Ideally we would like to have an internal way of including the potential which would also allow us to study reaction barriers at different potentials. Unfortunately, this is not a simple task. To faithfully describe the solid/liquid interface one needs to model the solid surface, the liquid electrolyte, the ions solvated in the liquid, the charge-transfer and the possibility of varying electrode potential. Several methods capable of including these effects have recently appeared within the framework of DFT.

In this chapter I will present in detail properties of the solid/liquid interface and the method we have devised to tune the surface charge and to study charge transfer reactions. The accuracy and the applicability of the method were subsequently benchmarked on the simplest possible electrochemical reaction – the hydrogen oxidation reaction (HOR).

The chapter is structured in the following way: first I will start by reviewing the historical development of the theoretical models used for describing the solid/liquid interface. Then I will present and compare different methods developed to control excess charges (potential) on the electrode surface within standard DFT calculations. Afterwards I will explain in details the method developed in-house and apply it to model the HOR. In the end I will introduce the extrapolation scheme used to alleviate effects associated with the finite size of the simulated cell.

4.1 The electrical double layer

The goal of our study is to model electro-catalytic reactions at the solid/liquid interface. As to be aware of what needs to be modeled, it is essential to know the features of the real electrical double layer (EDL). Therefore I begin by reviewing the general aspects of the EDL.

The solid/liquid interface has unique properties different from either of the bulk phases. In the bulk solution, water dipoles are randomly oriented and there is an even amount of charge. Consequently no net dipole will build up in any macroscopic volume of the solution and for this reason the solution will be electrically neutral. At the solid/liquid interface electro neutrality will cease to hold because of the force anisotropy acting from both sides of the phase. In a bulk phase a molecule is subject to forces of equal magnitude from all directions, whereas in the EDL, it is subject to the forces from both sides of the interface. Due to the force anisotropy, water molecules at the surface will show a certain preferential orientation. To respond to the charge rearrangement in the water layer, the electrons will be dragged to or from the metal surface. The same effect will occur if some ions are solvate close to the electrode surface. The charge separation on both sides of the interface will thus result in an electrostatic potential drop. The potential drop is restricted to the EDL region because the water dipoles will effectively screen the charge at larger distances. The potential drop will give rise to an electric field whose size can be quite substantial because of the small thickness (~3 Å) of the EDL.

The simplest model to describe the solid/liquid interface is presented in Fig. 4.1**a**. It was proposed by a German scientist, Hermann Ludwig Ferdinand von Helmholtz in 1853 [81]. In his view charges of opposite sign are localized in two planar surfaces pertinent to each side of the interface (cf. **Fig.** 4.1**a**). This interpretation is equivalent to the classical capacitor model where the linear potential drop is observed between the two oppositely charged plates. The downside of this model is that the capacitance of the EDL is independent on the potential and the concentration of ions in the solution. Furthermore such a simple model does not take into account ion diffusion, specific adsorption and solvent dipoles.

To overcome these shortcomings Gouy and Chapman [82,83] have refined the Helmholtz model in such a way that they did not assume *a priori* that the counter ions are immobilized at the electrode surface but dispersed toward the solution. The Gouy-Chapman model of the EDL is shown in Fig. 4.1**b**. In their view ions possess certain kinetic energies and hence they will be readily displaced from the surface of an electrode in compliance with some statistical distribution rule, e.g. the Boltzmann distribution. Accordingly, the potential should decay exponentially in the EDL and reach its value in the bulk of the solution at some distance from the electrode. Even though it seemed promising, the model gave erroneous results, that is, it predicted exponentially increase of capacitance with potential which was contrary to the experimental observation. This obvious disagreement originated from an incorrect assumption made during the integration of the Poisson equation. The electrode surface was taken to be the lower boundary in the integration because ions were considered to be point charges and hence they could completely approach the electrode.

Stern succeeded in reproducing the true capacitance behavior by successfully unifying the two approaches [84]. From the Helmholtz model he took the hypotheses that ions cannot approach the electrode closer than a radius of a hydrated ion[6] and from the Gouy-Chapman model he took the hypotheses that some of the counter charge is dispersed towards the solution. In his model the potential drop comprises of two regions, a linear one close to the electrode surface and an exponentially decaying one towards the bulk of the solution.

The term “double layer” in fact stems from the two qualitatively different regions. The distribution of charges and the potential profile in the Stern model is illustrated in Fig. 4.1**c**. The first region is bounded by the electrode surface and the plane cutting through the center of the ions at their closest approach to the electrode surface called as well “The Outer Helmholtz plane” (OHP). The second region is formed from the excess of ions that succeeded in escaping the electrostatic trap at the interface. This region is termed the Diffuse Layer and here the potential will decay exponentially due to the thermal motion of ions. The ions in the OHP and an excess of ions of the same sign in the diffuse layer will precisely counterbalance the induced charge in the metal.

[6] This equals to the distance between the two opposite charged planes in the Helmholtz model

Graham gave the last contribution to the development of the theoretical picture of the EDL taking into account also the ions adsorbed on the electrode surface[7] [85].

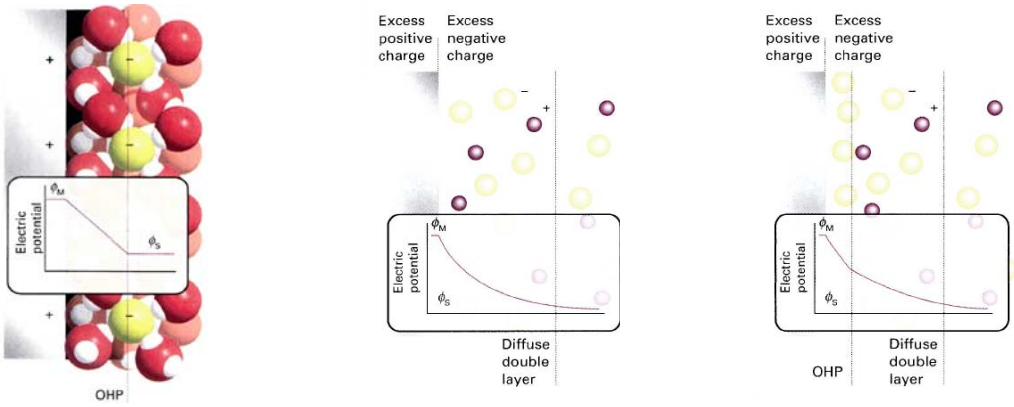

Fig. 4.1: *Graphical representation of the a) Helmholtz b) Gouy-Chapman and c) Stern model of the EDL. Adapted from ref. [86]*

4.2 Water structure at the interface

The structure and the property of water on metal surfaces are of fundamental importance to many scientific areas such as electrochemistry, heterogeneous catalysis, corrosion, biochemistry and others. The significance of establishing the true water structure rests upon the fact that many reactions take place in an aqueous solution where water is not just a mere spectator, but rather an active participant in a reaction. Water exerts its influence either by stabilizing the reactive species through hydrogen bonding or by actively taking part in a reaction mechanism. Therefore many experimental and theoretical research studies have been devoted to illuminating the exact binding structure of water on solid surfaces. The vast research efforts have resulted in disclosing ordered water films on solid surfaces [87,88, 89, 90 91,92].

Nowadays it is a well established picture that water binds in the form of an ice-like structure on the close packed surfaces of many transition metals [Ogasawara, Michaelides]. The structure covers 2/3 of a substrate surface and forms a honeycomb ($\sqrt{3}x\sqrt{3}$)R30 pattern. The structure was named “water bilayer” because of the two differently oriented water molecules. One water molecule is oriented planar to the surface and binds to an a-top surface atom via oxygen, whereas the second water molecule is

[7] The plane of the adsorbed ions is also called “The inner Helmholtz plane” (IHP).

oriented perpendicular to the surface with H atom pointing either away (H-up structure) or towards the metal surface (H-down structure). The appearance of the two structures is shown in **Fig. 4.2**. The planar water molecule binds to the surface in a same way as the single water monomer [93, 94]. The H-up and H-down structures were found to have comparable stabilities across transition metals [87,95,96,97]. In addition Michaelides et al. [97] have shown that the main contribution to the adsorption energy of such bilayers originates from the hydrogen bonding within the bilayer and to a much less extent from the substrate-bilayer interaction. Besides they have also observed that a variation in the latter was responsible for the difference among bilayer adsorption energies on metal surfaces.

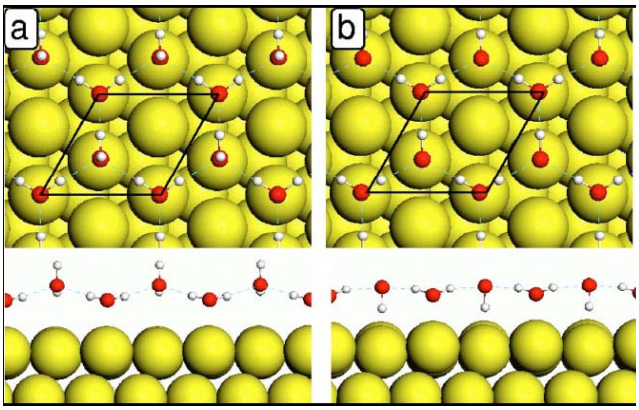

Fig. 4.2: *Side and top view the a) H-down bilayer and b) H-up bilayer. Taken from ref. [97]*

Recently it has been shown that water bilayers do not cause any major changes in the electronic structure of the substrate they bind to [95]. This implies that the binding energies are not considerably affected by the presence of a water bilayer, unless of course water induces stabilization indirectly e.g. by hydrogen bonding. Conversely a configuration of the water bilayer will have a great influence on the metal work function in the sense that different orientation of a non-saturated H bond in the H-up and the H-down structures leads to substantial changes in the metal workfunction. We have quantified this difference to be 2.7 V on Pt(111). Our result agrees well with 2.2 V reported by Schnur and Groβ [95]. This striking difference between the two bilayer structures was explained by the fact that a charge transfer is taking place from the water

bilayer to the middle of the solid/liquid interface. The charge transfer creates an additional dipole whose magnitude and sign depends on the orientation of the dangling H bond. In the case of the H-up structure the additional dipole superimposes with the intrinsic dipole moment which leads to a substantial reduction of the metal WF, whereas for the H-down configuration the additional dipole opposes the intrinsic dipole moment which causes a smaller change in the pristine metal WF. In the latter case the sign of the WF change depends on a metal substrate.

Most experimental studies aimed at elucidating the bonding nature of water adjacent to metal surfaces have been carried out under UHV conditions and at temperature below 200 K [87,98,99,100,101]. Since many electrochemical reactions take place at room temperature and atmospheric pressure, from an applied point of view it is more important to determine water structure under these conditions. There is no clear evidence that the water structure found under UHV conditions will be preserved under ambient conditions. The difference between a UHV cell and a real electrochemical cell is not merely in pressure and temperature, but also due to strong electric fields and co-adsorption of electrolyte ions that are present in a real system. Unfortunately most of the experimental techniques fail at this limit. This is not a problem from a theoretical point of view because finite temperature effects can be readily included in molecular dynamics (MD) simulations. Many MDs have thus been carried out in order to elucidate the bonding nature and properties of water on metal surfaces [102,103,104,105]. Here I will bring up one particularly interesting study.

Schnur and Gross have performed *ab initio* molecular dynamics (AIMD) simulations of water bilayers on different transition metal substrates thermalized to 300 K for about 8 ps [95]. For the initial guess they adopted the H-up and the H-down structure found in the UHV studies. After 8 ps AIMD run the hexagonal structure was lifted on metals with large lattice constants (Ag & Au) where originally the water bilayer was not strongly bound. On the other hand, on metals with a smaller lattice constant (Ru(0001) & Pt(111)) the hexagonal structure was retained, except that the dangling hydrogen atoms were randomly orientation up and down. The analysis clearly demonstrated that at room temperature a mixture of the H-up and the H-down structures will dominate. It is intuitive to expect that in a real electrochemical cell the hydrogen would tend to point down at

negative biases and up at positive biases. This can readily occur because of very small barriers needed to flip the hydrogen atom. The snapshot of the structure after 8 ps of thermal motion at 300 K on Pt(111) is shown in **Fig. 4.3a**. The authors have in addition presented a nice graph showing the evolution of the trajectories of the oxygen atoms in the water structure (**Fig. 4.3b**). From **Fig. 4.3** it is obvious that although some water reorganization is occurring, the hexagonal structure remains intact on Pt(111).

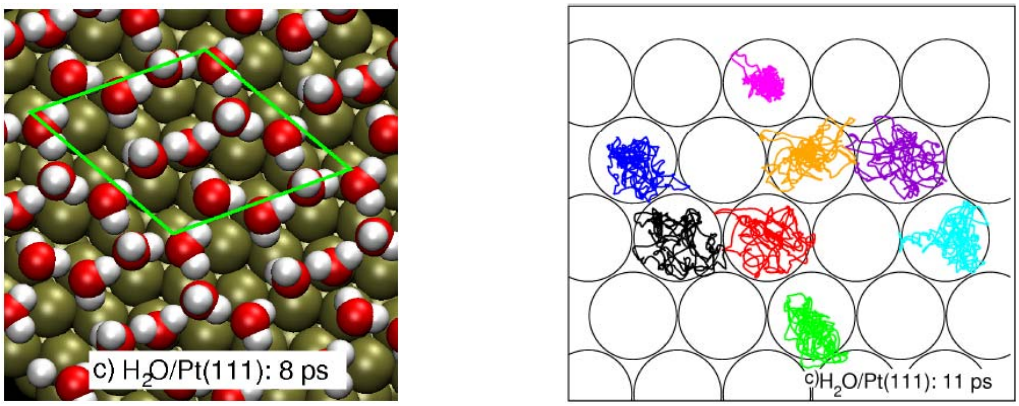

Fig. 4.3: *a) Snapshot of the water structure on Pt(111) from an AIMD simulation at 300 K. b) Trajectories of oxygen atoms in water molecules during an AIMD run. Trajectories of different oxygen atoms are color coded. Both figures are adapted from ref. [95].*

4.3 Methods for controlling the surface charge

In this subsection I will list the main methods recently developed to account for and tune the potential within the framework of DFT. First I will address their physical concepts, how the bias is controlled and to which extent the properties of the solid/liquid interface agrees with the postulated EDL models.

Electric fields can be straightforwardly included in standard DFT slab calculations introducing a dipole layer in the vacuum. Water at the interface will screen the charge and this will in turn give rise to an electrostatic potential drop. This approach does not introduce any excess charges so that the charge neutrality is maintained, but it is not straightforward to relate the applied dipole field to the corresponding electrode potential. The potential is typically calculated by assuming some width of the double layer through

$$U = \varepsilon \cdot d \tag{4.1}$$

where ε is the electric field strength and d the width of the EDL. For that reason a possibility of controlling the surface charge demands more advanced methods.

The first method I will discuss here is the effective screening medium (ESM) method introduced by Otani and Sugino [106,107,108]. The method was benchmarked on a Pt(111)/water interface by performing AIMD simulations. To alleviate the constraint of electro-neutrality imposed on the periodically repeated systems, the authors introduced an ESM which allowed for non-periodicity of the cell in the z direction. Their setup (**Fig. 4.4 a**) consisted of a slab sandwiched between two continuum mediums. The one at the lower end of the Pt(111) slab was set to represent a vacuum ($\varepsilon_r = 1$), whereas the one at the upper end of the cell was set to represent a perfect conductor ($\varepsilon_r = \infty$). The water environment was simulated by inclusion of 32 water molecules and in addition a single hydrogen atom was added to account for the strong acidic conditions they aimed to replicate. To prevent water molecules and electrons from leaving the surface the authors introduced a barrier potential for each species in the region between the water layer and the ideal conductor. The bias can now be tuned by adding/subtracting charge to/from the electrode. As a response to the generated surface charge, the counter charge will automatically build up in the perfect conductor. An electric field thus created will be effectively screened near the surface due to reorientation of the water dipoles. Screening will happen both in the region adjacent to the electrode surface, denoted here as a contact region, and region further away in the bulk, denoted here as bulk region. The screening will give rise to an electrostatic potential drop that will spread through both regions. They took for reference point the level in the bulk region of an uncharged calculation. All the potential when the system was charged are given compared to this reference value. For that reason all the reported potentials are given compared to the uncharged calculation or potential of zero charge of the specified system.

The advantage of this method is that a fraction of charge can be added to the system and hence the potential can be varied continuously. The downside is that the distance between the two opposite charges in the metal slab and the perfect conductor is ~18 Å which does not qualitatively agree with the theoretical picture where most of the counter

charge is localized in the vicinity of the electrode surface. Moreover the potential of zero charge scale they used is not a universal scale but strongly material dependent as we shall see in chapter 6.

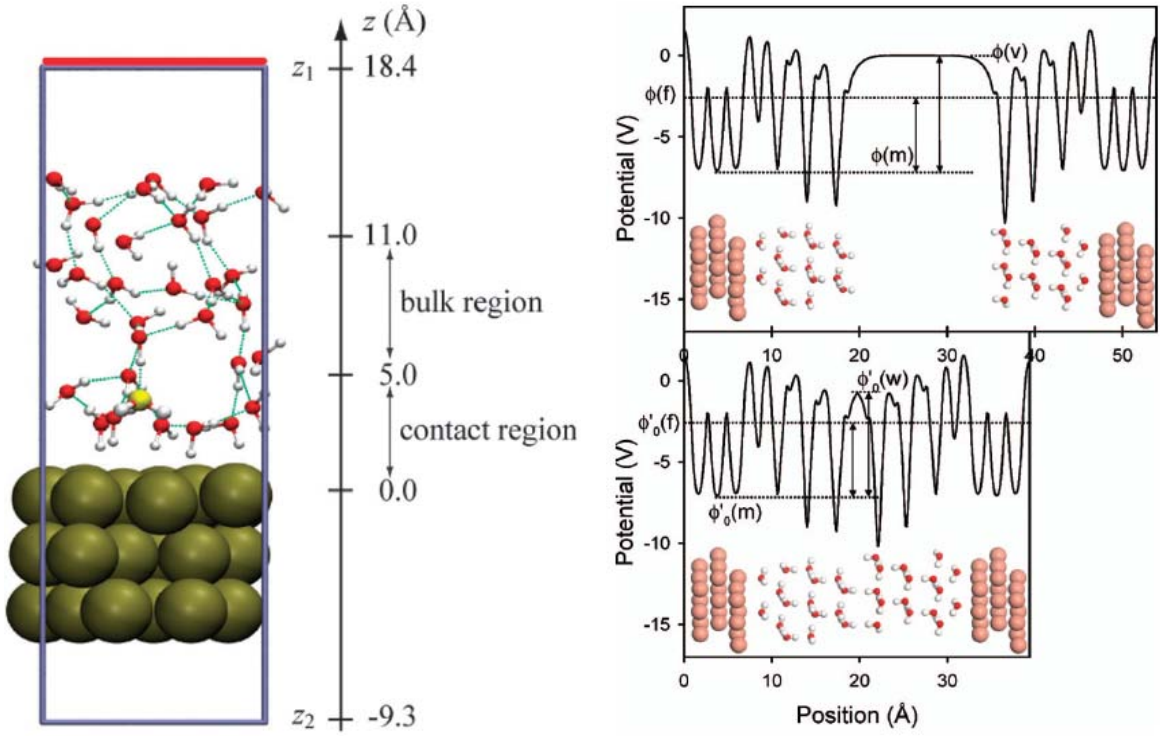

Fig. 4.4: *Computational setup for (a) the ESM method developed by Otani and Sugino,The red bar represents the onset of the perfect conductor region whereas red, white and tan spheres represent O, H and Pt atoms respectively and the yellow sphere represents the oxygen atom of a hydronium ion. (b) The double reference method developed by Filhol and Neurock where two figure panels depict the vacuum cleaved (upper panel) and the non-cleaved system (lower panel). The figures are adapted from refs. [108,109].*

Another approach to control the surface charge and the bias was introduced by Taylor and coworkers [109] and subsequently applied to metal/water interfaces [110,111]. The charge can again be continuously varied by giving an excess or deficit charge to the metal slab. The difference from the previous model is that the counter charge is now smeared out across the entire unit cell and not localized at some distance away from the surface. The smeared counter charge fulfills the requirement of electro neutrality and allows use of periodic boundary conditions. Again an electrical potential drop is created because of the water polarization. In this method the potential is deduced from the system workfunction (WF).

$$U = WF - U_{SHE}^{abs} \quad (4.2)$$

where U_{SHE}^{abs} is the absolute potential of the standard hydrogen electrode. This procedure was outlined by Trasatti [112] and afterwards exploited by others [113,114].

The WF of a system is useful because it measures the potential on an absolute potential scale, albeit absolute scales are meaningless if not converted to some known relative potential scale. For this purpose they used the experimental value for the absolute standard electrode potential (ASHEP). The problem with taking the experimental value is that a range of U_{NHE}^{abs} values (4.4-4.85) has been reported in the literature. This issue will be addressed in detail in chapter 6 of the thesis. Here we just stress that more accurate theoretical results are obtained with the internal measure of the ASHEP.

In the case of a charged slab the uniform background charge creates an electric field throughout the entire super cell, hence also in the vacuum region so that a vacuum reference point cannot be established. Authors have proposed a clever way to workaround this problem. They named the method the “double reference method” because it uses two references to determine the potential of a system. First they performed two calculations for an uncharged system; one with the unit cell filled with water (**Fig. 4.3b** lower panel) and the other one for the system having a vacuum inserted in the middle of the water (**Fig. 4.3b** upper panel). Note here that every point where the potential is flat can be regarded as a reference point. In bulk of the metal large number of electrons effectively screens the electrostatic potential whereas in the simulated water, the electrostatic potential converges upon inclusion of several water layers. Hence both points in the bulk phase can be taken as reference levels. Since the chemical potential of electrons at the Fermi level is the same in both cases, cleaved and non-cleaved, we can equate these levels and hence, obtain a link between the vacuum and the solution reference points.

As shown earlier in the case of a charged slab, the vacuum reference cannot be determined because the potential is no longer constant in this region. On the other hand the solution reference point can be readily established because the charge is here effectively screened regardless of its magnitude. The solution reference point can then be related back to the vacuum point through the link we established above. To obtain a

unique solution potential level a portion of water molecules in the middle of the cell had to be fixed, while the rest was allowed to relax.

The obvious advantage of this method is that the charge and potential can be varied continuously by adding any fraction of charge. The downside is that the counter charge is dispersed over the whole space (even the slab) which deviates from the classical description of the EDL where there is an accumulation of counter-ions in the near electrode region.

The third model presented here was introduced by Skúlason et al. [114]. In their study the authors investigated the HOR and the HER on Pt(111) substrate. They used only one H-down bilayer to emulate water on the metal slab which was appreciated by the fact that this particular water structure was found to be the most stable one under UHV conditions up to 200 K [87,95]. This is a reasonable model to assume because DFT anyhow yields results at 0 K. Besides, we have seen earlier that the bilayer structure on Pt(111) remains intact when thermalized to room temperature, except that some dipoles turn to point up.

To create a charged interface, the authors have added a hydrogen atom to the water bilayer. Since DFT is a ground state method, it automatically finds a minimum when the electron from the H atom has been transferred to the surface, leaving the solvated proton behind. The charge separation creates an electrical potential drop at the interface. The charged interface formed in this way corresponds exactly to the Helmholtz picture of the EDL. Protons are now correctly solvated just outside the metal slab and not far away or homogenously dispersed over the entire unit cell. We note here that this is not a first attempt to model the solid/liquid interface by explicitly adding atoms in the vicinity of the metal. Taylor et al. have compared their “double reference method” against the situation where they explicitly added a sodium atom (pseudopotential) in their unit cell, both in vacuum and water, at some distance from the surface [109]. The constraint was that the system had to be fixed because the sodium atom was unstable and reacted with water when allowed to relax. Skúlason et al. have demonstrated in their method that these difficulties are avoided when adding a simple hydrogen atom. The system setup is presented in **Fig. 4.5a, 5b** and **5c**.

The potential can be tuned by varying the surface charge, (the proton concentration in the unit cell). This is accomplished either by changing the size of the super cell or by adding more hydrogen atoms. The difference in the work functions (potentials) for two different proton concentrations is shown in **Fig. 4.5 c**. The potential is again deduced from the work function of the system as in the double reference method. The downside of the method is that the charge cannot be varied continuously but rather discrete. In other words one cannot add a fraction of an electron but only a whole electron. The good side is that the electrostatic potential drop looks like the one in the real system and that electric fields are accurately accounted for.

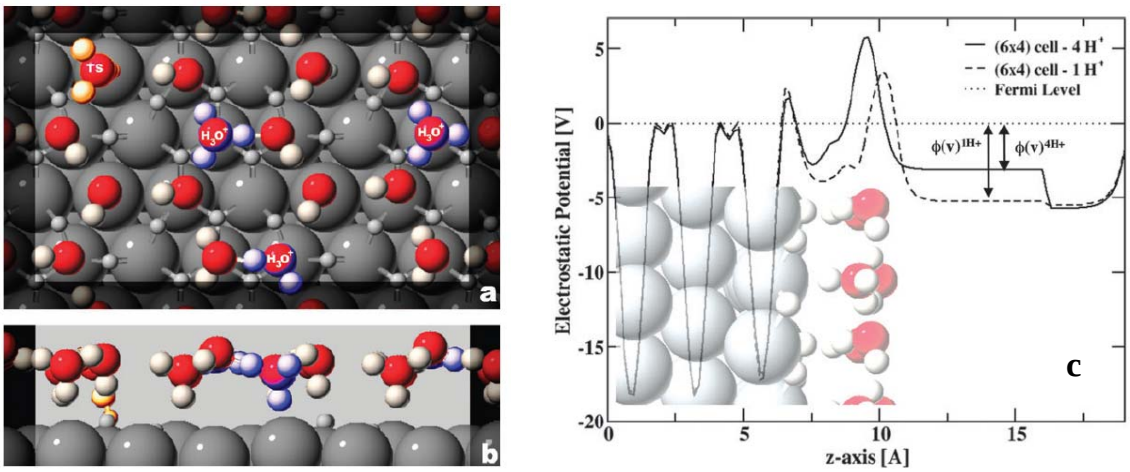

Fig. 4.5: *Top (a) and side (b) view of the system setup in the Skúlason model. The grey, red and white spheres represent Pt, O and H atoms respectively. Hydronium ions are highlighted in blue color. c) Laterally averaged variation of the electrostatic potential for two different proton concentrations. Proton concentrations correspond to 1 and 4 solvated protons in (6x4) unit cell. Adapted from ref. [114].*

The difference between the three presented methods is illustrated in **Fig. 4.6**. In the last method there is one to one corresponds between the surface charge, proton concentration and electric field and that is the reason this model most accurately reproduces the features of a real electrochemical half cell. In the case of the ESM method, charge is located far away from the surface, in the perfect conductor and therefore the potential drop and the electric field might not be accurately described. Furthermore as I have already pointed in this model water is not perfect in screening the surface charge

and this point has been exploited to deduce the potential. In the case of the double reference method the charge is dispersed over entire unit cell and not explicitly located in the OHP plane.

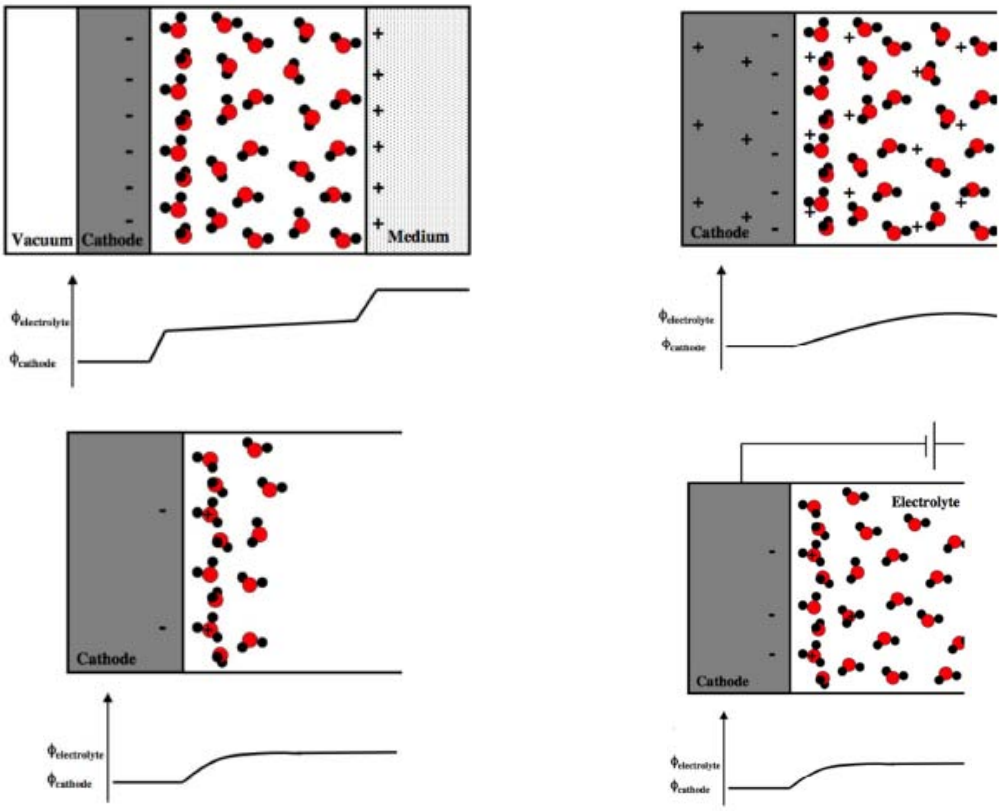

Fig. 4.6: *Illustration of the three different models and the potential drops for a) the ESM method b) the double reference method c) the method introduced by Skúlason et al. and d) a real electrochemical half cell. Figures are adapted from ref. [115]*

4.4 Our method

In this section I will elaborate on the properties of the EDL in the last method and use it to model the HOR/HER. Since I was involved to a large extent in developing and applying the method I will refer to it from now on as "our" method.

The charge separation taking place at the solid/liquid interface can be visualized by an isosurface plot of the electron density differences. Electron difference is calculated by performing three independent calculations; one for a full system with the metal slab, water bilayer and solvated proton(s) and two others for Pt slab & water layer and a H atom in separate cells. Naturally, in all calculations the positions of the atoms were held

fixed. If we subtract the density of the partial systems from the density of the whole system we obtain the charge redistribution upon insertion of a hydrogen atom.

$$\Delta\rho(r) = \rho_{(Pt+water+H)}(r) - \rho_{(Pt+water)}(r) - \rho_{H}(r) \tag{4.3}$$

In **Fig. 4.7** we present such a plot for Pt(111). Here the blue color represents the charge depletion or the positive region whereas the purple color represents charge accumulation or the negative region. As can be seen the positive charge is smeared out over the hydronium ion and three adjacent water molecules that are hydrogen bonded to it. It was found that in bulk water protons solvate with two to four water molecules yielding well-known Zundel ($H_5O_2^+$) [116] and Eigen complexes ($H_9O_4^+$), respectively [117]. The solvation shell in the bilayer resembles somewhat the Eigen complex although it is two dimensional rather than three dimensional. The size of the solvation shell in the bilayer is dictated by the hexagonal water structure. An important observation is that the charge does not spread out to the upper layers; meaning that it is enough to have just one bilayer to represent the solvation shell of a proton. On the other hand the negative charge on the surface seems much more dispersed.

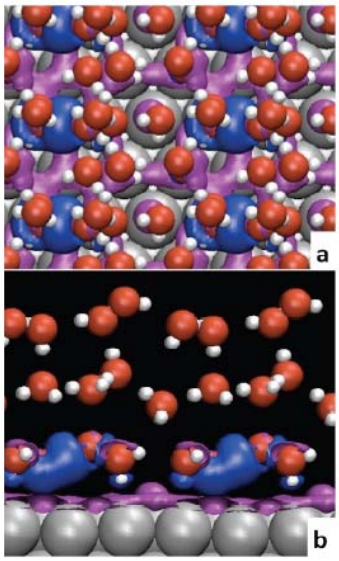

Fig. 4.7: *Top (a) and side view (b) of an isosurface plot demonstrating charge partitioning at the Pt(111)/water interface. The blue color is the surplus of positive charge located around solvated proton, whereas the purple is the surplus of negative charge delocalized on the metal surface.*

To quantify the charge separation taking place at the Pt(111)/water interface we have in addition calculated the potential drop by subtracting the potentials of the separate systems (water + H & slab) from the potential of the whole system in a similar way as when determining the charge density differences.

$$\Delta U(r) = U_{(Pt(111)+water+H)}(r) - U_{Pt(111)}(r) - U_{(water+H)}(r) \qquad (4.4)$$

The electrostatic potential (EP) difference averaged in the direction perpendicular to the surface versus the number of water layers is shown in **Fig. 4.8**. In addition, we have also included the EP profile obtained by taking the average over 60 random frames from a 3ps MD simulation of the system with three water layers equilibrated to room temperature. From the plot we can see that the EP is almost converged after addition of a single H-down bilayer whereas it becomes fully converged already when the second bilayer is added. The observed electrostatic potential drop is almost linear, which gives further evidence that this model faithfully reproduces the features of the Helmholtz EDL.

For future studies we will use just one water bilayer because as we have seen in **Fig. 4.7** the solvation shell and the EP drop are well described with this amount of water. Moreover, having fewer water layers drastically reduces the computational burden.

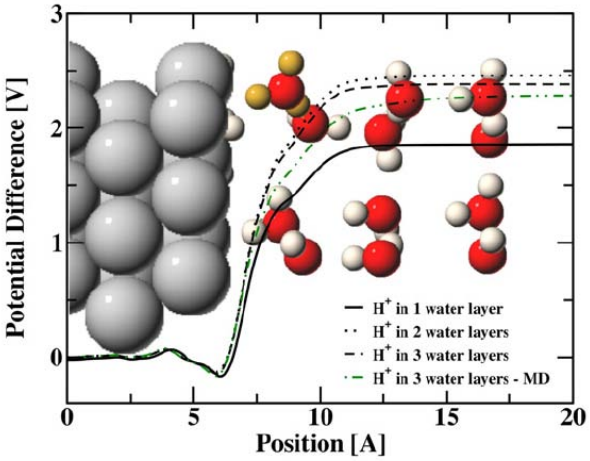

Fig. 4.8: *Lateral averaged EP for 1, 2 and 3 water layers having a single hydronium ion solvated in the first bilayer outside the Pt(111) surface. gray, red and white spheres represent platinum, oxygen and hydrogen atom, respectively. The hydrogen atoms of the hydronium ion are colored in yellow. For comparison we have also included the data from a MD simulation with 3 water layers.*

As we have seen the surface charge and hence the bias can be varied by changing the proton concentration. The effect of the varying surface charge is visualized in **Fig. 4.9**. Here we employ three different unit cell sizes and we show that there is no change in the distribution of the charge in the water layer and the metal surface with respect to the unit cell used. Here we used only one water bilayer because it significantly reduces the computational cost.

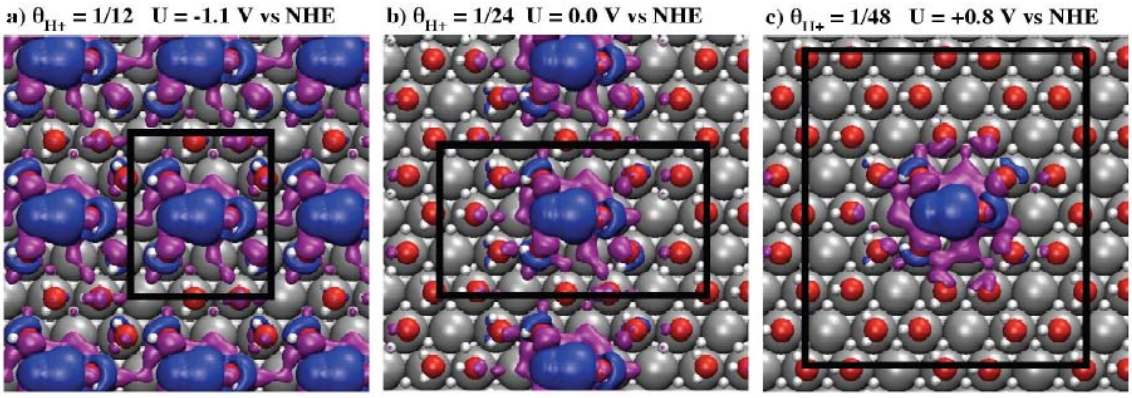

Fig. 4.9: *Top view of isosurface plots of a solvated proton in unit cells of varying size. The blue and purple colors represent positive and negative charge. The unit cell size is designated by the black bounding box. Proton concentrations and corresponding potentials are indicated above the figure panels.*

As mentioned earlier, this model of the solid/liquid interface resembles the Helmholtz model of the EDL. Therefore it should also share the same properties as the classical capacitor model. We will investigate these below by addressing the free energy stored in the solid/liquid interface. The total or the free integral energy of a system with n protons and N number of surface atoms normalized per surface area (or N in this case) is calculated as

$$G_{int} = (G(N,n) - G(N,0) - n\mu_{H_2}) / N \qquad (4.5)$$

Here we have chosen μ_{H_2} so that the minimum of G_{int} is obtained for the system with no protons in the bilayer. The free integral energies were calculated using H_2 in the gas phase as a reference state for protons in the bilayer. The entropy of the $H_2(g)$[8] was taken

[8] The entropy of the proton in the bilayer was neglected. For the explanation see p. 113.

from standard molecular tables [86] and the zero point of H_2(g) and H^+(bilayer) has been calculated using normal mode vibrational analysis. Since protons have a tendency to strongly repel each other the configurational entropy term can be neglected. Because of the analogy with the capacitor model the energy stored in the EDL should be quadratic in potential.

$$G_{int} = \frac{1}{2} C\left(U - U_{pzc}\right)^2 = \frac{1}{2} Ce^2\theta^2 \tag{4.6}$$

where C is the capacitance, θ=n/N the proton concentration and U_{pzc} potential of zero charge or the potential of a system with no specifically adsorbed ions. Potentials are deduced from the system workfunction in the same way as in the double reference method (see Eq. (4.2)) and referred to the U_{pzc} scale. In Eq. (4.6) we exploited the fact that charge ($e\theta$) is given by

$$e\theta = C\left(U - U_{pzc}\right). \tag{4.7}$$

In **Fig. 4.10** we have plotted G_{int} for various proton concentrations (θ). A nice parabolic feature is clearly observed. For the sake of simplicity from now on we will refer to these curves as *parabolas*. By the construction of a parabola the minimum in G_{int} is obtained for the U_{pzc}, hence all other potentials are given compared to this reference value. The U_{pzc} scale is not a universal scale but rather material dependent one.

Now if we set the μ_{H_2} to be equal to the energy of a proton and an electron in equilibrium with half of a hydrogen molecule at standard conditions, the minimum automatically shifts to a new value, and subsequently all the potentials are rescaled to this new reference value.

$$e\theta = C\left(U - U_{NHE}\right) \tag{4.8}$$

By definition this value corresponds to the value of the SHE on an absolute scale. In this way we have obtained an internal measure of the absolute standard hydrogen electrode potential. In theory this value should be universal and hence material independent, but as we shall see in chapter 6, in practice, this is not the case because of the inadequate

screening owing to the limited amount of water in the cell. The 1.07 V offset between the two minima in **Fig. 4.10** determines the difference between the two potential scales on Pt(111).

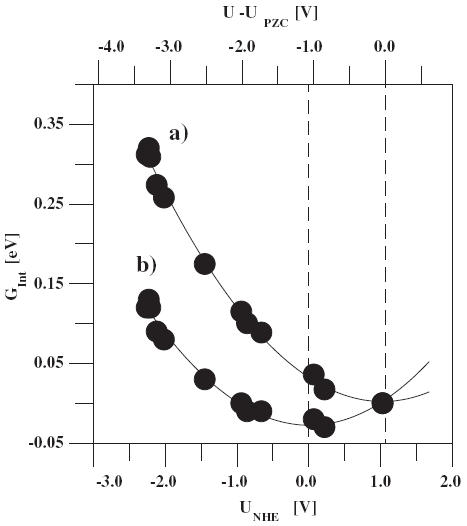

Fig. 4.10: *Integral free energy stored in the EDL plotted as a function of applied potential. We identified two different potential scales (SHE & PZC) depending on the value of the chemical potential of hydrogen in Eq. (4.5). The difference between the two scales is 1.07 V.*

In the previous section we have constrained our analysis on just one water structure, which is as we have seen only partially preserved at the room temperature. To show that our model is generally valid irrespective of the water structure, we performed the same analysis on 3 other water models. The results are presented in **Fig. 4.11** where all the parabolas are normalized compared to the SHE. Model 1 (yellow) is used for comparison and it represents the H-down structure shown in **Fig. 4.10** on an absolute (WF) scale. model 2 (red) and 3 (green) consist of 2 and 3 water films having all the dipoles in the firs layer pointing towards the surface whereas in the 2nd and the 3rd water layer there was an equal amount of dipoles pointing up and down. The resulting dipole was therefore the same as in the model 1. The similarity between the first three water layers is clearly observed in **Fig. 4.11**. Model 4 (blue) is qualitatively different because water dipoles in the 1st and the 2nd bilayer are oppositely oriented and for this reason they cancel out resulting in no net dipole for the whole system. The only dipole moment stems from a hydrogen atom added in the first bilayer to charge the interface. The capacitance is given by the curvature of the parabolas (see Eq. (4.8)) and as we can see it depends explicitly

on the orientation of the water dipoles. Since we do not know how many dipoles are pointing up and down at the room temperature it is hard to compare our capacitance with an experimental one. The best we can do is to make a reasonable estimate by taking the mean values between the two completely opposite models such as model 1 and model 2. The average value of the two obtained in this way (23.5 μF cm^{-2}) agrees well with the experimentally determined 20 μF cm^{-2}.

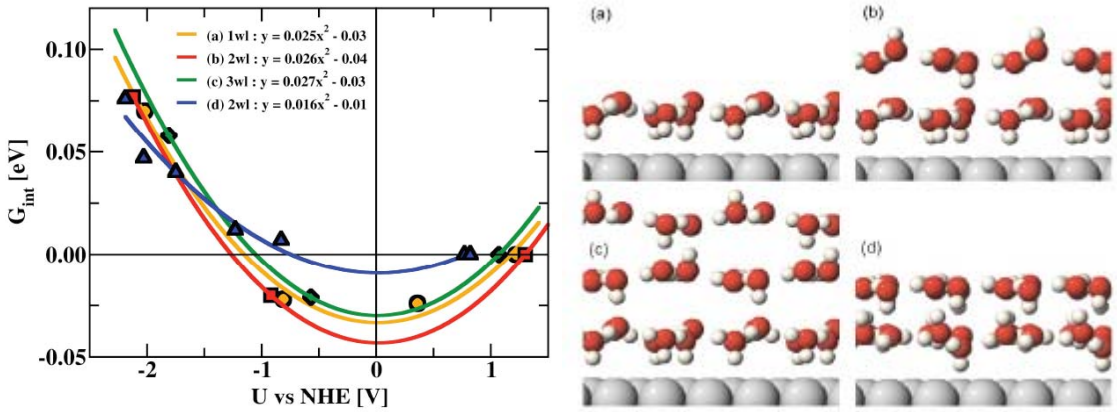

Fig. 4.11: *The integral free energy stored in the double layer plotted for four different water models, illustrated to the right, as a function of applied potential reported on the* U_{NHE} *scale a) the H–down structure (yellow) b) 2 bilayer structure with no net dipole in the 2nd layer c) 3 bilayer structure with no net dipole in the 2nd and the 3rd layer and d) 2 bilayer structure with no overall net dipole.*

4.5 Extrapolation scheme

When studying charge transfer reactions protons are allowed to react. Since protons initially set up the potential and the electric field, performing such a reaction changes the potential of an electrode along the reaction path. Since the bias determines the chemical potential of an electron it also affects the free energy of the states involving electrons. In other words reaction energies will also vary along the reaction coordinate. This effect arises because in our computer analysis we are restricted to use very small unit cell sizes. Therefore performing a single charge transfer reaction equals to reacting many protons at the same time as a consequence of the periodic boundary conditions. In reality this is not the case because protons react one at a time a hence the overall potential remains constant.

There is a little point in studying electrochemical reactions if one cannot determine the reaction enthalpy right.

The impact of the unit cell size on the surface dipole[9] and the energy change along the reaction coordinate for the Heyrovsky reaction is plotted in **Fig. 4.12**. As we can observe the problem is most pronounced for the smaller unit cell and here the potential changes dramatically upon a single proton transfer. Increasing the unit cell size reduces the severity of the problem which suggests that in the limit of a sufficiently large cell the problem would be automatically alleviated.

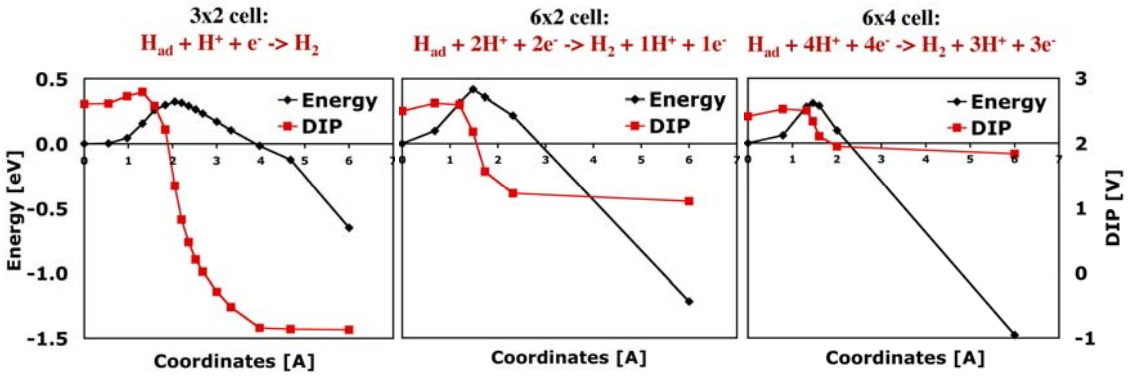

Fig. 4.12: *Change in surface dipole (red) and energy (black) along the reaction coordinate for the Heyrovsky reaction in different unit cell sizes with the same initial proton concentration. The unit cell size is indicated above the figure panel. Adapted from ref. [115].*

To benchmark our method we have studied the HOR since this is the simplest conceivable reaction involving charge transfer. Although we stress here that this method should be generally valid and applicable for any charge transfer reaction. For the time being I will assume that the HOR reaction goes trough the Heyrovsky-Volmer reaction mechanism[10]. In the following I will demonstrate the strength of our scheme by focusing on the Volmer reaction, but nevertheless I will also show the results for the Heyrovsky reaction.

The Volmer reaction is the inevitable step in the HOR and HER direction regardless of the reaction mechanism.

[9] The surface dipole is given by the change in the WF between two sides of the slab. Since one side is always free, the surface dipole equals the change in the WF upon adsorption of a water bilayer on the other side.

[10] Although in the next chapter we will show that the actual mechanism is Tafel-Volmer.

$$H^{*} \rightarrow H^{+} + e^{-} \tag{4.9}$$

The calculated reaction energies, $\Delta E = E_{FS} - E_{IS}$ for the HOR direction, are plotted in **Fig. 4.13** as a function of the change in bias, ΔU, during the reaction. The different labels correspond to the different proton concentrations whereas different colors represent different coverages of the adsorbed H^{*}. The data with the same proton concentration (initial or final) and the same H^{*} coverage were then fitted with the lines of slope ½ which gave nice linear correlations. The slope of ½ is not an arbitrary number but in fact it has a deeper physical meaning. It stems from the structural resemblance between the EDL and the classical capacitor model. When a charge is transferred between the two plates of capacitor (water layer and metal slab) the concentration changes with

$$\Delta\theta = \frac{n}{N} - \frac{(n-1)}{N} = \frac{1}{N} \tag{4.10}$$

The change in the proton concentration causes the change in the reaction energy (cf. **Fig. 4.12**)

$$\Delta G = N\left(G_{int}(N, n-1) - G_{int}(N, n)\right) = N\left(\frac{1}{2}e^{2}\left(\theta - \frac{1}{N}\right)^{2} / C - \frac{1}{2}e^{2}\theta^{2} / C\right) \tag{4.11}$$

where we employed the definition of Eq. (4.7). After some rearrangements Eq. (4.11) can be rewritten in the form

$$\Delta G = -eU - \frac{1}{2}e\Delta U \tag{4.12}$$

Here the number ½ comes in the forefront. Whenever a unit of charge is transferred, the energy changes by ½ of the change in potential. ΔE is always defined for the same reaction direction, in our case the HOR direction, and it is associated with the energy needed to desorb an H^{*} and solvate it as a proton in the water bilayer. ΔU equals the ΔWF[11] and it can be defined both as $WF_{FS} - WF_{IS}$ or $WF_{FS} - WF_{IS}$ depending on which

[11] Remember that the potential was initially deduced from the WF

state, final or initial, we are extrapolating to. I will try to explain this better by focusing on some of the data sets in **Fig. 4.13**.

Take for example the data set for θ=1/6 (black squares). Three points here correspond to three different unit cell sizes. The point closest to ΔU=0 V is calculated for the largest unit cell (6x4), hence the ΔU is the least. The two other points are obtained for the smaller unit cells (3x2 & 3x4) and hence they lie further away from the ΔU=0 V, since the finite size effects are more pronounced. A common thing between all three points is the same final state (FS) proton concentration (θ=1/6, 2/12, 4/24). In the initial state (IS), there is one less proton in the bilayer. Difference in unit cell sizes will also make the difference in the IS proton concentration θ=0/6, 1/12, 3/24. In this case the ΔU for the three points is given by $\Delta U = WF_{FS} - WF_{IS}$. Since the WF_{FS} is always lower than the WF_{IS} (more protons → lower potential) ΔU<0. Extrapolating these values to the ΔU=0 V corresponds to extrapolating the reaction energies to the limit where the potential does not change during the reaction. In the intersection the reaction energy is given for the FS potential, thus we have implicitly assigned the FS proton concentration to the IS.

Let's now consider the white triangles in **Fig. 4.13**. Here all the IS have the same proton concentration, having no proton in the bilayer. In the FS though, from the same reasons, the proton concentration will be different θ=1/6, 1/12 and 1/24. Here we take the ΔU to equal the difference $WF_{IS} - WF_{FS}$. Under these circumstances the ΔU>0 and the intercept yields the reaction energy as if the reaction was taking place at the IS potential. Notice that the difference between taking the ΔU as $WF_{IS} - WF_{FS}$ or $WF_{FS} - WF_{IS}$ results only in the change of sign. In some cases the values of the intercepts were obtained by interpolation from both sides of ΔU=0 V. As a rule of thumb it is worth remembering that we always subtract the WF of the states that have different proton concentrations from the WF of the states that have the same proton concentrations or saying it in other words we always subtract from the WF of a state we are extrapolating (interpolating) to.

All the points in the graph were calculated for the H-down water structure, but to show that the method is generally valid we have also performed a test calculation for a different water structure. For this we chose the water model shown in **Fig. 4.11 d**. The points are denoted with the empty blue circles and again fairly well fitted to a slope of

½[12]. The same slope for all the points can be rationalized in the following way: whenever a hydrogen atom is solvated near the surface, a full charge transfer will occur regardless of the water structure. Since Heyrovsky reaction also involves a charge transfer, we can apply the same scheme to obtain reaction energies at constant potentials.

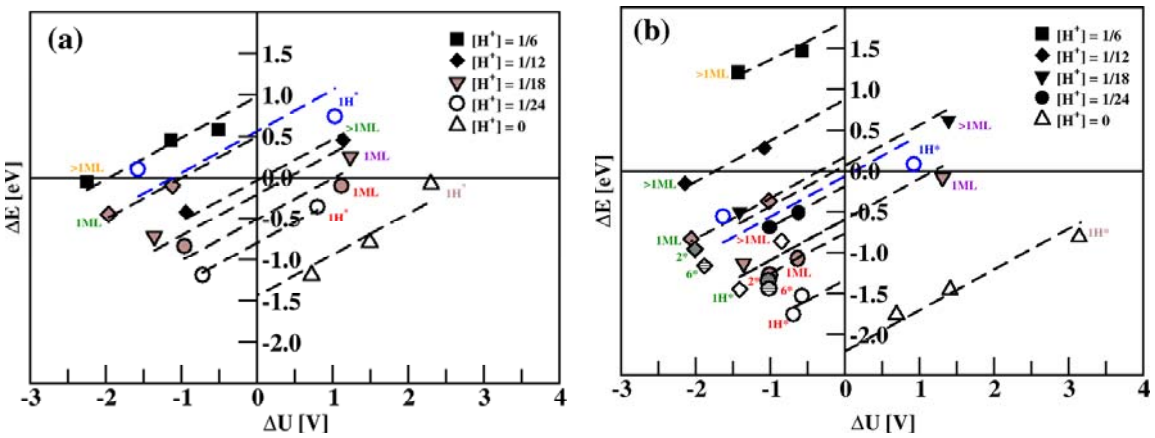

Fig. 4.13: *Reaction energies of the a) Volmer and b) Heyrovsky reactions in the hydrogen oxidation direction shown as a function of the change in electrode potential. Data sets are fitted to the slope of ½ with the broken lines. Intercepts at ΔU=0 V give reaction energies in the limit of a real electrochemical cell where the bias does not change during charge transfer reaction. All the data have been calculated with the H-down structure except for the blue circles where we tested our method on qualitatively different water structure.*

The same approach can be used to determine the activation energies. The activation energy is always defined as $E_a = E_{TS} - E_{IS}$, whereas the expression for ΔU again depends on the state we are extrapolating to. Following the previous guidelines, when FSs have the same proton concentration the difference is written as $U_{FS} - U_{TS}$ (ΔU<0). On the other hand when ISs have the same proton concentration the difference we take is $U_{IS} - U_{TS}$ (ΔU>0). For the activation energies the two values do not differ merely in sign because the transition state is not necessarily located half way between the IS and the FS. The slope of the lines cannot be determined *a priori* because there is a partial rather than a full charge transfer that depends on the location of the TS.

The extrapolation of the Volmer and Heyrovsky activation energies is shown in **Fig. 4.13**.

[12] A somewhat larger deviation from the ½ slope can be attributed to a larger dipole shift between the IS and FS.

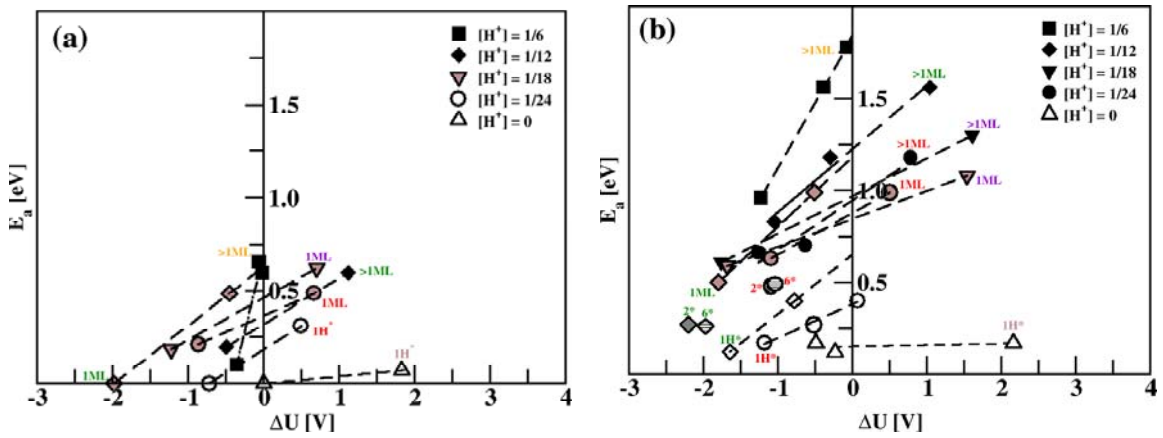

Fig. 4.14: *Activation energy for the a) Volmer and b) Heyrovsky reactions on Pt(111) shown as a function of the change in electrode potential. Intercepts at ΔU = 0 V give activation energies in the limit of a real electrochemical cell where the bias does not change during charge transfer reaction. The slopes of the lines cannot be determined a priori in this case.*

Finally we can test the accuracy of our method if we add the Volmer and the Heyrovsky reaction together in the HOR direction. The overall reaction in the HOR direction reads

$$H_2(g) \rightarrow 2H^+ + 2e^- \tag{4.13}$$

The free energy of the overall reaction is therefore equal to $\Delta G_{HOR} = -2U_{HOR}$ since there are two electrons involved in the reaction. The free energy is obtained by adding the ZPE and entropy to the reaction energies in **Fig. 4.13**. Since we have performed both reactions at several discrete electrode potentials we always add the two that have the same proton concentration.

$$\Delta G_{HOR} = \Delta G_{Heyrovsky} + \Delta G_{Volmer} \tag{4.14}$$

$$U_{HOR} = \frac{U_{Heyrovsky} + U_{Volmer}}{2} \tag{4.15}$$

Here the $\Delta G_{Heyrovsky}$ and ΔG_{Volmer} are the intercepts at ΔU=0 V in **Fig. 4.13**. The values for $U_{Heyrovski}$ and U_{Volmer} are obtained from the WFs of the system we are extrapolating to (systems with the same proton concentration).

The results are plotted in **Fig. 4.15**. Dashed line represents the ideal situation where the ΔG_{HOR} and $2U_{HOR}$ coincide. The small offset we get from the dashed line corroborates the strength of our method.

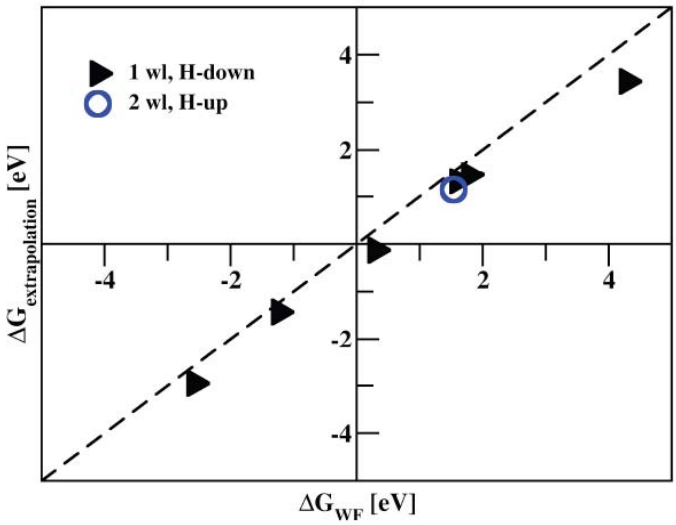

Fig. 4.15: *Free energy of the HOR obtained from the sum of the intercepts for the Volmer and Heyrovsky reactions plotted as a function of the sum of the two potentials obtained from the WFs of the individual reactions. The empty blue circle is obtained for the water model shown in Fig. 4.10d.*

4.6 Summary

To recap, in this chapter we have outlined the best methods known in the literature to control the surface charge and hence the bias. The interface models arising from such methods were subsequently compared to a Stern model of a real electrochemical half-cell. I have elaborated on our model of the charged solid/liquid interface and benchmarked its properties by performing charge density and electrostatic potential difference analysis. Furthermore we have shown that this model agrees perfectly with the Helmholtz picture of the EDL and that it captures all the features of a classical capacitor model (linear potential drop, quadratic behavior of the energy stored in the interface).

In the second part we have introduced the extrapolation scheme to alleviate some of the constraints in our method and after that we have successfully benchmarked our interface model and the method for tuning the bias on the example of a simple hydrogen

evolution/oxidation reaction. Besides we have shown that our method is generally valid irrespective of the water film structure on the surface.

5 Hydrogen evolution and oxidation reactions

In this chapter the solid/liquid interface model and the method for controlling the surface charge will be applied to the elementary reaction steps of the HOR/HER. We concentrate our research efforts on Pt(111), however, in paper II we have also conducted a thorough analysis on other Pt single crystal facets, other transition metals and their steps. For the sake of simplicity results for those surfaces will be omitted in this chapter, except in the very end where they will be invoked for the purpose of kinetic analysis.

The chapter is structured in the following way: first I will briefly address the importance of the HER/HOR and list some of the recent developments in the field of HER/HOR catalyst design. After that, I will apply the extrapolation scheme to obtain right reaction and activation energies for the charge transfer steps (Volmer & Heyrovsky) on Pt(111). Upon comparison of the reaction barriers among the elementary reaction steps, we concluded that the Tafel reaction is the rate determining step on Pt(111). Moreover, because of the small differences in hydrogen binding energies among different metals and facets we concluded that the Tafel step will prevail on all metal surfaces we have investigated. Finally, we used the obtained data as input to a kinetic model to demonstrate the degree of agreement between theory and experiments.

5.1 Introduction

We used Pt(111) throughout our work because it is the best and most widely used catalyst for the HER/HOR. Finding a viable alternative to Pt is a major scientific challenge and one of the key prerequisites for establishing a hydrogen society. Pt is nowadays the archetypical catalyst for the HOR in the PEMFCs. The amount of Pt used at the anode is ~0.05 mgPt/cm^{-2} [17]. Albeit, in alkaline FCs, which have recently regained interest, the amount increases 4 times because of the sluggishness of the HOR under those conditions [118,131].

Modeling the HOR, we at the same time automatically model its reverse, the HER. This reaction is industrially important in the fields of electrodeposition and corrosion of metals, energy storage via H_2 production and other.

It has been proven many times that nature has already given answers to the problems we seek to solve. For example there are certain types of enzymes called hydrogenases and nitrogenases that are quite effective catalysts for the HER [119,120,121]. The most intriguing thing is that their active centers are made of earth abundant materials such as Fe, Ni, and Mo, so obviously nature has found a way to avoid the use of scarce and inaccessible materials such as noble metals. These enzymes have a very low specific activity due to the very low active site density. From an energy point of view this is quite comprehensible since the energy needed to sustain life is much lower than e.g. the energy needed to run vehicles. The challenge is to learn from nature and try to make inorganic analogues with a sufficiently high specific activity. Recently it became possible to anchor hydrogenases to an electrode surface [122,123] and from that time considerable progress has been made to synthesize compounds resembling hydrogenases's active site, which exhibit high activity for the HER [6,124].

Another approach to a successful catalyst design is to promote activity of known catalysts by modifying their electronic structure by means of alloying [125]. It is a well acknowledged fact that the HER/HOR activity is associated with the hydrogen adsorption energy via Volcano plots [43,126]. Recently, a simple and fast systematic approach that uses adsorption free energies calculated by DFT was used to model the HER/HOR [124]. Result of that study is shown in **Fig.** 5.1**.** As we can see, a simple kinetic model reproduced surprisingly well the trends in exchange current densities. The best catalyst material was found to be the one close to $\Delta G_{H^*} = 0\ \mathrm{eV}$. Absolute magnitudes were of course wrong because no kinetics (barriers) were included at the time. An astonishing fact about this study is that activity trends were so nicely captured by the values of hydrogen chemisorption energies alone. This key discovery allowed for large scale screening studies where the only activity criterion was the H binding energy. These studies resulted in identification of some promising candidates for the HER [6, 125].

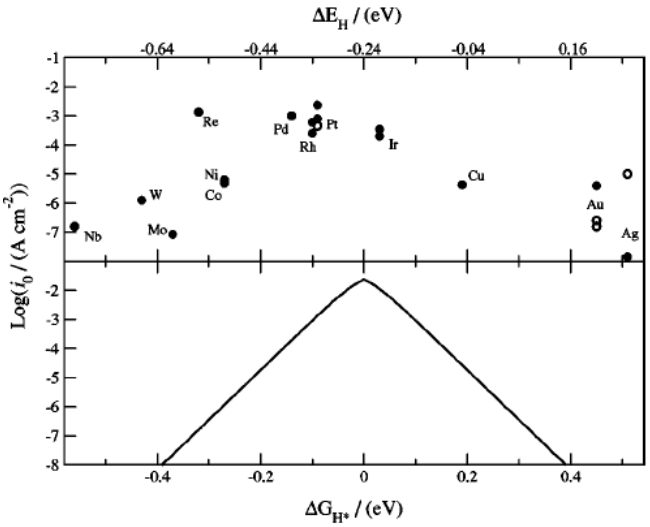

Fig. 5.1: *(top) Experimentally measured exchange current for the HER over different metal surfaces, plotted as a function of the calculated hydrogen chemisorption energy (top axis). (bottom) The result of a simple kinetic model. A free fitting parameter was used to adjust the magnitude of the volcano. Adapted from ref. [43]*

Although a simple thermodynamic property gives a good estimate of the activity, to get a full molecular level insight into a reaction it is necessary to know both the thermodynamics and the kinetics. Since the hydrogen adsorption energy is the governing factor in determining the activity it will also be the best place to start our investigation.

5.2 Hydrogen coverage dependent potential scale

It has previously been shown that the DFT calculated hydrogen isotherms on Pt(111) agreed extremely well with isotherms obtained from CV measurements [127]. Moreover, to be as close as possible to the real system we have to achieve consistency between the potential and the hydrogen coverage. As we shall see later, this is of a particular importance when studying the Tafel reaction.

To calculate the free differential adsorption as a function of coverage (H isotherm) we invoke Eq. (3.53).

$$\Delta G(U,pH) = \Delta E + \Delta ZPE - T\Delta S - T\frac{dS_{conf}}{d\theta_{H^*}} - 0.059pH - nU + \Delta E_{w,water} + \Delta E(\varepsilon(U)) \quad (5.1)$$

where n is the number of electrons involved in the reaction. All of these terms will be addressed individually below. The differential hydrogen adsorption energy (ΔE) is calculated as

$$\Delta E_{H^*} = E_{(n+1)H^*} - E_{nH^*} - \frac{1}{2} E_{H_2(g)} \tag{5.2}$$

where n is the number of hydrogen atoms on the surface. In this way we compare the hydrogen adsorption energy to H_2 in the gas phase. To get a free energy, the change in zero point energy (ΔZPE) and entropy (TΔS) of H^* compared to its reference state, $H_2(g)$, has to be added to the value of ΔE_{H^*}. The ZPE of H^* has been calculated from normal mode analysis on a number of transition metals elsewhere [128]. The value is almost constant regardless of the metal substrate (0.14-0.18 eV). In our study we assumed the average value (0.16 eV). The ZPE and entropy[13] of $H_2(g)$ (0.27 eV & 0.41 eV) have been taken from standard molecular tables [129]. A configuration entropy term also has to be taken into account if hydrogen atoms on the surface are not interacting. This is true below 1ML where hydrogen atoms are adsorbed in FCC sites, whereas above 1ML hydrogen atoms are adsorbed in on-top positions where they become more interacting.

$$\frac{dS_{conf}}{d\theta_{H^*}} = k_B T \ln\left(\frac{1-\theta_{H^*}}{\theta_{H^*}}\right) \tag{5.3}$$

We take pH=0 since we are mimicking highly acidic environments. The pH term thus vanishes. This brings us to the last two terms in Eq. (5.1) that take into account the effect of water and an electric field on the adsorption energy. Their influence on the ΔE_{H^*} as a function the H coverage is plotted in **Fig. 5.2**.

[13] The vibrational entropy for H^* was calculated to be TS^{vib} =0.01 eV and thus it was neglected in further analyses.

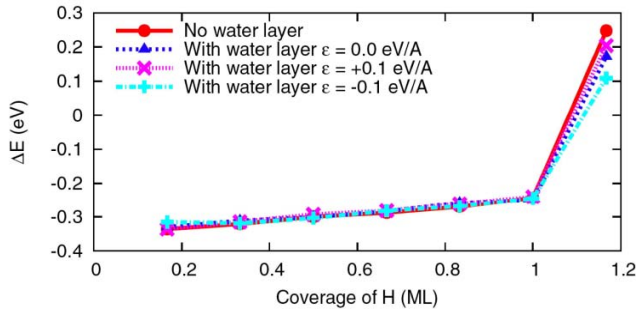

Fig. 5.2: *Differential hydrogen adsorption energy as a function of hydrogen coverage on a pristine Pt(111) surface and under presence of water and an applied electric field. Adapted from ref. [127]*

It is clearly seen that the electric field and water induce only minor changes in the H adsorption energy in the entire reported H coverage range. Although some small influence on the order of 0.1 eV is discernible above 1ML[14]. After dropping all the redundant terms, Eq. (5.1) reduces to

$$\Delta G(U) = \Delta E + \Delta ZPE - T\Delta S - T\frac{dS_{conf}}{d\theta_{H^*}} - nU. \qquad (5.4)$$

The hydrogen adsorption energy and free energy are presented in **Fig. 5.3.**

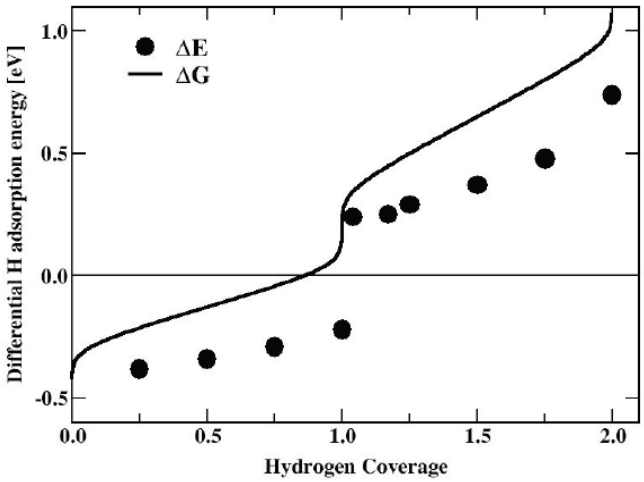

Fig. 5.3: *Differential adsorption energy (ΔE) and free adsorption energy (ΔG) as a function of the hydrogen coverage on Pt(111).*

[14] This is because above 1ML, H^* binds to an on-top position where it has larger perpendicular dipole moment than when it is bound in the fcc position below 1ML [108].

In the construction of **Fig. 5.3** we have implicitly assumed, by setting $H_2(g)$ to be the reference state for H^*, that the hydrogen adsorbs from the gas phase. In reality hydrogen stems from a proton in the solution and an electron in the electrode.

$$H^+ + e^- \rightarrow H* \tag{5.5}$$

The hydrogen coverage is determined by the chemical potential of electrons and protons in the solution. The chemical potential of protons is fixed because the solution is maintained at a constant pH while the chemical potential of electrons varies under influence of the potential. The chemical potential of H^* at some finite U can be written as

$$\Delta G_{H^*}(U) = \Delta G_{H^*}(0) - eU \tag{5.6}$$

If we assume the Volmer reaction (1.9) to be in equilibrium which we will ascertain later, the coverage of H^* on the surface will be given by the chemical potential of $H_2(g)$. This implies that at U=0 V, $\Delta G_{H^*}(0) = 0$ and hence

$$\Delta G_{H*}(U) = -eU. \tag{5.7}$$

This is an extremely important relation because it enables the conversion of the free energy scale in **Fig. 5.3** into an electrode potential scale. In this way we have established a simple U scale which is dependent on the hydrogen coverage. When the bias is decreased from a positive value, at ca. 0.4 V, the hydrogen starts to adsorb on the surface and at U=0 V it reaches the coverage of 0.86 ML[15]. This compares semi-quantitatively to 2/3 ML measured in CVs [11]. However, the same authors have recently corrected their estimate to ~0.9 ML at U=0 V by finding some extra charge [130].

We stress here that this approach is general and in paper II we have used it equally on other metals and facets to relate the hydrogen coverage and SHE potential scale.

[15] ML is defined on the bases of one H^* per Pt surface atom.

5.3 Reaction mechanism

Even though the HER and HOR have been intensively scrutinized on low indexed Pt facets in the past [11,113,115,131,132,133,134,135,136,137], no consensus has been reached as to what is the predominant reaction mechanism and rate determining step. Some studies, based on modeling of the kinetics of the HOR on Pt electrodes over the entire relevant potential region, concluded that the Volmer-Tafel pathway dominates at low overpotentials, whereas the Volmer-Heyrovsky route becomes more important at high overpotentials [138]. What these studies agreed on is that the HER/HOR involves, in principle, 3 elementary reaction steps. To illustrate these I will assume the HER direction. The first step is the Volmer reaction where a proton initially discharges to form adsorbed hydrogen on the surface.

$$\text{Volmer}: H^+ + e^- \rightarrow H^* \tag{5.8}$$

There is no doubt that this step is very fast and not a rate determining one [131].

Regarding the second step two qualitative different reactions have been proposed in the literature where the Tafel reaction was found to be the rate limiting step on some Pt facets [11,131,133, 139], whereas Heyrovsky was found on others [11,134,137]. No conclusive evidence in favor of either reaction has so far been reported on Pt(111) [11,134]. The current view appears to be that different metal facets open up different reaction mechanisms for HOR and HER.

The Heyrovsky reaction is also a discharge step, where a proton from the solution reacts with the hydrogen already adsorbed on the surface to form H_2(g). The second possibility, the Tafel reaction, is that two protons, initially discharged from the solution through the Volmer step, react on the surface. This is thus a typical example of a Langmuir-Hinshelwood reaction[16].

$$\text{Tafel}: H^* + H^* \rightarrow H_2(g) \tag{5.9}$$

$$\text{Heyrovski}: H^+ + e^- + H^* \rightarrow H_2(g) \tag{5.10}$$

[16] Langmuir-Hinshelwood reaction is a type of reaction where both molecules first adsorb before undergoing a bimolecular reaction.

All the elementary steps are illustrated in **Fig. 5.4**.

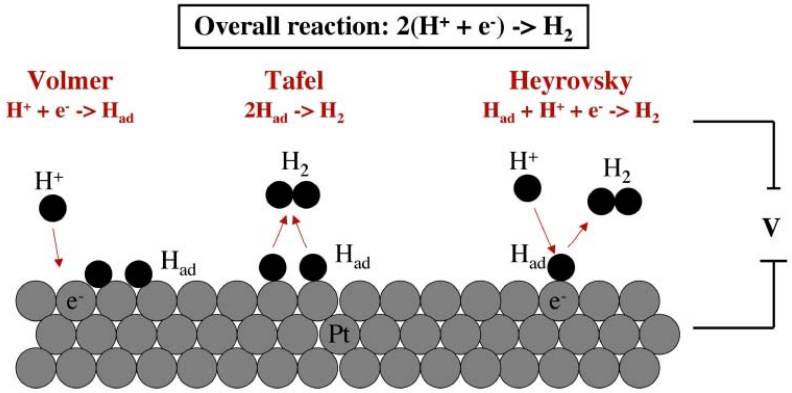

Fig. 5.4: *Schematics of the HER and its reverse HOR, illustrating the three possible elementary reaction steps through which these reactions proceed. Adapted from ref. [115].*

It is important to note here that most of the experimental data about barriers' height and reaction mechanisms comes from rate measurements. As we have seen in the introduction chapter activation barriers are usually obtained from Tafel slopes (Eq. (2.6)) or from the current density in the micropolarazation region (Eq. (2.3)). The kinetic rate is measured macroscopically and therefore it is a sum of many processes occurring concurrently on the surface (e.g. proton diffusion) and not a single reaction. Another problem is that the HER/HOR is extremely fast on Pt and hence it will very quickly come under diffusion control [11]. There is a very narrow potential region where the reaction is under kinetic control and where the Tafel equation holds. It is thus very difficult to get correct estimates of the Tafel slopes and hence the reaction barriers.

There have not been many theoretical studies on the kinetics of the HER/HOR because it was impossible until just recently to explicitly include potential and electric field in standard DFT calculations. This has motivated the scientific community to invest some time into development of methods that could allow studies of electrochemical reactions at different biases. In the following we will apply the method described in the previous chapter to study the Volmer and Heyrovsky reactions at different potentials, whereas the coverage dependent H electrode potential scale will be used to study the Tafel reaction at different biases.

5.3.1 Volmer Reaction

The first reaction in the reaction mechanism I will consider here is the Volmer reaction. Since this reaction involves charge transfer it requires a full double layer setup consisting of a metal slab, water bilayer and protons. We implement the extrapolation scheme and report all the energies in the limit where the potential does not change during a charge transfer reaction. In this way we have calculated reaction and activation energies at a few discrete electrode potentials (proton concentrations). These results are displayed in the form of activation energy, E_a, against reaction energy, ΔE, plots in **Fig. 5.5** in both the HER and HOR direction. The values of the ΔE and E_a were obtained from **Fig. 4.13** & **Fig. 4.14**. A nice linear relationship appears which is yet another manifestation of the Brønsted-Evans-Polanyi (BEP) relationship frequently observed in surface science studies [140,141,142,143,144]. The intercept in both HER and HOR directions is the same (0.44 eV)[17], since at $\Delta E=0$ both activation barriers are of equal height.

Additionally we have also presented the results on a U scale in **Fig. 5.6**, where we dropped all the points where the H coverage was not consistent with the bias through **Fig. 5.3**. A linear relationship is again clearly observed. The intercepts are now dependent on the reaction direction and they amount to 0.72/0.43 eV in the HER/HOR direction respectively.

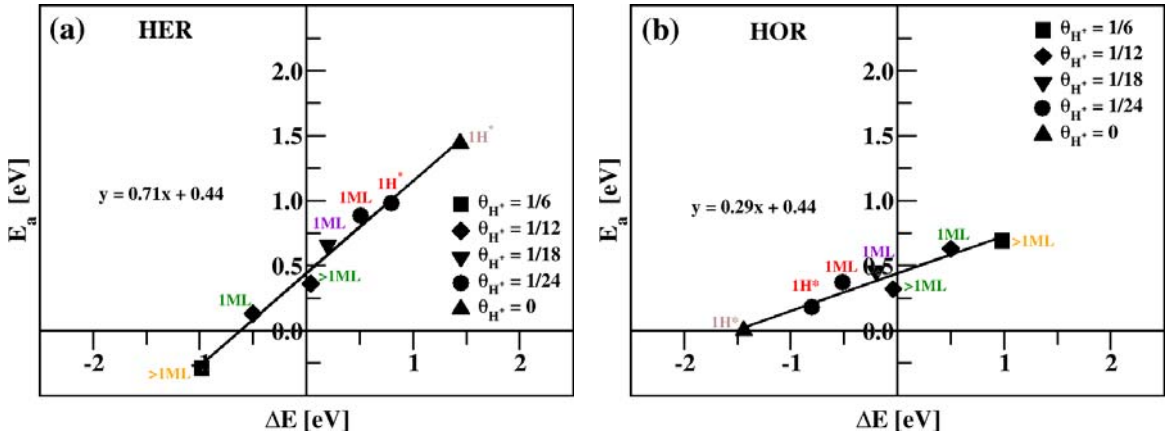

Fig. 5.5: *Activation energy for the Volmer reaction on Pt(111) as a function of reaction energy in a) the HER and b) HOR direction.*

[17] Notice also that the two slopes add to one.

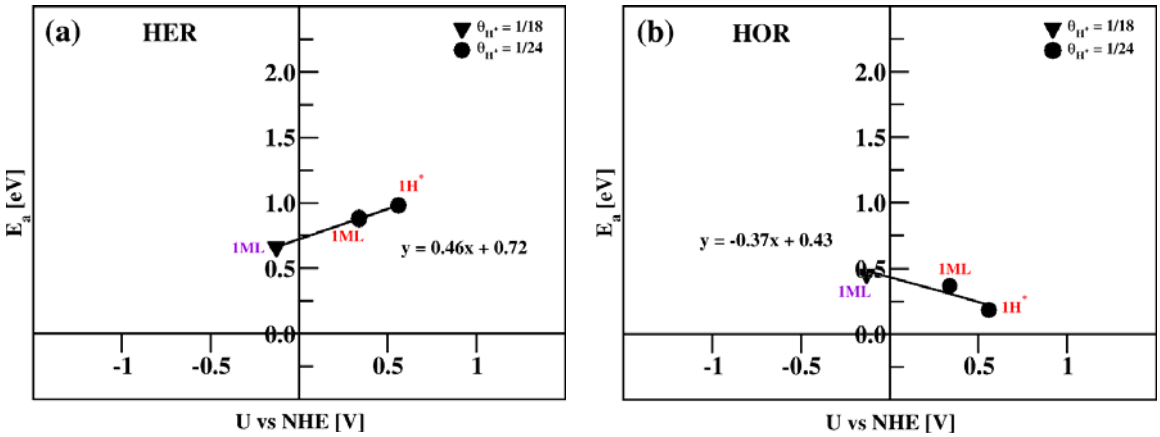

Fig. 5.6: *Activation energy for the Volmer reaction on Pt(111) as a function of the electrode potential in a) the HER and b) HOR direction.*

5.3.2 Heyrovsky reaction

Since the Heyrovsky reaction is also a charge transfer reaction we had to employ exactly the same setup as for the Volmer reaction. Once again we vary the proton concentration in order to span a large potential window. We report our results in the form of Ea vs ΔE and Ea vs U plots for both reaction directions in **Fig. 5.7** and **Fig. 5.8**. In the case of the Ea vs U plot, only data with a right H coverage have been included. The intercept vs ΔE is 1.04 eV which is substantially larger than the one obtained in the case of the Volmer reaction (0.44 eV). The intercepts in the Ea vs U plots are 1.40/0.8 eV in the HER/HOR direction respectively. The values of the intercepts for the Heyrovsky reaction (1.40/0.8 eV) are much higher than for the Volmer reaction (0.72/0.43 eV). Our analysis thus indicates that the Heyrovsky reaction will be very slow on the Pt(111) surface at U=0 V.

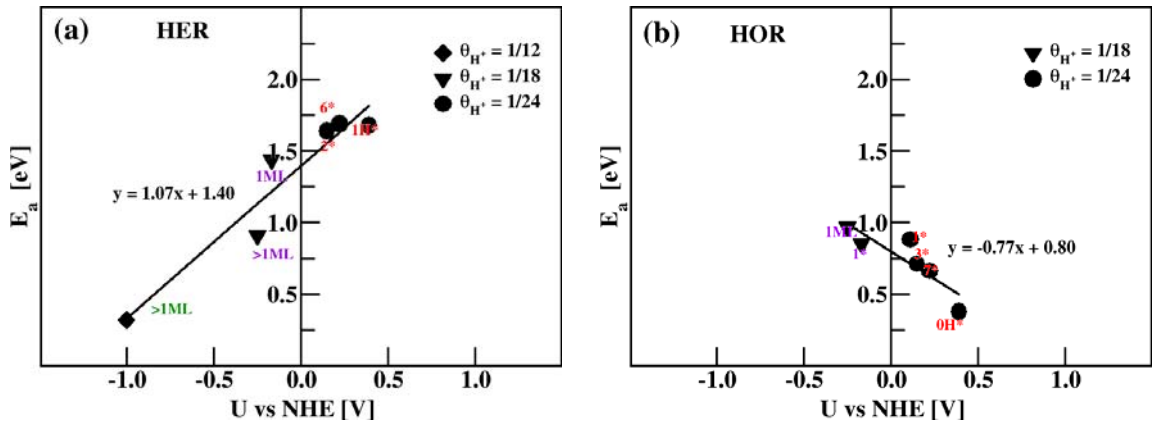

Fig. 5.7: *Activation barrier for the Heyrovsky reaction on Pt(111) as a function of reaction energy in a) the HER and b) HOR direction.*

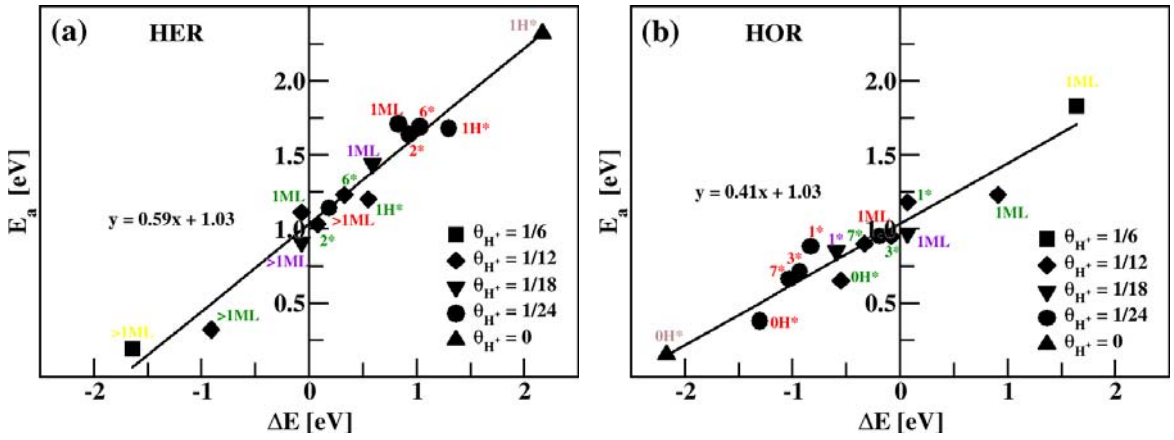

Fig. 5.8: *Activation barrier for the Heyrovsky reaction on Pt(111) as a function of the electrode potential in a) the HER and b) HOR direction.*

5.3.3 Tafel reaction

The Tafel reaction is a typical Langmuir-Hinshelwood-type reaction where two H^* on the surface react to form H_2(g). We have previously shown (cf. **Fig. 5.2**) that water and electric field exert minor influence on the hydrogen adsorption energy. The system size was thus reduced to just having a metal slab and adsorbed hydrogen. This lowered the computational cost considerably and hence allowed us to study the Tafel reaction on many different metals and facets. Since the Tafel reaction does not involve any electrons, at first sight it might be regarded as potential independent. This is not true though because the potential implicitly comes into play via the hydrogen coverage (cf. **Fig. 5.3**).

In **Fig. 5.9** we have plotted activation energy, E_a, against the reaction energy, ΔE, in the HER and HOR direction on Pt(111). The variation in both E_a and ΔE originates from different H coverages. The E_a and ΔE are again well linearly correlated having the intercept 0.55 eV. Incidence of linear relationships in both charge transfer reactions (Volmer & Heyrovsky) and surface reactions (Tafel) demonstrates the universality of BEP relationships in electrochemistry and surface science. The 0.55 eV barrier is considerably lower than 1.03 eV obtained for the Heyrovsky reaction at ΔE=0. Since the Tafel reaction is also implicitly potential dependent through the H coverage, we have as well displayed our results on a U scale in **Fig. 5.10**. The potentials were obtained from **Fig. 5.3** when the free energy scale was converted to a potential scale via Eq. (5.7). At U=0 V the activation barriers in the HER/HOR directions are ~0.85/0.55 eV respectively.

At U close to 0 V almost all the surface is covered by hydrogen[18] and therefore one vacancy is used to account for the empty sites. When H_2 dissociates on the surface, one hydrogen atom is forced to adsorb on an on-top site. Locally there might be more free neighboring sites on the surface. If we model the surface with a dimmer vacancy the barrier reduces to 0.4 eV at U=0 V (white rectangle in **Fig. 5.9** and **Fig. 5.10**. Hence the Tafel barrier depends strongly on the local hydrogen coverage. This issue will be thoroughly dealt with in next section.

To recap, we have seen that in both directions the activation barriers both vs ΔE and U are almost half as low as the ones obtained for the Heyrovsky reaction at U=0V. Moreover the Tafel barrier is lower in the entire investigated potential range. This strongly suggests that the Tafel reaction is much faster than the Heyrovsky and therefore the predominant step on Pt(111). Compared to the Volmer reaction the activation barrier of 0.85 eV for the Tafel reaction in the HER direction is higher than the one for the Volmer step at U=0 V (0.72 eV for the HER). In the reverse direction the barriers are, however, similar (0.4 eV vs 0.43 eV). Our results indicate that the Volmer-Tafel route is the predominant reaction mechanism for both HER and HOR on Pt(111) at U=0 V. Hence we can concentrate only on the Tafel reaction in the following kinetic analysis.

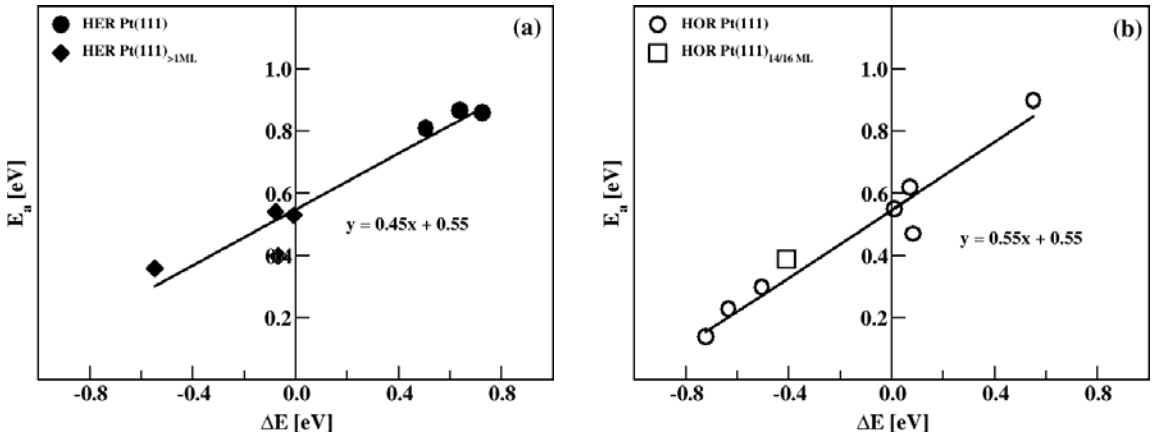

Fig. 5.9: *Activation barrier for the Tafel reaction on Pt(111) as a function of reaction energy in a) HER and b) HOR direction .*

[18] The hydrogen coverage is 0.86 ML to be precise.

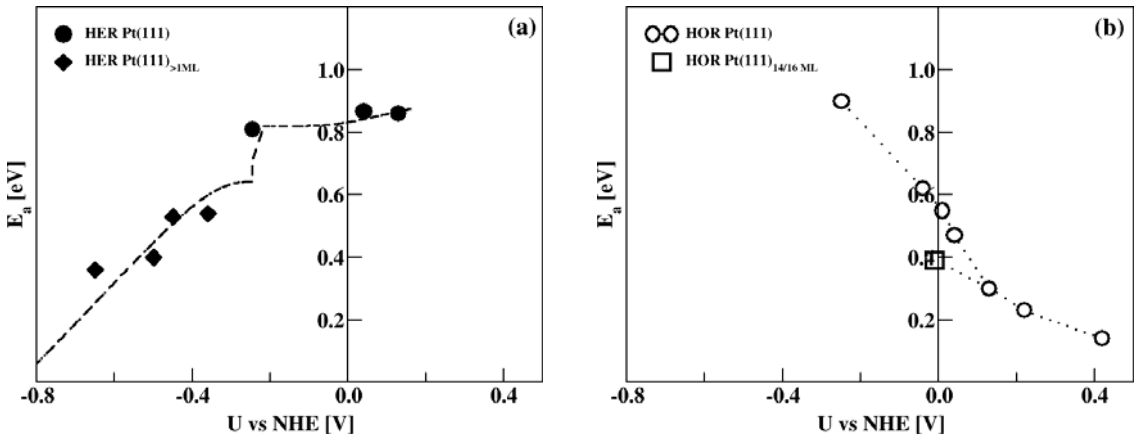

Fig. 5.10: *Activation barrier for the Tafel reaction on Pt(111) as a function of the electrode potential in a) HER and b) HOR direction.*

5.4 Kinetic model

We saw in previous section that the height of the Tafel barrier depends strongly on the local hydrogen coverage. Therefore instead of assigning each activation barrier to a given H coverage, we will associate an activation barrier to each configuration described by the number of H nearest neighbors (NN). Here we use the convention that NN is taken for the FS in the HOR direction and hence for the IS in the HER direction. These are the states determining the actual heights of the barriers.

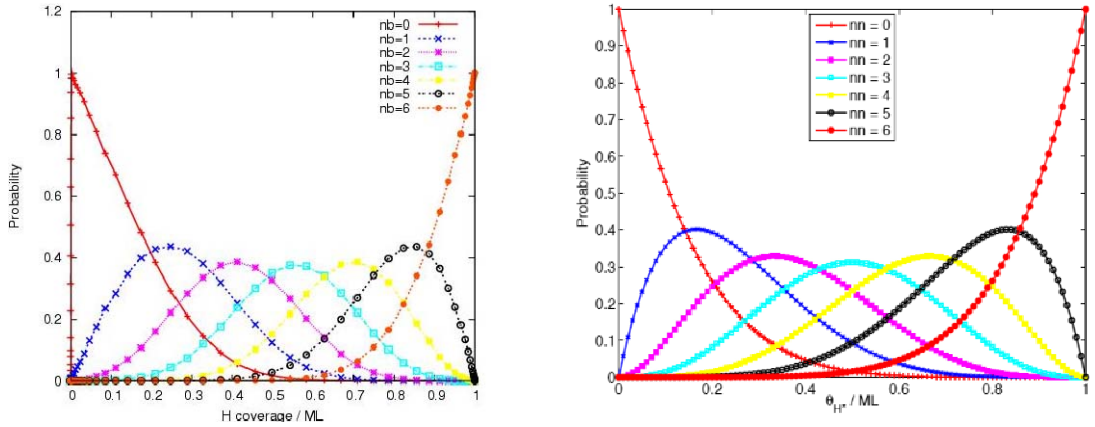

Fig. 5.11: *Probability of having a given number of nearest neighbors (NN) as a function of H coverage, calculated with a) Metropolis Monte Carlo simulations including adsorbate interactions and b) analytically without interactions.*

Since we are mainly interested in the potential region around U=0 V, we have chosen only to consider data for 1 ML H coverage or below (cf. **Fig. 5.3**). In **Fig. 5.11** we have

calculated the probability of having a given nearest neighbor (NN) configuration at a certain H coverage ranging from 0 to 1 ML, both with an interacting lattice model using Metropolis Monte Carlo (MC) simulations and analytically with a non-interacting lattice model.

As can be seen from **Fig. 5.11**, the two models yield very similar results. We chose the analytical model for the sake of simplicity. For the MC simulation a hexagonal fcc(111) surface is modeled with a simple lattice model where each H in an FCC site can interact with up to 6 nearest neighbors. The analytical hexagonal lattice model is non-interacting and is thus given by the binomial coefficients:

$$P_i(\theta) = \left(\frac{i!}{i!(6-i)!}\right)\theta^i(1-\theta)^{6-i} \tag{5.11}$$

The equation for the rate constant is given by the Arrhenius equation (Eq. (2.10)). Since there are 7 possible numbers for the NN the rate constant is given by the sum over weighted rate constants

$$k_T = \sum_{i=0}^{6} P_i(\theta)\,\nu \exp\left(\frac{-E_{a,i}}{k_b T}\right) \tag{5.12}$$

where we assumed the normal value of $\nu = 10^{13}\,\mathrm{site}^{-1}\mathrm{s}^{-1}$ for the preexponential factor (attempt frequency). The rates in the HER and HOR directions are given by

$$r_T^{HER} = \theta^2 k_T^{HER} = \nu \cdot \sum_{i=0}^{6}\left(\frac{i!}{i!(6-i)!}\right)\theta^{i+2}(1-\theta)^{6-i} \cdot \exp\left(\frac{-E_{a,i}^{HER}}{k_b T}\right) \tag{5.13}$$

$$r_T^{HOR} = (1-\theta)^2 k_T^{HOR} = \nu \cdot e^{(\Delta S/k_B)} \sum_{i=0}^{6}\left(\frac{i!}{i!(6-i)!}\right)\theta^{i}(1-\theta)^{8-i} \cdot \exp\left(\frac{-E_{a,i}^{HOR}}{k_b T}\right) \tag{5.14}$$

where $e^{(\Delta S/k_B)} = 1.3 \cdot 10^{-7}$ is the entropy barrier or loss of entropy when H_2 comes from the gas phase and dissociates on the surface. In **Fig. 5.12** we present the results of the calculated rate constants as a function of the H coverage at 300 K.

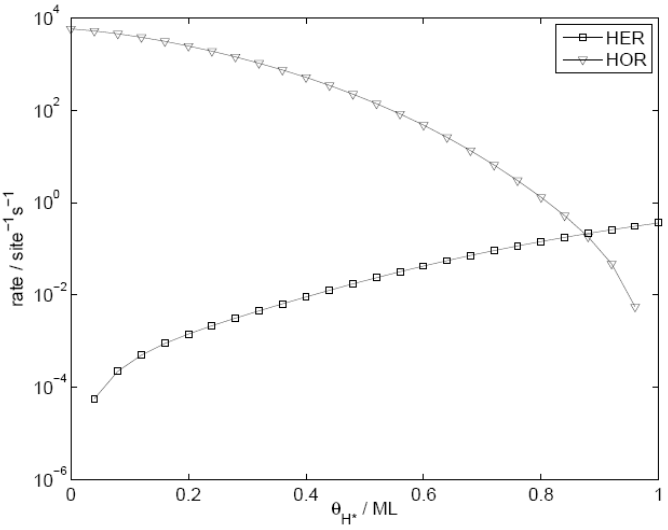

Fig. 5.12: *Tafel HER and HOR rates at 300 K as a function of the H coverage.*

At equilibrium (U=0 V), the calculated rates for the HER and HOR are identical, $4.5*10^{-4}$ A cm^{-2}, and there is no net flow of current. This value compares extremely well with, $i_0 = 4.5*10^{-4}$ A cm^{-2} which is the experimental value for the exchange current density on Pt(111) at 303 K [8]. Another important observation is that the equilibrium H coverage (0.87 ML) lies very close to 0.86 ML obtained with another approach (cf. **Fig. 5.3**). On the other hand the measured barrier for the Tafel reaction ~0.2 eV [8] is much lower than what we get in our analysis. If we assume a barrier of 0.2 eV, the prefactor in the Arrhenius equation would be on the order of $\nu = 10^3 \text{site}^{-1}\text{s}^{-1}$ or 10 orders of magnitude lower than the normal prefactor for the proton diffusion in water and ice. Since it is hard to believe in such a low prefactor, we speculate that the low activation barrier might originate from some other surface process, such as proton diffusion in water which has a barrier of 0.1-0.15 eV [91,145,146,147]. As we have seen in the introduction chapter it is not so straightforward to infer activation barriers from rate measurements, especially in the case where the reaction kinetics is extremely fast as for the HER/HOR on Pt(111).

5.5 Activity volcano

In this section we will make an estimate of activities based on insight and data from the aforementioned analysis. In the previous DFT analysis [124] it was established how a simple kinetic model based solely on the variation of the hydrogen adsorption energy describes well the HER activity trends across different metals (cf. **Fig. 5.1**). The model however failed to capture the absolute magnitude since no kinetic parameters were included at that time. This simple picture demonstrated that if there are any kinetic barriers they should be essentially of the same magnitude, otherwise trends would not be so accurately described from thermodynamical parameters alone. Furthermore the authors assumed a low (0.25 ML) coverage for all the metals. This is not entirely correct because the metals that bind stronger will be almost filled with H at U=0 V. Here we employ a more advanced kinetic model where all the parameters are obtained from the first-principle calculations presented in this work. We emphasize that no fitting parameter has been used. For the attempt frequency we assumed a normal value ($\nu = 10^{13}\ \mathrm{site}^{-1}\mathrm{s}^{-1}$) which is a usual value found for proton diffusion in water and ice [148, 149, 150, 151,152]. We take the Tafel reaction to be the rate determining step and we assume that the Volmer reaction is in equilibrium. Furthermore we assume that we can describe the variation in E_a for all the metals with the BEP relation established for Pt(111), shown in **Fig. 5.8**. Small changes in the H adsorption energy for all the metals studied in this work at U=0 V will result in a small change in the activation energy. We also considered defects such as steps in our analysis because these could have higher H binding energy and also might follow different BEP relationships. We found that the H binding energy on the steps is similar to fcc surfaces at U=0 V meaning the steps will fall on the same BEP line as Pt(111).

In **Fig.** 5.13 the experimentally measured exchange current densities (symbols) are plotted against H adsorption free energies from DFT calculations. For the metals on the left side of ΔG = 0 eV we use high coverage (1 ML) data since these metals will be filled with H at U=0 V. However for the metals on the right side - Cu, Au, and Ag - we use low H coverage (0.25 ML) because these will fail to adsorb almost any hydrogen at U=0 V. Here, the data falls nicely on the volcano curve predicted by our model (solid and dashed

line). Notice that the left leg of the volcano is indicated by a dashed line to stress that these metals will most likely form oxides. However, in our modeling we used the hydrogen binding energy on a pristine metal surface, and remarkably we get these points to fall directly on the volcano as well. The good agreement throughout the metal series is another evidence the Tafel barrier is the rate limiting step on all the metal electrodes displayed in **Fig.** 5.13.

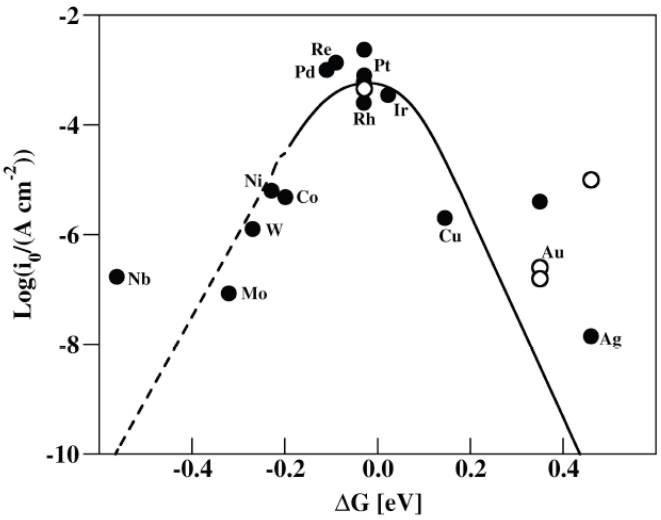

Fig. 5.13: *Experimentally measured exchange current densities (symbols) plotted versus calculated free H adsorption energies at U=0 V. The metals on the left side of the volcano have high H coverage (1 ML) whereas the metals on the right side have low H coverage (0.25 ML). The line is a prediction by a kinetic model where all inputs have been taken from DFT calculations. The dashed line indicates that the metals which bind H stronger than 0.2 eV/H usually form oxides at U=0 V. The open circles are (111) data while the filled circles are polycrystalline data.*

5.6 Summary

We have performed a detailed study of the Heyrovsky and Volmer reactions on Pt(111) and of the Tafel reaction on many transition metals surfaces and steps. We have concluded that due to the large difference between the Heyrovsky and Tafel barriers on Pt(111) the Volmer-Tafel pathway will prevail on all the surfaces investigated in this work. We used the BEP line from Pt(111) as input to our kinetic model, which reproduced the experimentally measured activities remarkably well. The only

disagreement is that the height of the Tafel barrier is four times larger than the one deduced from CV measurements, albeit the theoretically predicted and experimentally measured exchange currents are in perfect balance. Presently we are not able to explain these inconsistencies.

6 Computational standard hydrogen electrode

In DFT based studies of electrochemical reaction electrochemical cells are typically split into two half-cells, which can then be studied separately. Here the absolute potential enters as a key parameter because it is no longer possible to measure potential difference between the two electrodes. As exemplified in chapter 4, methods to explicitly account for potentials have recently appeared within the framework of DFT. This success has contributed significantly to the studies of electrochemical processes. Regardless of the formalism and implementation, in most of the methods the potential was inferred from the difference between the system's WF and the experimentally measured absolute standard hydrogen electrode potential (ASHEP)[19] (cf. Eq. (4.2)). The problem is that the ASHEP cannot be precisely measured and the experimental error bar of 0.2-0.4 V can significantly affect the values of the computed potentials. Even worse, due to the limited amount of water that can be afforded in a typical DFT calculation, the calculated work function depends explicitly on the structure of the water at the metal/aqueous interface, which further adds to the uncertainty of the computed potentials. Here I will show how these errors can be avoided if an internal measure of the ASHEP is instead used as a reference.

The chapter is structured in a following way: in the beginning I will introduce some of the theoretical concepts behind absolute standard electrode potentials, developed by Trasatti and others [112,153,154,155,156,157,158]. Most of the time I will devote to explaining what is the single electrode potential and what is the best choice for a reference state for an electron in theoretical models and, in particular, in DFT setups. From the available experimental data I will make the best estimate of the ASHEP and finally I will show how the internal (theoretical) measure of the ASHEP strongly depends

[19] This is the same as the WF of the standard hydrogen electrode.

on the structure of the interfacial water by analyzing two qualitatively different water models.

Before starting I would like to take the opportunity to pay honor to Sergio Trasatti for all the excellent contemplative work he has done trying to elucidate the true nature of absolute electrode potentials.

6.1 Introduction

I will begin by introducing and explaining some quantities that are vital for the purpose of the following discussion.

The inner or the Galvani potential (φ) is the electric potential difference between two points in the bulk of two phases. It can be written as a sum of two terms

$$\varphi = \psi + \chi \tag{6.1}$$

Free charges at the interface give rise to an outer potential (ψ), while different spatial arrangement of dipoles at the interface compared to the bulk gives rise to a surface potential (χ).

The quantity that we will mostly exploit is the WF. The WF measures the work to transfer an electron from the Fermi level of a metal to a chosen reference state. For the pristine metal surface we can think of two such plausible states, near-field vacuum VL(s) of far-field vacuum VL(∞). The VL(s) is a variant energy level since the potential of an electron in the near-field vacuum is not relinquished of the influence of surface dipoles. The surface dipoles (electron density tail) arise as a consequence of the Friedel oscillations, which trace back to the wave property of electrons. Since the Fermi level is a common level inside a solid, the dependence of the WF for different facets arises because of differences in the surface dipoles. The magnitude of the surface dipoles depends on the degree of surface corrugation. Close-packed facets will always have higher WFs because on more open facets a so-called Smoluchovski effect[20] of charge smoothing [159],

[20] The Smoluchowski effect is a redistribution of the electron cloud on a metal surface with a strong corrugation.

creates an additional dipole moment that opposes the intrinsic dipole created by the electron density tail and hence lowers the WF. The VL(∞), as an invariant energy level, might therefore seem a better choice for the reference. Unfortunately this level is not directly amenable to experimental determination. All the physical quantities such as the ionization energy (I), electron affinity (A) and work function (Φ) are measured compared to the energy level of an electron at rest in the VL(s). The fluctuations of the VL(s) depending on the crystalline orientation and the difference between the VL(s) and VL(∞) are illustrated in **Fig. 6.1**.

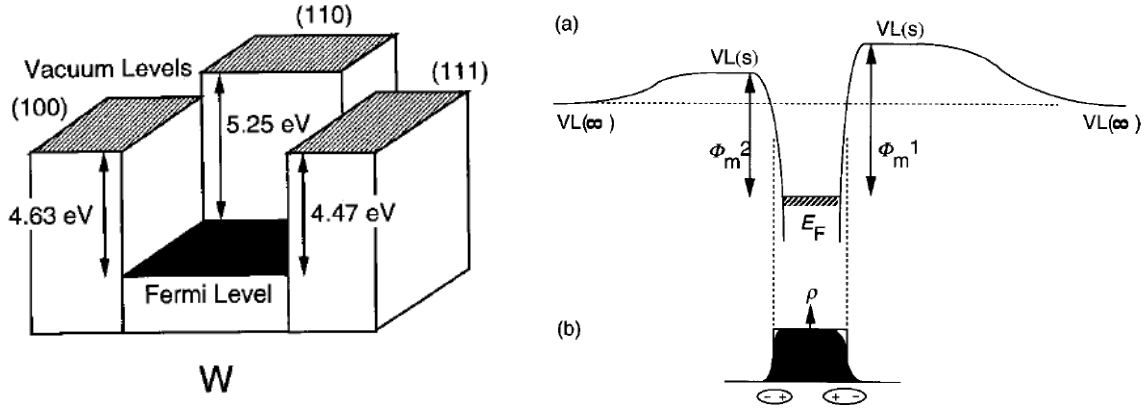

Fig. 6.1: *a) Schematics showing the dependence of the work function on the orientation of the crystallographic plane for a tungsten crystal. The Fermi level is a common energy level inside the bulk. b) Potential energy diagram indicating different vacuum levels outside of a metal and corresponding work functions,* Φ_m^1 *and* Φ_m^2*, to take an electron from the bulk to near-field vacuum levels. Figures are adapted from [160].*

6.2 Single electrode potentials

In this section I will concisely summarize some of Trasatti's work on single electrode potentials. Unless stated otherwise, the information from this chapter is taken from ref. [112,126,153,155,156,154,161,162,163,164]. For more details about the single electrode potentials I therefore refer to those works.

The electrostatic potential drop (EPD) in electrochemistry measures the potential difference between a point in the bulk of the solid and a point in the bulk of the electrolyte solution ($\Delta_S^M\varphi$).

$$\Delta E = \Delta\varphi_S^M = \varphi^M - \varphi^S \tag{6.2}$$

where subscripts M and S stand for the metal and solution phase. The EPD between two dissimilar phases is not directly measurable. What is measured instead is the potential difference between the two terminals of the measuring instrument that is utilized to measure the potential difference between M and S. This situation can be depicted with the following cell:

$$M \mid S \mid M_1 \mid M'$$

where M and M' are the two metal connectors (terminals) of the measuring instrument. The measured potential is

$$\Delta E = \varphi^{M'} - \varphi^M. \tag{6.3}$$

Since the above cell is comprised of three different interfaces the total EPD can be equally written as a sum of three individual EPDs

$$\Delta E = (\varphi^{M'} - \varphi^{M_1}) + (\varphi^{M_1} - \varphi^S) + (\varphi^S - \varphi^M). \tag{6.4}$$

Exploiting the fact that M' and M_1 are in electronic equilibrium and that M and M' have the same chemical potentials (Fermi levels)[21] it can be easily derived that

$$(\varphi^{M'} - \varphi^{M_1}) = \left(\mu_e^M - \mu_e^{M_1}\right)/e. \tag{6.5}$$

This is analogous to the case when n and p semiconductors are brought together. The EPD is observed at the junction of the two semiconductors. Substitution of Eq. (6.5) in Eq. (6.4) yields

$$\Delta E = (\Delta_S^{M_1}\varphi - \mu_e^{M_1}/e) - (\Delta_S^M\varphi - \mu_e^M/e) = E^{M_1} - E^M. \tag{6.6}$$

[21] They are made of the same metal.

where E is the single electrode potential. If one chooses for E^{M} some reference electrode, then E^{M_1} will be given on the scale of that reference. Finding some stable reproducible reaction, against which all other potentials can be measured, circumvents the problem of defining the potential on an absolute scale in many electrochemical experiments. Usually a standard calomel or standard hydrogen electrode (SHE) are used as reference systems. Nevertheless absolute electrode potentials are of great importance when comparing electrochemical and UHV experiments as we shall see later and, in particular, when trying to match semiconductor and solution energy levels in for instance photo-electrochemical devices.

It is obvious from Eq. (6.6) that the measured electrode potential, ΔE, does not coincide with the electric potential drop between M and S ($\Delta_S^M\varphi$). In other words when we are measuring an electrode potential we do not merely measure the relative value of $\Delta_S^M\varphi$ but also the difference in the chemical potentials[22]. On the other hand, since the chemical terms are always constant, the change of the electrode potential equals the change in the $\Delta_S^M\varphi$.

The $e\Delta E$ is experimentally defined in terms of the work to take an electron from the bulk of M to the bulk of M_1. In that respect, the potential of each single electrode can be defined as the work to transfer an electron from the metal bulk to a chosen reference level. As Trasatti clearly pointed out there are three possible paths for the electron to travel from M to M', which are associated with three different reference states for an electron at rest. The latter assertion can be explained with the schematics of the aforementioned cell, vacuum-cleaved in the middle.

In path A, an electron is taken from the Fermi level of the metal M to the VL(∞) and from there to the Fermi level of metal M_1. The other viable route is to transfer an electron internally. There are 2 alternative ways, B and C, to achieve this. Path B implies that an electron travels through the near-vacuum levels of the metal and solution, whereas path C is for an electron that travels through the solution phase between the two metal electrodes.

[22] The only exception to the rules is when M_1 and M are made of same metal so they have the same Fermi levels.

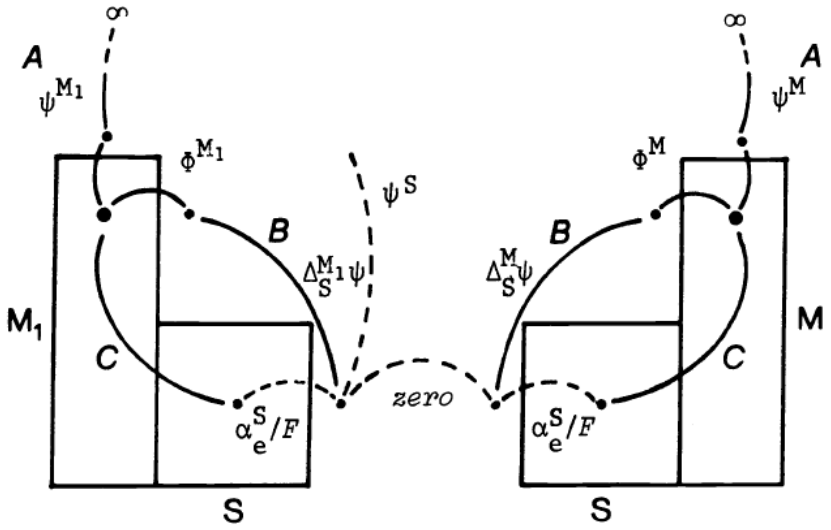

Fig. 6.2: *Schematics of an electrochemical cell with a vacuum layer inserted halfway between the two electrodes. Three viable paths (A, B and C) to transfer an electron from M_1 to M are indicated along with the corresponding potentials. The figure is adapted from ref. [153]*

The reference levels for paths A, B and C are, respectively, VL(∞), VL(s) and an electron at rest in the bulk of the solution. Since there are three possible reference levels, one cannot really talk about absolute potentials but rather single electrode potentials. The three single electrode potentials can be expressed as.

$$E_V^M = \Phi^M / e + \psi^M \tag{6.7}$$

$$E_S^M = \Phi^M / e + \Delta_S^M\Phi / e + \alpha_e^S \tag{6.8}$$

$$E_k^M = \Phi^M / e + \Delta_S^M\Phi / e \tag{6.9}$$

It can be readily shown that the best choice for an absolute potential is E_k^M since both the WF, Φ^M, and the Volta potential difference (change of the WF upon adsorption of water), $\Delta_S^M\Phi$, can be assessed experimentally (*vide supra*)[23]. Moreover, Eq. (6.9) allows for a direct comparison between the WF, which is a physical quantity, and the absolute electrode potential of a given metal (potential of zero charge) in electrochemistry.

[23] Trasatti has shown in his work that there exists a truly absolute potential scale, which is a common denominator to all three single electrode potential scales. He thus named it a reduced potential. This value cannot be measured.

Here, we argued the best reference state of an electron in experiments is the near-field vacuum VL(s). In the continuation we will show how these concepts also apply to the usual DFT setup.

6.3 Single electrode potentials in DFT

A typical electrochemical cell is schematically drawn in **Fig. 6.3**. M_1 and M_2 are the two metal electrodes immersed in the same solution, S. In the figure we have also indicated 4 different WFs representing the work to take an electron from the Fermi level of a metal M_α to a given reference state.

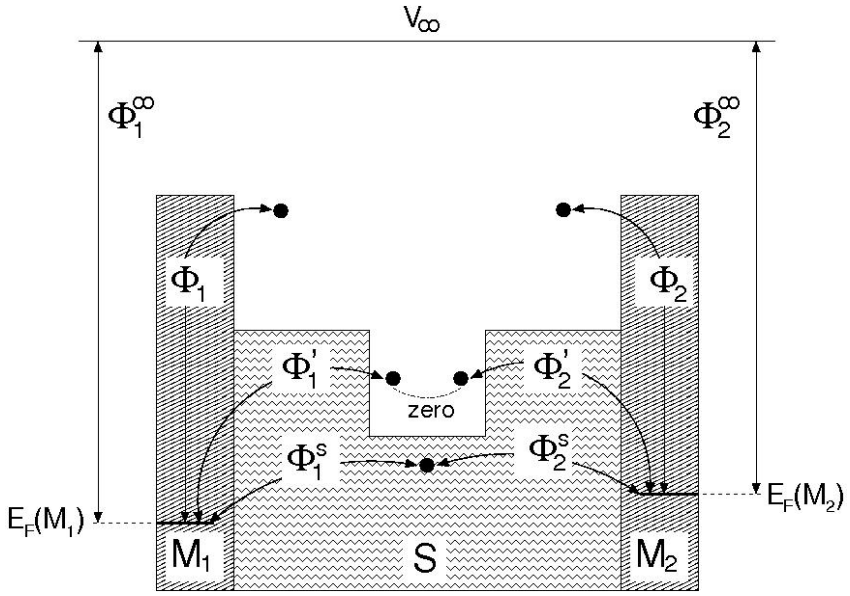

Fig. 6.3: *Schematics of an electrochemical cell showing a set of work functions, Φ_α^k, measuring the work needed to take an electron from the Fermi level of the metal to four different free electron reference states.*

A typical electrochemical cell is illustrated in **Fig. 6.3**. The half-cells are obtained when an electrochemical cell is vacuum cleaved at the point where the solution potential is converged. Four WFs required to bring an electron from the Fermi level of the metal M_α to a chosen reference state are indicated, where labels Φ_α^∞, Φ_α^S, Φ_α, and $\Phi_\alpha^{'}$ stand for far (or infinite) vacuum, bulk solution, near vacuum, and near-solution vacuum WFs.

In conventional periodic DFT calculations Φ_α^∞ is not defined because of infinite surfaces imposed by periodic boundary conditions. This means that even a point at an infinitively large distance in vacuum will still feel the presence of the surface dipoles. We can thus discard Φ_α^∞**.**The second plausible reference is the point in the bulk solution, Φ_α^S. This reference state can be used only if the potential is flat in this region, which is customarily accomplished if there is enough water in the system to effectively screen the surface charge. The downside in theory for this level is that the EP in bulk solution depends on the nature of the solvent. However, this is not a big problem in DFT, since all of the studies so far have been limited to aqueous systems. In fact, as we have previously seen, there are some studies in the literature which relied on this reference state[24] [109,110]. To ensure that the charge is effectively screened in these studies, several water layers needed to be included in the simulated cell. This increased the system size and along with it the computational cost to perform structure minimization. Moreover, a portion of water, where the reference value was taken, had to be fixed because wiggling of the water molecules could otherwise shift the reference point[25]. Taking the VL(s) as a reference is readily accomplished in DFT by measuring the WF and moreover it does not entail any confinements.

So far we have restricted our analysis to single electrode potentials of metal electrodes. These are not of a great importance since they are almost never used as reference electrodes in experiments; using them would thus incapacitate any comparison with experiments. Moreover, having them as a reference in DFT would entail two electrode setup (cf. **Fig. 6.4**). Thus, it is better to have a more universal value that could be used as a reference in half-electrode setups. Here the ASHEP comes in the forefront.

The ASHEP is defined as the potential where the reaction $H^+(S) + e^-(M_1) \leftrightarrow ½\ H_2(g)$ is in equilibrium at standard conditions. These conditions are met in the minimum of the parabolas, since there we used the definition of the SHE to replace the energy of a proton and an electron with the energy of half of a hydrogen molecule. Since the free energies of

[24] For more details look in the method chapter under section “Methods for controlling the surface charge”.
[25] Notice that this is again an artifact of the simulated cell. Macroscopically in a real electrochemical cell this level would be constant.

$H_2(g)$ and $H^+(S)$ are independent of the metal used as an electrode [158], the value of Φ_α' should, in principle, be the same for all metals M_α at the potential of the SHE.

The DFT counterpart to an electrochemical cell is shown in **Fig. 6.4 b**. In DFT simulations of such setups, the Fermi levels will be always aligned irrespective of the potential and the electrode material[26]. Once the Fermi levels of M_1 and M_2 are aligned, Φ_1' and Φ_2' should also become equal, given that the solution phase is thick and polarizable enough to screen the fields from the metals. However, this is usually not the case in DFT calculations due to the limited amount of water that one can afford to include in the simulations. Convergence of the EP profiles for a Pt(111)|water|vacuum|water|Pd(111) cell with the number of water layers is displayed in **Fig. 6.4**. A gradual improvement of the near-solution-surface reference point with increasing thickness of the water is clearly observed. The mid-vacuum EP discontinuity (obtained by electrostatical decoupling of periodically repeated supercells) is fairly large in the cell containing only a single water layer, however, it becomes much smaller after addition of a second and a third water layer.

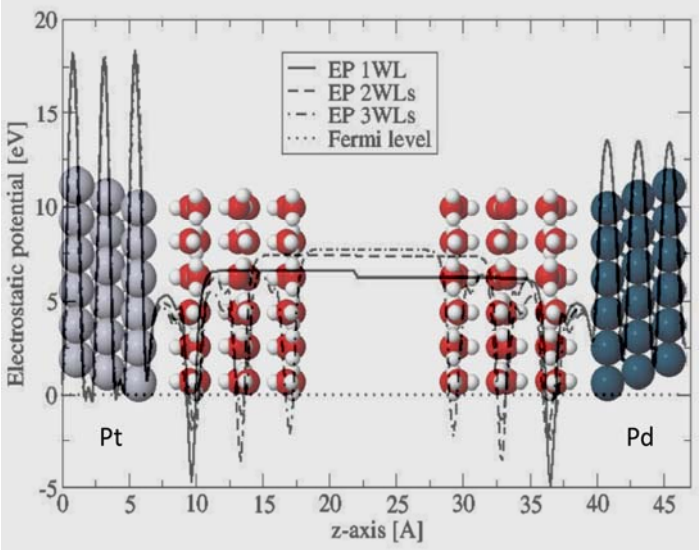

Fig. 6.4: *DFT model of an electrochemical cell made of Pt(111) and Pd(111) electrodes immersed in a common uncharged aqueous solution, vacuum cleaved half-way between the electrodes. The figure illustrates the convergence of the electrostatic potential with the number of water layers.*

[26] In a real electrochemical cell, if the cell is not short circuited this only holds at SHE conditions.

6.4 Experimental estimates of the ASHEP

In experiments the value of the ASHEP is usually deduced from

$$E_{H_2}(\text{abs}) = \Phi^M / e + \Delta\Phi^M / e - E^M_{pzc}(\text{she}) \qquad (6.10)$$

where $\Phi^M + \Delta\Phi^M$ is the potential of zero charge on an absolute potential scale of a given metal electrode M (cf. Eq. 0.9) whereas the $E^M_{pzc}(\text{she})$ is the potential of zero charge on a SHE scale. M here can be, in principle, any metal although mercury is usually used since its WF is very accurately known and $\Delta\Phi^{Hg} / e - E^{Hg}_{pzc}$ can be easily deduced from the Hg | air | H^+ | H_2 Pt cell. The reason for a relatively large scatter in ASHEP reported for this method is presumably surface contamination or/and incipient surface oxidation during measurements. The second approach to deduce the ASHEP is to directly measure the WF of a pristine metal, Φ^M, and the change of the WF upon water adsorption, $\Delta\Phi^M$, in UHV experiments. The method also rests on Eq. (6.9), however, it entails two independent measurements and most likely the state of the surface will not be exactly identical in the two cases. The third possibility is to use a so-called immersed electrodes setup. If the metal electrode is partly immersed in solution, the other, emersed part of the electrode, will drag off a portion of the solution. The WFs in the vacuum outside of the metal surface and outside of the emersed part of the solution can thus be directly measured. At first glimpse this seems to be the best way to measure the ASHEP since two independent measurements are avoided. However, the problem is that the dragged part of the solution does not retain the properties of the bulk solution phase. The bottom line is that there is no perfect method to determine the ASHEP and therefore we have to rely on the best estimates that range from 4.44 to 4.85 V [165,166,167,168,169,170,171,172]. The 0.4 V is a huge difference and hence taking a wrong value can produce substantial errors. If we recall the CV on Pt(111) monocrystal (cf. **Fig. 2.3**), the entire measured potential range is 0.8 V, or twice as much as the possible error introduced by an incorrect value of the ASHEP. The most reliable value recommended by Trasatti and subsequently adopted by IUPAC is 4.44 V [166].

All of these approaches were indirect in the sense that the ASHEP was in all cases deduced from the system WF. A second and more direct approach to measure the ASHEP is through the Born-Haber cycle shown in **Fig. 6.5**.

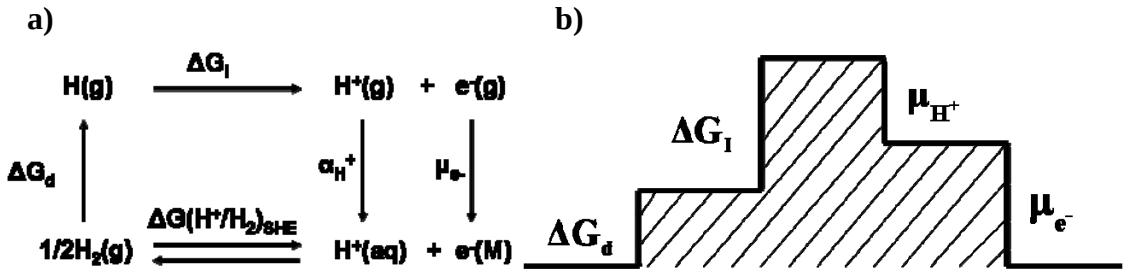

Fig. 6.5: *(a) Born-Haber cycle for the standard hydrogen electrode. (b) Energies in (a) shown schematically on a step diagram. The ASHEP is equal to* μe^-.

Here ΔG_d, ΔG_I, α_{H^+} and μ_e denote dissociation, ionization, real solvation free energy and the chemical potential of electron in its reference state. The ASHEP can be determined from the Born-Haber cycle if the real solvation energy is accurately measured. $\alpha_{aq}(H^+)$ has been recently very precisely estimated from the cluster-pair-based approximation [173] to be 4.42 V [174,175] which is very close to the 4.44 V recommended by Trasatti. It is highly unlikely that this striking agreement between two completely different approaches can be result of a bare coincidence. Hence we take 4.42-4.44 V to be the true value of the ASHEP and a benchmark against which the values determined from DFT calculations will be compared.

6.5 Results and discussion

In the following we will present results for the computational ASHEP on 8 different close-packed transition metal surfaces (Ru, Pd, Pt, Au, Ag, Re, Rh and Ir) obtained with two qualitatively different water models, shown in **Fig. 6.6**.

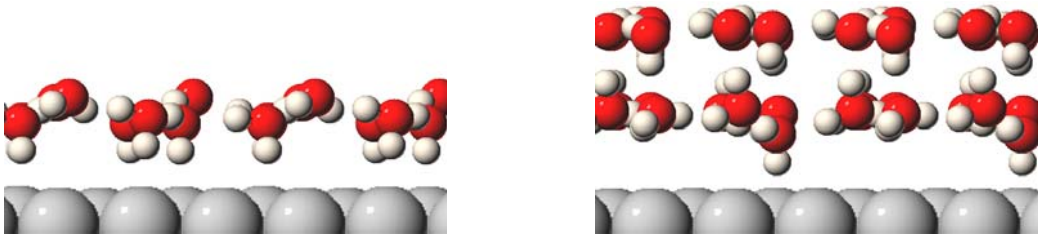

Fig. 6.6: *Structure of two different water models with a single hydrogen atom added to charge the interface. a) Model 1: water bilayer with dipoles pointing to the surface b) Model 2: two adhering water bilayers with no net dipole except for the added H atom.*

Since system size in DFT is dictated by the computational power, our study was limited to having just a few water layers [176]. Nevertheless, the ultimate goal would certainly be to include enough water to emulate water in the bulk. Model 1 (**Fig. 6.6a**) is a single water bilayer where every second water molecule points towards the surface. This structure was found to be the dominant one under UHV studies on many single metal facets, among others Pt(111) [177], Ru(001) [178], Pd(111) [179], Rh(111) [180] used in this study. In chapter 4 we have used it to model the HER/HOR. Model 2 (**Fig. 6.6b**) consists of two adhering water bilayers where dipoles in the first bilayer point towards planar water molecules in the second bilayer and vice versa. As a result of this particular spatial arrangement, the resulting dipole comes only from the hydrogen atom added to charge the interface. We should bear in mind that this model is highly unrealistic and whenever a positive ion is solvated near the surface, water dipoles will reorient towards the surface to screen the negative charge[27]. In model 2 we have included the second bilayer merely to prevent water reorientation during relaxation. Model 1 will clearly illustrate the errors introduced when using a water structure containing a net dipole and model 2 will show the errors caused by insufficient charge screening. We should keep in mind that both models are unrealistic. At standard conditions water dipoles at the interface will be randomly oriented up and down [95]. Herein, we will use the models merely to emphasize the implication of structural differences on values of the computed ASHEP.

In **Fig. 6.7** the integral free energy G_{int} obtained with models 1 and 2, respectively has been plotted versus the WF calculated for the metal in the metal/water/vacuum setup

[27] Looking at the parabolas in this chapter or in chapters 3 & 4, it is clearly visible that all the points are always at the positive potential compared to the U_{pzc}.

(Φ'). The points G_{int}=0 to the far right in the graphs are obtained for uncharged systems, without any additional hydrogen in the water, and thus correspond to the U_{pzc} of the different metals. On the other hand, as we have seen, the minima of the parabolas correspond to the U_{she}.

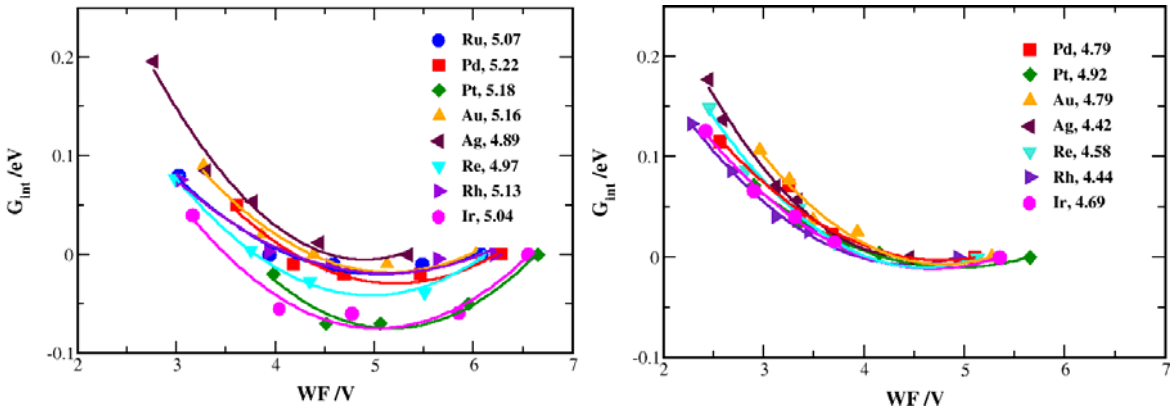

Fig. 6.7: *Dependence of the integral free energy, G_{int}, on the work function of the metal in contact with water for the 8 investigated transition metals shown for a) water model 1 and b) water model 2. The mean average values and standard deviations of the ASHEP for model 1 and 2 are (5.08/0.11) and (4.66/0.19) V respectively.*

Additionally, in **Fig. 6.8**, the U_{PZC} and U_{SHE} of the different metal electrodes have been plotted against the work function of the corresponding pristine metal surface, Φ.

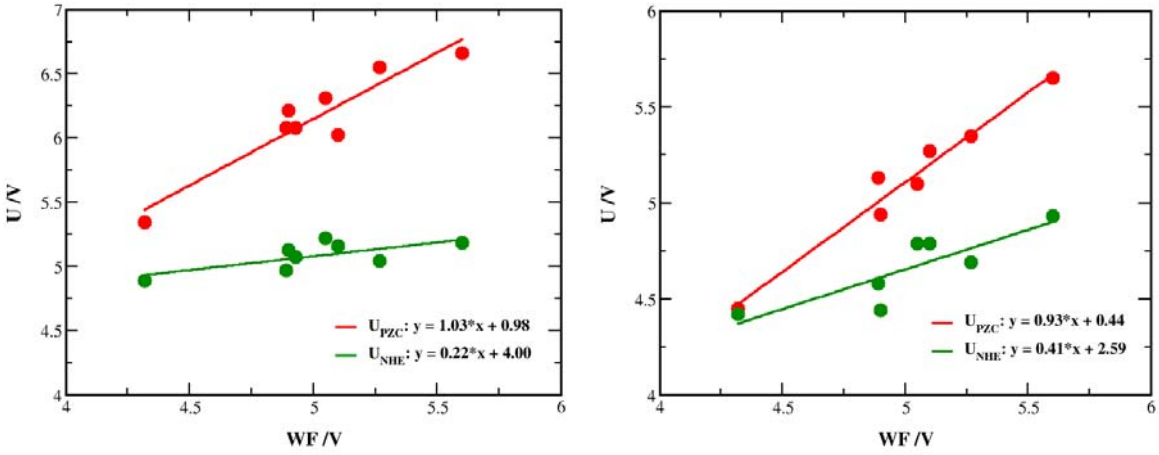

Fig. 6.8: *Dependence of the absolute potential of zero charge (red) and the potential of the standard hydrogen electrode (green) as a function of the pristine metal work function for a) model 1 and b) model 2.*

As observed, the U_{PZC} varies linearly with the WF with a slope close to 1. In both models, the capacitances (curvatures of the parabolas) across different metals are alike, implying that the chemical potentials (derivative of the parabolas) will be the same in all cases. The shift in G_{int} for different metals observed in **Fig. 6.7a** is thus just an artifact of having U_{PZC} as a reference. Moreover, it is clear that the value of the U_{PZC} is dictated by the simulated water structure, incapacitating thus any direct comparison between experiments and theory. The same one to one correspondence between WF and U_{PZC} has been theoretically argued by Bockris [157] and seen in measurements for different facets of Au and Ag [161]. In general this is only valid as long as the water structure of the interface is fairly constant, which is the case for our artificially constructed water films. In order to get the correct U_{PZC} it is necessary to perform *e.g.* molecular dynamics simulation at room temperature starting from a random water structure.

All the differences pertaining to U_{PZC} should, in principle, be eliminated at SHE conditions (minima in G_{int}), and therefore ideally the slope of the $U_{SHE}(\Phi)$ should be zero. The $U_{SHE}(\Phi)$ slope other than zero, thus reflects the imperfect screening of the water used in the simulation. As can be seen, model 1, with only one but a rather flexible water bilayer that can easily adjust to the electrostatic field, does a much better job at screening than model 2, in which the two bilayers of opposite polarity form a rather rigid water structure. The variations of the ASHEP compared to the experimental reference (4.42-4.44 V) largely stems from lack of cancellation between the dipoles of the individual bilayers. The mean average values for the ASHEP in model 1 and 2 are 5.08 & 4.66 V, respectively. Obviously the latter one falls much closer to the experimental value. This can be appreciated by the fact that model 2 features no net dipole and hence it resembles more the experimental situation where the ASHEP is measured in bulk solution. Naturally, the best option would be to find a water structure that meets both of criteria, that is, perfect charge screening and no net dipole. However, since the internal reference is used the errors made by model 1 and model 2 cancel when two different potentials are compared. Hence for studying charge transfer reaction we do not expect that the exact water model, capable of screening and solvating the proton, will make any significant difference to the results. We have previously ascertained this point by showing that the

energetics of the HER/HOR are conserved regardless of the interfacial water structure (cf. **Fig. 4.15**).

6.6 Summary

An absolute potential scale, in density functional theory (DFT) based electrochemistry calculations, is a challenge for two reasons. Firstly, the potential scale is typically estimated by subtracting the experimental value of the ASHEP from the WF of the electrode placed in an electrode/water/vacuum environment. Commonly, experimental values reported in the literature are not well defined (reported values range from 4.42 to 4.85 V). Secondly, the absolute reference level for the electrons in the calculations is directly dependent on the structure of the water included in the simulations. These problems obvious call for an internal reference for the ASHEP.

In this paper we have been discussed how these discouraging issues can be addressed. First, by reviewing the literature, we identified the most reliable experimental value for the ASHEP. Due to present limitations in computer power it is not practically feasible to emulate bulk water in a large-scale electrochemistry study. Instead, one is usually limited to much less sophisticated water models. Here, two simple, but different, water models have been analyzed in detail and variations caused by insufficient screening and net dipoles have been quantified. Finally, it has been shown how an internal (system dependent) theoretical ASHEP can be deduced for a metal/electrolyte system. By applying such an internal reference, when comparing different electrode materials and potentials, one can avoid most of the errors caused by insufficient charge screening and net dipoles and thus obtain more trustworthy results, despite using a fairly simple description of the water.

7 Oxygen reduction reaction

In this chapter I will model the ORR, the reaction taking place at the cathode of the PEMFC device. Huge activation losses (0.4 V) and necessity of using Pt are the largest hurdles that prevent putting the PEMFC technology on the road. The problem here is 8 times more sever that in the case of the anode because this is exactly how much more Pt is needed per cm^2. The goal of the current research is to significantly reduce the amount of platinum at the cathode or even completely eliminate it [17, 18]. As we have seen in the introduction chapter, a good catalyst should meet three main criteria: activity, stability and price. Recent research efforts have illuminated new promising candidate satisfying some of these criteria [53,54,55,56,181], but finding a catalyst that fulfills all the three simultaneously, proves to be a daunting task. Especially stability enters as a key parameter because it constrains search to a very few metals and alloys that are stable against dissolution at high operating voltages and harsh working environment at the cathode.

The aim of the work presented in this chapter is to elucidate the reaction mechanism of the ORR on the most studied catalyst facet, that is Pt(111). Understanding of the reaction mechanism is a prerequisite to a successful catalyst design.

This chapter is organized in a following way: first I will justify the choice of the water structure that was used to model the surface environment. Subsequently, the reaction mechanism through which we believe the ORR is taking place will be presented and deconvoluted in three consecutive reaction steps. These steps will be then addressed separately and finally we will show that there are very small activation barriers pertaining to each step.

7.1 Water structure

In order to faithfully emulate the electrochemical reactions at surfaces one has to explicitly take into account the surface environment, i.e. specifically adsorbed ions, electric potential, electric field and the water molecules. We have seen how these have been incorporated into the interface model presented in chapter 3. Here we mimicked the interfacial water on Pt(111) by the water bilayer since it has been found experimentally and theoretically to be the prevalent water structure from 0 K up to room temperature [87,91,92,95].

Feibelman ascertained that the water bilayer is not a common water adlayer on all close-packed transition metal surfaces. Instead he proposed, studying Ru(0001), a more stable water film where every second water molecule in the water bilayer dissociates to OH [88]. Subsequently the new structure was termed the half dissociated water layer (HDWL) since it consisted of alternating OH and H_2O moieties. The same hexagonal pattern it shares with the bilayer structure is the main reason it remained elusive for so long time to surface scientists. The LEED spectroscopy, that was readily employed to elucidate the position of the O atoms on metal substrates, could not image the position of the H atoms and hence could not reveal the HDWL phase. Current view is that the HDWL structure usually dominates on metals that bind strong enough[28] to enable water dissociation [97]. In addition Groβ and Schnur have demonstrated that this phase will also be stable on Ru(0001) under ambient conditions [95]. Clay et al. have shown, using different spectroscopic techniques, that this particular water structure forms even on Pt(111) when the platinum surface is pre-covered with oxygen. By studying water uptake on a pre-covered O surface as a function of the O coverage and water dosage, they concluded that the hexagonal backbone will survive over a range (~2-4) of H_2O/O ratios. The high stability of the HDWL on Pt(111) is attributed to a very strong OH-H_2O bond strength [92,182]. The strength of the interaction was found to be ~0.45 eV, which is much higher than the interaction energy between the OH-OH and H_2O-H_2O. The most stable structure was the one where the ratio of H_2O/OH was 3:1, since here the number of the OH-H_2O pairs is maximized. The mean interaction energy for the H_2O/OH overlayers

[28] Mostly transition metals to the left in the periodic table.

on Pt(111) is presented in **Fig. 7.1**. It comes in the forefront that the highest interaction energy is obtained when c(OH) and c(H_2O) are 1/3 ML.

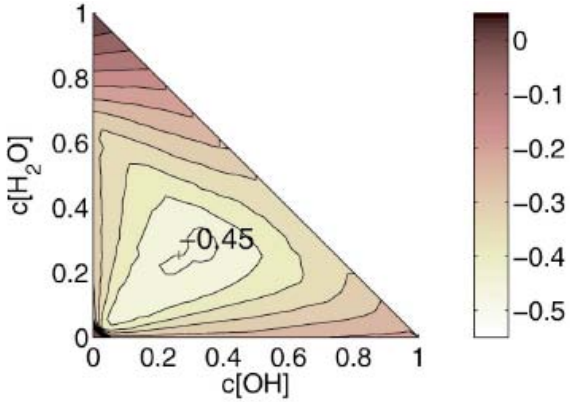

Fig. 7.1: *Mean interaction energy for all molecules in the hexagonal overlayer as a function of the OH and H_2O coverage at T=150 K. The distance between the contour lines are 0.05 eV. Adapted from ref. [182].*

Michaelides et al. have shown that the strongest contribution to the HDWL binding energy comes from the adsorbate-adsorbate interactions and to a much less extent from the hydrogen H-bonding within the overlayer; exactly opposite to what they found for the water bilayer [97]. Moreover the hydrogen bond strength was insensitive to the lattice constant of the metal substrate. The variation of the adsorption energy of the HDWL on several close-packed transition metal surfaces is shown in **Fig. 7.2**.

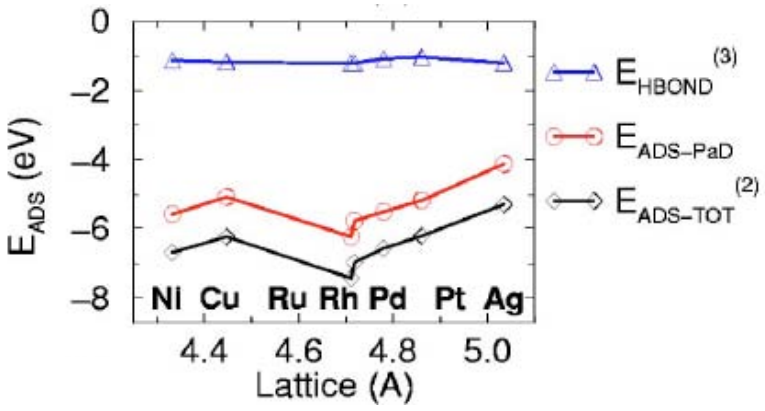

Fig. 7.2: *Variation of the total adsorption energy of the half-dissociated water layer and two of its components, substrate-adsorbate ($E_{ADS\text{-}PaD}$) and adsorbate-adsorbate interactions (E_{HBOND}), on several close-packed transition metals surfaces. Adapted from ref. [97]*

The previous analyses were confined to zero bias, whereas here we are more interested in water structure at potentials of interest for the ORR (0.8-0.9 V). Unfortunately it is not so easy to obtain the exact surface structure via *in situ* experiments at standard conditions and finite bias. An oxidation peak around 0.8 V vs. Reversible Hydrogen Electrode (RHE) that is readily observed in CV measurements on Pt(111) is believed to correspond to the water oxidation (dissociation) [183,184,185]. Nørskov et al. have shown, employing DFT calculations, that this peak is indeed related to splitting of water into adsorbed OH^* and $H^+ + e^-$ [43]. Moreover this molecular level insight has been used to construct an activity volcano where one of the two potential limiting steps was the formation of the HDWL. Further evidence corroborating existence of the HDWL is that the charge in the oxidation peak in CV experiments on Pt(111) seems to be well reproduced assuming an isotherm with the HDWL structure(s) [186]. Herein, I will show that this is definitely the most stable structure by calculating the differential adsorption energy of hydroxyl species as a function of the OH coverage in the water overlayers.

The average free energy of OH is defined as the average adsorption energy per number of OH groups, n, in the simulated cell. This energy shows the interaction strength among the adsorbed OH species.

The integral free energy scheme was thoroughly addressed in chapter 4 of the thesis. To summarize briefly, the integral free energy is the energy stored in the EDL, normalized with respect to the size of the simulated cell or equivalently the number of the surface atoms, N. Here it is obtained by multiplying the average free energy with the OH coverage, whereas in chapter 4 it has been calculated directly through Eq. (4.5). There is no difference between the two approaches, apart from that the one used here is a “pure differential”, whereas the one used in chapter 4 was “finite differential” since there we took the finite differences between consecutive discrete points.

The differential free adsorption energy is obtained by differentiating the free integral energy with respect to the OH coverage[29]. By applying the definition of the SHE, the differential adsorption free energy can be converted into the potential scale in the same way as it was previously done in the case of H (cf. **Fig. 5.3**).

[29] In the HER/HOR chapter we used a finite difference approach to determine the ΔG_{H^*}

The relationship between the three different energy schemes can be written as

$$\frac{dG}{Nd\theta} = \frac{d\left(G_{avg}\theta\right)}{d\theta} = \frac{d\left(G_{int}\right)}{d\theta}, \quad \theta = \frac{n}{N} \tag{7.1}$$

The average free energy of the water overlayers as a function of the OH coverage is presented in **Fig. 7.3** (black squares).

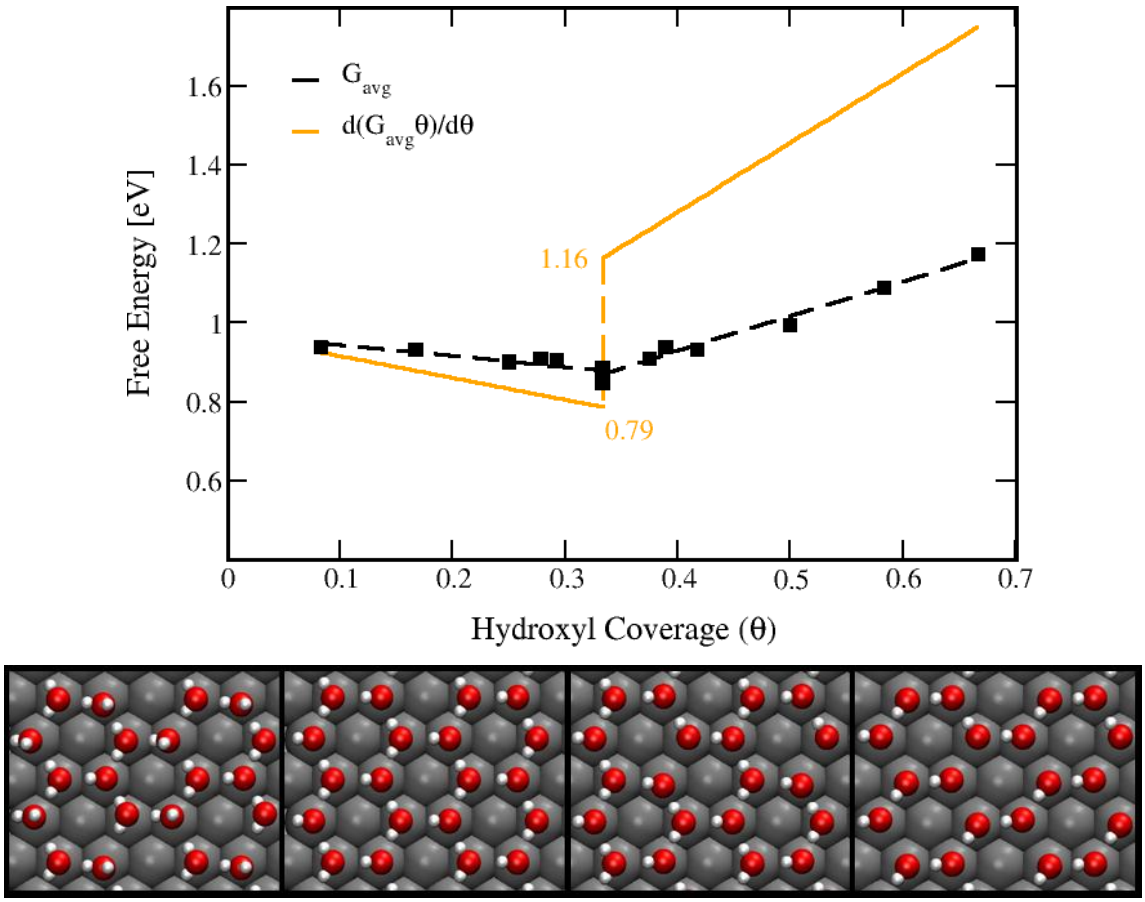

Fig. 7.3: *(a) Average free adsorption energy of hydroxyl species on Pt(111). Discrete values (black squares) are linearly fitted (black dashed line) from low and high coverage end to 1/3 of hydroxyl coverage. Fits are used to get the differential adsorption energy of OH on the surface (yellow line). Dashed yellow line represents the discontinuity in the differential free energy at 1/3 ML hydroxyl coverage. Differential free energies of hydroxyl at different ends of discontinuity, 0.79 and 1.16 eV are also indicated.*
(b) Top view of four representative water overlayer structures, at very low hydroxyl coverage (0.08 ML), at different ends of discontinuity (0.33 and 0.42 ML) and at very high hydroxyl coverage (0.66 ML), in the order from left to right respectively.

The points were calculated, in the direction from left to right, by removing stepwise H atoms from the water bilayer. When 1/3 ML is reached, further H_2O oxidation can only happen through abstraction of one of the hydrogen atoms from the water molecules parallel to the surface, *i.e.* removing one of the hydrogen bonds. The 2/3 ML is reached when one hydrogen atom has been removed from all the water molecules. We note here that this high OH coverage is unrealistic under electrochemical conditions because at such high potentials oxide layer will instead build up on the surface [73,187]. The free average energy adsorption profile (dashed black line) is obtained by linearly fitting discrete points from both, the low and high coverage end to the coverage of 1/3 ML. As seen from **Fig. 1**, the OH-OH interaction energy features a cusp in the middle. The cusp shows that the interactions are attractive below 1/3 ML and repulsive above 1/3 ML.

There are two ways in which the adsorption energy of OH can be calculated depending on the chosen reference state. We will illustrate this by looking at the integral energy. The first way is to compare the adsorption energies of OH on the surface to the liquid water and hydrogen molecules in the gas phase. In this case water in the bilayer is used as a reference for water molecules in the overlayer.

$$E_{OH}^{int} = E(\theta OH+(\frac{2}{3}-\theta)H_2O)-E_{slab}-\frac{2}{3}E(H_2O)+\frac{1}{2}\theta E(H_2)- (\frac{2}{3}-\theta)(E(H_2O^*)-E_{slab}-E(H_2O)) \quad (7.2)$$

where $E(H_2O^*)$ is the average adsorption energy of a single water molecule in the water bilayer[30]. Another more direct way of calculating the adsorption energy is through

$$E_{OH}^{int} = E(\theta OH+(\frac{2}{3}-\theta)H_2O)-E_{slab}+\frac{1}{2}\theta E(H_2)-\frac{2}{3}E(H_2O^*) \quad (7.3)$$

[30] Note that Eqs. (7.2) and (7.3) are written in terms of the coverage and it is thus irrespective of the unit cell size.

This corresponds to using water in the bilayer as a reference for OH instead of the liquid water and H_2 in the gas phase. If the water in the bilayer was in equilibrium with liquid water, Eqs. (7.2) and (7.3) would yield the same result. The challenge is that in the standard GGA simulations the stability of water in the bilayer is underestimated mainly due to lack of van der Waals forces[31]. The water is thus destabilized and consequently the potential for water oxidation will be underestimated as well. The inclusion of the van der Waals interactions stabilizes each water molecule with ~0.15 eV compared to the standard RPBE-GGA calculations. This brings the oxidation potential calculated with Eq. (7.3) closer to the one obtained with Eq.(7.2). In following we will use the first of the two methods to calculate adsorption energies. In order to obtain the free adsorption energy at 300 K the energies are corrected for zero point energy and entropy contributions.

The DFE (yellow line) is obtained by differentiating the integral free energy with respect to the OH coverage. In this way, the cusp in the average free energy becomes a discontinuity (yellow dashed line) in the DFE scheme. We find that the DFEs of OH at different ends of the discontinuity at 1/3 ML are 0.79 and 1.16 eV, respectively. The difference (0.37 eV) between the two corresponds to the amount needed to remove one $H^+ + e^-$ from the HD water, that is, one hydrogen bond. The value is in agreement with the similar values reported in previous DFT studies on the HDWL [182, 186]. Next, we apply the computational standard hydrogen electrode [43] to convert the DFE scale into an electric potential scale [114]. Upon conversion, **Fig. 7.3** can be as well interpreted as the potential needed to oxidize the OH-H_2O structure at a given OH coverage. At 1/3 ML coverage this value is 0.79 V[32] and it agrees nicely with 0.78 V reported elsewhere [43]. The values at both ends of the discontinuity in **Fig. 7.3** will be later used to fix the free energy levels between different electrochemical steps in the free energy diagrams (FED) in **Fig. 7.9** and **Fig. 7.10**.

Since we have established the relevant surface structure at potentials of interest, we will model all ORR intermediates embodied in the HDWL hydrogen bonded network.

[31] This is primarily because of the underestimation of the hydrogen bond energy.
[32] In other words H_2O and OH are in equilibrium

7.2 Reaction mechanism

Even tough it looks rather simple, the ORR is in principle a very complicated multi-electron reaction that involves a number of elementary steps and reaction intermediates. The complex network of the possible reactions can be best summarized with a scheme proposed by Wroblowa [188].

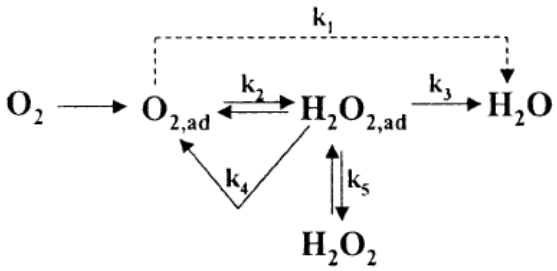

Fig. 7.4: *The oxygen reduction reaction mechanism*

where k_i are the rate constants of different reactions. Current view is that the ORR can take place through two different mechanisms, a so-called direct reduction without peroxide as an intermediate or through series pathway where peroxide is one of the intermediates. In the latter case, the reaction can proceed either trough peroxide desorption ($2e^-$ reduction) or through complete oxygen reduction to water ($4e^-$ reduction). It is still unclear which of the three mechanisms dominates but what has been ascertained is that the rate limiting step is always the O-O bond breaking [189,190]. The activation barriers inferred from the rate measurements fall in the range from 0.26 to 0.6 eV. Some of them have been obtained at U=0.8 V [13,191], while the others have been reported at equilibrium potential U=1.23 V [192].

The barriers for the O_2 splitting in O_2, OOH and HOOH intermediates on Pt(111) have been calculated by Mavrikakis et al. in the absence of water and an applied bias [193]. The first charge transfer reaction of the ORR has also been modeled previously by Janik and co-workers in a water environment at a constant bias [194]. In this study the authors found very minute barrier for O_2 dissociation. The reaction was modeled having water on the surface, however, at the potentials of interest (~0.8 V) the surface will start to oxidize. The OH coverage will be substantial (1/3 ML) which could have a large effect on the reaction energetics [73].

In our study we will assume that the reaction mechanism unfolds in three consecutive steps: 1) a proton is transferred to OH somewhere on the surface where it picks up an electron; 2) the proton then diffuses to the vicinity of the adsorbed oxygen molecule where 3) it reduces oxygen to other intermediate species in the ORR path. This process is repeated four times after which the oxygen reduces to two water molecules. A schematic illustration of the proposed reaction mechanism is shown in **Fig. 7.5**. We note here that the surface diffusion could be avoided, if a proton transfers directly to the adsorbed oxygen. This path would only reduce the barrier relative to what has been found in this paper. Since the barrier, as we shall see later, is already small enough, this will not upset conclusions of our study.

In the ensuing discussion we will give a quantitative assessment of the activation barriers in all three reaction steps and in to which degree they are influenced by the potential.

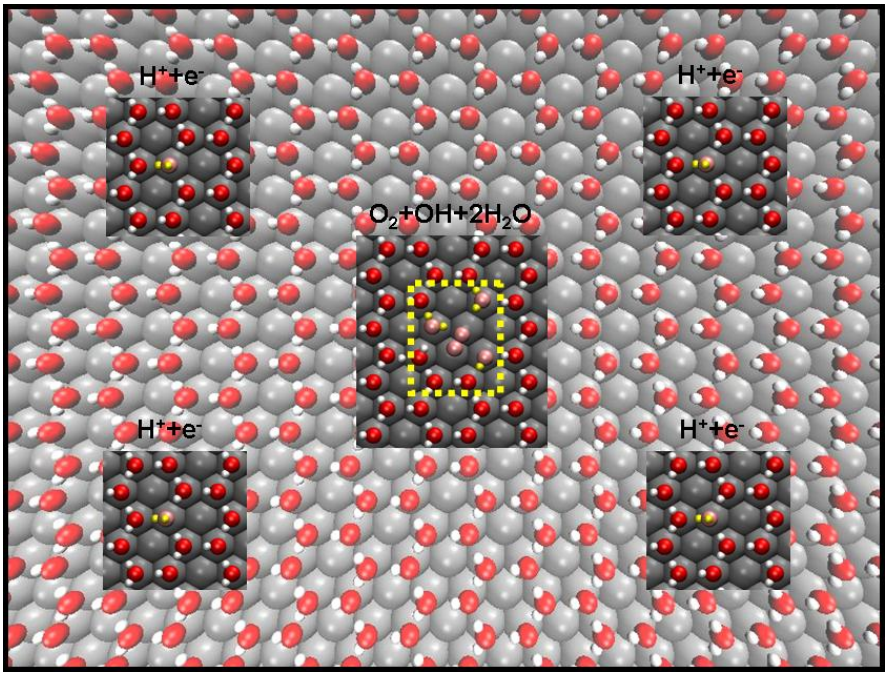

Fig. 7.5: *Schematic illustration of the proposed reaction mechanism. At 0.8-0.9 V, the Pt(111) surface is covered with the half dissociated water layer (transparent background). Four hydrogen atoms (discharge protons) are indicated in the left and right panels. They can easily diffuse to the reaction center (middle panel) and reduce the ORR intermediates. The dashed yellow box represents the simulated unitcell.*

7.3 Charge transfer

The HDWL on the surface can be also viewed as the inner Helmholtz plane in the classical description of the EDL. The outer Helmholtz plane of the EDL is set up between a charged water layer and the HDWL on the surface. Most of the potential drop will happen in the inner Helmholtz plane. This assertion can be appreciated by the fact that the experimental isotherm obtained from integrated CV measurements on Pt(111) agrees well with the simple binding model of OH on the surface [186]. Hence, the surface charge will not be significantly affected by the proton concentration in the charged second water layer. All the hurdles encountered when the charge was allowed to react in the HER/HOR can thus be avoided [195].

We simulate the reduction of the HDWL (charge transfer) in a following approximate way: we transfer a proton from the second water layer to the OH in the HDWL on the surface. For the largest simulated cell we observed no change in the reaction free energy for the charge transfer[33]. This means that the potential of this point corresponds to 0.79 V, or the lower value in the discontinuity in **Fig. 7.3.** Since 0.79 V corresponds to equilibrium, the potential of all other points can be easily deduced from the free reaction energy. In this way we established a simple potential scale for the OH reduction. In **Fig. 7.6 a** we present results at three different potentials. For the most relevant point (green line) we find a 0.26 eV barrier for the proton transfer. We note that a low additional barrier for proton transfer to adsorbed oxygen molecule was also found in the previous DFT study on Pt(111) [194]. In addition in **Fig. 7.6 b** the reaction barriers have been plotted against the change in reaction energy. The straight line that emerges is another manifestation of the BEP "law". Since ΔE equals ΔU (*vide infra*), the slope of the plot represents the transfer coefficient for the ORR. We find this value to be in perfect agreement with the one reported in the experiments [13]. Although the striking coincidence between the two values might be somewhat fortuitous, since the HDWL structure will not exist at the potentials below 0.79 V where the two data points have been calculated.

[33] The entropy and ZPE are the same in the IS and FS hence the energy scale equals free energy scale.

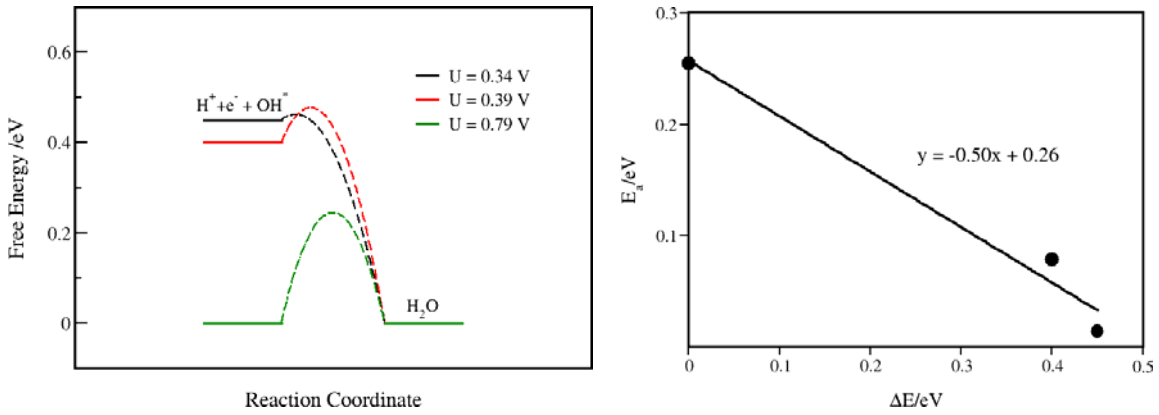

Fig. 7.6: *a) Potential energy profiles for reducing one OH in the half dissociated water network by a proton residing in the second water layer at three different potentials. b) The BEP relationship for the charge transfer to the surface OH. The transfer coefficient (BEP slope) and reaction barrier at equilibrium are 0.5 and 0.26 eV, respectively.*

7.4 Surface diffusion

Proton diffusion parallel to the surface occurs readily through interchange of hydrogen bonds within the water network. The barrier estimated in our work is 0.09 eV close to what was previously found [196].

The effect of an electric field on the transition state energy for the proton diffusion is shown in **Fig. 7.7**. As observed, the electric field has a negligible influence on the activation energy for the proton diffusion in the large electric field window from -0.4 to +0.4 V $Å^{-1}$. Hence, the proton diffusion can be regarded as a field and potential independent step.

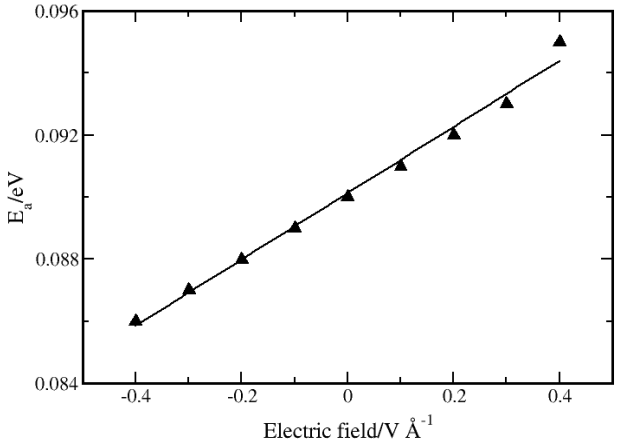

Fig. 7.7: *The transition state energy for proton diffusion within the HDWL as a function of an applied field. The dipole moment perpendicular to the surface for the TS is very small, 0.011 eÅ, indicating that the proton diffusion is a potential independent step.*

Michaelides et al. [197] have recently performed an *ab initio* path integral molecular dynamics (AIPIMD) investigation in order to study hydrogen dynamics in the HDWL. The difference between the AIPIMD and AIMD we encountered earlier is that in the former one both the electrons and nuclei are treated quantum mechanically. The authors concluded that there will be, in general, no barrier for proton hopping between the water and OH on in the HDWL structure.

Either way being 0.09 eV or less, the barrier can be neglected compared to 0.26 eV found for the charge transfer.

7.5 Free energy diagram

The free energy diagram (FED) for the ORR reduction is presented in **Fig. 7.8** with the corresponding structures shown in **Fig. 7.9**. The FED is constructed from the adsorption energies of different ORR species and the differential free energy of OH. Since the ORR is taking place just on specific sites on the surface, we assume that the global OH coverage remains constant. Therefore by locally changing OH coverage as a consequence of the ORR, we can just infinitesimally move away from the global surface coverage of 1/3 ML.

We analyze the free energy diagram at U=0 V backwards, starting from the last electrochemical step. The difference between the two states in the last electrochemical step is set to 0.79 eV, or the lower value in the discontinuity in **Fig. 7.3**. This value corresponds to the energy needed to subtract one H^+ and e^- from H_2O at local OH coverage below 1/3 ML. The removal of one H bond yields the HDWL structure and increases the global OH coverage infinitesimally from the left to 1/3 ML. In other words, the water dissociation will become feasible at potentials greater than 0.79 V (*vide infra*). The second and the third electrochemical steps are in the same way fixed to 1.16 eV; the value at the other end of discontinuity. This is because we are now removing one $H^+ + e^-$ from the HDWL and hence increasing the OH coverage infinitesimally above 1/3 ML. The fourth electrochemical step is set to 0.79 eV between the two states with the adsorbed oxygen on the surface under different local OH coverage. Again this is because we remove one $H^+ + e^-$ near the adsorbed oxygen molecule where both states are below

1/3 ML coverage. The states that we get in the reaction path can have different orientation of adsorbed species than the most stable structures with the same species. Therefore one also needs to correct for the difference between the most stable structure with certain OH coverage (ones in **Fig. 7.3**) and the ones obtained as a product of the reaction mechanism in the FED. These corrections are indicated by d_1 and d_2 in **Fig. 7.8**.

First, we construct the FED at 0 V. We can obtain the FED at any desired potential by shifting the relative positions of all the states at U=0 V by chemical potential of the electrons. We shift the states to 0.9 V potential since this is a potential relevant for the ORR and within a potential window where the half dissociated water layer is stable.

The O_2 adsorption is the first step in the FED. The O_2 level in the gas phase is fixed to a value of 4.92 eV compared to the liquid water and hydrogen in the gas phase. This value corresponds to the maximum work that can be extracted from the system. There are two viable routes after the initial O_2 adsorption. The O_2 can either react with one proton and electron from the surrounding water molecules to form OOH, or dissociate. The relative stability of the O_2 and OOH depends on the local OH coverage. After a proton transfer to the OH in the vicinity of O_2, dissociation becomes more facile. This is related to water at the surface being a stronger proton donor than OH [182]. The dissociation barriers and bond lengths depending on the number of hydrogen bonds coordinated to the most stable oxygen species are tabulated in **Table 1**. For the O-O bond scission in the most stable intermediate in each electrochemical step, we get the lowest barrier to be 0.37 eV which is considerably less than 0.73 eV we calculated on pristine Pt(111) surface. If we include the electric field correction at 0.9 V for transition state of the O_2 dissociation from ref. [74], the barrier shifts upwards by additional 0.06 eV.

The OOH can further react with nearby water molecules to form HOOH. This reaction step is energetically unfavorable which is in agreement with rotating ring disc experiments [13]. The hydrogen peroxide energy level in aqueous solution [198] is also indicated for comparison with the green dashed line in the second and the third panel in **Fig. 7.8**. Difference between the two peroxide This analysis confirms our previous established thermodynamically picture that OOH is the most stable reaction intermediate after first reduction step. levels in aqueous solution is 0.79 eV due to the way the FED was constructed.

Table 1 *Dissociation barriers and bond lengths for the most stable oxygen species on the bare Pt(111) slab coordinated to different number of water molecules. The bond length for O_2 in vacuum from RPBE-DFT calculation is also included for comparison.*

	E^{diss}/eV	Bond length/nm
O_2 (g)		0.124
O_2 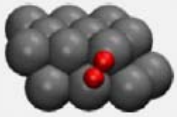	0.73	0.135
$O_2 + H_2O$ 	0.67	0.140
$O_2 + 2H_2O$ 	0.48	0.142
$OOH^a + 2H_2O$ 	0.37	0.144

As a product of the O-O bond scission we can either get O or 2OH since the nearest water molecules can donate a hydrogen atom to oxygen to form 2OH. We find very similar reaction energies and activation barriers for the two reactions. The following three consecutive electrochemical steps are simple proton transfer steps. In the final structure there is one more water molecule due to an extra hydrogen atom sitting on-top of one OH in the HDWL. This additional water molecule can be readily replaced by O_2 [199] and thus completing the catalytic cycle.

The barrier for breaking the O–O bond is potential independent, which means it will not show up when comparing activities at different potentials. This is also the reason why the analysis based on the binding energies of the intermediates gives qualitatively correct polarizations curves [186]. However, the barrier might change if the catalyst is changed,

this could have an affect on the previously established volcano plots. We speculate that less reactive catalysts might be predicted too active compared to Pt without explicitly including the kinetics.

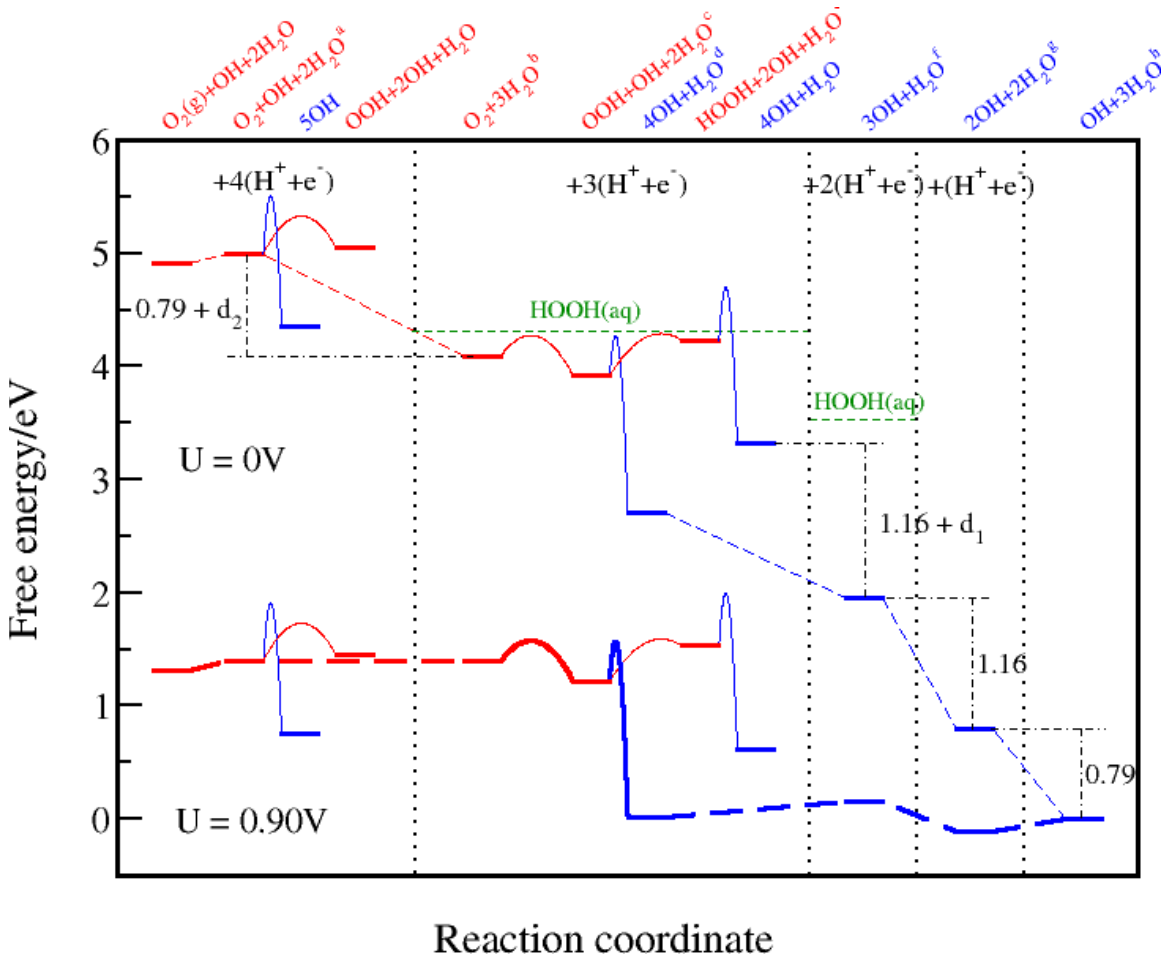

Fig. 7.8: *Free energy diagram for the O_2 reduction at two different potentials, 0 (upper) and 0.9V (lower) respectively. The red color indicates the associated species and barriers between them. The blue color indicates dissociated species and barriers for dissociation. The local structures are indicated above the figure panel following the same color code as the species they designate. Labels a-h correspond to the structures shown in Fig. 7.9. Only the species in the reactive center are displayed. The thin solid and dashed lines represent the chemical and electrochemical reaction steps. At 0 V, peroxide levels in aqueous solution after first and second proton transfer are also indicated (green dashed line). Different electrochemical steps are fixed to 0.79 & 1.16 values in Fig. 7.3 (cf. text). The d_1 (0.21 eV) and d_2 (0.12 eV) stand for the energy difference between a structure in the reaction path and the most stable corresponding structure in Fig. 7.3. The minimum energy path at 0.9 V is highlighted.*

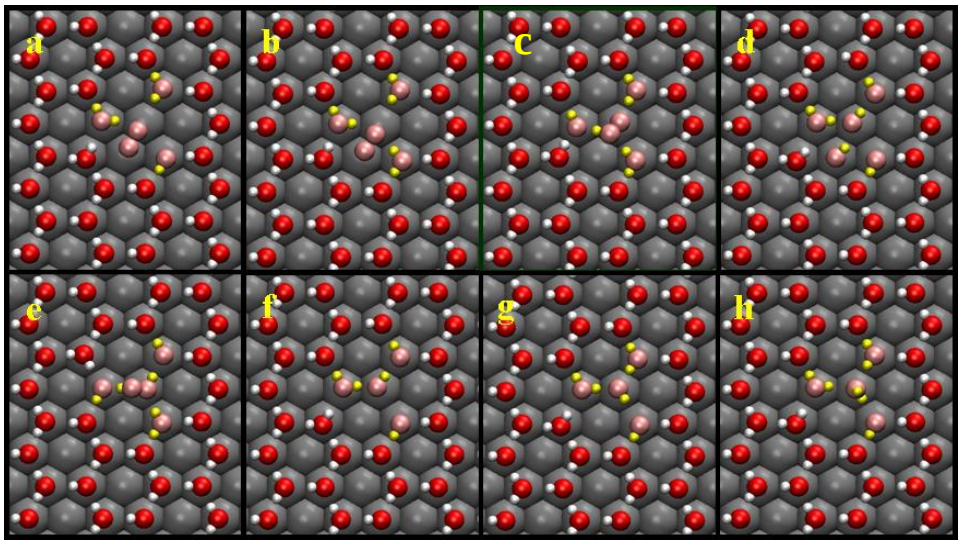

Fig. 7.9: *The most important structures on the ORR potential energy landscape embodied in the HDWL network, labeled from a-h. Pt(111) slab, oxygen and hydrogen atoms are colored in dark gray, red and white, whereas the oxygen and hydrogen atoms indicated in the FED are colored in pink and yellow, respectively.*

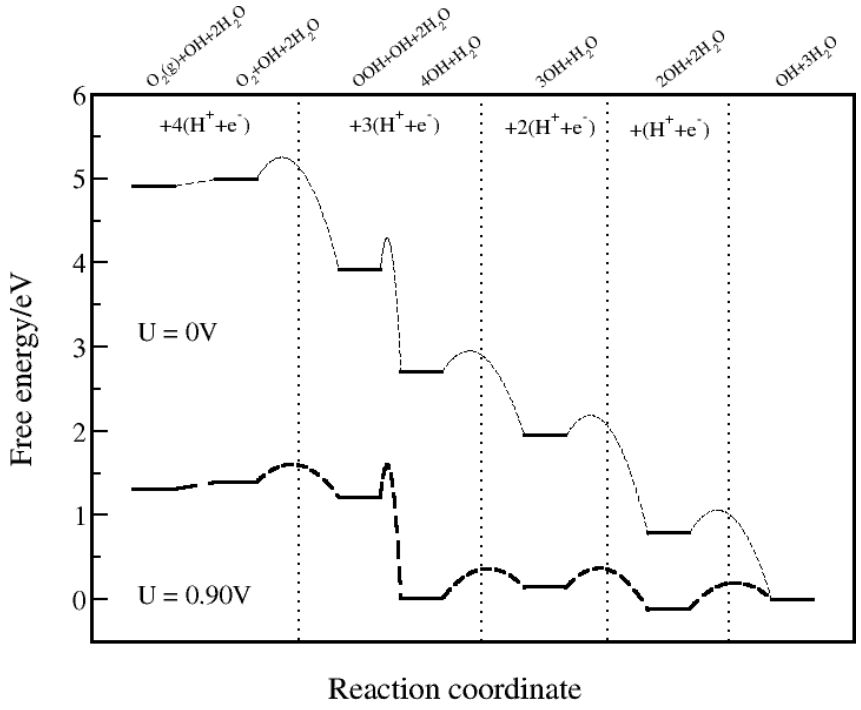

Fig. 7.10: *Simplified free energy diagram for the O_2 reduction at 0 V (up) and 0.9 V (bottom) potential. The most stable states in each electrochemical step, as well as the minimum reaction barrier for O-O bond splitting are indicated. The electrochemical reduction steps are separated by dashed vertical lines. The barriers for proton transfer to the reaction center in the electrochemical steps are indicated with dashed black lines. The minimum energy path at 0.9 V is highlighted.*

The most stable intermediate in each electrochemical step is shown in **Fig. 7.10**, a simplified version of **Fig. 7.9**. The minimum energy barrier for the OOH dissociation is also indicated, as well as the barriers for the charge transfer between different electrochemical steps. At U=0.9 V the OOH formation and OH removal step in **Fig. 7.10** have very similar barriers. We speculate that inclusion of more water (larger unit cells) could slightly stabilize these species on the surface. Any stabilization would reduce the barrier for the OOH dissociation and increase the barrier for the H_2O formation.

7.6 Summary

In summary, we have calculated the reaction path and barriers for the ORR on Pt(111). We would like to highlight that this approach differs from others in a way that we take explicitly into account the right water structure and we subsequently model all the ORR intermediates this water network. As we have seen, water does not merely contribute with hydrogen bonds but also it is actively involved in the reaction mechanism.

The reaction mechanism was deconvoluted into potential-dependent charge transfer step and potential-independent surface diffusion and intermediates reduction steps. We find small activation barriers related to each step. We note here that the direct transfer of proton to one of the ORR intermediates could yield smaller barrier, however, since the barriers for the transfer via surface are already small, this will not affect the conclusions of our study.

We have constructed the differential adsorption free energy diagram and we have determined the most stable surface structure at potentials of interest for the ORR. We find a discontinuity in the free adsorption energy at 1/3 ML of OH coverage. Upon this knowledge, we constructed the FED for the O_2 reduction at 0.9 V. The results are in agreement with the previously established picture that on Pt(111), the OH reduction is the potential determining step. In addition we also find that the most stable species after first proton transfer is the OOH with the moderate potential-independent dissociation barrier of 0.37 eV. We have also shown that the O_2 reduction proceeds via so-called direct pathway, and not through the peroxo intermediate.

8 Zinc/air battery

In this Chapter I will use DFT to investigate zinc dissolution at the anode in Zn/air battery. The assets and drawbacks of the zinc-air (metal/air) battery will be first addressed in the introduction; afterwards, the model used to simulate dissolution of zinc will be explained and finally, the obtained results will be compared against experiments. Although dissolution processes have been previously successfully studied with DFT [73,200,201,202,203], this is a first attempt, to the best of our knowledge, to model the dissolution of zinc with this approach.

8.1 Introduction

Batteries are similar to Fuel Cells (FC) apart from the fact that the FC is an energy converting device whereas the battery is an energy storage device. The FCs represent thermodynamical open systems, where fuel is replenished from an external source. On the other hand batteries are closed thermodynamic systems that store energy chemically. Besides, batteries rely on earth abundant materials that are cheap to produce in contrast to FCs which rely on the precious Pt-based catalysts.

Although the technology originates from 19th century, the metal/air battery was first put in commercial use in the beginning of the 20th century. It became increasingly popular in the seventies when the first so-called “button” cells appeared on the market. These cells were primarily used in hearing aids and other small medical appliances. Depletion of the fossil fuel reserves has inspired the pursuit of alternative energy sources. This has brought the battery technology once again under spotlight and it has encouraged the scientific community to revisit and overcome problems that impede its large scale utilization.

The Zinc/air battery is a member of a broad family of metal/air cells. In the past, few potential candidates such as Li, Ca, Mg, Al, Zn and Fe had been scrutinized as possible

energy carriers in batteries [204,205]. Some of the batteries like Al/air and the Li/air have even higher gravimetric energy density than Zn, but they were never commercialized because of low stability in aqueous and alkaline solutions [206]. The problem with Al is that it corrodes in alkaline media whereas Li spontaneously degrades in the presence of trace amounts of water. The reason for such a huge interest in this technology lies in the very high gravimetric (practical: ~200 Wh kg^{-1}, theoretical: 1350 Wh kg^{-1}) and volumetric energy density (~225 Wh L^{-1}), higher than any other primary battery system [207]. The striking advantage of the zinc/air system with respect to other primary battery systems originates from the use of oxygen from the air as the cathode oxidant, which enables very high zinc loads in the battery. This allows the zinc/air cell to be filled with more zinc, which is the only material consumed during discharge. Furthermore, this system is characterized by a very flat discharge profile which points to a minute potential loss over time [208].

The zinc/air battery is usually regarded as a primary (non-rechargeable) battery cell. Companies and research groups worldwide are investing huge efforts to make it secondary (rechargeable). This could be achieved with a bifunctional catalyst capable of performing both the ORR during discharging cycle and the OER during charge. We have previously shown what are the best catalysts for the ORR [43,51] and OER [34,209] among different classes of materials, but the challenge still persists in combining the two [210,211]. Another plausible technical solution is to make a three electrode cell with two cathodes, one for the ORR and other for the OER but this design would add significantly to the size and complexity of the cell [212]. Recently a company called ReVolt claimed it succeeded in developing the rechargeable zinc/air cell. The performance of their cell is benchmarked to other primary batteries systems in **Fig. 8.1**.

The advantage of the zinc/air cell is that they can store large energy density, they are cheap to produce and to maintain and moreover they are environmentally friendly. Conversely the zinc/air cell possesses significant drawbacks which are responsible for presently very limited extent of the technology. Among these the most important ones are anode corrosion caused by hydrogen evolution, carbonate formation from the CO_2 in the air which decreases the conductivity of the electrolyte, high sensitivity to temperature and humidity, high self discharge and zinc dendrite formation where the zinc builds unevenly

in the form of branch-like structures that can short circuit the electrodes and eventually kill the battery [206].

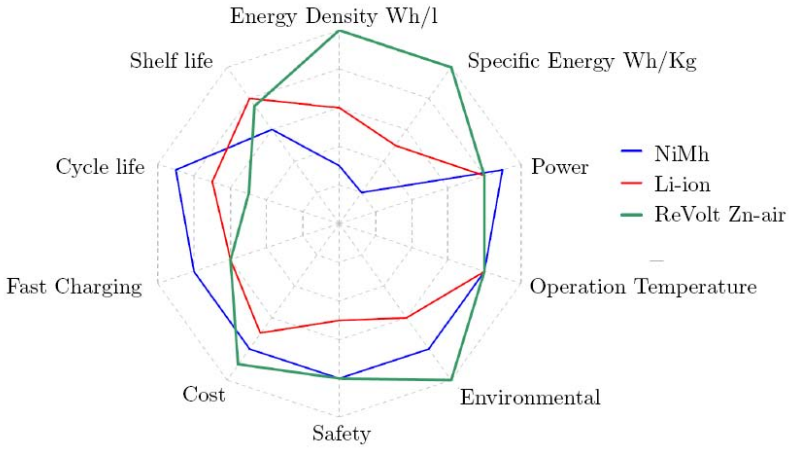

Fig. 8.1: *Performance of the rechargeable zinc/air battery developed by ReVolt evaluated against Li-ion and nickel-metal-hydride batteries respectively. Taken from* [213].

8.2 Composition and chemistry

The zinc/air cell is composed of the zinc anode, an aqueous alkaline electrolyte and an air cathode. A schematic of the cell is shown in **Fig. 8.2**.

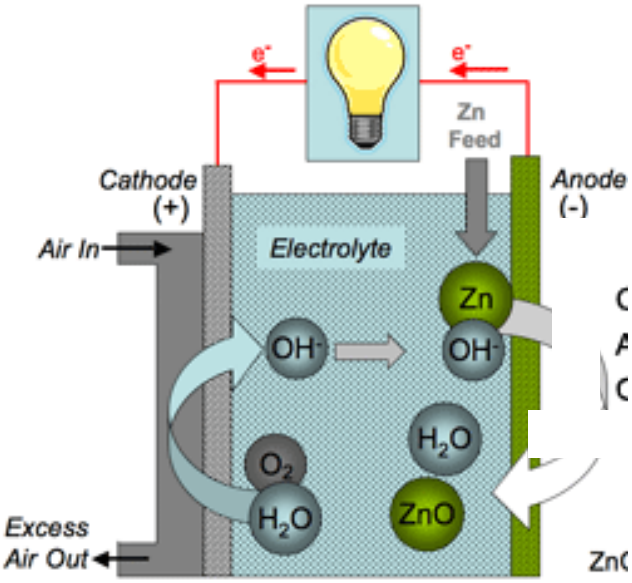

Fig. 8.2: *Schematics of the zinc/air cell. Adapted from ref. [214]*

Power is produced from zinc oxidation at the anode and ORR at the cathode. The anode of the zinc/air cell is in the form of zinc paste. In the excess of hydroxyl species, zinc dissolves to form the $Zn(OH)^{4-}$ ion, while two electrons are released and transferred to the cathode where oxygen is reduced to hydroxyl. The non-precious MnO_2 catalyst is a frequent choice for the cathode material. KOH is usually chosen as the electrolyte due to a very good ionic conductance. During the discharge the zincate ions spontaneously precipitate in the solution to form ZnO. The half reactions at the anode and cathode are shown below

$$\textbf{Anode:}\quad Zn + 4OH^- \rightarrow Zn(OH)^{4-} + 2e^- \qquad E = 1.25\ V \qquad (8.1)$$

$$Zn(OH)^{4-} \rightarrow ZnO + H_2O + 2OH^-$$

$$\textbf{Cathode:}\quad 1/2O_2 + 2H_2O + 2e^- \rightarrow 2OH^- \qquad E=0.4\ V \qquad (8.2)$$

By definition, standard potentials are given at standard conditions in 1 M solution of each aqueous species. Hence, the dissolution potentials in Eqs. (8.1) and (8.2) are given at pH=14. Adding the two electrode reactions and potentials together, yields the overall reaction and potential for the system.

$$\textbf{Overall:}\quad Zn + 1/2O_2 \rightarrow ZnO \qquad E=1.65V \qquad (8.3)$$

The maximum (theoretical) work that can be extracted from the system is 1.65 eV per electron, albeit the operating voltage is only ~1.30 V [208] mainly due to the kinetic losses at the cathode.

8.3 Method

All the electronic structure calculations, related to this work, have been carried out using GPAW program package which is a density functional theory implementation based on the projector-augmented wave (all electron, frozen core approximation) method that uses real-space uniform grids [215]. The grid spacing was set to h=0.15 Å, as a tradeoff between computational efficiency and accuracy. For description of exchange and correlation the standard GGA-RPBE functional was chosen [65].

The Zn surface was modeled as a kink represented by periodically repeated 6 layer slab separated by approximately 18 Å of vacuum. The two bottom layers were held fixed while the rest was allowed to relax until the sum of the absolute interatomic forces was less than 0.05 eV $Å^{-1}$. The Brillouin zone was sampled by (3x4x1) Monkhorst-Pack grid [75] and symmetry was applied to further reduce the number of k-points. Fermi smearing was set to 0.1 eV and all the energies were extrapolated to the electronic temperature of 0 K. All calculations were performed in the ASE simulation environment [80].

8.4 Results and discussion

We start by addressing some simple issues regarding lattice constants and model of the surface. Our optimized lattice constants of zinc (a=2.66, c=5.37, a/c=2.02) compare well with other theoretical DFT-GGA (a=2.65, c=5.12, a/c=1.93) [216] and experimental (a=2.67, c=4.95, a/c=1.86) [217] values found in the literature. The same agreement holds for the wurtzite structure of $Zn(OH)_2$ (a=4.96, b=5.23, c=8.91) where we compared our data to the only experimental source available (a=4.92, b=5.16, c=8.49) [218]. We have also calculated formation energy of bulk $Zn(OH)_2$ to be 2.35 eV, which is very close to the experimentally determined 2.5 eV [219].

We adopted a kinked surface as our model system. There are two reasons for choosing the kink. Firstly, the kink atoms make the strongest bonds (most undercoordinated sites) to adsorbates and thus they will be the first ones to dissolve. Secondly, when a kink atom is dissolved, it leaves another kink on the surface. Hence, there is no qualitative change in the surface morphology. The difference in energy, before and after the dissolution of the kink atom will thus correspond to the energy of one zink atom in the bulk. In this way the bulk dissolution can be effectively emulated by surface dissolution of kink atoms.

We began our study by probing the most stable adsorption sites for hydroxyl species and concluded that the bridge site between the kink and adjacent Zn atom is preferential for the first OH adsorption (cf. **Fig. 8.3**). Subsequent OH groups will adsorb on the step, until all the step sites have been covered. In the end, each zinc atom at the step is bonded to two OH groups. Any additional OH species will bind to the kink atom pulling it out

(dissolving it) from the surface. This finding clearly demonstrates that the zink anode will dissolve kink atom by kink atom.

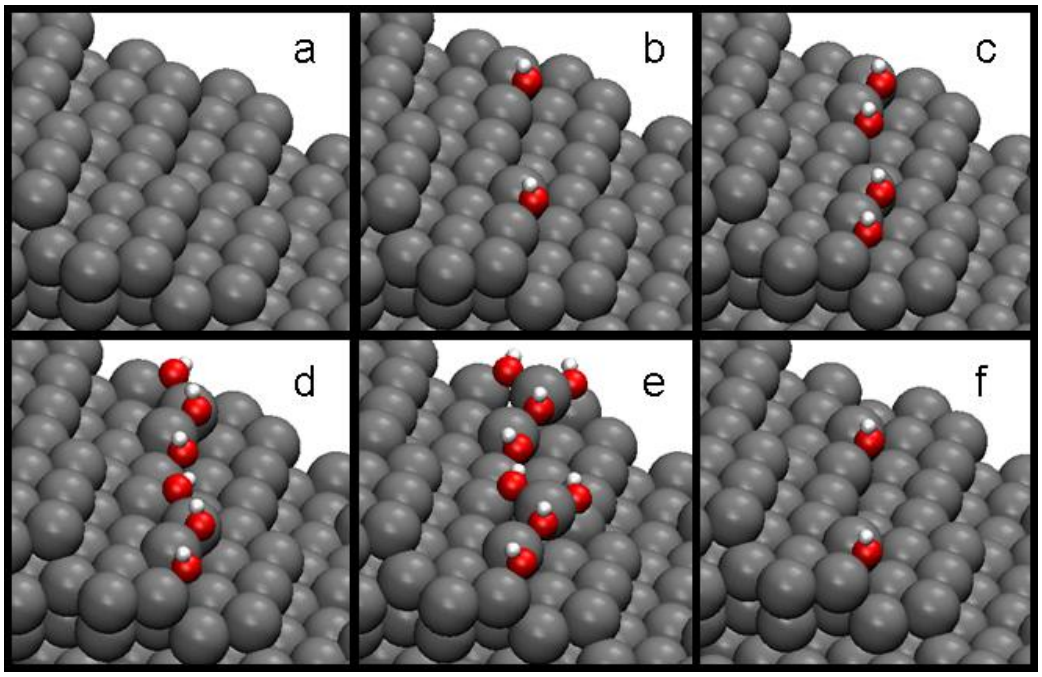

Fig. 8.3: *Snapshot a is the bare Zn kink, while snapshots b-f illustrate the steps in one dissolution cycle. The unit cell has been repeated twice in the y direction.*

In experiments zink undergoes sequential dissolution to form $[Zn(OH)_4]^{2-}$ ion.

$$Zn + OH^- \rightarrow ZnOH + e^- \quad (8.4)$$

$$ZnOH + OH^- + e^- \rightarrow Zn(OH)_2 + 2e^- \quad (8.5)$$

$$Zn(OH)_2 + OH^- \rightarrow [Zn(OH)_3]^- \quad (8.6)$$

$$[Zn(OH)_3]^- + OH^- \rightarrow [Zn(OH)_4]^{2-} \quad (8.7)$$

where Zn(OH) and $Zn(OH)_2$ are bulk hydroxides. The equilibrium potential for the formation of the ionic species $[Zn(OH)_3]^-$ and $[Zn(OH)_4]^{2-}$ is 1.15 and 1.25 V, respectively [219]. In our model, the kink atom dissolves after the adsorption of the third hydroxyl group which mimics the experimental observation.

We present our results in **Fig. 8.4** in the form of the free energy diagram (FED). Here, the first and last two steps are fixed to the values of dissolution potentials of zinc forming

$[Zn(OH)_3]^-$ and $[Zn(OH)_4]^{2-}$ ions. The experimental values have been used since it is very hard to estimate free energy levels of solvated ions within DFT. To obtain the free energy levels of the solid phases, Zn(OH) and $Zn(OH)_2$ corresponding to the second and the third step in the FED, we used method outlined elsewhere [43]. Using this approach the total free adsorption energy of OH is expressed as

$$\Delta G = \Delta E + \Delta ZPE - T\Delta S - 0.059 * pH + E_{w,water} \quad (8.8)$$

where ΔE is the reaction enthalpy which has been calculated by referencing the OH adsorption energy to water in the liquid and hydrogen in the gas phase. The ΔZPE – TΔS is the zero point energy and entropy contribution, estimated from the normal mode analysis and thermodynamic tables [70] to be 0.39 eV per OH species at room temperature. Since the pH cannot be explicitly included in the calculations, it is added *a posteriori* by shifting the free energy levels of OH by –0.059*pH or in our case by -0.83 eV at pH=14. This is equal to using OH^-(aq) as the reference for the OH^* instead of the H_2O(l). The $E_{w,water}$ is the water induced stabilization energy of OH species. This effect has previously found to be quite substantial on Pt(111) (~0.6 eV) [43]. In the present analysis it amounts to 0.57 eV per OH group. The value was deduced by comparing the free energy level of $[Zn(OH)_3]^-$, when it was moved far away in the vacuum region and the experimentally determined dissolution potential for $[Zn(OH)_3]^-$.

The FED is shown at two different potentials, U=0 V and U=-1.08 V i.e. the lowest potential where all the reaction steps are still downhill in free energy. The FED at U = -1.08 V is obtained by shifting up the free energy levels at U=0 V by the chemical potential of the electrons, neU, where n is the number of electrons involved in the electrochemical reaction. In **Fig. 8.4**, we have also denoted the bulk formation energy of $Zn(OH)_2$ in blue. The small energy difference in the bulk formation energy of $Zn(OH)_2$ obtained from two qualitatively different approaches (bulk and surface calculations) validates the model we assumed. The difference between the theoretical equilibrium potential of -1.25 V and -1.08 V is the overpotential (0.17 V) needed to run the reaction. This is close to the experimental observation that the reaction does not feature large

overpotential. It is clearly seen from snapshots b and f in **Fig. 8.3** that the surface morphology does not change after the dissolution of the kink atom.

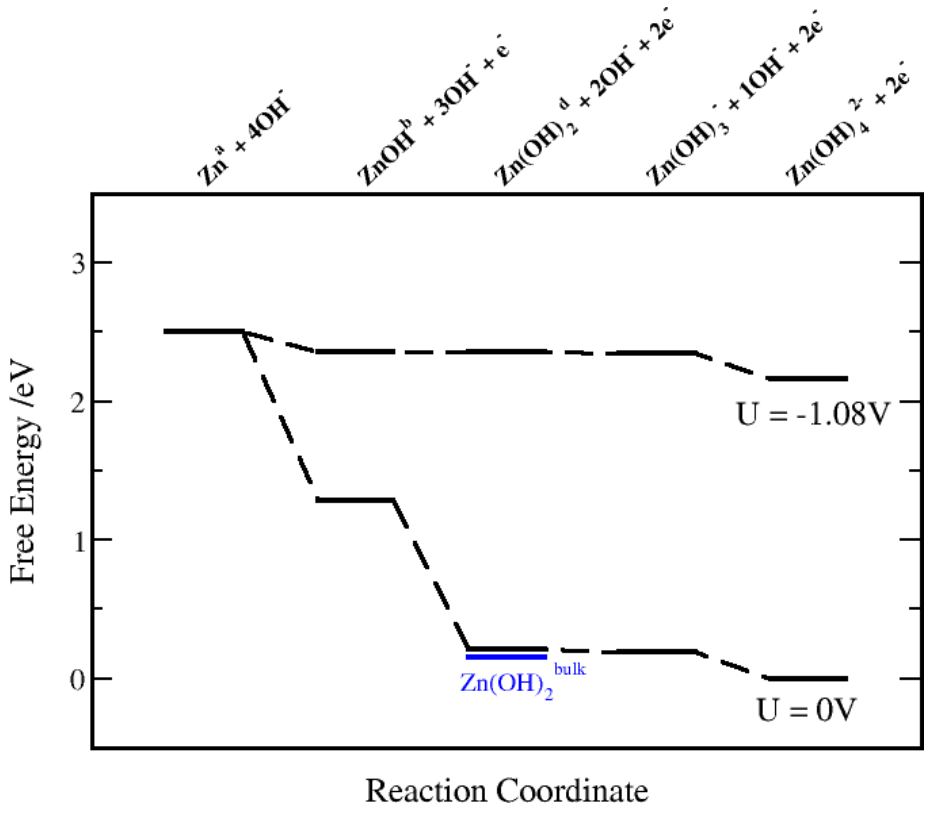

Fig. 8.4: *Free energy diagram for Zn dissolution at the anode, shown at two potentials, 0 V and -1.08 V respectively. The $[Zn(OH)_3]^-$ and $[Zn(OH)_4]^{2-}$ levels are fixed to the experimental determined dissolution potentials. The $Zn(OH)_2$ level calculated from the formation energy of bulk $Zn(OH)_2$ is indicated in blue for comparison. Labels a, b and d correspond to the structures in Fig. 8.3.*

8.5 Summary

In summary, we have presented a simple analysis of the anode dissolution in the zinc/air battery. The novelty of this approach is that we have emulated bulk dissolution by the surface adsorption on a Zn kink. From the calculated OH adsorption energies and dissolution potentials we have mapped out the FED and we have shown that there is a very small overpotential, 0.17 V, associated with this reaction. This finding agrees well with the experimental evidence. The close agreement between the two values substantiates the validity of the assumed model and furthermore it demonstrates the versatility of DFT calculations in modeling dissolution processes on metal surfaces.

9 Summary & outlook

In the present work we have demonstrated how electrochemical reactions can be successfully modeled in standard DFT calculations without the complexity of introducing unphysical features to regulate the surface charge. The properties of the EDL, generated by our method, emulated most authentically the genuine EDL model in contrast to other methodologies present in the literature. The limited size of the unit cell that can be afforded in the calculations, both in the surface plane and in the direction perpendicular to the surface, has sever implications on reaction energetics for charge transfer reactions and the value of the ASHEP. The former can be resolved by extrapolating reaction and activation energies to the limit where the potential does not change during the reaction. This approach is generally valid and thus applicable to any charge transfer reaction. It was not applied to treat the charge transfer in the ORR since the variation of the potential was negligible in this case, owing to a different surface environment. On the other hand the errors associated with the fluctuating value of the ASHEP are cancelled out if an internal measure of the ASHEP, calculated independently for every system, is used instead of an experimental value.

Furthermore we have emphasized the importance of explicitly including the right surface water structure. In the case of the HER/HOR we choose the water bilayer having free hydrogen bonds oriented towards the metal surface. To strengthen our method we have shown that the physics is preserved by performing a test calculation with a completely different water structure. In the case of the ORR we choose a half dissociated water layer because we find that this is the most stable water phase at potentials relevant for the ORR on Pt(111). In all cases we used one water layer to relieve the computational burden. We have demonstrated that inclusion of more water layers will not alter the conclusions of our studies.

The purpose of the method development was to create a tool capable of studying reactions at different biases in order to assess the reaction mechanisms of thr electrochemical reactions. We have accomplished this by disclosing the Volmer-Tafel route being the predominant reaction pathway for the HER/HOR on Pt(111). Moreover, due to the large difference between the Tafel and Heyrovski barriers heights and the small differences in hydrogen chemisorption energy, we have concluded that the Heyrovski pathway will prevail on all the transition metals and facets investigated in this work. A propos the ORR, we find that there is a very small barrier for splitting the O_2 bond. We speculate that the barrier is similar on all the transition metals.

The future perspective would be to furthermore substantiate our method by extending it to treat other charge transfer reactions, *e.g.* electrochemical ammonia synthesis, methanation reaction, and, in particular, charge transfer reactions where the proton comes from water rather than a hydronium ion. The latter point would enable studies of reaction energetics in an alkaline media.

After all, understanding of the reaction mechanism is a major prerequisite to successful catalyst design. New catalyst materials, relinquished of dependence on Pt and other noble metals, are a necessity for the establishment of the hydrogen society.

References

1 http://www.bp.com/statisticalreview.

2 http://www.theglobaleducationproject.org/earth/energy-supply.php.

3 Smil (2006), p. 12, 15.

4 N. S. Lewis, *Science* **315** (2007) 798.

5 F. Jiao, H. Frei, *Angewandte Chemie* **48** (2009) 1841.

6 T. F. Jaramillo, K. P. Jørgensen, J. Bonde, J. H. Nielsen, S. Horch, Ib Chorkendorff, *Science* **317** (2007) 100.

7 http://www.case.dtu.dk/upload/centre/case/forskning/pdf

8 http://www.nsf.gov/news/news_images.jsp?cntn_id=112154&org=NSF.

9 J. O'M. Bockris, A.K.N. Reddy, M. Gamboa-Aldeco, "Modern Electrochemistry 2A. Fundamentals of Electrodics.", Second Edition, Kluwer Academic/Plenum Publishers, 2000.

10 E. Gileadi, “Electrode Kinetics”, VCH, 1993, New York

11 N. M. Markovic, B. N. Grgur, P. N. Ross, *J. Phys. Chem. B* **101** (1997) 5405.

12 A. Berná, V. Clíment, J. M. Feliu, *Electrochem. Commun.* **9** (2007) 2789.

13 B. N. Grgur, N. M. Markovic, P. N. Ross, *Can. J. Chem.* **75** (1997) 1465.

14 Grove, W. R., *Compte Rendus* **8** (1839) 497**.**

15 http://www.compositesworld.com/articles/composites-fuel-growth-of-fuel-cell-technology

16 J. Larminie, A. Dicks, “Fuel Cell systems explained”, Second Edition, John Wiley & Sons Ltd., 2003.

17 H. A. Gasteiger, S. S. Kocha, B. Sompalli, F. T. Wagner, *App. Caalt. B - Env* **56** (2005) 9.

18 F. T. Wagner, B. Lakshmanan, M. F. Mathias, *J. Phys. Chem. Lett.* **1** (2010) 2204.

19 http://www.platinum.matthey.com/

20 V. Smil, Scientific American July, **75** (1997).

21 J. M. Thomas & W.-J. Thomas, “*Principle and Practice of Heterogeneous Catalysis”* (VCH, 1997)

22 D. G. Nocera, *Inorganic Chem* **48** (2009) 10001.

23 J. K. Nørskov, T. Bligaard, J. Rossmeisl1, C. H. Christensen *Nature Chem.* **1** (2009) 37.

24 K. Reuter, D. Frenkel, M. Scheffler, *Phys. Rev. Let.* **93** (2004) 116105.

25 K. Honkala, A. Hellman, I. N. Remediakis, A. Logadottir, A. Carlsson, S. Dahl, C. H. Christensen, J. K. Nørskov, *Science* **307** (2005) 555.

26 E. W. Hansena, M. Neurock, *J. Catal.* **196** (2000) 241.

27 S. Linic, M. A. Barteau, *J. Catal*. **214** (2003) 200.

28 F. Abild-Pedersen, J. Greeley, F. Studt, J. Rossmeisl, T. R. Munter, P.G. Moses, E. Skúlason, T. Bligaard, J. K. Nørskov, *Phys. Rev. Lett.* **99** (2007) 016105.

29 J. Greeley, J. Rossmeisl, A. Hellman, J.K. Nørskov, *Z. Phys. Chem*. **221** (2007) 1209.

30 N. Lopez, T.V.W. Janssens, B.S. Clausen, Y. Xu, M. Mavrikakis, T. Bligaard, J.K. Nørskov, *J. Catal.* **223** (2004) 232.

31 J. K. Nørskov, T. Bligaard, B. Hvolbæk, F. Abild-Pedersen, I. Chorkendorff, C. H. Christensen, *Chem. Soc. Rev*. **37** (2008) 2163.

32 P. Sabatier, J. B. Sanders, *Compte Rendus Acad. Sci. Paris* **134** (1902) 514.

33 J. Rossmeisl, A. Logadottir, J. K. Nørskov, *J. Chem. Phys.* **319** (2005) 178.

34 J. Rossmeisl, Z.–W. Qu, H. Zhu, G.-J. Kroes, J. K. Nørskov, *J. Electroanal. Chem.* **607** (2007) 83.

35 J. O'M. Bockris, "*Modern Aspects of Electrochemistry", Vol. 1,* Butterworths, London, 1954.

36 A. T. Petrenko, *Zh. Fiz. Khim.* **39** (1965) 2097.

37 H. Kita, *J. Electrochem. Soc* **113** (1966) 1095.

38 D. B. Matthews, Ph.D. Thesis, University of Pennsylvania, 1965.

39 R. Parsons, *Trans. Faraday Soc.* **54** (1958) 1053.

40 H. Gerischer, *Bull. Soc. Chim. Belg.* **67** (1958) 506.

41 L. I. Krishtalik in P. Delahay (Ed.), "*Advances in Electrochemistry and Electrochemical Engineering", Vol.* 7, Interscience, New York, 1970.

42 J. K. Nørskov, J. Rossmeisl, A. Logadottir, L. Lindqvist, J. R. Kitchin, T. Bligaard, H. Jónsson, *J. Phys. Chem. B* **108** (2004) 17886.

43 J. K. Nørskov, T. Bligaard, A. Logadottir, J. R. Kitchin, J. G. Chen, S. Pandelov, U. Stimming, *J. Electrochem. Soc.* **152** (2005) J23

44 C. J. H. Jacobsen, S. Dahl, B.S. Clausen, S. Bahn , A. Logadottir , J. K. Nørskov, *J. Am. Chem. Soc.* **123** (2001) 8404.

45 T. Bligaard, J.K. Nørskov, S. Dahl, J. Matthiesen, C.H. Christensen, J. Sehested, *J. Catal.* **224** (2004) 206.

46 H. Falsig, T. Bligaard, C. H. Christensen, J. K. Nørskov, *Pure & App. Chem.* **79** (2006) 1895.

47 J. Kleis, G. Jones, F. Abild-Pedersen, V. Tripkovic, T. Bligaard, J. Rossmeisl, *J. Electrochem. Soc.* **156** (2009) B1447.

48 H. Falsig, B. Hvolbæk, I. S. Kristensen, T. Jiang, T. Bligaard, C. H. Christensen, J. K. Nørskov **47** (2008) 4835.

49 P. Ferrin, A. U. Nilekar, J. Greeley, M. Mavrikakis, Jan Rossmeisl, *Surf. Sci.* **602** (2008) 3424.

50 M.T.M. Koper, *to be published in J. Electroanal Chem.*

51 J. Greeley, I. E. L. Stephens, A. S. Bondarenko, T. P. Johansson, H. A. Hansen, T. F. Jaramillo, J. Rossmeisl, I. Chorkendorff, J. K. Nørskov, *Nature Chem.* **1** (2009) 552.

52 S. Mukerjee, S. Srinivasan, *J. Electroanal. Chem.* **357** (1993) 201.

53 V. R. Stamenkovic, B. Fowler, B. S. Mun, G. Wang, P. N. Ross, C. A. Lucas, N. M. Markovic, *Science* **315** (2007) 493.

54 V. R. Stamenkovic, B. S. Mun, M. Arenz, K. J. J. Mayrhofer, C. A. Lucas, G. Wang, P. N. Ross, N. M. Markovic, *Nature* **6** (2007) 241.

55 S. Koh, P. Strasser, *J. Am. Chem. Soc.* **129** (2007) 12624.

56 A. U. Nilekar, Y. Xu, J. Zhang, M. B. Vukmirovic, K. Sasaki, R. R. Adzic, M. Mavrikakis, *Top. Catal.* **26** (2007) 276.

57 S. Linic, J. Jankowiak, M. A. Barteau, *J. Catal*. **224** (2004) 489.

58 F. Studt, F. Abild-Pedersen, T. Bligaard, R. Z. Sørensen, C. H. Christensen, J. K. Nørskov, *Science* **320** (2008) 1320.

59 M. Lefèvre, E. Proietti, F. Jaouen, J.-P. Dodelet, *Science* **71** (2009) 324.

60 M. P. Andersson, T. Bligaard, A. Kustov, K. E. Larsen, J. Greeley, T. Johannessen, C. H. Christensen, J. K. Nørskov, *J. Catal.* **239** (2006) 501.

61 P. Hohenberg, W. Kohn *Phys. Rev. B* **136** (1964) B864

62 W. Kohn, L. J. Sham, *Phys. Rev.* **140** (1965) 1133

63 J. P. Perdew, K. Burke, M. Ernzerhof, *Phys. Rev. Lett.* **78** (1997) 1396.

64 J. P. Perdew, K. Burke, and M. Ernzerhof, *Phys. Rev. Lett.* **77** (1996) 3865,

65 B. Hammer, L. B. Hansen, J. K. Nørskov, *Phys. Rev. B* **59** (1998) 7413.

66 M. Dion, H. Rydberg, E. Schröder, D. C. Langreth, B. I. Lundqvist, *Phys Rev. Lett* **92** (2004) 246401.

67 Y. Zhang and W. Yang, *Phys. Rev. Lett.* **80** (1998) 890.

68 J. Klimeš, D. R Bowler, A. Michaelides, *J. Phys. Condens. Matter* 22 (2010) 022201.

69 C. Kittel, "*Introduction to Solid State Physics",* Wiley, New York, 1996.

70 Atkins, P. W. *Physical Chemistry*, 6th ed., Oxford University Press: Oxford, U.K., 1998; pp 485, 925-927, 942.

71 H. Jónsson, G. Mills and K. W. Jacobsen, in Classical and Quantum Dynamics in Condensed Phase Simulations, ed. B. J. Berne, G. Ciccotti and D. F. Coker, World Scientific, Singapore, 1998.

72 G. Henkelman, H. Jónsson, *J. Chem. Phys.* **113** (2000) 9978.

73 H. A. Hansen, J. Rossmeisl, J. K. Nørskov, *Phys. Chem. Chem. Phys.* **10** (2008) 3722.

74 G. S. Karlberg, J. Rossmeisl, J. K. Nørskov, *Phys. Chem. Chem. Phys.* **9** (2007) 5158.

75 H. J. Monkhorst; J. D. Pack, *Phys. Rev. B* **13** (1976) 5188.

76 D. Vanderbilt, *Phys.Rev. B* **41** (1990) 7892.

77 Y. Zhang, W. Yang, *Phys Rev. Lett* **80** (1998) 890.

78 Dacapo pseudopotential code, URL: https.//wiki.fysik.dtu.dk/dacapo, Center for Atomic Scale Materiale Design (CAMD), Technical University of Denmark, Lyngby.

79 J. J. Mortensen, L. B. Hansen, K. W. Jacobsen, *Phys. Rev. B* **71** (2005) 035109.

80 Atomic Simulation Environment (ASE), URL: https/wiki.fysik.dtu.dk/ase, Center for Atomic Scale Materiale Design (CAMD), Technical University of Denmark, Lyngby.

81 H. von Helmholtz, *Ann. Phys.* **89** (1853) 211.

82 G. Gouy, *Compte. Rend.* **149** (1910) 654.

83 D. Chapman, *Philos. Mag.* **25** (1913) 475.

84 O. Stern, Z. *Electrochem.* **30** (1924) 508.

85 D. Grahame, *Chem. Rev.* **41** (1947) 441.

86 Atkins, P. W. *Physical Chemistry*, 10th ed., Oxford University Press: Oxford, U.K., 1998.

87 H. Ogasawara, B. Brena, D. Nordlund, M. Nyberg, A. Pelmenschikov, L. G. M. Petterson, A. Nilsson, *Phys. Rev. Lett.* **89** (2002) 276102.

88 P. J. Feibelman, *Science* **295** (2002) 99.

89 C. Clay, S. Haq, A. Hodgson, *Phys. Rev. Lett.* **92** (2004) 46102.

90 G. Held, D. Menzel, *Surf. Sci.* **92** (1994) 316.

91 A. Michaelides, P. Hu, *J. Am. Chem. Soc.* **123** (2001) 4235.

92 G. S. Karlberg, G. Wahnström, *Phys. Rev. Lett.* **92** (2004) 136103

93 A. Michaelides, V. A. Ranea, P. L. de Andres, D. A. King, *Phys. Rev. Lett.* **90** (2003) 216102.

94 J. Carrasco, A. Michaelides, M. Scheffler, *J. Chem. Phys.* **130** (2009) 184707.

95 S. Schnur, A. Groβ, New J. Phys. **11** (2009), 125003.

96 A. Roudgar, A. Groβ, *Chem. Phys. Lett.* **409** (2005) 157.

97 A. Michaelides, A. Alavi, D. A. King, *Phys Rev. B* **64** (2004) 113404.

98 A. Glebov, A. P. Graham, A. Menzel, J. P. Toennies, *J. Chem. Phys.* **106** (1997) 9382.

99 S. Haq, J. Harnett, and A. Hodgson, *Surf. Sci.* **505** (2002) 171.

100 M. Morgenstern, T. Michely, G. Comsa, *Phys. Rev. Lett.* **77** (1996) 703.

101 M. Morgenstern, J. Muller, T. Michely, G. Comsa, *Z. Phys. Chem.* **198** (1997) 43.

102 S. Izvekov, A. Mazzolo, K. Van Opdorp, G. A. Voth, *J. Chem. Phys.* **114** (2001) 3284.

103 S. Izvekov and G. A. Voth, *J. Chem. Phys.* **115** (2001) 7196.

104 S. Meng, L. F. Xu, E. G. Wang, and S. W. Gao, *Phys. Rev. Lett.* **89** (2002) 176104.

105 S. Meng, E. G. Wang, S. Gao, *Phys. Rev. B* **69** (2004) 195404.

106 M. Otani, O. Sugino, *Phys. Rev. B* **73**, (2006) 115407.

107 O. Sugino, I. Hamada, M. Otani, Y. Morikawa, T. Ikeshoji, Y. Okamoto, *Surf. Sci.* **601** (2007) 5237.

108 M. Otani, I. Hamada, O. Sugino, Y. Morikawa, Y. Okamoto, T. Ikeshoji, *Phys. Chem. Chem. Phys.* **10** (2008) 3609.

109 J.-S. Filhol, M. Neurock, *Angew. Chem. Int. Ed*. **45** (2006) 402.

110 C. D. Taylor, S. A. Wasileski, J.-S. Filhol, M. Neurock, *Phys. Rev B* **73** (2006) 65402.

111 M. J. Janik, C. D. Taylor, M. Neurock, *J. Electrochem. Soc.* **156** (2009) B126.

112 S. Trasatti, *Electrochim. Acta* **36** (1991) 1659.

113 Y. Cai, A. B. Anderson, *J. Phys. Chem. B* **108** (2004) 9829.

114 E. Skúlason, G.S. Karlberg, J. Rossmeisl, T. Bligaard, J. Greeley, H. Jónsson and J.K. Nørskov, *Phys. Chem. Chem. Phys.*, **9** (2007) 3241.

115 Ph.D thesis by Egill Skúlason, July (2009).

116 G. Zundel, H. Metzger, Z. Physik. Chem. (N.F.) 58 (1968) 225.

117 M. Eigen, Angew. Chem. Int. Ed. 3, 1 (1964).

118 N. M. Markovic, S. T. Sarraf, H. A. Gasteiger, . N. Ross, Jr., *J. Chem. Soc. Faraday Trans.* **92** (3719) 1996.

119 A. Vollbeda, J. C. Fontecilla-Camps, *J. Chem. Soc., Dalton Trans.* **21** (2003) 4030.

120 D. C. Rees, J. B. Howard, *Science* **300** (2003) 929.

121 Siegbahn, P. E. M. *Ad*V. *Inorg. Chem.* **2004**, *56*, 101.

122 Meija-Rodriguez, D. Chong, J. H. Reibenspies, M. P. Soriaga, M. Y. Darensbourg, *J. Am. Chem. Soc.* **126** (2004) 12004.

123 M. Razavet, S. C. Davies, D. L. Hughes, J. E Barclay, D. J. Evans, S. A. Fairhurst, X. Liu, C. Pickett, *J. Chem. Soc., Dalton Trans.* **4** (2003) 586.

124 B. Hinnemann, P. G. Moses, J. Bonde, K. P. Jørgensen, J. H. Nielsen, S. Horch, I. Chorkendorff, J. K. Nørskov. *J. Am. Chem. Soc.* **130** (2009) 184707.

125 J. Greeley, T. F. Jaramillo, J. Bonde, I. Chorkendorff, J. K. Nørskov, *Nature materials* **5** (2006) 909.

126 S. Trasatti, *Electroanal. Chem.* **39** (1972) 163.

127 G. S. Karlberg, T. F. Jaramillo, E. Skúlason, J. Rossmeisl, T. Bligaard, J. K. Nørskov, *Phys. Rev. Lett.* **99** (2007) 126101.

128 J. Greeley, M. Mavrikakis, *J. Phys. Chem. B* **109** (2005) 3460.

129 Atkins, P. W. *Physical Chemistry*, 6th ed., Oxford University Press: Oxford, U.K., 1998; pp 485, 925-927, 942.

130 D. Strmcnik , D. Tripković, D. van der Vliet, V. Stamenkovic, N.M. Markovic, *Electrochem. Comm.*, **10** (2008) 1602.

131 N. M. Markovic, P. N. Ross Jr., *Surf. Sci. Reports* **45** (2002) 117.

132 K. Kunimatsu, T. Senzaki, M. Tsushima, M. Osawa, *Chem. Phys. Lett.* **401** (2005) 451.

133 J. Barber, S. Morin, B. E. Conway, *J. Electroanal. Chem.* **446** (1998) 125.

134 M. C. Tavares, S. A. S. Machado, L. H. Mazo, *Electrochim. Acta* **46** (2001) 4359.

135 J. A. Santana, J. J. Mateo, Y. Ishikawa, *J. Phys. Chem. C* **114** (2010) 4995.

136 T. E. Shubina, M. T. M. Koper, *Electrochem. Commun*. **8** (2006) 703.

137 Y. Cai, A. B. Anderson, J. C. Angus, L. N. Kostadinov, *Electrochem. & Solid-State Lett.*, **8** (2005) E62.

138 J. X. Wang, T. E. Springer, R. R. Adzic, *J. Electrochem. Soc*. **153** (2006) A1732.

139 B. E. Conway, G. Jerkiewicz, *Electrochim. Acta* **45** (2000) *4075.*

140 J. K. Nørskov, T. Bligaard, A. Logadottir, S. Bahn, M. Bollinger, L. B. Hansen, H. Bengaard, B. Hammer, Z. Sljivancanin, M. Mavrikakis, Y. Xu, S. Dahl. C. J. H. Jacobsen, *J. Catal*. **209** (2002) 275.

141 V. Pallasana, M. Neurock, *J. Catal*. **191** (2000) 301.

142 Z. P. Liu. P. Hu, *J. Chem. Phys*. **114** (2001) 8244.

143 A. Logadottir, T. H. Rod, J. K. Nørskov, B. Hammer, S. Dahl, C. J. H. Jacobsen, *J. Catal*. **197** (2001) 229.

144 P. Ferrin, D. Simonetti, S. Kandoi, E. Kunkes, J. A. Dumesic, J. K. Nørskov, M. Mavrikakis, *J. Am. Chem. Soc.* **131** (2009) 5809.

145 N. Agmon, *Chem. Phys. Lett.* **244** (1995) 456.

146 J. P. Guthrie, *J. Am. Chem. Soc.* **118** (1996) 12886.

147 O. Pecina, W. Schmickler, *J. Chem. Phys.* **128** (1998) 265.

148 T. Dippel, K. Kreuer, *Solid State Ionics* **46** (1991) 3.

149 S. Walbran, A. Kornysheva, *J. Chem. Phys.* **114** (2001) 10039.

150 A. Kornyshev, A. Kuznetsov, E. Spohr, J. Ulstrup, *J. Phys. Chem. B* **107** (2003) 3351.

151 E. Pines, D. Huppert, *Chem. Phys. Lett.* **116** (1985) 295.

152 M. Maidique, A. von Hippel, W. Westphal, *J. Chem. Phys.* **54** (1971) 150.

153 S. Trasatti, *Pure & Appl. Chem.* **58** (1986) 955.

154 S.Trasatti, *Surf. Sci.* **335** (1995) 1.

155 S. Trasatti, E. Lust, Modern Aspect of Electrochemistry, Number 33, edited by Ralph E. White et al., Kluwer Academic/Plenum Publishers, New York, 1999.

156 S. Trasatti, *J. Electroanal. Chem.* **139** (1982) 1.

157 J. O'M Bochris, S. D. Argade, *J. Chem. Phys.* **49** (1968).

158 D. Tsiplakides, C. G. Vayenas, *J. Electrochem. Soc.* **148** (2001) E189.

159 R. Smoluchowski, *Phys. Rev.* **60** (1941) 661.

160 H. Ishii, K. Sugiyama, E. Ito, K. Seki, *Adv. Mat.* **11** (1999) 8.

161 S. Trasatti, *J. Electroanal. Chem.* **39** (1972) 163.

162 S. Trasatti, *J. Electroanal. Chem.* **33** (1971) 351

163 S. Trasatti, L. M. Doubova, *J. Chem. Soc. Faraday Trans.*, **91** (1995) 3311.

164 S. Trasatti, *Surf. Sci.* **335** (1995) 1.

165 J. E. B. Randles, *Trans. Faraday Soc.* **52** (1956) 1973

166 J. R. Farrell, P. McTigue, *J. Electroanal. Chem.* **139** *(1982) 37.*

167 R. Gomer, G. Tryson, *J. Them. Phys* **66** (1977) 4413.

168 W. N. Hansen, D. M. Kolb, *J. Electroanal. Chem.* **100** (1979) 493.

169 E. R. Kötz, H. Neff, K. Müller, *J. Electroanal. Chem.* **215** (1986) 331.

170 J. Schneider, d. Franke, D. M. Kolb, *Surf. Sci.* **198** (1988) 277.

171 W. N. Hansen, G. J. Hansen, *Phys. Rev. A* **36** (1987) 1396.

172 H. Reiss, A. Heller, *J. Phys. Chem.* **89** (1985) 4207.

173 M. D. Tissandier, K. A. Cowen, W. Y. Feng, E. Gundlach, M. H. Cohen, A. D. Earhart, J. V. Coe, *J. Phys. Chem. A* **102** (1998) 7787.

174 W. R. Fawcett, *Lanqmuir* **24** (2008) 9868.

175 A. A. Isse, A. Gennaro, J. Phys. Chem. B 114 (2010) 7894.

176 J. Rossmeisl, E. Skúlason, M. E. Björketun, V. Tripković, J. K. Nørskov, *Chem. Phys. Lett.* **466** (2008) 68.

177 C. Clay, S. Haq, A. Hodgson, *Phys. Rev. Lett.*, **92** (2004) 46102.

178 C. Clay, S. Haq, A. Hodgson, *Phys. Chem. Lett* **92** (2004) 136103.

179 C. Clay, L. Cummings, A. Hodgson, *Surf. Sci.* **601** (2007) 562.

180 F. T. Wagner, T. E. Moylan, *Surf. Sci.* **191** (1987) 121.

181 M. K. Debe, A. K. Schmoeckel, G. D. Vernstrom, R. Atanasoski, *J. Power Sources* **161** (2006) 1002.

182 G. S. Karlberg, G. Wahnström, *J. Chem. Phys.* **122** (2005) 194705.

183 G. S. Karlberg, T. F. Jaramillo, E. Skúlason, J. Rossmeisl, T. Bligaard, J. K. Nørskov, *Phys. Rev. Lett.* **99** (2007) 126101.

184 N. M. Markovic, H. A. Gasteiger, P. N. Ross, *J. Phys Chem.* **99** (1995) 3411.

185 J. X. Wang, N. M. Markovic, R. R. Adzic, *J. Phys Chem. B* **108** (2004) 4127.

186 J. Rossmeisl, G. S. Karlberg, T. Jaramillo, J. K. Nørskov, *Faraday Discussions* **140** (2008) 337.

187 M- Wakisaka, H. Suzuki, S. Mitsui, H. Uchida, M. Watanabe, *J. Phys. Chem C* **112** (2008) 2750.

188 K. Kinoshita, "Electrochemical Oxygen Technology", Wiley, New York, 1992

189 N. M. Markovic, H. A. Gasteiger, B. N. Grgur, P. N. Ross, *J. Electroanal. Chem.* **467** (1999) 157

190 V. Stamenkovic, N. M. Markovic, P. N. Ross Jr., *J. Electroanal. Chem.* **500** (2000) 44.

191 A. Damjanovic, D. B. Sepa, *Electrochim. Acta* **35** (1990) 1157

192 A. J. Appleby, *J. Electrochem. Soc.* **117** (1970) 328.

193 U. Nilekar, M. Mavrikakis, *Surf. Sci.* **602** (2008) 89.

194 M. J. Janik, C. D. Taylor, M. Neurock, *J. Electrochem. Soc.* **156** (2009) 126.

195 J. Rossmeisl, E. Skúlason, M. E. Björketun, V. Tripkovic, J. K. Nørskov, *Chem. Phys. Lett.* **466** (2008) 68.

196 A. Michaelides, P. Hu, *J. Am. Chem. Soc.* **123** (2001) 4235.

197 X.-Z. Li, M. I. J. Probert, A. Alavi, A. Michaelides, *Phys. Rev. Lett.* **104** (2010) 066102

198 F. Tian, R. Jinnouchi, A. B. Anderson, *J. Chem. Phys.* **113** (2009) 17484.

199 K. Y. Yeh, S. A. Wasileski, M. J. Janik, *Phys. Chem. Chem. Phys.* **11** (2009) 10108.

200 J. Greeley, J. K. Nørskov, *Electrochim. Acta* **52** (2007) 5829.

201 P. Strasser, S. Koh, J. Greeley, *Phys. Chem. Chem. Phys.* **10** (2008) 3670.

202 Y. Ma, P. B. Balbuena, *J. Phys. Chem. C* **112** (2008) 14520.

203 Z. Gu, P. B. Balbuena, *J. Phys. Chem. A* **110** (2006) 9783.

204 G. Koscher, K. Kordesch, *J. Power Sources* **136** (2004) 215.

205 M. J. Riezenman, *IEEE spectrum* **38** (2001) 55.

206 P. Sapkota, H. Kim, *J. Ind. & Eng. Chem.* **15** (2009) 445.

207 J. Goldstein, I. Brown, B. Koretz, *J. Power Sources* **80** (1999) 171.

208 Duracell Technical/OEM primary systems, http://www1.duracell.com/OEM/Primary/Zinc/zinc_air_tech.asp

209 J. Rossmeisl, Á. Logadóttir, J. K. Nørskov, *Chem. Phys.* **319** (2005) 178.

210 K. Kinoshita, "Electrochemical Oxygen Technology", John Wiley & Sons Inc., New York, 1992.

211 Y. Gorlin, T. Jaramillo, *to be published in J. Am. Chem. Soc.*

212 S. F. Bender, J. W. Cretzmeyer, T. F. Reise, "Handbook of Batteries", McGraw-Hill, Inc., New York, 1995, p. 13.1.

213 http://www.greencarcongress.com/2009/01/rwe-innogy-inve.html

214 http://www.zincenergystorage.org/battery.html

215 J. J. Mortensen, L. B. Hansen, K. W. Jacobsen, *Phys. Rev. B* **71** (2005) 035109.

216 U. Wedig, M. Jansen, B. Paulus, K. Rosciszewski, P Sony, *Phys Rev. B* **75** (2007) 215123.

217 CRC Handbook of Chemistry and Physics, 77th (Ed.), CRC Press, New York, 1996.

218 H. Jacobs, A. Niemann, W. Kockelmann, *Z. Anorg. und Allg. Chem.* **631** (2005) 1247.

219 M. Cai, S-M. Park, *J. Electrochem. Soc.* **143** (1996) 2125.

Included Papers

Paper I

Modeling the electrified solid-liquid interface

J. Rossmeisl, E. Skúlason, M. E. Björketun, V. Tripković, J. K. Nørskov

Chemical Physics Letters, **466** (2008) 68

Chemical Physics Letters 466 (2008) 68–71

Contents lists available at ScienceDirect

Chemical Physics Letters

journal homepage: www.elsevier.com/locate/cplett

Modeling the electrified solid–liquid interface

Jan Rossmeisl *, Egill Skúlason, Mårten E. Björketun, Vladimir Tripkovic, Jens K. Nørskov

Center for Atomic-scale Materials Design (CAMD), Department of Physics, Nano-DTU, Technical University of Denmark, Building 311, Kgs. Lyngby 2800, Denmark

ARTICLE INFO

Article history:
Received 7 August 2008
In final form 6 October 2008
Available online 15 October 2008

ABSTRACT

A detailed atomistic model based on density functional theory calculations is presented of the charged solid–electrolyte interface. Having protons solvated in a water bilayer outside a Pt(1 1 1) slab with excess electrons, we show how the interface capacitance is well described and how the work function can be related directly to the potential scale of the normal hydrogen electrode. We also show how finite-size effects in common periodic slab-type calculations can be avoided in calculations of activation energies and reaction energies for charge transfer reactions, where we use the Heyrovsky reaction for hydrogen oxidation over a Pt(1 1 1) electrode as an example.

An understanding of the structure and dynamics of the interface between a solid and an electrolyte is a prerequisite to a molecular-level understanding of many adsorption phenomena and of electrochemical processes. Modelling the solid–electrolyte interface is extremely demanding. One needs to describe the solid surface, the liquid, the ions solvated in the liquid and the charge-transfer taking place at the interface during electrochemical reaction. In addition one needs to be able to describe the effect of varying the electrical potential of the electrode. While models of the interface have been formulated for decades [1–5] the methods of density functional theory (DFT), which have been very important for the present understanding of the gas–solid interface, have only been applied recently [6–20] and still in a quite approximate way. In the present Letter we propose a method for calculating the energetics of interface reactions on the basis of standard DFT slab calculations and show that the method gives values for the interface capacitance in agreement with experiments and provide a measure of the vacuum potential relative to the normal hydrogen electrode (NHE).

Consider a metal electrode in contact with water with ions dissolved. Since the electrolyte is conducting the interface region must be charge neutral and the charge on the solid surface will be counteracted by an opposite charge built up by ions just outside the surface. This interface region, the Helmholtz layer, is often approximated by a ca. 3 Å thick electrical double layer [21]. The double layer has a strong electrical field, which is central to the properties of the interface. The strength of the field is given by the charge, which in turn is determined by the chemical potential of the electrons. The potential is measured relative to a counter electrode which is also immersed in the electrolyte. Because there is no electrical field in the electrolyte, the electrode and the counter electrode can be considered independent of each other and can be studied separately. However, with an electrochemical reaction running, the system is out of equilibrium. Locally at the interface charge is consumed or produced, which gives rise to a small field driving the charge to or from the interface.

Fig. 1 shows the main components of an atomistic model of a metal–electrolyte interface. It is possible to carry out DFT calculations for such a system using slab calculations to model the surface [19], but the calculations are hampered by the fact that for realistic electrode potentials the charge on the surface is small, often considerably less than one electron charge per 10 surface atoms. Unit cells with a large surface area are therefore needed. An even more severe problem is that if a charge transfer reaction takes place – say a proton is transferred to the surface – and the unit cell area is small, the potential changes significantly during the reaction. This finite-size effect can severely affect the results.

Recent developments have made important steps towards a method that can treat the electrified solid–liquid interface. Filhol and Neurock have performed calculations where they charge the surface by adding or subtracting electrons from the slab modelling the metal electrode [17]. This means that a homogenous background charge of the opposite sign is introduced implicitly to make the system neutral. The advantage of this method is that a fraction of an electron can be introduced, and the charge can be varied continuously. Large area unit cells can therefore be avoided. The drawback is that the counter-ions are now not in the water layer just outside the electrode surface but spread out everywhere in space. The field just outside the surface is, therefore, too small [22]. Otani and Sugino [18] and Sugino et al. [20] have introduced the possibility of charging the surface and placing the counter charge in a layer beyond the water, ca. 15–20 Å from the electrode. Again the charge can be varied continuously and due to the polarization of the water between the counter charge and the surface, most of the potential drop happens correctly just outside the surface. The drawback is that again the counter charge is placed far from the electrode and the polarization of the water may therefore not be entirely

* Corresponding author.
E-mail address: jross@fysik.dtu.dk (J. Rossmeisl).

0009-2614/$ - see front matter © 2008 Elsevier B.V. All rights reserved.
doi:10.1016/j.cplett.2008.10.024

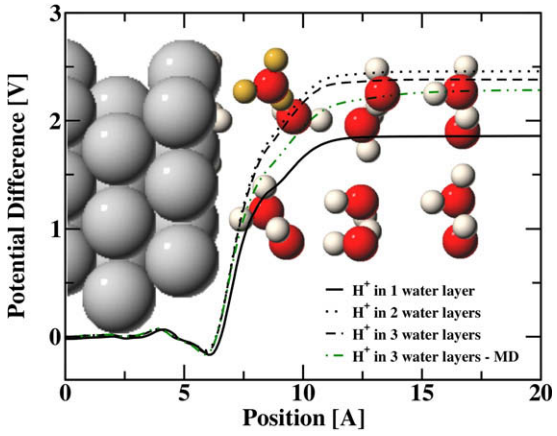

Fig. 1. A charged Pt(1 1 1) slab with 3 water layers outside and one solvated hydronium ion (yellow) per unit cell. The electrode potential, due to the charged interface, averaged parallel to the surface is shown for systems with 1, 2 and 3 relaxed water layers along with results from a DFT molecular dynamics simulation of a proton solvated in 3 water layers. The latter potential profile is an average over 30 frames, picked randomly along a 3 ps trajectory, obtained after equilibration of the system at room temperature.

correct. Jinnouchi and Anderson have recently developed a different approach not including the water molecules directly but distributing the counter charge in a continuum dielectric medium using a Poisson–Boltzmann method [23].

A problem with all models described until now is that it is difficult to assign a potential scale to the electrode. The work function of the slab defines the potential of the electrons (at the Fermi level) relative to vacuum. One therefore needs to relate this to e.g. the NHE which is defined thermodynamically as the potential where the reaction $H^+ + e^- \leftrightarrow 1/2H_2$ is in equilibrium at standard conditions (pH 0, $P_{H_2} = 1\text{bar}, T = 298\text{K}$). The value of the vacuum potential relative to NHE, ϕ, is not well determined, values from the literature ranging from $\phi = 4.44$ V to $\phi = 4.85$ V [24,25].

In the following we will consider the complete model including electrons and counter-ions depicted in Fig. 1. We will show that it provides a quite detailed picture of the solid–liquid interface for varying potential. We will identify a direct link between the thermodynamic definition of the NHE potential and the calculated work function so that an internal definition of the absolute potential scale can be obtained. Finally, we will show that by making not one but several calculations for varying unit cell size (but the same proton coverage or electrode potential) we can calculate reaction energies at given bias associated with charge transfer reaction without finite size errors.

We will consider a Pt(1 1 1) slab consisting of surface unit cells of varying size and periodic boundary conditions. Outside the surface we place a varying number of water layers as discussed in Refs. [26,27]. Roughly a monolayer of hydrogen atoms adsorbed on the surface is included (depending on the system, see Supplementary material), since Pt(1 1 1) at negative potentials will have a high coverage of hydrogen [19,28,29]. The two bottom layers of Pt are fixed in their bulk positions, all other ions are relaxed to their minimum energy structure. A varying number of additional hydrogen atoms are placed in the ice-like water layers. The electron density is non-constrained and the ground state density is determined adiabatically according to the positions of the ions. The charge of the additional hydrogen atoms in the water is found to spontaneously separate into protons solvated in the water and electrons in the metal slab. The two charged layers set up an electric field in the interface region. We perform DFT calculations using the RPBE-GGA functional [30]; see Ref. [19] for details.

The calculated variation in the electrostatic potential in the direction perpendicular to the metal surface is shown in Fig. 1 (see ESI). The figure also shows the dependence of the potential on the number of water layers included in the calculation. It can be seen that even a single layer describes the potential variation very well and it seems that it is completely converged after two layers. We also investigated the effect of thermal motion of the water molecules by performing DFT molecular dynamics simulations at room temperature. In Fig. 1 the average potential profile of 30 random frames of a 3 ps run after thermalization is shown to be very similar to the zero temperature profile. Qualitatively the potential profiles look similar to what comes out of classic double layer models such as the Stern and Grahame model [21]. In the following we report results for one water layer since that is computationally least demanding.

We will start by focusing on the energy of the solid/liquid interface as it is charged with protons and electrons. Let us consider a number of different area super cells with N surface metal atoms and n protons in the double layer. The total free energy or the integral free energy, G_{int}, per surface metal atom (or surface area) relative to H_2 is calculated as

$$G_{\text{int}} = (G(N,n) - G(N,0) - n\mu_{H_2}/2)/N. \quad (1)$$

G_{int} is a function of charge per surface area $\theta = n/N$ and not directly dependent on the area of the unit cell, N. μ_{H_2} is the chemical potential of hydrogen. First, we choose μ_{H_2} so that G_{int} has its minimum for the configuration with no protons in the water layer, where G_{int} is zero by definition. This corresponds to a potential scale of $U - U_{\text{pzc}}$, where U is the electrode potential calculated from the work function and U_{pzc} is the potential of zero charge (PZC). We note that in this study the Pt surface is covered with adsorbed hydrogen meaning that the PZC obtained here cannot be compared to experiments.

G_{int} corresponds to the free energy stored in the capacitor set up by the protons in the water layer and their counter charge in the metal, and it should therefore be quadratic in potential:

$$G_{\text{int}} = 1/2C(U - U_{\text{pzc}})^2 = 1/2e^2\theta^2/C, \quad (2)$$

where C is the capacitance and we use that by definition $e\theta = C(U - U_{\text{pzc}})$. In Fig. 2 we show data from the DFT calculations at varying unit cell sizes and varying charge, and the expected quadratic behavior is clearly observed. From the curvature we can determine the capacitance to be $C = 26.0\ \mu\text{F/cm}^2$. This is to be compared to the experimentally obtained capacitance for Pt(1 1 1) of $20\ \mu\text{F/cm}^2$ [31]. The good comparison to experiment gives further confidence concerning the structural model of the water/solid interface.

If we choose the chemical potential, μ_{H_2}, to equal the free energy of H_2 at standard conditions, the minimum of G_{int} moves to a new U-value, which defines the potential of the NHE. Applying the NHE reference implicitly assumes that the protons at the interface are in equilibrium with the protons in solution, this is discussed later in this Letter. We have calculated the free energy change from H_2 in the gas phase by using the standard entropy of hydrogen gas and changes in zero-point energies obtained from the calculated harmonic frequencies of the protons in the water layer. The configurational entropy of the protons in the water layer is neglected, since the protons are strongly repelling and will therefore always maximize their internal distance. The calculated G_{int} relative to standard H_2 is included in Fig. 2. The minimum shifts to -1.07 V relative to the PZC. This makes it possible to link the potential obtained from the work function to the thermochemical NHE without using experimental numbers for the vacuum potential level. We therefore have an internal measure of the vacuum level potential vs. NHE. We find that the work function for the non-

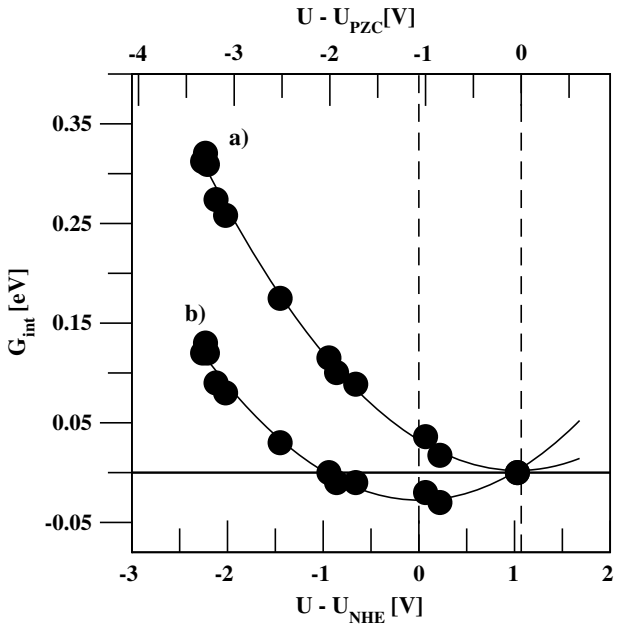

Fig. 2. The integral free energy stored in the double layer as a function of the electrode potential obtained via the work-function method. In (a) the chemical potential of hydrogen in Eq. (1) is chosen such that the minimum energy occurs at the potential of zero charge. Choosing the standard chemical potential of hydrogen gas (b) the minimum energy defines zero potential vs. NHE, which is 1.07 V lower than the potential of zero charge.

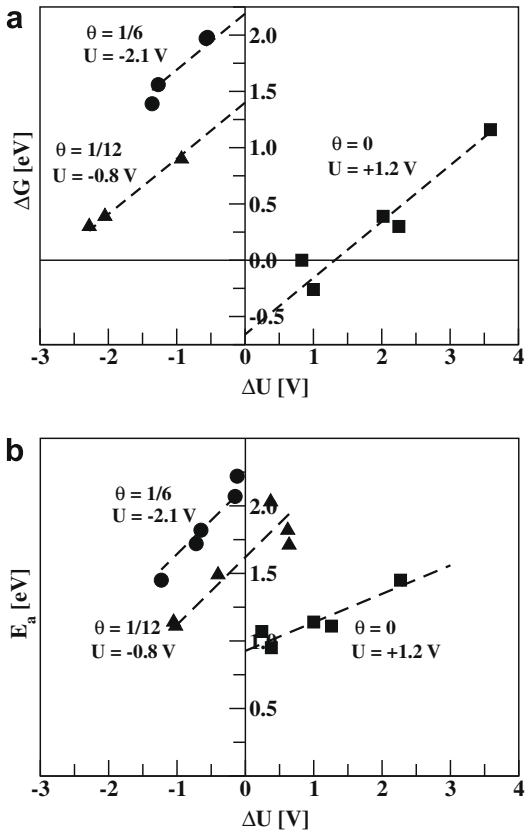

Fig. 3. (a) The reaction free energy of the Heyrovsky reaction: $H_2 \rightarrow H^+ + e^- + H^*$ as a function of the electrode potential change during the reaction, shown for different potentials. The extrapolation to $\Delta U = 0$ gives the free energy values at given potential (or proton coverage) in the limit when the potential does not change during the electron-transfer reaction. The slope of the extrapolation is fixed to the theoretical value of 1/2. (b) Same as (a) but for the energy of the transition state E_a. The slopes do not need being ½ as for the ΔG.

charged system is 6.24 eV, and the shift of 1.07 V compared to PZC, means that the vacuum level is 5.17 V vs. NHE. This is in reasonable proximity of the experimentally determined range 4.44–4.85 V. The result might of course change slightly as more water layers are included.

We now turn to the question of calculating reaction energies and activation energies for charge transfer reactions without finite size errors. To illustrate the approach we will consider a simple Heyrovsky type reaction where H_2 in the gas phase reacts with the Pt(1 1 1) electrode and forms a proton in the water bilayer just outside the surface, a H atom adsorbed on the surface and an electron is delivered to the metal:

$$H_2(g) + * \rightarrow H^+(bi) + e^- + H^* \quad (3)$$

This is a step in the hydrogen oxidation reaction (HOR), whose reverse is named hydrogen evolution reaction (HER). We would like to have the energy of the transition state (TS) and that of the final state (FS) relative to that of the initial state (IS) at a fixed potential, U. A straightforward calculation of the reaction energetics of the proton transfer reaction [19] will give activation barriers and reaction energies where the charge and hence the potential varies along the reaction path. The approach we will take in the following is to calculate the energies for several different unit cell sizes and show how to extrapolate the results to the limit of an infinite unit cell or, equivalently the limit where the change in potential, ΔU, during the reaction approaches zero.

We extrapolate to $\Delta U = 0$. In Fig. 3a the calculated reaction free energy, ΔG, is plotted as a function of ΔU for different values of the surface charge density, θ, or, equivalently potentials in the FS when $\Delta U < 0$ and IS when $\Delta U > 0$. The variation in ΔU is obtained by using different size unit cells, N, with a fixed ratio of charges, n, and unit cell size $n/N = \theta$. An approximately linear dependence is observed and we propose that by extrapolating the result to $\Delta U = 0$ we obtain a good approximation to the true value of the reaction free energy in an infinite unit cell.

When a charge, e, is transferred from one electrode to the other in a capacitor with potential, U, and surface area N, the charge density, θ, changes with, $\Delta\theta = n/N - (n-1)/N = 1/N$, and the potential changes by a proportional amount ΔU. The energy change is then (see Eqs. (1) and (2)):

$$\begin{aligned}\Delta G_{\text{capacitor}} &= N(G_{\text{int}}(N, n-1) - G_{\text{int}}(N, n)) \\ &= N(1/2e^2(\theta - 1/N)^2/C - 1/2e^2\theta^2/C) \\ &= -eU - 1/2e\Delta U \end{aligned} \quad (4)$$

The last term is a correction for the finite area effect of the charge that is removed. We would expect the change in capacitor energy to constitute the main part of the ΔU variation of the reaction free energy, ΔG, of reaction (3). Eq. (4) therefore suggests that the slope of $\Delta G(\Delta U)$ should be 1/2. This is exactly what we find in Fig. 3a. The lines are fitted to the calculated data using a slope of 1/2. The extrapolation scheme can therefore be used to determine the reaction energy for the Heyrovsky reaction (3). It is seen that for the small area unit cells (ΔU large) the finite size error is quite substantial, of the order eV. However, in the larger unit cells (small ΔU) the problem is much smaller.

The same approach can be used to estimate the TS energy of the Heyrovsky reaction (3). The calculations are again done in unit cells of varying surface area. The potential is changed as the proton is moved from the TS to the water layer (or similarly from the TS to H_2 molecule in the gas phase). In other words the calculations done with n protons in the water layer plus one proton in the TS are effectively done at θ between $(n+1)/N$ and n/N. This means that

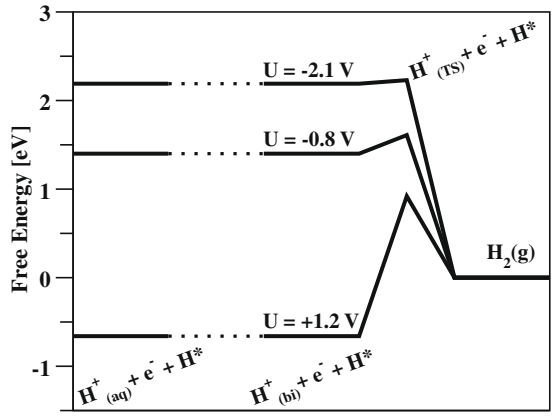

Fig. 4. The free energy diagram including the activation barriers of forming hydrogen molecules via the Heyrovsky mechanism at different potentials calculated in the limit where the potential is constant via the extrapolation scheme.

$\Delta U = 0$ can be approached from both the negative and the positive region. The activation energy, E_a, is shown at different electrode potentials in Fig. 3b.

For E_a we cannot determine the slope of the ΔU dependence *a priori*, since the charge of the H^+ in the transition state does not have to be the same as the charge of the proton solvated in the water layer. The slope at negative ΔU's is steeper than the one at positive ΔU's.

It is now possible to construct the energy diagram for the HER, reaction (3) reversed, at a constant potential. This is done in Fig. 4 at several different potentials. The reaction barrier is potential dependent. For negative potentials where the reaction is down-hill in terms of free energy there is only a small barrier for the reaction, but for positive potentials where hydrogen evolution is up-hill in free energy there is a barrier in addition to the reaction energy. We note that all reactions are done here for a slightly more than a full monolayer of adsorbed hydrogen (1.04–1.17 ML). For the most positive potential the coverage of hydrogen will be smaller, and that may change the barrier. The main purpose of the present results is just to illustrate the applicability of the method.

In Fig. 4 we have included the free energy of the proton solvated far from the electrode surface and the electron in the metal slab. The chemical potential of the proton solvated in water is just:

$$\mu(H^+(aq), e^-) = kT \ln(a(H^+)) - eU \quad (5)$$

where the first term is zero at pH 0. This is exactly the same as the free energy of the proton in the water bilayer, Eq. (4). This just expresses that we have implicitly assumed equilibrium between protons in solution and protons in the water bilayer. Or i.e. assuming that the electrode potential is the same in the first bilayer as in the bulk solution, justified by Fig. 1, the free energy of a proton in the water bilayer outside the electrode (coming from our DFT calculations) is the same as the free energy of a proton solvated far from the electrode (using Eq. (5) where the U is coming from the work function in our DFT calculations). We have not included barriers for proton transfer in the water but that has been calculated to be very low or 0.1–0.2 eV [32–34].

In conclusion, we have constructed a realistic atomic model for the solid–liquid interface at electrode surfaces. In addition we have suggested a method for calculating reaction energies associated with charge transfer reactions at the solid–liquid interfaces where finite size effects do not matter. The calculations require several calculations for different unit cell sizes in order to extrapolate to the limit of an infinite surface unit cell, and it is therefore considerably more cumbersome than ordinary calculations for surface reactions. It does, however, open up the possibility of detailed, realistic calculations of electrochemical reaction energetics.

Acknowledgments

CAMD is funded by the Lundbeck foundation. This work was supported by the Danish Center for Scientific Computing through grant no. HDW-1103-06 and by the EU through the FC-Anode network, STREP no. NMP-2007-032175.

Appendix A. Supplementary material

Supplementary data associated with this article can be found, in the online version, at doi:10.1016/j.cplett.2008.10.024.

References

[1] H.L.F. von Helmholtz, Ann. Phys. 89 (1853) 211.
[2] G. Gouy, Compt. Rend. 149 (1910) 654.
[3] D.L. Chapman, Philos. Mag. 25 (1913) 475.
[4] O. Stern, Z. Electrochem. 30 (1924) 508.
[5] D.C. Grahame, Chem. Rev. 41 (1947) 441.
[6] A.B. Anderson, T.V. Albu, J. Am. Chem. Soc. 121 (1999) 11855.
[7] A.B. Anderson, T.V. Albu, J. Electrochem. Soc. 147 (2000) 4229.
[8] J. Greeley, M. Mavrikakis, J. Am. Chem. Soc. 126 (2004) 3910.
[9] J.K. Nørskov, J. Rossmeisl, A. Logadottir, L. Lindqvist, J.R. Kitchin, T. Bligaard, H. Jónsson, J. Phys. Chem. B 108 (2004) 17886.
[10] J. Rossmeisl, J.K. Nørskov, C.D. Taylor, M.J. Janik, M. Neurock, J. Phys. Chem. B 110 (2006) 21833–21839.
[11] J.K. Nørskov, T. Bligaard, A. Logadottir, J.R. Kitchin, J.G. Chen, S. Pandelov, U. Stimming, J. Electrochem. Soc. 152 (2005) J23.
[12] G.S. Karlberg, Phys. Rev. B 74 (2006) 153414.
[13] T.E. Shubina, M.T.M. Koper, Electrochem. Commun. 8 (2006) 703.
[14] P. Vassilev, R.A. van Santen, M.T.M. Koper, J. Chem. Phys. 122 (2005) 054701.
[15] A. Roudgar, A. Gross, Chem. Phys. Lett. 409 (2005) 157.
[16] Y. Okamoto, O. Sugino, Y. Mochizuki, T. Ikeshoji, Y. Morikawa, Chem. Phys. Lett. 377 (2003) 236.
[17] J.S. Filhol, M. Neurock, Angew. Chem. Int. Ed. 45 (2006) 402.
[18] M. Otani, O. Sugino, Phys. Rev. B 73 (2006) 115407.
[19] E. Skúlason, G.S. Karlberg, J. Rossmeisl, T. Bligaard, J. Greeley, H. Jónsson, J.K. Nørskov, Phys. Chem. Chem. Phys. 9 (2007) 3241.
[20] O. Sugino, I. Hamada, M. Otani, Y. Morikawa, T. Ikeshoji, Y. Okamoto, Surf. Sci. 601 (2007) 5237.
[21] E. Gileadi, E. Kirowa-Eisner, J. Penciner, Interfacial Electrochemistry – An Experimental Approach, Addison-Wesley Publishing Company Inc., Massachusetts US, 1975 (Chapter 1).
[22] C.D. Taylor, S.A. Wasileski, J.-S. Filhol, M. Neurock, Phys. Rev. B 73 (2006) 165402.
[23] R. Jinnouchi, A.B. Anderson, J. Phys. Chem. C 112 (2008) 8747–8750.
[24] J.E.B. Randles, Trans. Faraday Soc. 52 (1956) 1573.
[25] E.R. Kötz, H. Neff, K. Müller, J. Electroanal. Chem. 215 (1986) 331.
[26] H. Ogasawara, B. Brena, D. Nordlund, M. Nyberg, A. Pelmenschikov, L.G.M. Pettersson, A. Nilsson, Phys. Rev. Lett. 89 (2002) 276102.
[27] A. Michaelides, P. Hu, J. Am. Chem. Soc. 123 (2001) 4235.
[28] G.S. Karlberg, T. Jaramillo, E. Skúlason, J. Rossmeisl, T. Bligaard, J.K. Nørskov, Phys. Rev. Lett. 99 (2007) 126101.
[29] N.M. Markovic, B.N. Grgur, P.N. Ross, J. Phys. Chem. B 101 (1997) 5405.
[30] B. Hammer, L.B. Hansen, J.K. Nørskov, Phys. Rev. B 59 (1999) 7413.
[31] T. Pajkossy, D.M. Kolb, Electrochim. Acta 46 (2001) 3063.
[32] N. Agmon, Chem. Phys. Lett. 244 (1995) 456.
[33] J.P. Guthrie, J. Am. Chem. Soc. 118 (1996) 12886.
[34] O. Pecina, W. Schmickler, Chem. Phys. 128 (1998) 265.

Paper II

Modeling the electrochemical hydrogen oxidation and evolution reactions on the basis of density functional theory calculations

E. Skúlason, V. Tripković, M. E. Björketun, S. Guðmundsdóttir, G. Karlberg, J. Rossmeisl, T. Bligaard, H. Jónsson, J. K. Nørskov

The Journal of Physical Chemistry C

Modeling the electrochemical hydrogen oxidation and evolution reactions on the basis of density functional theory calculations

Egill Skúlason[1,2], Vladimir Tripkovic[1], Mårten E. Björketun[1], Sigríður Guðmundsdóttir[2], Gustav Karlberg[1], Jan Rossmeisl[1], Thomas Bligaard[1], Hannes Jónsson[3], Jens K. Nørskov[1]

[1]*Center for Atomic-scale Materials Design, Department of Physics, Building 311, Technical University of Denmark, DK-2800 Lyngby, Denmark*
[2]*Science Institute, VR-III, University of Iceland, IS-107 Reykjavik, Iceland*
[3]*Faculty of Science, VR-III, University of Iceland, IS-107 Reykjavik, Iceland*

Density functional theory calculations have been performed for the three elementary steps – Tafel, Heyrovsky and Volmer - involved in the hydrogen oxidation reaction (HOR) and its reverse, the hydrogen evolution reaction (HER). For the Pt(111) surface a detailed model consisting of a negatively charged Pt(111) slab and solvated protons in up to three water bilayers is considered and reaction energies and activation barriers are determined using a newly developed computational scheme where the potential can be kept constant during a charge transfer reaction. We determine the rate limiting reaction on Pt(111) to be Tafel-Volmer for HOR and Volmer-Tafel for HER. Calculated rates agree well with experimental data. Both the H adsorption energy and the energy barrier for the Tafel reaction is then calculated for a range of metal electrodes, including Au, Ag, Cu, Pt, Pd, Ni, Ir, Rh, Co, Ru, Re, W, Mo, Nb, different facets and step of surfaces. We compare the results for different facets of the Pt electrode to experimental data. Our results suggest that the most important parameter for describing the HOR or the HER activity of an electrode is its binding free energy of H. We present a detailed kinetic model based entirely on the DFT reactions and show that the exchange current follows a volcano curve when plotted against the H adsorption free energy in excellent agreement with experimental data.

1. Introduction

Any hydrogen-based energy conversion scenario relies on effective and cheap catalysts for oxidation and reduction of hydrogen [1]. Platinum-based catalysts are effective and stable for both hydrogen oxidation reaction (HOR) and hydrogen evolution reaction (HER) under acidic conditions as it is found in a polymer electrolyte fuel cell or electrolyzer. However, since Pt is rare and expensive there is a need for the development of electrodes made of cheaper materials. In order to be able to design new electrodes for the hydrogen evolution or oxidation reactions, it may well proof essential to acquire insight into their mechanism at the atomic level [2, 3, 4, 5, 6, 7].

It is generally accepted that the overall HOR/HER reaction $H_2 \leftrightarrow 2(H^+ + e^-)$, taking place at an electrode in contact with an electrolyte, involves three elementary reactions. In the first step, H_2 is dissociated and H adsorbed. This is accomplished either by the Tafel reaction H_2 -> 2H* (H* denotes hydrogen adsorbed on the surface) or by the Heyrovsky reaction H_2 -> $H^* + H^+ + e^-$. The adsorbed H is then discharged, following the Volmer route H* -> $H^+ + e^-$. Despite intensive research efforts it is still unclear which of the two

pathways, Tafel-Volmer or Heyrovsky-Volmer, dominates under different conditions even on the most studied electrode material, Pt. The Volmer reaction is usually considered fast [3] but the literature contains conflicting reports about the other two reactions. From some experimental studies it has been inferred that the Tafel reaction is the predominant mechanism and rate limiting step on Pt(110) [2] and different facets of Pt [4, 5, 6]. This was recently supported by first principles calculations at the Pt(110)/water interface [8]. At the same time, other investigations report the Heyrovsky reaction to be the rate determining step; both on Pt(100) [2] and on polycrystalline Pt [7]. In simulations a similar conclusion has been obtained for a single Pt atom [9] and on a diamond electrode [10]. The picture is equally confusing on the Pt(111) electrode surface [2, 11]. The current view appears to be that different metal facets open up different reaction mechanisms for HOR and HER. Other studies, based on modeling the kinetics of HOR on Pt electrodes over the entire relevant potential region, conclude that the Volmer-Tafel pathway is dominating at low overpotentials whereas the Volmer-Heyrovsky route becomes important at high overpotentials [12].

Most experimental insight about the mechanism has been inferred from rate measurements. Such a procedure will typically not provide conclusive evidence for a mechanism, since the measured rate depends on several elementary steps. Quantum chemical calculations can serve as a valuable complement. The calculations can be used to model electrochemical systems and have the potential to provide unique molecular-level information about processes at the interface. However, due to the complex environment it has only recently been possible to model electrochemical systems using first-principles methods [8, 9, 10, 11, 13, 14, 15, 16, 17, 18, 19, 20, 21, 22].

Recently we introduced a general density functional theory (DFT) based model of the electrochemical half-cell that captures many of the features of the electrical double layer [11]. The atomic setup consists of a metal slab, hydrogen atoms (or other atomic species if required) adsorbed on the metal surface, and an electrolyte represented by water layers outside the surface. The electrical double layer is formed by adding extra hydrogen atoms to the water layer. The hydrogen atom spontaneously separates into a proton becoming solvated in the water and an electron ending up at the surface of the metal slab. We can vary the surface charge, and hence the potential, by changing the concentration of protons (hydronium ions) in the electrolyte. This is completely analogous to the experimental situation where the electrochemical double layer is set up by an equal number of electrons and counter-ions. It avoids the introduction of artificial counter-charge smeared out all over space [18] or located far from the surface [19]. The down-side of our approach is that we need to treat large surface unit cells in order to vary the charge or potential semi-continuously.

A further challenge arises when studying chemical reactions involving charge transfer, as is the case for the Heyrovsky and Volmer reactions. In a real system, where the area of the interface can be considered infinite on an atomic scale, the electrode potential will stay fixed during single charge transfer reactions. However, since the simulation unit cells used in the calculations are relatively small, the charge, and hence the potential, will vary considerably along the reaction path. Sometimes this introduces large errors in the

calculated reaction energies and activation barriers. To avoid this artifact, we recently devised a scheme that enables calculation of activation and reaction energies in the limit where the bias is constant during the reaction [21]. Since this scheme has been employed throughout this work a short review of the main ideas behind it will be given below.

In the present work, we study the HOR and HER in detail by means of first-principles DFT. Since the Pt(111) electrode is the most studied electrode for HOR and HER we first apply our detailed solid-liquid interface model to study the elementary steps over Pt(111). We conclude the Tafel reaction to be the rate limiting reaction step, and a detailed analysis of the kinetics is carried out for that reaction. We study the structure-dependence of the reaction by comparing the calculated rate over Pt(111) to those of Pt(100) and Pt(110). We then determine the H adsorption energy at varying H coverage on various electrode materials, including different transition metals and various surface structures. Finally, we use the energy profiles as input to a kinetic model of the HOR/HER current. This enables direct comparison with experimental data.

2. Method

2.1 Calculation details

The electronic structure calculations have been carried out using self-consistent DFT in a plane-wave pseudopotential implementation, with 26 Ry (354 eV) cutoff for both the plane waves and the densities [23, 24, 25]. Most calculations were performed with the DACAPO code using the RPBE exchange-correlation functional [26,27]. However, the Pt(100) and the Pt(110) surfaces were treated using the VASP code [28, 29] and the revPBE functional. A few test calculations were performed to compare the two xc-functionals and the reaction energy differences were less than 0.07 eV in all cases. All activation barriers have been calculated with the nudged elastic band (NEB) method [30, 31].

In order to model the proton/electron transfer reactions - Volmer and Heyrovsky reactions - we have used the double layer model described in more detail below. In order to keep the potential constant during charge transfer we apply an extrapolation scheme [21], which is also explained in some detail later in this Section. Since these barrier calculations are quite time-consuming, we have only performed the full extrapolation scheme on Pt(111) for the Volmer and Heyrovsky reactions. We have also performed such calculations of both the reactions over Ru(0001), Pd(111) and Au(111) for a few different potentials and in general they agree well with the Pt calculations. In all these barrier calculations the slabs have been modeled with 3 metal layers, but the surface dimensions have been varied: (3x2), (3x4), (6x2), (6x3), (6x4), and (6x8) repeated unit cells have been employed, with (4x6), (4x3), (2x6), (2x4), (2x3), and (2x1) k-point sampling, respectively. The two bottom layers of the slabs were fixed at the respective RPBE lattice constants, while the remaining atoms were allowed to adjust until the magnitude of all residual forces was less than 0.01 eV/Å.

For the Tafel reaction and H adsorption it has been shown that the reaction energies and activation energies are almost unaffected by water, electric potentials and electric fields

[11, 32]. This is not surprising since there is no electron transfer to and from the electrode during this reaction ($2H^* \rightarrow H_2$) and the dipole of the adsorbed H is small in the direction perpendicular to the surface. Hence these effects can be neglected and only a surface slab and adsorbed hydrogen have to be included in the atomic model. This makes the problem computationally much less demanding. We can thus afford calculating the Tafel reaction and H adsorption energies as a function of H coverage for a large set of close-packed FCC, HCP and BCC surfaces and also for other facets and steps. In these calculations the close-packed surfaces are modeled with three layers where the two bottom layers are kept fixed while the top layer is allowed to relax with the adsorbed hydrogens. Pt(100) is modeled using four layers, where the two bottom layers are fixed while the two top layers are relaxed with the hydrogens. The close-packed surfaces are typically modeled with (2x2) unit cells and (4x4) k-points but in a few cases we have increased the unit cells to (3x2), (4x4) and (6x4) in order to represent coverages close to an important discontinuity in the adsorption energy, appearing at 1ML H coverage. This point will be clarified later. The (211) steps have three close-packed layers underneath the step and a (2x3) unit cell with (4x4) k-point sampling. The Pt(110) surface is modeled with 8 Pt layers in total with a (3x4) unit cell and (4x4) k-point sampling.

2.2 Model of the electrochemical double layer

A typical set-up of the calculation is illustrated in Fig. 1. When adding an additional H atom into the first water layer, the electron from this H atom spontaneously enters the metal slab and a solvated hydronium ion (H_3O^+) is formed. In Fig. 1 the charge iso-surfaces are plotted when having a solvated proton in the first water bi-layer out of three water bi-layers in total. The iso-surfaces are constructed by calculating the charge density differences of the whole system ($\rho_{Pt + e^- + water + H^+}(\mathbf{r})$) and two uncharged reference systems, when having the Pt slab and neutral water above it in one supercell ($\rho_{Pt + water}(\mathbf{r})$) and the additional H atom in another cell ($\rho_H(\mathbf{r})$):

$$\rho_{difference}(\mathbf{r}) = \rho_{Pt + e^- + water + H^+}(\mathbf{r}) - \rho_{Pt + water}(\mathbf{r}) - \rho_H(\mathbf{r}) \qquad (1)$$

Fig. 1 shows that the positive charge is localized in the first water bi-layer and does not spread out to the water above. In other words, the positive charge is solvated in a two-dimensional plane at the solid-liquid interface. This indicates that we can solvate the proton by only using one water bi-layer above the slab.

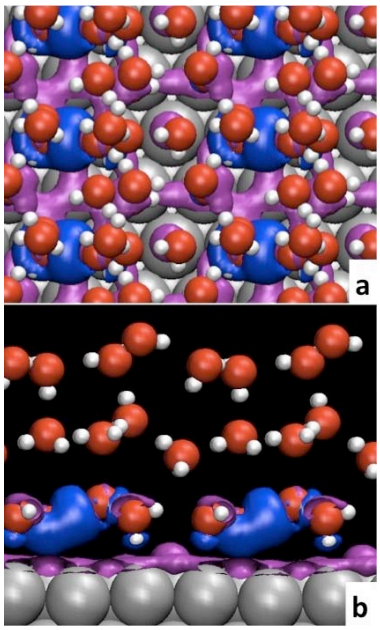

Fig 1: *a) Top view and b) side view of a solvated proton in 3 water layers ontop of a Pt(111) electrode. The blue iso-surfaces (iso-value: -0.0018 e bohr^{-3}) are regions of positive charge around the proton solvated in the water. The purple iso-surface (iso-value: +0.0012 e bohr^{-3}) on the Pt surface are regions of negative charge at the electrode surface. In this case the proton concentration is very high (1 proton per 6 surface atoms).*

In Fig. 2 the charge iso-surfaces are plotted at several proton concentrations/electrode potentials. Here, we use a single water bi-layer above a Pt(111) slab. The positive (blue) charge is quite localized around the H_3O^+ complex but some positive charge is associated with the three water molecules in the solvation cell. The solvation shell is in-between the Zundel structure [33, 34] where the proton is shared between two water molecules forming an $H_5O_2^+$ complex, and the Eigen structure [35, 36] where the hydronium ion is hydrogen bonded to three water molecules, forming an $H_9O_4^+$ complex. Here the solvation structure is two-dimensional in the vicinity of the surface, whereas the solvation shells are three-dimensional in bulk water [37].

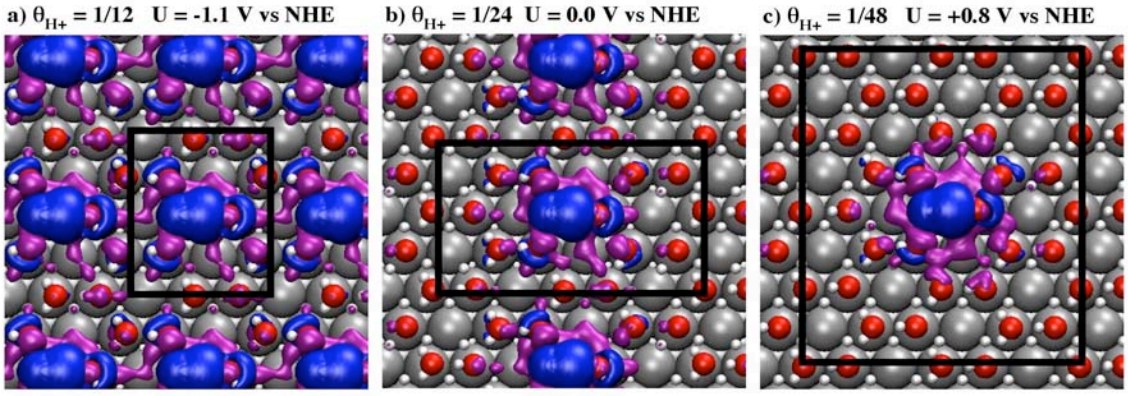

Fig 2: *Solvated protons in a water bi-layer ontop of Pt(111) slab. The blue iso-surfaces are positive charge of the proton and the purple iso-surfaces are negative charge on the*

surface. The figures show different proton concentrations θ_{H+} in the unit cells, i.e. the unit cells are enlarged but in each case there is 1 proton per unit cell; a) 1 proton per 12 Pt surface atoms, b) 1 proton per 24 surface atoms and c) 1 proton per 48 surface atoms. The iso-values are -0.0005 e bohr^{-3} in all cases for the positive charge. For the negative charge the iso-values are +0.0008, +0.0005 and +0.0003 e bohr^{-3} for the 1/12, 1/24 and 1/48 proton concentrations, respectively.

We note that the negative charge (purple) of the additional electrons on the surface are rather localized underneath the proton involving of the order 6-9 Pt atoms. This suggests that models that describe the double-layer as homogeneous along the surface may not include all relevant electrostatic effects in the calculation. There are, however, a number of situations where such effects are of minor importance.

Each proton concentration corresponds to a certain electrode potential (U) versus the normal hydrogen electrode (NHE). The U values are varying here from negative to positive values. The link to an absolute U scale will be discussed in the following.

In Ref [21] we introduced a direct link between the thermodynamic definition of the NHE electrode and the calculated work function (WF). Hence, we have an internal definition of the absolute potential scale for the solid/liquid interface as it is charged with protons and electrons. The total free energy or the integral free energy, G_{int}, is calculated per surface metal atom (or surface area) relative to H_2 in the gas phase:

$$G_{int}=(G(N,n)-G(N,0)-n\mu_{H2}/2)/N \qquad (2)$$

where N is the number of surface metal atoms in the surface unit cell and n is the number of protons in the double layer (per super cell). In Fig. 3 we have calculated the integral free energy of the charged double layer including 1, 2 and 3 water bi-layers, see the atomistic structures in (a), (b), and (c) of Fig. 3, respectively. The variation in the WF (U scale) comes from variations of the proton/electron concentration. The reference WF values we need to shift the parabolic functions in order to have the minimum in free energy at U = 0 V vs. NHE are very similar for the different water layer systems or; 5.28 V for 1 and 3 water layers and 5.13 for the 2 water layers. The experimental value of the WF of the NHE compared to vacuum is usually measured to be 4.44 ± 0.02 V [38] while value of 4.85 V has also been reported [39].

It should be noted that when considering more than one water bi-layer we have altered the orientations of the water molecules in the second and third layers in order to avoid building up net dipoles from the water network. The first water bi-layer has an H-down structure in systems (a), (b) and (c) in Fig. 3 where structures (b) and (c) have no net dipoles in the remaining layers. System (d) has an H-up structure of the first water bi-layer but that system will be discussed at a later point in this Section. Since we are using an atomistic model of the water at the interface, the reference value in our internal measure cannot be compared directly with the experimental value, obtained at real conditions and at room temperature. In reality the water structure will be thermally distorted and not having every other water molecule of the first water layer pointing the

O-H bond toward the surface as structures (a), (b), and (c) in Fig. 3.

Schnur and Groß have recently studied the metal-water interface with *ab initio* molecular dynamic simulations at room temperature [40]. There it is shown explicitly that the first water layer is neither purely a H-down structure nor a H-up structure, but a mixture of them both. The WF of the thermalized metal-water interface is also found to be somewhere in between the WF of the H-down and the H-up structures.

We calculate the WF of a Pt(111) slab having one water layer to be 6.7 V for the water-down structure while it is 4.1 V with the water-up structure. This 2.6 V difference between the two water structures on Pt(111) is to be compared with a value of around 2.2 V difference for the same systems in the calculations by Schnur and Groß [40]. Similar differences in WF are found for these two water layer models for all other metals considered in that study.

The WF's time evolution is reported only for the Ru(0001)-water system [40]. At time zero, the difference in WF between H-up and H-down is around 2.5 V. After 6 ps simulation time the WF of these two systems have reached the same value, which is around 30% from the H-down WF value and 70% from the H-up value. That means that at room temperature, the neutral water layer and its WF is somewhere in between the H-down and the H-up structure, where presumable more water dipoles are pointing towards the surface than from it. It should be noted that there is only a single water layer included in the study by Schnur and Groß and these results could change when more water layers are included.

If we would use the water-up structure throughout this investigation, our internal measure of the reference WF would be approximately 2.7 V instead of approximately 5.3 V for the water-down structures. In reality we might have some water pointing up and others pointing down, as suggested by Schnur and Groß [40]. By assuming the same 30/70% difference from the H-down/H-up WFs on the Pt(111) surface as found on the Ru(0001) surface due to thermalization [40] the reference WF value would be 4.5 V, in close agreement with the experimental value of 4.44 V.

There seems to exist many different water structures which all are very close in energy [41]. Since all energies of interest in the following are energy differences, they are not sensitive to the exact model of the water as long as we are consistently using the same model in calculating the energy differences and as long as we choose a reasonable model in a local minimum structure. A strength of the approach is that we have an internal reference point defining the zero of the potential for the exact structure we are using.

More work is needed to address the question of water structures further but that may have to await exchange-correlation functionals that can confidently determine van der Waals interactions. In the meanwhile we note that the curvature of the parabolas can be used to determine the capacitance of the double layer in excellent agreement with experiment. We get $C = 22.7\ \mu F/cm^2$ for 1 water layer, $C = 23.6\ \mu F/cm^2$ for 2 water layers and $C = 24.5\ \mu F/cm^2$ for 3 water layers, while the experimentally measured value is C = 20

$\mu F/cm^2$ on Pt(111) [42]. This good comparison to experiments and the small difference in modeling the system with 1, 2 or 3 water layers provides confidence in the present description and indicates that a single water bi-layer is sufficient to describe the interface. We use this observation when analyzing the Volmer and the Heyrovsky reactions in the rest of the study.

In Fig. 3 we have included the integral free energy of systems having H-up configuration of the first water bi-layer whereas the second water bi-layer has a H-down structure. The atomistic structure is shown in (d) of Fig. 3. This model system is unrealistic in the sense that the first bi-layer has an H-up structure while at the same time the surface is negatively charged. It is an extreme case and will be included later on in next Sections to show that the energy differences that we calculate throughout this study are not sensitive to our chose of water models.

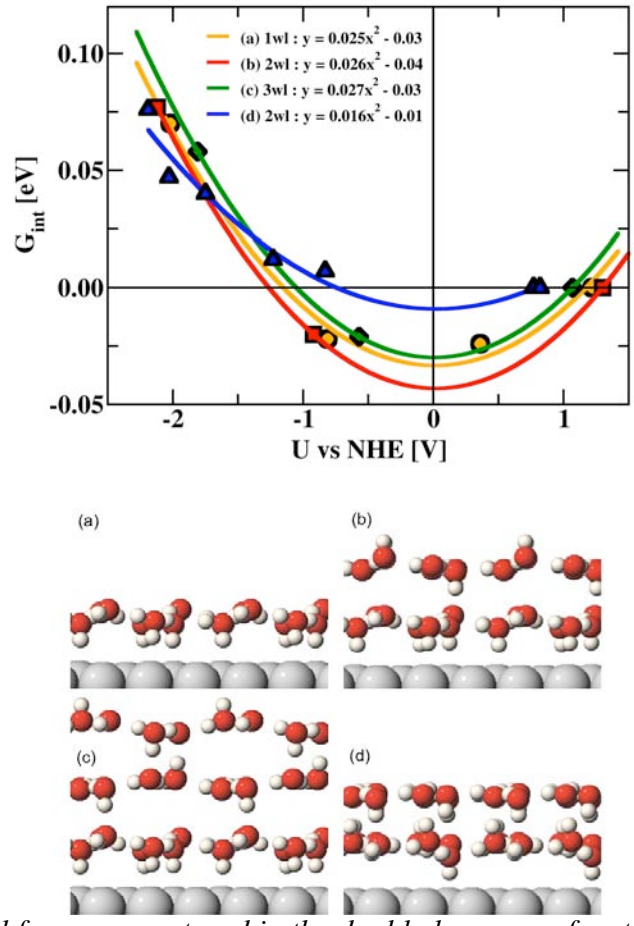

Fig 3: *The integral free energy stored in the double layer as a function of the electrode potential when having (a) 1, (b) 2 and (c) 3 water layers with a H-down configuration of the first water bi-layer and (d) 2 water layers with a H-up configuration of the first water bi-layer on a Pt(111) electrode.*

2.3 Extrapolation scheme

In the model presented above, where the ions are explicitly localized in the Helmholtz layer, a problem arises when these ions react with electrons from the surface. Since we have periodic boundary conditions and are limited to using finite size unit cells, performing one proton-electron transfer reaction in a unit cell corresponds to a simultaneous transfer in each unit cell. Since the ions set up the potential and the field, performing such a reaction changes the potential of the electrode along the reaction path. That can affect the energetics considerably. This problem is most severe for the smallest unit cells we consider here in which the bias can change by up to 3.5 V for the Heyrovsky reaction.

The approach we take to circumvent this problem is referred to as "the extrapolation scheme" and has been explained in detail elsewhere [21]. When calculating reaction energies and activation energies for a charge transfer reaction such as the Heyrovsky or the Volmer reactions, we calculate the energies for several different unit cell sizes. We extrapolate the results to the limit of an infinitely large unit cell or equivalently to the limit where the change in potential, ΔU, during the reaction approaches zero. That mimics the situation in a real electrochemical system. This is explained in detail below.

The Heyrovsky reaction for the HOR direction is shown as an example, but the approach can be used for any kind of charge transfer surface reaction. We extrapolate to $\Delta U = 0$, where ΔU is the difference of the initial state's (IS) and final state's (FS) work functions (WF). The variation in ΔU is obtained by using unit cells of different sizes, N, with a number of charges, n, determined so that the surface concentration of charge, $\theta = n/N$ is fixed.

In Fig. 4a the calculated reaction energy, $\Delta E = E_{FS} - E_{IS}$, for HOR is plotted as a function of ΔU for different values of the surface charge density, θ, or equivalently potentials in the FS when $\Delta U < 0$ and IS when $\Delta U > 0$. The differences in energies are always presented for the same reaction direction, here for the HOR direction. The differences in WF are calculated with respect to the state we are extrapolating to. Take for example the data set for $\theta = 1/6$ (filled squares) where both of the FSs are the same, having 2 protons in a (6x2) cell and 4 protons in a (6x4) cell. The IS (having H_2 in gas phase) do, however, not have the same proton concentration, 1/12 and 3/24, respectively. In this case we calculate $\Delta U = WF_{FS} - WF_{IS}$, since both systems have the same FS proton concentration, 1/6. If we now extrapolate these data points to $\Delta U = 0$ we are in fact extrapolating to the FS proton concentration. This limit describes the situation where the IS and FS would have the same proton concentration.

If we now take exactly the opposite example, where we extrapolate to $\theta = 0$ (open triangles), where all the IS have no protons in the water bilayer. The FS for the HOR direction, all have 1 proton in (6x4), (3x4) and (3x2) unit cells. This difference in concentration results in the change in WFs. In this case, since we are extrapolating to $\theta = 0$ of the IS, ΔU is calculated as $WF_{IS} - WF_{FS}$.

As can be seen, we always subtract the WF of the states that are not having the same proton concentration from the WF of the states that have the same proton concentration. For the reaction energy versus ΔU this only results in a sign change of ΔU. We will, however, see that this formalism is important to use in the right way when doing extrapolations for the activation energies since the difference between the WF of the TS is not the same if we calculate it relative to the WF_{IS} or the WF_{FS}, since the WF_{TS} is not necessarily exactly in the middle between the WF of the IS and FS.

When plotting the reaction energy as a function of the difference in potential as explained above an approximately linear dependence is observed and we propose that by extrapolating the result to $\Delta U = 0$ we obtain a good approximation to the true value of the reaction energy in an infinite unit cell. The slope of this line should be 1/2, since we are transferring one charge in a capacitor [21]. This is exactly what we find in Fig. 4a. The lines are fitted to the calculated data using a slope of 1/2.

The same approach can be used to estimate the activation energy of HOR via the Heyrovsky reaction, see Fig. 4b. The calculations are again done in unit cells of varying surface area. The activation energy is obtained via the NEB method and is always calculated for the HOR direction in this example, $E_a = E_{TS} - E_{IS}$ where E is the total energy. The differences in potentials, ΔU, are calculated in a similar way as for the reaction energy, where we take the WF of the state we are extrapolating to and we subtract the WF of the TS from that. In the case of $\theta = 1/6$ we subtract the WF of the TS from the WF of the FS; $\Delta U = WF_{FS} - WF_{TS}$, where the FS have $\theta = 1/6$.

As before, a similar procedure is used when extrapolating to $\theta = 0$ where all the IS have no protons in the water bilayer. ΔU is now $WF_{IS} - WF_{TS}$. In Fig. 4b we have also in some cases interpolated from both negative and positive regions, where we have used a mixture of the two ΔUs explained above. In this case we always interpolate to the same proton concentration, where in some cases it is in the IS whereas in others in the FS. The data points are now both on the left side and the right side of $\Delta U = 0$, and we draw a straight line in between and read off the intercept at $\Delta U = 0$. For E_a we have not determined the slope of the ΔU dependence *a priori*.

The same approach can now be applied to the Volmer reaction. The extrapolated and the interpolated values (intercepts) are the reaction and activation energies when the bias does not change during the discharge reaction $H^* \rightarrow H^+ + e^-$. These are shown in Fig 4c and 4d, respectively.

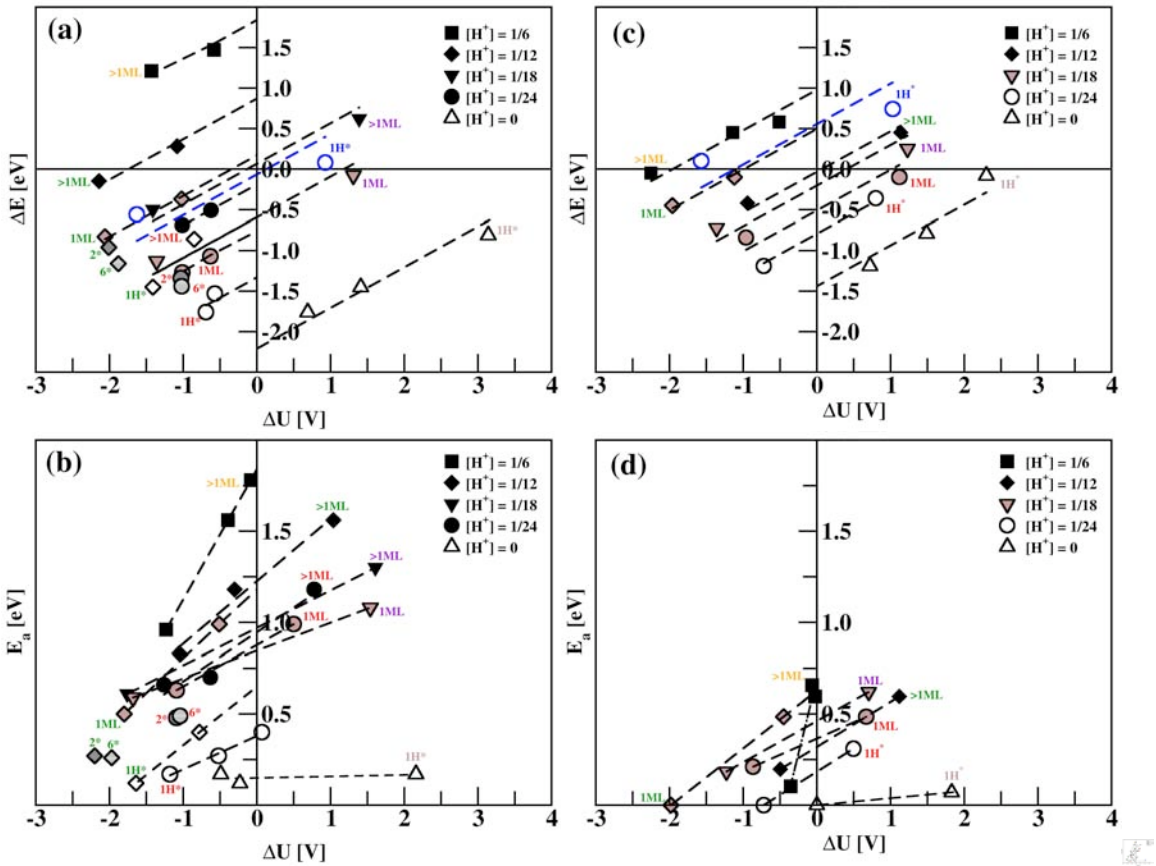

Fig 4: *The reaction energy (a & c) and the activation energy (b & d) for the hydrogen oxidation reaction via the Heyrovsky reaction (a & b) and the Volmer reaction (c & d) on a Pt(111) electrode vs. the change in electrode potential ΔU for those reactions. Each set of data point connected by a line corresponds to a fixed concentration of protons and hence a fixed potential. The crossing with ΔU=0 signifies the reaction energy or the activation energy for the Heyrovsky or the Volmer reaction when the bias does not change during the reaction. All the data points are calculated with model system shown in structure (a) of Fig. 3, except for the blue circles where structure (d) of Fig. 3 was used.*

Let us now consider the HOR direction. Fig. 4a contains the reaction energy of the Heyrovsky reaction, H_2 -> $H^+ + e^- + H^*$, while Fig. 4c contains the reaction energy of the Volmer reaction, $H^+ + e^- + H^*$ -> $2H^+ + 2e^-$, both at several electrode potentials. If the Heyrovsky reaction is added to the Volmer reaction (at some fixed electrode potential) we obtain the overall HOR, H_2 -> $2H^+ + 2e^-$, at several discrete electrode potentials. The reaction energy values are converted into reaction free energy values by including appropriate values for the ZPEs and entropy. The free energy of the overall HOR should be equal to two times the electrode potential, $\Delta G_{HOR} = -2U$, since two electrons are involved in this overall reaction. See Ref: [43] and Section 2.4, Eq. (8), and Section 3.1.4 below for more details. Notice that the effect of the H* adsorption energy of the individual reactions cancels out when the two reactions are added together. This is indeed what is observed in Fig. 5 where the free energy $\Delta G_{extrapolation} = \Delta G_{Heyrovsky} + \Delta G_{Volmer}$ is

plotted as a function of the free energy coming from the U deduced from the work function, $\Delta G_{WF} = -(U_{Heyrovsky} + U_{Volmer})$ for systems having the same proton concentrations and hence similar electrode potentials.

Fig. 5 shows clearly that the energetics of the Heyrovsky and Volmer reactions are not dependent on the model of the water used. Here we use both a model system having only a single water bi-layer with an H-down configuration (Fig 3a) and a more unrealistic two-water layer model with an H-up configuration in the first layer (Fig 3d). Overall, we have a one-to-one correspondence between free energies from the extrapolation scheme and free energies deduces from the WF, when we use a U scale which is insensitive of the water model.

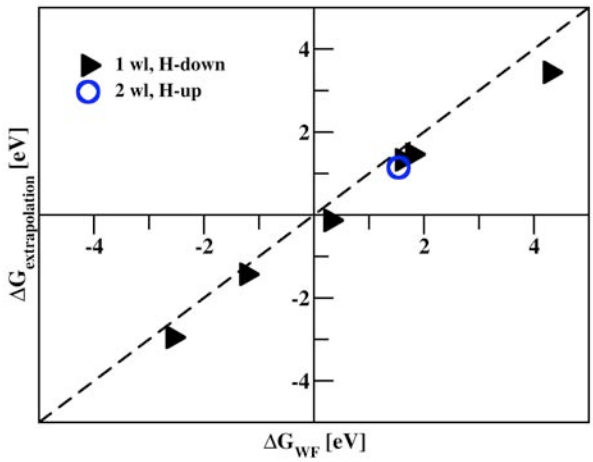

Fig 5*: The free energy, $\Delta G_{extrapolation}$, of the two-electron process of the summed Heyrovsky and Volmer reaction from the combined extrapolations in Fig. 4a and c as a function of the free energy, $\Delta G_{WF} = -2U$, when U is determined from the work function (WF) of the systems. Two different models of the water bi-layers are shown; 1 water layer with H-down configuration (black triangles) and 2 water layers with an H-up configuration of the first bi-layer and an H-down configuration of the second bi-layer (blue circle). The dashed line is y = x.*

2.4 Hydrogen coverage-dependent electrode potential scale

As mentioned above, the energetics of adsorbed H is not affected by including water, electric fields and potentials in the calculations, and the same is true for the energetics along the reaction path for the Tafel reaction. In order to assign an electrode potential scale to that reaction it is therefore not necessary to use the detailed atomistic double layer model presented above. However, since the activation barrier of the Tafel reaction is affected by the H coverage on the surface, we introduced another type of U-scale for that reaction [11]. This will be reviewed again here in the following.

The integral H adsorption energy is defined by

$$E_{int}(\theta_{H*}) = (E(surface + nH^*) - E(surface) - n/2\ E(H_2))/N, \qquad (3)$$

where E(surface + nH*) is the energy of the surface plus n hydrogen adsorbates, E(surface) is the energy of the clean surface, $E(H_2)$ is the energy of hydrogen molecules in the gas phase, N is the number of surface metal atoms in the super cell and θ_{H*} = n/N is the H coverage. E_{int} is the integral energy or the total adsorption energy of all the H atoms adsorbed on the surface (relative to H_2 in the gas phase) per surface metal atom.

In order to calculate the differential H adsorption energy as a function of the H coverage we multiply the $E_{int}(\theta_{H*})$ in Eq. (3) with N and take the derivative with respect to n

$$\begin{aligned}\Delta E_{H^*} = E_{diff}(\theta_{H*}) &= \delta(N^* E_{int}(\theta_{H*}))/\delta n \\ &= N^* \delta E_{int}(n/N)/\delta n \\ &= N(E_{int}(n/N) - E_{int}((n-1)/N))/\Delta n \qquad (4)\end{aligned}$$

and $\Delta n \equiv 1$.

The differential adsorption free energy is calculated as:

$$\Delta G_{H^*} = \Delta E_{H^*} + \Delta(\mathrm{ZPE}) - T\Delta S \qquad (5)$$

where Δ(ZPE) and ΔS are the differences in zero point energy and entropy, respectively, between the adsorbed hydrogen atoms and the hydrogen molecules in the gas phase. Greeley and Mavrikakis have calculated ZPE of adsorbed H on a range of transition metal surfaces using normal mode analysis with DFT calculations [44]. All ZPE are between 0.14 and 0.18 eV/H* for H adsorbed on FCC hollow sites. We calculate $TS^{vib}_{H^*}$ = 0.01 eV/H* at 300 K on FCC hollow site on Pt(111) with similar calculations. The ZPE of 0.27 eV/H_2 and TS of 0.41 eV/H_2 at 300 K of H_2 in gas phase are taken from standard molecular tables [45]. Adding these values together, using Eq. (5), we get 0.22 eV/H* that we need to add to the electronic energy to get the free energy. Here we use a value of ZPE_{H^*} = 0.16 eV/H*, in between the ZPE_{H^*} = 0.14-0.18 eV/H* from Greeley and Mavrikakis.

We also need to include the configuration part of the entropy of the adsorbed H*. The differential configurationally entropy, $dS_{config}/d\theta_{H*}$, is estimated by

$$dS_{config}/d\theta_{H*} = k_B T \ln((1-\theta_{H*})/\theta_{H*}), \qquad (6)$$

(for $0 < \theta_H < 1$) which previously has been found to compare well with Monte Carlo simulations [32].

Fig. 6 shows the calculated differential H adsorption energies on Pt(111). It also contains the full free energy profile at 300K. The difference between the full profile and the corresponding differential adsorption energy curve demonstrates the contribution to the differential free energy from the ZPE and the entropy. H adsorbs in 3-fold FCC sites up to a coverage of 1 ML. When exceeding 1 ML, additional H starts occupying on-top sites.

At room temperature, ΔG_{H^*} is negative on Pt(111) as long as $\theta_{H^*} \leq 0.86$ ML in this model, which means that the surface will be nearly covered at $\Delta G_{H^*} = 0$.

The hydrogen coverage will be dependent on the potential via the reaction:

$$H^+ + e^- + * \rightarrow H^* \qquad (7)$$

At standard conditions (298K, pH=0, 1bar H_2) and U=0 V vs. NHE, the left hand side is in equilibrium with hydrogen gas. At finite bias, U, the chemical potential of the electron will be linearly dependent on the bias. The reaction free energy of Eq. (7) can be written as [11, 13]:

$$\Delta G_{H^*}(U) = \Delta G_{H^*} - eU. \qquad (8)$$

$\Delta G_{H^*} = -eU$ defines the chemical potential of H*. If we make this conversion of scales in Fig. 6, i.e. changing ΔG_{H^*} to $-eU$, we find that the coverage will be about 0.86 ML at U = 0 V vs. NHE on Pt(111).

By calculating the free energy of H adsorption as a function of H coverage as in Fig. 6 we can now convert the free energy scale to an electrode potential scale, or U scale U = -ΔG/e. With this we have established a simple U scale, which is dependent on the H coverage. This is exactly what happens when measuring a cyclic voltammogram. When the bias is decreased from +0.4 V vs. NHE the H starts to adsorb on the surface via the Volmer reaction. At U = 0 the surface is nearly covered with H and hydrogen gas is formed. The measured H coverage is 2/3 ML [3] when the evolution starts whereas we calculate 0.86 here. Recently, it has been concluded experimentally that the H coverage is higher than 2/3 ML at the reversible potential and a full monolayer is reached at -0.1 V vs. NHE [46].

We note that in the case of interacting adsorbed H atoms, the expression, Eq. 6, for the configurational entropy is not entirely correct. We have, however, also made Monte Carlo simulations and find the differences to be very small. We will return to this point later.

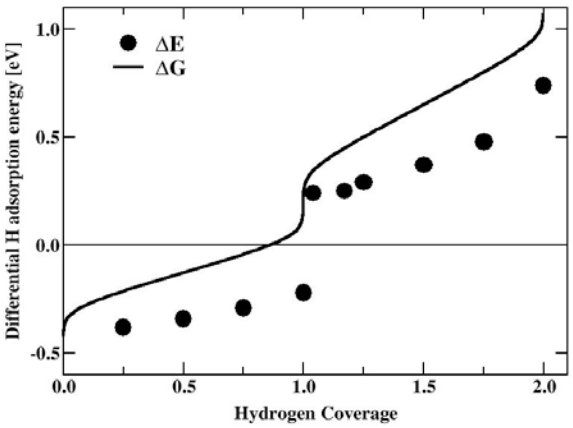

Fig 6*: Differential H adsorption energy and free energy on Pt(111).*

3. Results

In this Section we will start by discussing the results obtained for Pt(111) where we calculated all the elementary steps for HER and HOR. We will start by looking at the Volmer reaction. Next we take the Heyrovsky reaction and finally the results for the Tafel reaction are presented. As we conclude that the Tafel reaction is most likely the rate-determining step for both HER and HOR, we consider that reaction in more detail when we calculate the activation energies and the exchange currents. Then we consider the structure dependence of different facets of the Pt crystal. After that, a range of different metals and facets is discussed. Finally, we use all the DFT calculated values in a kinetic model where we construct a volcano for HER and HOR.

3.1 Elementary reaction steps on Pt(111)

3.1.1 Volmer reaction

In the initial step of HER, the Volmer step,

$H^+ + e^- \rightarrow H^*$,

an electron and a proton recombine to form adsorbed H on the surface. Being a charge transfer reaction, it requires some special considerations. First of all, the full electrochemical double layer setup, including a water bi-layer outside the metal surface, is needed in order to accurately treat the solvation of the proton and to account for the extra charge in the slab. Secondly, we use the extrapolation scheme presented above and we report all energies at different absolute electrode potentials in the limit where the potential does not change during the reaction (cf. Fig. 4c and 4d).

Reaction and activation energies have been extracted at five different proton concentrations: θ_{H^*}=1/6, θ_{H^*}=1/12, θ_{H^*}=1/18, θ_{H^*}=1/24 and θ_{H^*}=0. We also vary the H coverage on the surface to obtain self-consistency between the electrode potential and the H coverage according to Fig. 6 or any cyclic voltammogram on Pt(111) [3]. In the following we will only use systems having the right correspondence between H coverage and *U,* except when considering the activation barrier as a function of reaction energy where we include all the data for completeness.

Fig. 7 shows the activation barrier for the Volmer reaction, both in the HER and the HOR direction, as a function of the reaction energy and the electrode potential. In all cases the dependence is essentially linear. The linear relation between E_a and ΔE observed in Fig. 7 for the electrochemical processes is well-known in gas-phase/solid-state heterogeneous catalysis as a Brønsted-Evans-Polanyi (BEP) relationship [47, 48, 49, 50, 51] and also generally in chemistry [52]. For the HER direction, the energy barrier is 0.44 eV at ΔE = 0 and 0.72 eV at U = 0 V vs. NHE. For HOR direction, the energy barrier is also 0.44 eV at ΔE = 0 and 0.43 eV at U = 0 V vs. NHE. The 0.29 eV difference between the barrier heights for HER and HOR at U = 0 V (equilibrium) is due to the difference in the reaction energies for those two reactions.

If we assume a normal prefactor, 10^{13} site^{-1}s^{-1}, for the Volmer reaction, as we obtained from our calculations for the Heyrovsky reaction [11], the rate of the Volmer reaction will be very high around U=0, in agreement with experiments [2]. We will show later that other elementary steps in the HER/HOR have larger barriers at U=0, and conclude from our first principles calculations that the Volmer reaction can be treated as being in equilibrium at room temperature during HER/HOR and the coverage of H on the surface is given by the chemical potential of hydrogen, or the electrode potential.

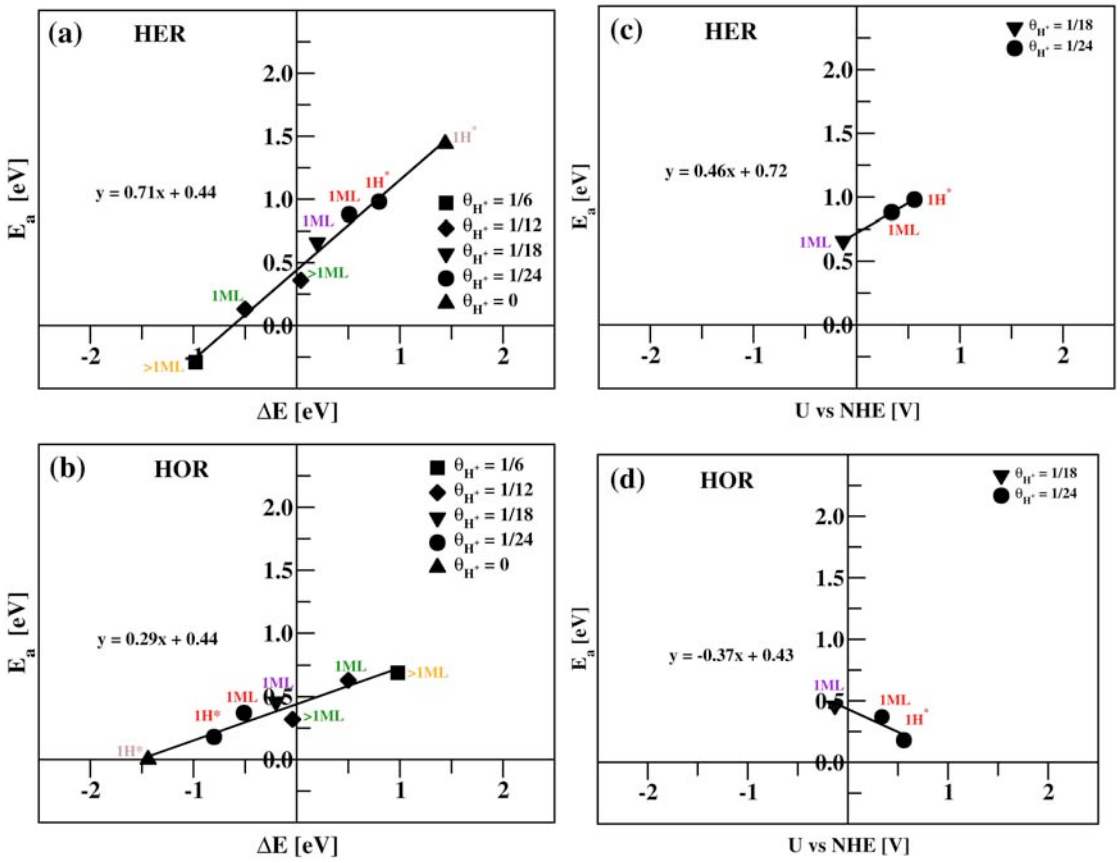

Fig 7: *Activation barriers, E_a, for the Volmer step in (a & c) the HER ($H^+ + e^- \rightarrow H^*$) and (b & d) the HOR ($H^* \rightarrow H^+ + e^-$) as a function of (a & b) the reaction energy, ΔE, and (c & d) the electrode potential, U vs. NHE, on the Pt(111) electrode.*

3.1.2 Heyrovsky reaction

In the final step of the HER, two possibilities for desorbing H_2 are available; the Tafel reaction or the Heyrovsky reaction. We start with the Heyrovsky reaction:

$$H^* + H^+ + e^- \rightarrow H_2$$

where a solvated proton from the electrolyte reacts with an adsorbed H and an electron from the surface to form H_2 molecule. Since this is also a charge transfer reaction, an

accurate analysis of the energetics requires the double layer model and the extrapolation scheme previously applied to the Volmer reaction. Using the information obtained in Fig. 4a and 4b when both the reaction energies and activation energies have been extrapolated to ΔU=0, we can now plot the extrapolated activation energies against the extrapolated reaction energies as shown in Fig. 8 for HER and HOR, respectively, on Pt(111). The proton concentration, θ_{H+}, in the water bi-layer has been varied and so has the H coverage on the surface, from having slightly more than 1 ML on the surface to having very low coverage (or 1 H* in a super cell). The relation between the activation energy and the reaction energy is clearly linear with an intercept at ΔE = 0 of 1.03 eV for both reactions. The intercept is slightly higher here than what we reported in Ref. [11], where it was 0.86 eV. Besides the fact that we are including more variation in proton concentration and especially the H coverage, we have applied the extrapolation scheme so both the activation barriers and the reaction energies are extrapolated to ΔU=0. Another important difference is that now all the activation barriers are calculated via the NEB method whereas we made a less detailed approximation for the TS in the earlier work.

In Fig. 8 (right) we include the activation barriers for HER and HOR versus the electrode potential, obtained from the WF of the systems and with our internal measure of the electrode potential as discussed in Section 2.2. As for the Volmer reaction above we attempt to have a H coverage on the surface that is consistent with the potential. Here we have obtained a semi-quantitative agreement between the H coverage and the potential with both experimental CVs [3] and our theoretical CVs [32]. The activation barrier for HOR is around 0.8 eV at U = 0 V vs. NHE, whereas it is around 1.4 eV at U = 0 for HER. As for the Volmer reaction, the difference between the HER and the HOR barriers is coming from the reaction energies. Our analysis indicates that the Heyrovsky reaction should be very slow on the Pt(111) surface at U = 0 V. At extremely high overpontials, around -1 V for HER and +0.5 V for HOR, the barrier for the Heyrovsky reaction becomes much lower or around 0.3 eV. The size of the overpotential seems to be somewhat greater here than in the study by Wang *et al.* [12] in which they conclude that the Volmer-Heyrovsky route becomes important for HOR at around +0.25 V vs. NHE. These results are in qualitative agreement though.

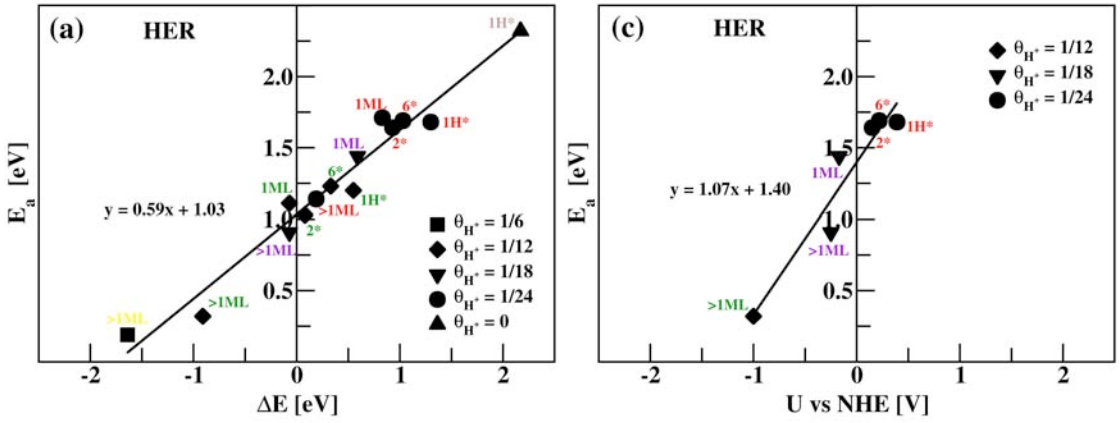

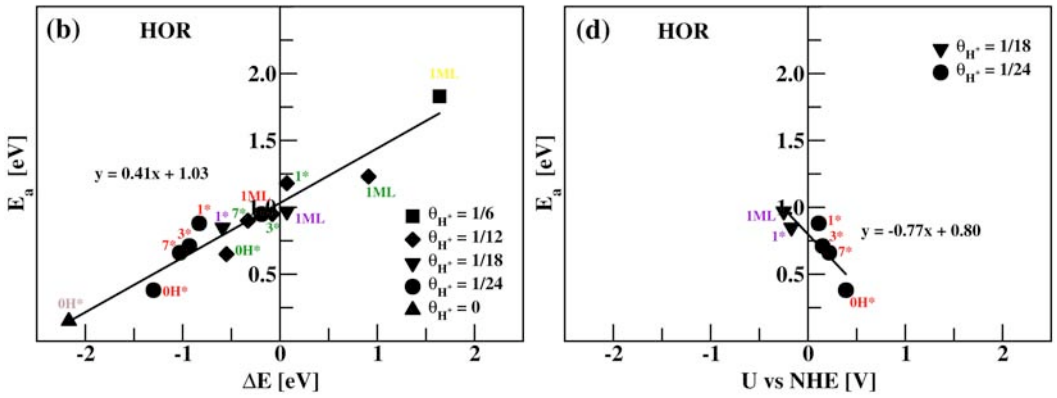

Fig 8: *Activation barrier for (a & c) the HER and (b & d) the HOR on Pt(111) via the Heyrovsky reaction as a function of (a & b) the reaction energy, ΔE, and (c & d) the electrode potential, U vs. NHE.*

3.1.3 Tafel reaction

The other possible elementary step for evolving H_2 in HER (or dissociating H_2 in HOR) is the Tafel reaction:

$2H^* <-> H_2+2^*$

Since the Tafel reaction is a homolytic reaction (a Langmuir-Hinshelwood type reaction) it is not necessary to explicitly include water, ions, electric potentials or electric fields [11] in order to describe it in an electrochemical environment. It should be noted that Gohda *et al*. calculated a 0.17 eV increase in activation energy when including water in the simulations of the Tafel reaction in the HOR direction [53] whereas we find negligible difference for the Tafel reaction in the HER direction [11]. This increase in barrier height when including water is not coming from the weak water-induced modification of the electronic structure of Pt(111). It is due to the interaction of H_2 with the water when H_2 propagates through the water layer [53]. The effect of water on the energetics of HER and HOR is thus a surface-independent parameter.

Avoiding inclusion of water simplifies the DFT calculations enormously as only a surface slab and adsorbed hydrogen have to be included in the model. However, as mentioned above, the coverage is a function of the potential and the coverage will affect the Tafel reaction. In this indirect way the electrochemical potential is playing a role.

In Fig. 9a we have plotted the activation energies, E_a, against the reaction energies, ΔE, in both the HER and the HOR directions on Pt(111). The variation in both E_a and ΔE is due to differences in H coverage. E_a and ΔE are linearly correlated, following BEP relationship. The slope is 0.45 for HER and 0.55 for HOR and the intercept is 0.55 eV for both directions. This is a considerably lower activation energies than obtained for the Heyrovsky reaction at ΔE = 0, where it is 1.03 eV. This strongly indicates that the Tafel reaction is much faster than the Heyrovsky and the predominant mechanism on Pt(111).

Using Fig. 6, and Eq. (8) the H adsorption free energy scale can be converted into a potential scale vs. NHE as shown in Fig. 9b. It is seen that for the *U*-values of interest when considering HER, i.e. just below 0 V vs. NHE, the activation barriers are around 0.85 eV. Fig. 9b shows the corresponding barriers for the Tafel reaction in the HOR direction. At positive potentials the activation barriers are low, 0.2-0.3 eV, whereas getting closer to U = 0 V the barriers start to increase and are around 0.4-0.6 eV. This is due to the fact that in the small unit cells (2x2) we are using, all those calculations have only one empty site on the surface and when dissociating H_2, the on-top sites become occupied which are high in energy, as we saw in Fig. 6 above 1 ML. If we now introduce a dimer vacancy in a bigger unit cell (4x4) where we have an initial H coverage of 14/16 ML and we dissociate H_2 to end up with 1 ML on the surface, the barrier decreases at U = 0 V to 0.4 eV (open square in Fig 9b). One could actually have a triple vacancy and get even lower barriers according to studies on the Pd(111) surface [54, 55, 56] but the probability of creating empty sites and the aggregation energy would affect the total rate in the end. We will analyze this further in the next section.

The barrier for the Tafel reaction for HER around 0.85 eV and HOR around 0.4 eV at U=0V are considerably lower than the ones for the Heyrovsky reaction at U=0V (1.4 eV for HER and 0.8 eV for HOR). The barrier for the Tafel reaction is also lower than the Heyrovsky reaction barrier for the whole potential region from -1 V to + 0.5 V. At these extremes in potentials, the barriers for the Heyrovsky and Tafel reactions become, however, somewhat similar in size.

The activation barrier of 0.85 eV for the Tafel reaction in HER direction is higher than the one for the Volmer step at U=0V (0.72 eV for HER). The barriers for the Tafel and the Volmer reactions are, however, similar in the HOR direction, 0.4 eV and 0.43 eV, respectively. Our results indicate that the Volmer-Tafel route is the predominant mechanism for both HER and HOR on Pt(111) at U=0V. Thus, we can focus on the Tafel reaction when analyzing the kinetics further and when considering other metal surfaces, facets and steps. Before we analyze the Tafel reaction in detail we construct a free energy diagram of all the elementary steps in next section.

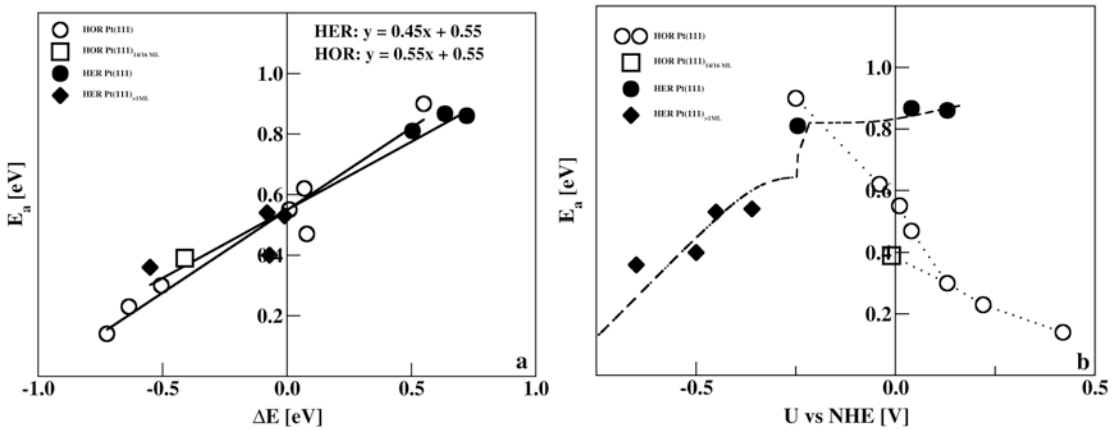

Fig 9: *Activation barrier, E_a, for HER and HOR on Pt(111) via the Tafel reaction as a function of a) the reaction energy, ΔE, and b) the electrode potential, U.*

3.1.4 Standard free energy diagram

To construct an overall picture of the energetics of the three elementary reaction steps - Volmer, Heyrovsky, and Tafel - a standard free energy diagram (FED) is constructed in Fig. 10. We define this as a *standard free energy* since there is no configurational part of the entropy included. Hence all the free energy states in Fig. 10 are at a fixed H* coverage. For the Volmer and the Heyrovsky steps we have picked out the three systems closest to zero electrode potential from Fig. 5. It should be noted that here the analysis becomes more transparent if we add together the reaction free energies of the Volmer and Heyrovsky steps. It is equivalent to adding the negative of the two individual electrode potentials, since the H* energy cancels out. It is obvious from Fig. 10 that while the Heyrovsky state ($1H^+ + 1e^- + H^*$) changes by $1U$ plus the H adsorption energy, the Volmer state ($2H^+ + 2e^-$) changes by $2U$ from the H_2 state. These explicit DFT calculations show how the chemical potential, μ, is related to the electric potential, U, via the simple equation; $\mu = -eU$, where e is the transferred charge. It is noted here that if the configurational part of the entropy had been included, all the free energy levels would be in equilibrium, and have the same free energy value.

In Fig. 10a the extrapolated activation free energy barriers for the Volmer and the Heyrovsky reactions, obtained from Fig. 4d and 4b, are also included.[1] It is evident while the activation barriers are quite low for the Volmer reaction they are very high for the Heyrovsky reaction. For comparison the activation free energy barriers of the Volmer-Tafel route has been included in Fig. 10b. The barrier for the Tafel reaction is approximately half as high as the barrier for the Heyrovsky reaction, whereas it is only slightly higher than the barrier for the Volmer reaction. Thereby, we conclude that the Volmer step is the fastest step of these elementary steps and the Tafel step is the rate-determining step.

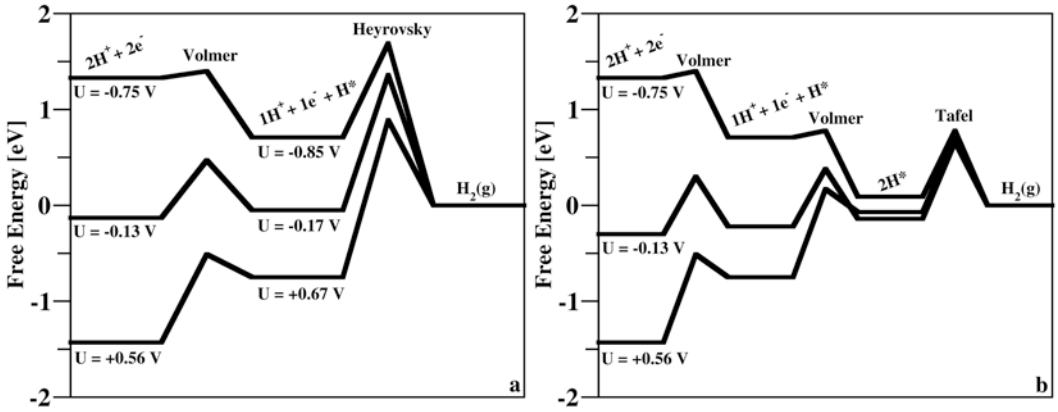

Fig 10: *Standard free energy diagram for the Volmer-Heyrovsky route (a), and Volmer-Tafel route (b) on Pt(111). The electric potential, U, deduced from the WF is given for each free energy level.*

[1] The ZPE of the TS structure is calculated via NMA DFT calculations to be 0.20 eV for the Volmer TS and 0.26 eV for the Heyrovsky TS. The entropy terms have been neglected as explained elsewhere [21].

3.2 Detailed analysis on the kinetics of the Tafel reaction on Pt(111)

The calculations we have performed for the activation energy as a function of H coverage for the Tafel reaction on Pt(111) can be considered as the mean field solution to the problem. Here we will present more elaborate analysis of the kinetics of HER and HOR on Pt(111). Instead of assigning each activation barrier to a given H coverage, we will associate an activation barrier to each configuration described by the number of H nearest neighbors (NN). In Table 1 we show the barriers and reaction energies for HER and HOR from Fig. 9a as a function of the NN configuration. We use the convention that NN is for the FS for HOR and hence for the IS for HER. These are the states determining the actual heights of the barriers. We have chosen to only consider data for 1 ML H coverage or less, since we will mainly be interested in potential around U = 0 V vs. NHE where the coverage on Pt(111) does not exceed 1 ML, c.f. Fig. 6.

Table 1: *Tafel (HER/HOR) activation energies, E_a, and reaction energies, dE, at different nearest-neighbor (NN) configurations. All energies are in eV/H_2. For the NN configuration marked (*) a linear interpolation has been taken for the E_a and dE from NN=2 and NN=5.*

HOR FS nn / HER IS nn	E_a^{HOR}	dE^{HOR}	E_a^{HER}
0	0.14	-0.72	0.86
1	0.14	-0.72	0.86
2	0.23	-0.64	0.87
3 (*)	0.25	-0.60	0.85
4 (*)	0.27	-0.56	0.83
5	0.30	-0.51	0.81
6	0.39	-0.41	0.80

In Fig. 11 we have calculated the probability of having a given nearest neighbor (NN) configuration at certain H coverages from 0 to 1 ML, both with an interacting lattice model using Metropolis Monte Carlo (MC) simulations and analytically with a non-interacting lattice model. For the MC simulation a hexagonal FCC(111) surface is modeled with a simple lattice model where each H in FCC site can interact with up to 6 nearest neighbors. The analytical hexagonal lattice model is non-interacting and is given by the binomial coefficients:

$$P_i(\theta) = \binom{6}{i}\theta^i(1-\theta)^{6-i} \tag{9}$$

As can be seen from Fig. 11, the MC simulation (including interactions) does not deviate much from the non-interacting analytical model. We therefore use the analytical model in the following analysis since it is more transparent.

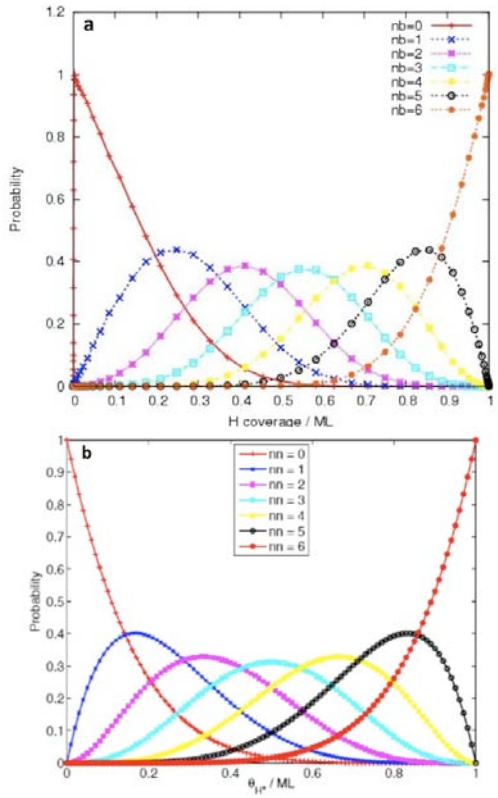

Fig 11: *Probability of having a given nearest neighbor (NN) configuration at varying H coverage, calculated with a) Metropolis Monte Carlo and b) Analytically.*

The Tafel HER rate is given by θ^2 times a sum over weighted (with $P_i(\theta)$ in Eq. 9) rate constants $k_{T,i}^{HER} = \nu * \exp(-E_{a,i}^{HER}/k_BT)$. We use the approximate attempt frequency, $\nu = 10^{13}$ site^{-1} s^{-1}, as the prefactor which we found to agree well with the measured absolute rate for HER when used together with our calculated activation barriers [11]. The activation energies $E_{a,i}^{HER}$ are given in Table 1. We get the rate equation

$$r_{\mathrm{T}}^{\mathrm{HER}}(\theta) = \theta^2 \sum_{i=0}^{6} P_i(\theta) k_{\mathrm{T},i}^{\mathrm{HER}} \tag{10}$$

With the expression for $P_i(\theta)$ in Eq. (9) inserted into Eq. (10) we end up with the following expression for the Tafel HER rate:

$$r_{\mathrm{T}}^{\mathrm{HER}}(\theta) = \nu \sum_{i=0}^{6} \binom{6}{i} \theta^{i+2} (1-\theta)^{6-i} \times \exp(-E_{\mathrm{a},i}^{\mathrm{HER}}/k_{\mathrm{B}}T) \tag{11}$$

The corresponding expression for the HOR rate can be written as

$$r_{\mathrm{T}}^{\mathrm{HOR}}(\theta) = \nu \times \exp(\Delta S/k_{\mathrm{B}}) \sum_{i=0}^{6} \binom{6}{i} \theta^{i}(1-\theta)^{8-i} \times \exp(-E_{\mathrm{a},i}^{\mathrm{HOR}}/k_{\mathrm{B}}T) \qquad (12)$$

where $\Delta S/k_B$ = -15.86 => $\exp(\Delta S/k_B)$ = 1.3 * 10^{-7} is the entropic barrier or loss of entropy when H_2 comes from the gas phase and dissociates on the surface, -TΔS=0.41 eV at standard conditions.

For a given H coverage we calculate the rate of both the HER and the HOR using Eq. (11) and (12). In Fig 11 the result is shown as a function of the H coverage at 300 K. At equilibrium, the rates for HER and HOR are the same and there is no net flow of current. This corresponds to U = 0 V vs. NHE at standard conditions and where the H coverage is 0.87 ML. This can be compared to the value 0.86 ML obtained with another approach in Fig. 6.

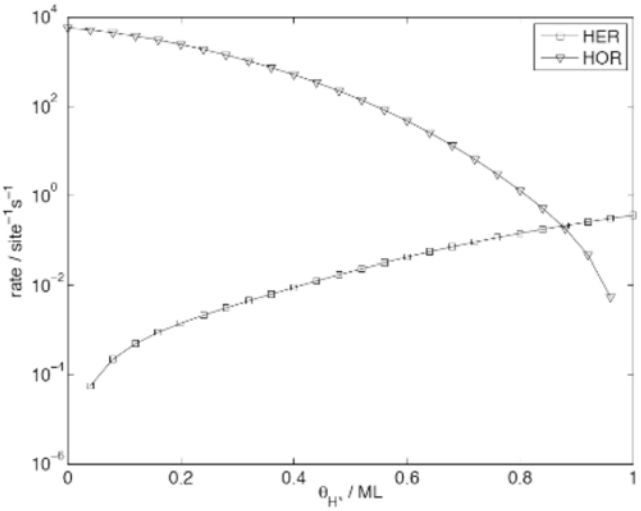

Fig 12: *Total Tafel HER and HOR rates at 300 K, plotted vs. the H coverage.*

At equilibrium, the exchange rate is 0.21 site^{-1} s^{-1} at 300 K. By changing units we get i_0 = 5.1*10^{-5} A cm^{-2} for the exchange current density. This is to be compared with the experimental value for the exchange current density on Pt(111) at 303 K, i_0 = 4.5*10^{-4} A cm^{-2} [2].

Here we show that our calculated barrier for the Tafel reaction gives a similar rate as experiments on the same surface. However, experimentally the activation barrier obtained from Arrhenius type analysis is around 0.2 eV for HER and HOR on Pt(111) [2]. This corresponds to a prefactor on the order of 10^3 site^{-1} s^{-1}, or 10 orders of magnitude lower than a normal prefactor. We are presently not able to explain these experimental data.

3.3 Structure dependence over Pt(111), Pt(100) and Pt(110)

In the following Section we discuss the HER and HOR rates for different facets of Pt and compare it with experiments by Markovic *et al* [2]. First we study the heat of adsorption vs. coverage. Then we compare the calculated rates obtained solely from the Tafel activation barriers with the measured ones. We will assume that the Volmer reaction is in equilibrium on all facets as generally found in experiments [3]. We will assume that the Heyrovsky pathway is not active on any of these surfaces since our calculations on the Pt(111) electrode shows that it is so far from active that the relatively small difference that we find in energetics between the different facets cannot change that picture.

3.3.1 Heat of adsorption

In Fig. 13 we report the differential adsorption energy (Eq. 4) as a function of H coverage for the Pt (111), (110) and (100) facets. As before, H occupies FCC sites up to 1ML and on-top sites above 1ML on the (111) facet. On the (100) facet, however, it adsorbs on the bridge sites all the way up to 2ML.

The Pt(110) electrode was modeled with a missing row reconstruction in accord with experimental observations under electrochemical conditions [3]. The first hydrogen atoms prefer to bind to the rim of the outermost Pt row. After those states have been filled, we find that it is most favorable for H to adsorb on-top the Pt atoms next to the rim [57]. This is in agreement with recent experimental and theoretical work on the Pt(110) surface [58] but in contrast to theoretical work on Ni(110) and Pd(110) where the adsorption instead starts on the (111) microfacet [59, 60]. When all the surface atoms have been covered (at 1ML) the next H to be adsorbed prefers to bind on bridge sites down in the valley.

The discontinuity in the energy profile when going beyond 1 ML is much less pronounced on Pt(100) than on Pt(111) and it is more or less smeared out on the rough Pt(110) surface. The effect this will have on the Tafel reaction when H_2 desorbs from these different facets or dissociates on them, at varying H coverage (or electrode potential) is investigated below.

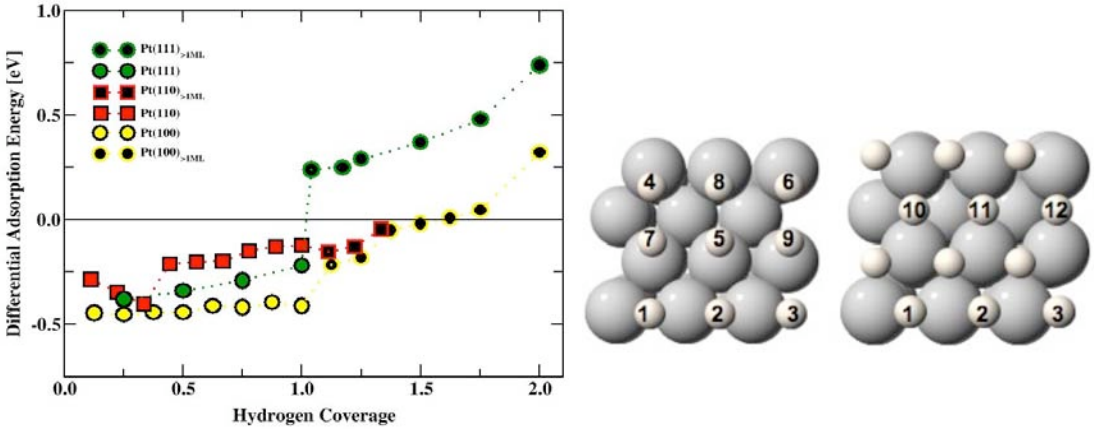

Fig 13: *Differential H adsorption energy as a function of H coverage for the three most stable crystal facets of Pt - the (111), (110) and (100) facets. For convenience, we have*

made the symbols black in the middle when exceeding 1 ML. The atomic structures show the order of H adsorption on the Pt(110) surface.

3.3.2 Tafel reaction

In Fig. 14 we have calculated activation barriers for HER and HOR via the Tafel reaction on Pt(111), Pt(100) and Pt(110). We vary the H coverage, which gives us both variations in the reaction energy and in the electrode potential. We assume that the prefactors are the same for all the facets. That allows us to compare our calculated rates to the measured rates for these facets which we do because the measured activation barriers coming from the Arrhenius analysis are all around 0.1-0.2 eV for these facets [2], or much lower than our HER barriers (around 0.8 eV) at U=0.

In the following we will calculate the HER rates for the different facets at U=0V vs. NHE. The HER barriers on the (111) and (100) are both around 0.85 eV at U = 0 V whereas the barrier on the (110) facet is around 0.74 eV at U=0V. Since for these facets every activation barrier is calculated for only one particular H coverage, we use our elaborate analysis from Section 3.2 for the Pt(111) facet as a starting point when comparing the facets. Since Pt(111) and Pt(100) have the same activation barriers at U=0 (Fig. 14c) the Pt(100) facet has the same exchange current as Pt(111), or $i_0 = 5.1* 10^{-5}$ Acm^{-2} (calculated in Section 3.2). This is in a agreement with the measured ones, $6.0*10^{-4}$ Acm^{-2} for Pt(100) and $4.5*10^{-4}$ Acm^{-2} for Pt(111), at 303 K [2]. From the difference in activation barriers between Pt(111) and Pt(110) we calculate $i_0 = 3.7*10^{-3}$ Acm^{-2} for Pt(110) in good agreement with the measured one, $9.8*10^{-4}$ Acm^{-2}, on Pt(110) [2].

We see similar structure dependence on the rates as Markovic *et al.* [2] and our absolute values are in quite good agreement with their measured ones. However, our activation barriers do not agree with the experimental ones obtained via Arrhenius analysis. We calculate around 0.74-0.85 eV at U=0V whereas their values are around 0.1-0.2 eV.

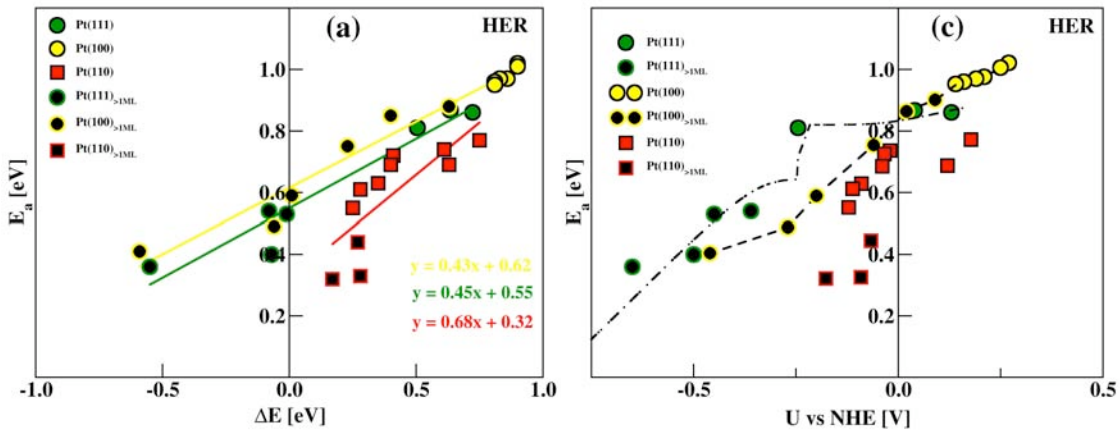

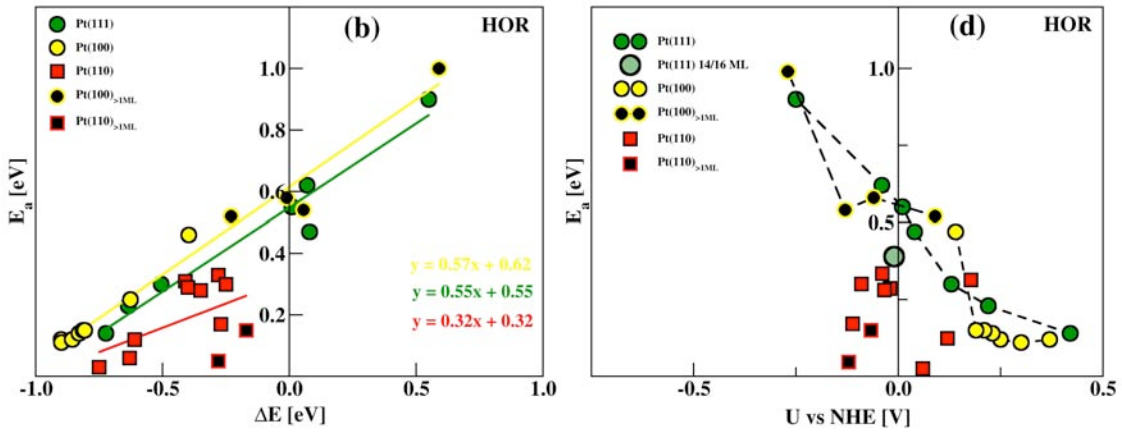

Fig 14: *Activation barrier for the HER (a & c) and the HOR (b & d) on Pt(111), Pt(100) and Pt(110) via the Tafel reaction as a function of the reaction energy (a & b) and the electrode potential, U vs. NHE (c & d).*

3.4 Heat of adsorption on other electrodes

In this section we will consider other metals, both in their close-packed structures and other facets and steps. This includes Au, Ag, Cu, Pt, Pd, Ni, Ir, Rh, Co, Ru, Re, W, Mo, and Nb. First we calculate the H adsorption energy and free energy on these different metal surfaces. Then we calculate the rate of the Tafel reaction on the complete range of surfaces.

3.4.1 Close-packed surfaces

Fig. 15a shows the calculated differential H adsorption energies for a range of close-packed transition metals. In Fig 15b the free energy profile, calculated via Eq. (5), at 300K for Ni, Au, Ru, Cu, and Pt is shown. On the close-packed surfaces, H is adsorbed in 3-fold FCC sites up to a coverage of 1 ML. When exceeding 1 ML, additional H starts occupying on-top sites and there is a discontinuity in the energy profile. At room temperature, ΔG_{H^*} is negative on the more reactive metals (Nb, W, Mo, Ni, Re, and Co) as long as $\theta_{H^*} \leq 1$ ML, which means that these surfaces will be fully covered. On the less reactive metals, like Pt, the H coverage is on the other hand a bit less than 1ML when $\Delta G_{H^*} = 0$. Finally, the H coverage on the inert metals (Cu, Ag, and Au) is very small at room temperature since $\Delta G_{H^*} > 0$ for all except the lowest coverage.

If we make the conversion of scales, i.e. changing ΔG_{H^*} to $-eU$, we find that the coverage will be about 1 ML at $U = 0$ V vs. NHE on the most reactive metals, but very low on the noble metals: Cu, Ag, and Au. For the noble metals a substantial negative bias is required in order to adsorb any appreciable amounts of H. We further notice that a coverage exceeding 1ML could in principle be achieved on the reactive metals by decreasing U to approximately –0.5 to –0.8 V vs. NHE. However, before that coverage is reached hydrogen molecules start forming on the surface via the Tafel reaction.

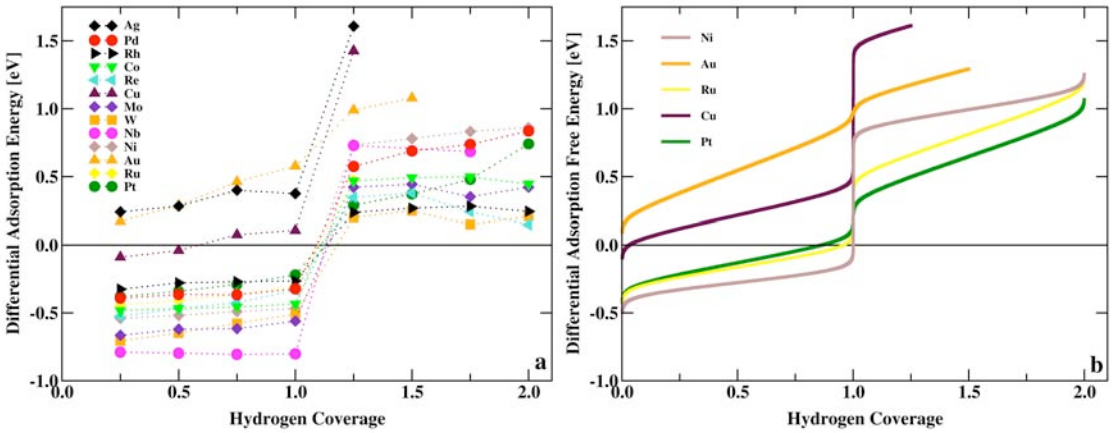

Fig 15*: a) Differential energy of H adsorption on close-packed metals. b) Differential free energy of H adsorption on a few closed-packed metals.*

3.4.2 More open facets and steps

Since polycrystalline surfaces and nano-particles consist of different types of flat surfaces as well as steps, kinks and other defects, it is interesting to calculate the heat of adsorption for more open facets than the close-packed ones. Here we have considered the FCC Pt(100) facet and the BCC W(100) and Mo(100) facets. A number of different adsorption sites are considered and the bridge sites are found to be the most stable ones. Since we have two bridge sites for each metal atom, we can fill the surface with bridge sites up to 2 ML. We discussed the Pt(100) results above in connection with Fig. 13.

In Fig. 16 we have included a line indicating U = 0 V vs. NHE by applying Eq. (8) at standard conditions. The Pt(100) surface is able to adsorb slightly more than 1 ML according to this simple model. The more reactive Mo(100) and W(100) surfaces can both adsorb considerable more H on the surface than the Pt(100) surface. The Mo(100) surface will adsorb 2 ML of H at U=0V or fill all the bridge sites. Occupying the four-fold site above 2 ML would require around –0.25 V in overpotential. Similar situation is on the W(100) as on the Mo(100), besides that at 2 ML, H adsorbs much stronger on W than on Mo. It should be noted that quite strong reconstruction occurred on the W(100) surface when adsorbing 0.75 ML and 1 ML.

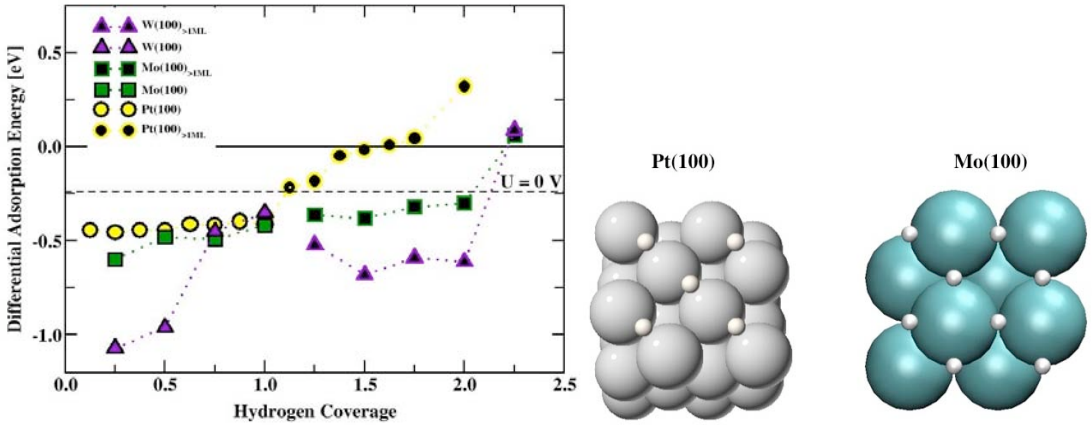

Fig 16: *Differential energy of H adsorption on open surfaces. The atomic structures show Pt(100) and Mo(100) surfaces with 1 ML and 2 ML of H adatoms, respectively.*

To model the effect of the low-coordinated defect sites on a real catalyst, the (211) stepped surface is used. In Fig. 16 we have calculated the H adsorption energy at different H coverage on a number of (211) metals. We have divided it into two sets of figures, where on the left we group Pd(211), Ni(211), and Co(211) together and on the right Pt(211), Ir(211), Re(211), and Rh(211). The metals are divided in the two groups based on the order in which the H atoms adsorb on the surface.

The general trend for all the metals is similar, however. The first H adsorb around the step, whereas the next H binds to the terrace. Around 1 ML (where 1 ML is defined here as 1 H per 1 surface metal atom), the next H binds to a new site around the (bottom of the) step. On these surfaces there is more space and more possibility of new adsorption sites which leads to much smoother and more continuous adsorption curve behavior than at the close-packed surfaces, where filling up all the three fold sites means that only the on-top sites are available above 1 ML.

If we compare Pd(211) and Pt(211) the first H adsorbs on a three-fold hollow site above the step on Pd(211) whereas the first H binds to the bridge site on the Pt(211) step. The tendency to occupy a three-fold site is larger on Pd than on Pt where bridge to three-fold energy differences are small, and H therefore easily moves to the bridge site to take full advantage of the high lying d-states at the step.

In Fig. 17 a line for U=0V has been added as for the (100) metals in Fig. 16. For most of the metals the steps have been occupied initially and the terrace has been filled with H at U=0. This means that at U=0, the close-packed structure is a sufficient model to capture the trends between the metals as we will discuss in the following Section 3.5. This means that the activation barrier at the close-packed surface is what determines the HER reactivity of e.g. a polycrystalline metal.

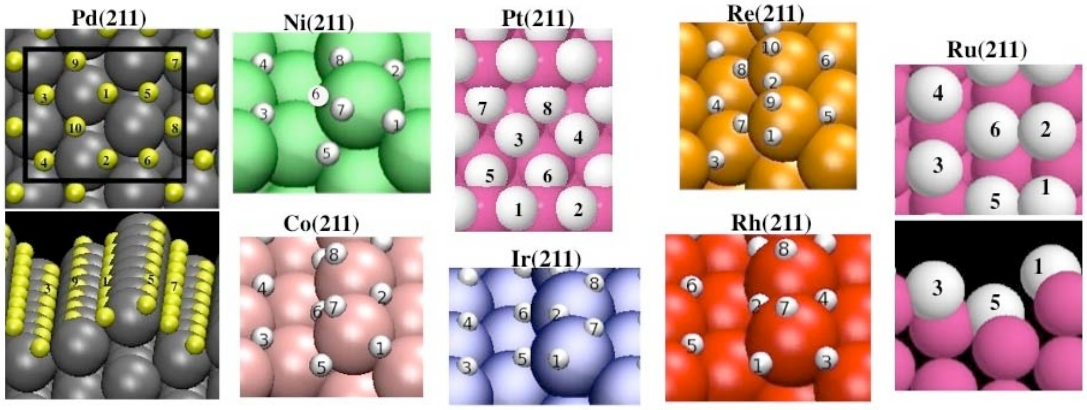

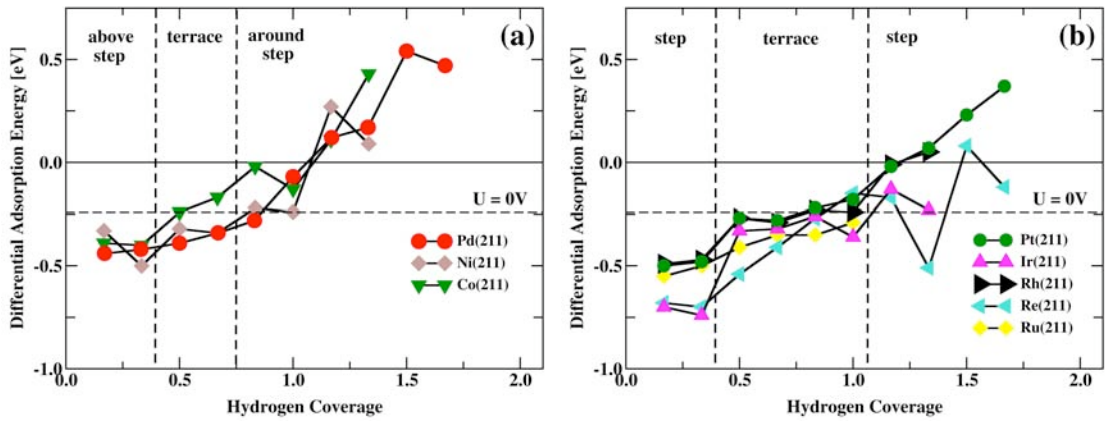

Fig 17*: Differential energy of H adsorption on stepped surfaces. The atomic structures above show the order of H adsorption.*

3.5 Trends in exchange currents for different metals – the volcano plot

The ability of a given metal to catalyze the HER (or HOR) is usually measured by the exchange current density, which is the rate of hydrogen evolution (or oxidation) per surface area at the potential where the reaction is at equilibrium (U=0 V vs. NHE at standard conditions). Different materials exhibit widely different exchange current densities. For over 50 years, it has been well established that if the exchange current density of the HER is plotted against some experimental measure of the metal hydrogen bond energy, a volcano-shaped curve is obtained [61, 62, 63, 64, 65].

Recently, a simple and fast systematic approach that uses adsorption free energies calculated using DFT was introduced [14]. When the measured exchange currents of various metals were plotted against the calculated binding, the apex of the volcano appeared close to $\Delta G_{H^*} = 0$. Ref. [14] also introduced a simple kinetic model of the exchange current, which reproduced the experimental data surprisingly well. Except for one free parameter, adjusting the overall magnitude of the volcano, the only input to this model was the calculated ΔG_{H^*}.

Here we employ a considerably more advanced kinetic model where all the parameters are obtained from the first-principle calculations presented in this work, i.e. no fitting parameter has been used. We assume the Volmer reaction to be in equilibrium as above. We discard the Heyrovsky reaction since it was concluded above that it is very slow on the Pt(111) electrode. The kinetics of the rate-limiting step found in this paper, the Tafel reaction, is used to get the overall magnitude and shape of the volcano plot, whereas in the simple kinetic model [14] the magnitude was modeled with a free adjustable parameter since there no activation barriers were included. The shape of the simple kinetic model was captured in Ref. [14] by assuming that the transfer coefficient is equal to one in the rate expressions. In the present study the activation barrier and its dependency on the reaction energy has been included, which describes the absolute rate and trends of the experiments extremely well, as discussed below.

In Fig. 18 the experimentally measured exchange current density (same as in Ref. [14]) is plotted against the H adsorption free energy, obtained with DFT calculations. For the metals on the left side of ΔG=0 we include high coverage (1 ML) since these metals will be filled with H at U=0. For the metals on the right side, Cu, Au, and Ag, we use low H coverage (0.25 ML) in accordance with Fig. 15b. In the volcano of Ref. [14] all ΔG_{H^*} were calculated at low H coverage (0.25 ML). Here, the data points fall nicely on a volcano shaped curve as expected. The metals on the left side of the volcano may be oxidized (indicated by a dashed line). This means that presumable these are metal oxides and not the pure metals in these particular experiments. However, when the measured exchange current on these metal oxides is plotted as a function of the H binding free energy of the pure metal, it falls directly on the volcano, predicted from the present more advanced kinetic model.

In order to model this, we calculate the exchange current from Eq. (11). We assume that we can describe the variation in E_a with a BEP relation for Pt(111) from Fig. 9a. The kinetic model agrees well with the experimental data and captures both the shape of the volcano and the absolute magnitude. Although the latter is probably fortuitous given the accuracy of our calculations. We also note that in the detailed analysis of the Tafel reaction on Pt(111) in Section 3.2 our calculated current was about an order of magnitude lower than what we have here. This is because for the construction of the volcano we use a BEP line for Pt(111) including H coverage above 1 ML in order to span more of the energy landscape. In Section 3.2 we, however, only included H coverage of 1 ML and less.

The good agreement throughout the metal series indicates that the Tafel barrier is the predominant and rate limiting step on all metal electrodes.

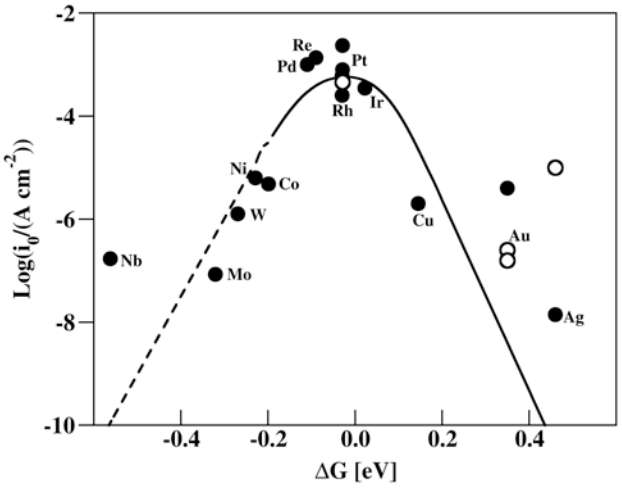

Fig 18: *A volcano plot. The data points are measured exchange current density plotted versus the calculated free energy of H adsorption at U = 0 V. The metals on the left side of the volcano have high H coverage (1 ML) and the metals on the right side low H coverage (0.25 ML). The line is a prediction by a kinetic model in which all input parameters are taken from DFT calculations. The dashed line indicates that the metals*

which bind H stronger than 0.2 eV/H usually form oxides at U = 0 V. The open circles are (111) data whereas the filled circles are polycrystalline.

4. Conclusions

Density functional theory results have been presented for the hydrogen oxidation reaction (HOR) and the hydrogen evolution reaction (HER) on a large number of transition metals with different surface structures.

Based on the calculated barriers, the BEP-relationships for the three elementary mechanisms (Tafel, Heyrovsky and Volmer) involved in the overall HOR, and HER have been established. It is found that the predominant reaction mechanism on the Pt(111) electrode is the Tafel reaction. We calculate a barrier of around 0.85 eV at U = 0 V vs. NHE which is not in agreement with the experimental one of 0.2 eV. The exchange current we calculate from this barrier is, however, in perfect agreement with the same experiment.

We studied the structure dependence of different facets of Pt for the Tafel reaction. Our calculated rates are in good agreement with the rates observed experimentally for the same facets.

In order to gain further insight into the kinetics of the Tafel reaction, we considered different metals, different facets and steps. Generally, the energetics follow a BEP relation which includes the Pt(111) data. Furthermore, the HER exchange current (current in the HER direction at U = 0 V vs. NHE) has been evaluated for a range of hydrogen adsorption free energies, using a kinetic model that takes the full free energy landscape as input. The agreement with experimental data is excellent.

References:

[1] *Hydrogen as a Future Energy Carrier*, edited by A. Züttel, A. Borgschulte, and L. Schlapback (Wiley-VCH, Weinheim, 2008).
[2] N. M. Markovic, B. N. Grgur and P. N. Ross, *J. Phys. Chem.* B **101** (1997) 5405
[3] N. M. Markovic and P. N. Ross Jr., *Surface Science Reports* **45** (2002) 117
[4] K. Kunimatsu, T. Senzaki, M. Tsushima and M. Osawa, *Chemical Physics Letters* **401** (2005) 451
[5] B. E. Conway and G. Jerkiewicz, *Electrochim. Acta* **45** (2000) *4075*
[6] J. Barber, S. Morin and B. E. Conway, *J. Electroanal. Chem.* **446** (1998) *125*
[7] M. C. Tavares, S. A. S. Machado and L. H. Mazo, *Electrochim. Acta* **46** (2001) *4359*
[8] J. A. Santana, J. J. Mateo and Y. Ishikawa, *J. Phys. Chem. C*, **114** (2010) 4995.
[9] Y. Cai and A. B. Anderson, *J.Phys.Chem.B* **108** (2004) 9829
[10] Y. Cai, A. B. Anderson, J. C. Angus, and L. N. Kostadinov, *Electrochemical and Solid-State Letters,* **8** (9) E62-E65 (2005)

[11] E. Skúlason, G.S. Karlberg, J. Rossmeisl, T. Bligaard, J. Greeley, H. Jónsson and J.K. Nørskov, *Phys. Chem. Chem. Phys.*, **9** (2007) 3241
[12] J. X. Wang, T. E. Springer and R. R. Adzic, *J. Electrochem. Soc*., **153** (2006) A1732
[13] J. Rossmeisl, J.K. Nørskov, C.D. Taylor, M.J. Janik and M. Neurock. *J. Phys. Chem. B.* **110**, (2006), 21833
[14] J. K. Nørskov, T. Bligaard, A. Logadottir, J. R. Kitchin, J. G. Chen, S. Pandelov and U. Stimming, *J. Electrochem. Soc.* **152** (2005) J23
[15] T. E. Shubina and M. T. M. Koper, *Electrochemistry Commun*. **8** (2006) 703
[16] P. Vassilev, R. A. van Santen and M. T. M. Koper, *J. Chem. Phys.* **122** (2005) 054701
[17] A. Roudgar and A. Groß, *Chem. Phys. Letters* **409** (2005) 157
[18] J. S. Filhol and M. Neurock, *Angew. Chem. Int. Ed.* **45** (2006) 402
[19] M. Otani and O. Sugino, *Phys. Rev. B* **73** (2006) 115407
[20] O. Sugino, I. Hamada, M. Otani, Y. Morikawa, T. Ikeshoji, Y. Okamoto, *Sur. Sci.* **601** (2007) 5237
[21] J. Rossmeisl, E. Skúlason, M.E. Björketun, V. Tripkovic and J.K. Nørskov, *Chem. Phys. Lett.*, **466** (2008) 68
[22] R. Jinnouchi, A.B. Anderson, *J. Phys. Chem. C*, **112** (2008) 8747
[23] M. C. Payne, M. P. Teter, D. C. Allan, T. A. Arias and J. D. Joannopoulos, *Rev. Mod. Phys*. **64** (1992) 1045
[24] G. Kresse and J. Furtmüller, *Comp. Mat. Sci.* **6** (1996) 15
[25] D. Vanderbilt, *Phys. Rev. B* **41** (1990) 7892
[26] Dacapo pseudopotential code, URL: https://wiki.fysik.dtu.dk/dacapo, Center for Atomic-scale Materials Design (CAMD), Technical University of Denmark, Lyngby (2006)
[27] B. Hammer, L. B. Hansen and J. K. Nørskov, *Phys. Rev. B* **59** (1999) 7413
[28] G. Kresse and J. Hafner, Phys. Rev. B **48**, 13115 (1993).
[29] G. Kresse and J. Furthmüller, Phys. Rev. B **54**, 11169 (1996).
[30] H. Jónsson, G. Mills and K. W. Jacobsen, in *Classical and Quantum Dynamics in Condensed Phase Simulations*, ed. B. J. Berne, G. Ciccotti and D. F. Coker, World Scientific, Singapore, 1998.
[31] G. Henkelman and H. Jónsson, *J. Chem. Phys.*, **113** (2000) 9978.
[32] G.S. Karlberg, T.F. Jaramillo, E. Skúlason, J. Rossmeisl, T. Bligaard, and J.K.Nørskov, *Phys. Rev. Lett.* **99** (2007) 126101
[33] G. Zundel and H. Metzger, *Z. Physik. Chem. (N.F.)* **58** (1968) 225
[34] G. Zundel, in *The Hydrogen Bond-Recent Developments in Theory and Experiments. II. Structure and Spectroscopy* (eds Schuster, P., Zundel, G. & Sandorfy, C.) 683-766 (North-Holland, Amsterdam, 1976).
[35] E. Wicke, M. Eigen and Th. Ackermann, *Z. Phys. Chem. (N.F.)* **1** (1954) 340
[36] M. Eigen, *Angew. Chem. Int. Ed*. **3** (1964) 1
[37] D. Marx, M. E. Tuckerman, J. Hutter & M. Parrinello, *Nature*, **397** (1999) 601
[38] J. E. B. Randles, *Trans. Faraday Soc.* **52** (1956) 1573
[39] E. R. Kötz, H. Neff and K. Müller, *J. Electroanal. Chem*. **215** (1986) 331
[40] S. Schnur and A. Groß, *New Journal of Physics*, 409 (2009) 157
[41] S. Haq, C. Clay, G. R. Darling, G. Zimbitas, and A. Hodgson, Phys. Rev. B, 73 (2006) 115414

[42] T. Pajkossy, D.M. Kolb *Electrochimica Acta* **46** (2001) 3063
[43] J. K. Nørskov, J. Rossmeisl, Á. Logadóttir, L. Lindqvist, J. R. Kitchin, T. Bligaard, and H. Jónsson, *J. Phys. Chem. B*, **108** (2004) 17886.
[44] J. Greeley and M. Mavrikakis, *J. Phys. Chem. B*, **109** (2005) 3460
[45] P. W. Atkins, *Physical Chemistry*, 6th ed., p. 485, 925, and 942, (Oxford University Press, Oxford, 1998).
[46] D. Strmcnik , D. Tripkovic, D. van der Vliet, V. Stamenkovic and N.M. Markovic, *Electrochem. Communications*, **10** (2008) 1602
[47] J. K. Nørskov, T. Bligaard, A. Logadottir, S. Bahn, M. Bollinger, L. B. Hansen, H. Bengaard, B. Hammer, Z. Sljivancanin, M. Mavrikakis, Y. Xu, S. Dahl and C. J. H. Jacobsen, *J. Catal*. **209** (2002) 275
[48] V. Pallasana and M. Neurock, *J. Catal*. **191** (2000) 301
[49] Z. P. Liu and P. Hu, *J. Chem. Phys*. **114** (2001) 8244
[50] A. Logadottir, T. H. Rod, J. K. Nørskov, B. Hammer, S. Dahl and C. J. H. Jacobsen, *J. Catal*. **197** (2001) 229
[51] P. Ferrin, D. Simonetti, S. Kandoi, E. Kunkes, J. A. Dumesic, J. K. Nørskov, and M. Mavrikakis, *J. Am. Chem. Soc.* **131** (2009) 5809
[52] L. P. Hammett and M. A. Paul, *J. Am. Chem. Soc*. **56** (1934) 830
[53] Y. Gohda, S. Schnur and Axel Groß, *Faraday Discuss*., **140** (2008) 233
[54] T. Mitsui, M. K. Rose, E. Fomin, D. F. Ogletree, M. Salmeron, *Nature* 422 (2003) 705
[55] N. Lopez, Z. Lodziana, F. Illas, M. Salmeron, *Phys. Rev. Lett.* **93** (2004) 146103.
[56] A. Groß and A. Dianat, *Phys. Rev. Lett.* **98** (2007) 206107
[57] S. Gudmundsdóttir, E. Skúlason, H. Jónsson, In preparation (2010)
[58] M. Minca, S. Penner, T. Loerting, A. Menzel, E. Bertel, R. Zucca and J. Redinger, *Topics in Catalysis* **46** (2007) 161
[59] G. Kresse and J. Hafner, *Surf. Sci.* **459** (2000) 287
[60] W. Dong, V. Ledentu, P. Sautet, E. Eichler and J. Hafner, *Surf. Sci*. **411** (1998) 123
[61] H. Gerischer, *Z. Phys. Chem. (N.F.)* **8** (1956)137.
[62] R. Parsons, *Trans. Faraday Soc.*, **54** (1958) 1053.
[63] L. Krishtalik, *Adv. Electrochem. Electrochem*. Eng., **7** (1970) 283.
[64] S. Trasatti, *J. Electroanal. Chem. Interfacial Electrochem*., **39** (1972) 163.
[65] S. Trasatti, *Adv. Electrochem. Electrochem. Eng*., **10** (1977) 213.

Paper III

The computational standard hydrogen electrode

V. Tripković, M. Björketun, E. Skúlason, J. K. Nørskov, J. Rossmeisl

In preparation

The computational standard hydrogen electrode

Vladimir Tripković[a], Mårten E. Björketun[a], Egill Skúlason[b], Jens K. Nørskov[c], Jan Rossmeisl[a]*.

[a]Center for Atomic-scale Materials Design (CAMD), Department of Physics, Technical University of Denmark, Kgs. Lyngby 2800, Denmark

[b]Science Institute, University of Iceland, Dunhaga 3, IS-107 Reykjavik, Iceland

[c]Department of Chemical Engineering, Stanford University, Stanford, CA 94305 and Center for Interface Science and Catalysis, SLAC National Accelerator Laboratory, 2575 Sand Hill Rd, Menlo Park, CA 94025, USA

**corresponding author jross@fysik.dtu.dk*

Methods to explicitly account for half-cell electrode potentials have recently appeared within the framework of density functional theory. This breakthrough has contributed significantly to the study of electrochemical reactions (DFT). However, they all relied on the experimental values of the absolute standard hydrogen electrode (SHE) potential, whose estimates vary within 4.44-4.85 V. The major challenge is to determine an absolute potential scale, internal to the system, that directly links a work function scale to the thermo-chemical scale of the SHE. In this paper we present DFT simulations of charge solid/liquid interfaces for different metals and different interfacial water structures. We show that even though the potential scale is dependent on the water surface structure, the differences cancel out if an internal calculated potential scale is used instead of the experimentally determined values.

1 Introduction

In electrochemistry all potentials are given relative to a chosen reference electrode of some well-known reaction, *e.g.* the standard calomel or the standard hydrogen electrode (SHE). Taking the difference between two electrode potentials alleviates the problem of determining the potential on an absolute scale in many electrochemistry experiments. Nevertheless, the absolute potential scale is of great importance when comparing

electrochemical and UHV experiments and, in particular, when trying to match semiconductor and solution energy levels [22] in for instance photo-electrochemical devices.

In DFT simulations of electrochemical systems, an electrochemical cell is customarily split in the two half-cells and the two redox reactions are then studied separately. Here the absolute potential enters as a key parameter because it is no longer possible to measure potential difference between the two electrodes.

For investigating equilibrium structures and reaction energies it is very often not needed to explicitly describe the full electrochemical double layer [1,2] setup. However, for addressing barriers of charge transfer reactions, an atomic model of the full double layer setup is a necessity.

Methods for studying reactions at the electrochemical interface have just started to appear. [3,4,5,6,7,8,9]. Despite differences in formalisms and implementations, they all faced the same fundamental problem, namely the simulations are done for micro-canonical systems where the number of electrons is kept constant. In reality, it should though be a grand-canonical system, where the chemical potential of the electrons is constant. The way to bridge the two is to perform a number of simulations with different number of electrons and to measure the differences in work-functions (potentials). By interpolating (taking derivative) between micro-canonical simulations it is possible to construct the situation of a constant chemical potential.

However, in order to obtain the relative potential scale, the work function (WF) scale needs to be coupled to the normal thermo-electrochemical scales of *e.g.* the SHE. This matter can be approached in two conceptually different ways. The most straightforward way is to use an experimental value for the standard hydrogen electrode potential (ASHEP), that is, the WF that corresponds to SHE conditions. However, there is a large uncertainty for the values of the ASHEP reported in the literature (4.42-4.85V) [10,11,12,13,14,15,16,17,37]. To get accurate results it is essential to use the correct experimental estimate and the real system has to be faithfully mimicked in the simulations, since the calculated WF depends explicitly on the structure of the water at the metal/aqueous interface [18]. Although, we note here, that it would be hard to capture properties of bulk water by including only a few water molecules in the super cell [6,19].

Alternatively, one can use a theoretical value of the ASHEP, internal to the system and perhaps different for different metal/water/vacuum setups. This approach has the advantage that it needs a less accurate representation of the simulated metal/water interface, but in turn it requires a scheme for determining the theoretical ASHEP. We have recently devised such a scheme [20] and subsequently successfully implemented it to model the hydrogen evolution and oxidation reactions [21].

In this paper we first determine the most accurate benchmark value for the ASHEP from the available literature. Subsequently, by briefly revisiting our earlier works, we show how an internal ASHEP reference can be readily established [21,21]. Invoking the fundamental concepts of the absolute potential scale, developed by Trasatti and others [22,23,24,25,26,27,28], we then examine the most appropriate choice for the reference point of the computed WFs. We calculate the ASHEP for a number of different electrode materials and we thoroughly quantify the variations in the WF originating from the inaccurate water structure. Finally, we point out how these variations to a large extent cancel out, if an internal ASHEP reference is used.

2 Computational details

All the electronic structure calculations have been carried out using density functional theory with the RPBE functional for exchange and correlation [29]. RPBE lattice constants were optimized for bulk metals. Metal electrodes were represented by periodically repeated 3 layer slabs separated by 12 Å of vacuum in the direction perpendicular to the surface. This amount of vacuum ensured convergence of work functions and energies. Inclusion of a 4^{th} layer had negligible influence on the presented results. Surface unit cells of various sizes – (3x2), (3x3), (3x4), (6x3) and (6x4) – sampled with (4x6), (4x4), (4x3), (2x4) and (2x3) Monkhorst-Pack k-point sampling grids [30] were used to account for different proton concentrations (potentials). In all cases symmetry was applied to further reduce the number of k-points. The dipole correction was used in all cases to decouple the electrostatic interaction between the periodically repeated slabs. The Kohn-Sham equations were solved using a plane wave basis set with a plane wave and density cutoff of 26 Ry, except for ruthenium where 28 Ry was used instead. Ionic cores were described with Vanderbilt ultrasoft

pseudopotentials [31]. A Fermi smearing of 0.1 eV was used and energies were extrapolated to an electronic temperature of 0 K. The two bottom layers of the slab were fixed in their bulk positions, while the top layer and adsorbents were allowed to relax until the sum of the absolute forces was less than 0.01 eV $Å^{-1}$. All calculations were performed using the Dacapo code [32], integrated with the Atomic Simulation Environment [33].

3 Results and discussion

3.1 Experimental estimates of the ASHEP

Experimental values of the ASHEP reported in the earlier literature resided mostly on measurements of changes in the WF upon water adsorption. The WF was measured by means of immersed electrode setups [13,14,15], UHV studies [34,35] or, similarly, through measurements of the potential difference across the Hg |air | H^+ | Pt,H_2 cell in the absence of any specific adsorption or charge transfer (so-called streaming Hg jet method) [10,11]. There is a large scatter, error bar, in reported values obtained using these techniques (4.44 to 4.85 V). The reason for these discrepancies has been attributed to surface contamination, to the orientation of water in UHV experiments being different from the one in bulk water, to partial charge transfer and other [23,25]. Here, it is worth noticing that the lower value has been identified as the most reliable one by Trasatti and also the value recommended by IUPAC.

A second and more direct approach to measure the ASHEP is through the Born-Haber cycle shown in Fig. 1, where ΔG_d, ΔG_I, $\alpha_{aq}(H^+)$ and μ_e are dissociation, ionization, solvation free energy and the chemical potential of electron with respect to its reference state.

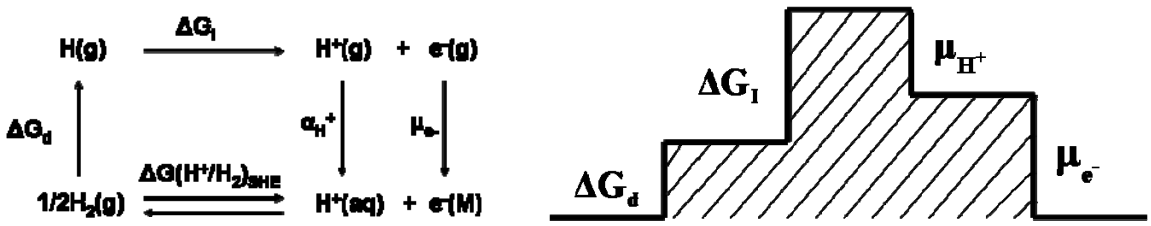

Fig. 1: *(a) Born-Haber cycle for the standard hydrogen electrode. (b) Energies in (a) shown schematically on a step diagram. The ASHEP is equal to* μ_e.

The free energy of $H_2(g)$ and $H^+(aq)$ will be independent of the metal used as an electrode, as long as the H^+ is solvated in the bulk solution. This implies that the reaction $H^+(S) + e^-(M_1) \leftrightarrow ½\ H_2(g)$ will hold if the metal Fermi levels ($e^-(M)$) at SHE conditions are equal. In other words, the amount of charge transferred on different metal surfaces will be always such, that the metal Fermi levels will become aligned at SHE conditions.

The ASHEP can be determined from the Born-Haber cycle if the real solvation energy is accurately measured. $\alpha_{aq}(H^+)$ has recently been very precisely estimated from the cluster-pair-based approximation [36] to be 4.42 V [37,38]. This value is very close to the 4.44 V recommended by Trasatti. In fact, it is highly unlikely that this striking agreement between two completely different approaches can be the result of a pure coincidence. In next section we will therefore use 4.42-4.44 V as the experimental values to benchmark our calculated ASHEPs against.

3.2 Free electron reference in experiments and DFT

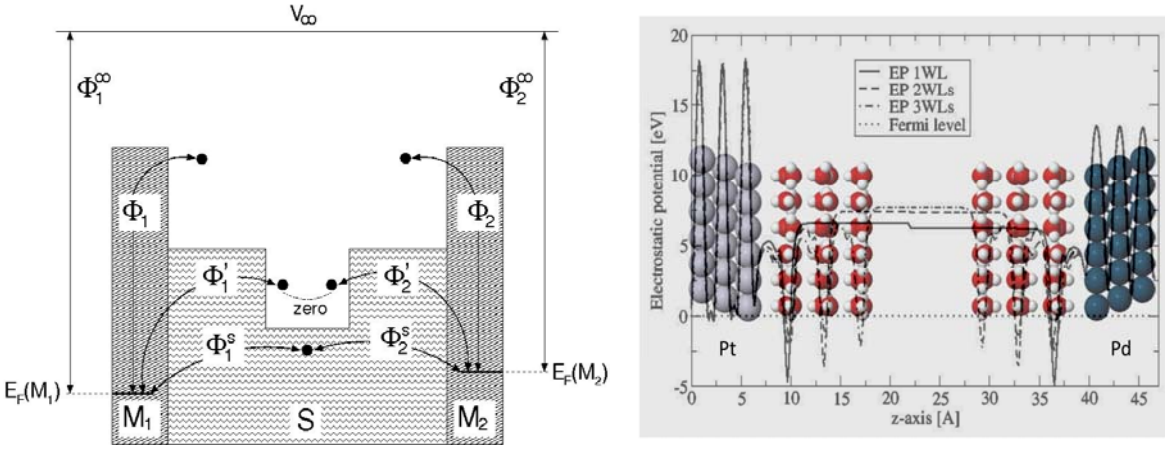

Fig. 2: *(a) Schematics of an electrochemical cell showing a set of work functions, Φ_α^k, measuring the work needed to take an electron from the Fermi level of the metal to four different free electron reference states (b) DFT model of the electrochemical cell comprised of Pt(111) and Pd(111) electrodes immersed in a common uncharged aqueous solution, vacuum cleaved half-way between the electrodes. The figure illustrates the convergence of the electrostatic potential with the number of water layers. The water layers are mirror imaged on the two electrodes.*

As Trasatti pointed out, the ASHEP depends on the chosen reference state for an electron at rest [22,23,26]. He has argued existence of three such physically conceivable levels: at rest in vacuum at infinity, in bulk electrolyte or in vacuum close to the surface

of the solution. From his analysis, he concluded that the best reference is the near surface vacuum because it enables a direct link between surface science and electrochemical experiments and furthermore it is amenable to experimental determination [22,26].

A typical electrochemical cell is illustrated in Fig. 2a. The half-cells are obtained when an electrochemical cell is vacuum cleaved at the point where the solution potential is converged. Four WFs required to bring an electron from the Fermi level of the metal M_α to a chosen reference state are indicated, where labels Φ_α^∞, Φ_α^S, Φ_α, and $\Phi_\alpha^{'}$ stand for far (or infinite) vacuum, bulk solution, near vacuum, and near-solution vacuum WFs.

In conventional periodic DFT calculations Φ_α^∞ is not defined because of infinite surfaces imposed by periodic boundary conditions. This means that even a point at an infinitively large distance in vacuum will still feel the presence of the surface dipoles.

The second plausible reference is the point in bulk solution. Obtaining a solution reference point can be readily achieved if several water layers are included in the cell. This, however, reflects on the system size and computational cost needed to perform such a relaxation. Additionally, a portion of water must be fixed because any wiggling of the water molecules can shift the reference level [6].

The near vacuum level can be readily measured by the WF in metal/water/vacuum setups and moreover, the measurement does not entail any confinements[1]. Hence, it is the most natural free electron reference state in DFT calculations and $\Phi_\alpha^{'}$ is thus a relevant WF.

The DFT counterpart to an electrochemical cell is shown in Fig. 2b. In DFT simulations of such setups, the Fermi levels will be always aligned irrespective of the potential and the electrode material[2]. Once the Fermi levels of M_1 and M_2 are aligned, Φ_1' and Φ_2' should also become equal, given that the solution phase is thick and polarizable enough to screen the fields from the metals. However, this is usually not the case in DFT calculations due to the limited amount of water that one can afford to include in the simulations. Convergence of the EP profiles for a Pt(111)|water|vacuum|water|Pd(111) cell with the number of water layers is displayed in Fig. 2b.

[1] The Φ_α and $\Phi_\alpha^{'}$ are phenomenologically the same because they both refer to the near vacuum levels.
[2] In a real electrochemical cell, if the cell is not short circuited this only holds at SHE conditions.

A gradual improvement of the near-solution-surface reference point with increasing thickness of the water is clearly observed. The mid-vacuum EP discontinuity (obtained by electrostatical decoupling of periodically repeated supercells) is fairly large in the cell containing only a single water layer, however, it becomes much smaller after addition of a second and a third water layer.

In section 3.4, we will demonstrate how inadequate water structures introduce, sometimes substantial, variations in the ASHEP and the potential of zero charge. However, we will also show how these inaccuracies can be addressed and readily accounted for *a posteriori*.

3.3 Establishing an internal reference for the ASHEP

In this section we will discuss how an internal reference for the ASHEP can be established in a DFT-based electrochemistry study. The methodology will be summarized here because of its relevance for the following study. For more details about the procedure we refer to our previous works [20,21].

We start with an atomic setup consisting of a metal slab and an electrolyte represented by water layers outside the surface (cf. Fig. 2b). The metal/electrolyte interface is charged by adding hydrogen atoms to the water layer at the surface. The hydrogen atoms spontaneously separate into protons that become solvated in the water bilayer and electrons that are transferred to the surface of the metal slab. The charge separation, in turn, creates an electrostatic potential drop across the interface. The surface charge, and hence the potential, can be varied in steps by changing the concentration of protons in the electrolyte.

The link between the potential and WF can be established by focusing on the free energy of the solid/liquid interface as it is charged with protons and electrons. The total or integral free energy per surface metal atom (or surface area) relative to H_2 for a system with n protons and N number of surface atoms is given by

$$G_{int} = \left(G(N,n) - G(N,0) - n\mu_{H_2} / 2 \right) / N \qquad (0.1)$$

where μ_{H_2} is the reference chemical potential of hydrogen. G_{int} corresponds to the free

energy stored at the interface set up by the protons in the water layer and their counter charge in the metal. G_{int} will be quadratic in potential, if the interface behaves as a perfect capacitor. The derivative of G_{int} with respect to the proton concentration is the chemical potential of protons and electrons

$$\frac{dG_{int}}{d(n/N)} = \mu\left(H^+ + e^-\right) - \frac{1}{2}\mu\left(H_2\right) \qquad (0.2)$$

The role of the $\mu(H_2)$ term is to define the reference. Hence, if we choose μ_{H_2} to equal the free energy of $H_2(g)$ at standard conditions, the WF corresponding to the minimum of G_{int} will define the potential of the SHE on an absolute scale. By taking the derivative of $G_{int}(U)$ it is possible to mimic the grand-canonical situation, *i.e.* to obtain the chemical potential of protons and electrons. The question is how the ASHEP changes as we change water model and electrode material.

3.4 Sensitivity of the ASHEP to water structure

We present results for the computational ASHEP on 8 different fcc(111) transition metal surfaces with two qualitatively different water models. Since system size in DFT is dictated by computational power, our study was limited to having just a few water layers [39].

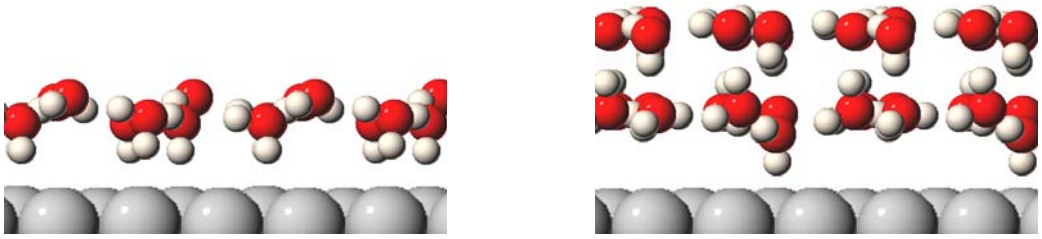

Fig. 3: *Structure of two different water models with a single hydrogen atom added to charge the interface. a) Model 1: water bilayer with dipoles pointing to the surface b) Model 2: two adhering water bilayers with no net dipole (apart from the added H).*

Both models are based on hexagonal layers of water films. Model 1 (Fig. 3a) is a single hexagonal water layer where every second water molecule points with a hydrogen towards the surface. This structure has been reported in UHV studies on many single

metal facets, among others Pt(111) [40], Ru(001) [41], Pd(111) [42], Rh(111) [43]. Due to its relevance for surface science studies it has been scrutinized in details with many experimental and theoretical tools [44,45,46]. We have also successfully used it previously to model oxygen reduction and hydrogen oxidation/evolution reactions [21,47]. Model 2 (Fig. 3b) consists of two adhering water bilayers where dipoles in the first bilayer point toward planar water molecules in the second bilayer and vice versa. The differences between the two models are in resulting dipole moment and flexibility of the hydrogen bonds. In that respect, model 1 has a net dipole moment normal to the electrode surface, whereas model 2 has no net dipole. On the other hand, model 1 has 'free' hydrogen bonds pointing towards the surface, whereas in model 2 all the hydrogen bonds are formed between the water layers, which render the structure more rigid. We should keep in mind that both models are unrealistic. At standard conditions water dipoles at the interface will be randomly oriented up and down [18]. Herein, we will use the models merely to emphasize the implication of structural differences on values of the computed ASHEP.

We will start the ensuing discussion by addressing the absolute potentials of the standard hydrogen electrode, U_{she}, and the potential of zero charge, U_{pzc}, for a range of transition metals (Ru, Pd, Pt, Au, Ag, Re, Rh and Ir), using the different metal/water models 1 and 2. Model 1 will clearly illustrate the errors introduced when using a water structure containing a net dipole and model 2 will show the errors caused by insufficient charge screening.

In Fig. 4 the integral free energy G_{int} obtained with models 1 and 2, respectively has been plotted versus the WF calculated for the metal in the metal/water/vacuum setup (Φ'). The points $G_{int}=0$ to the far right in the graphs are obtained for uncharged systems, without any additional hydrogen in the water, and thus correspond to the U_{pzc} of the different metals. On the other hand, as we have seen, the minima of the parabola correspond to the U_{she}.

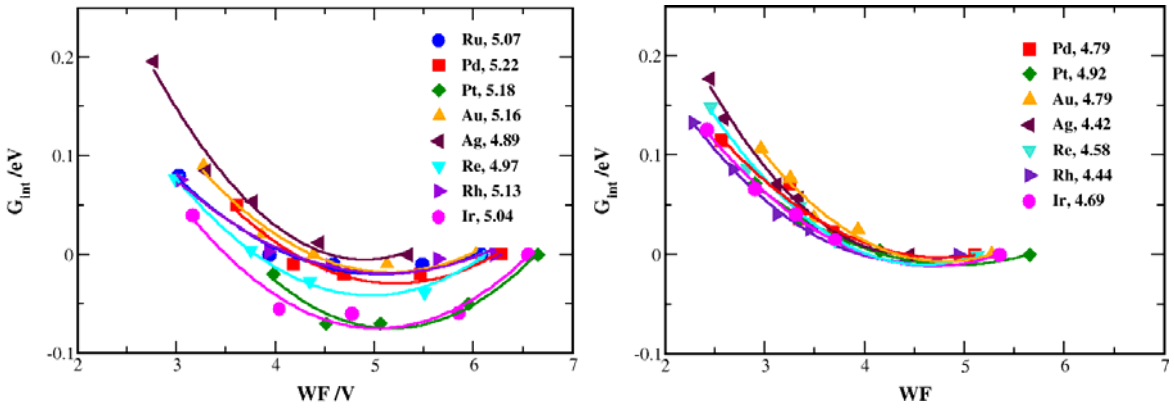

Fig. 4: *Dependence of the integral free energy, G_{int}, on the work function of the metal in contact with water for the 8 investigated transition metals shown for a) water model 1 and b) water model 2. The mean average values and standard deviations of the ASHEP for model 1 and 2 are (5.08/0.11) and (4.66/0.19) V respectively.*

Additionally, in Fig. 5, the U_{PZC} and U_{SHE} of the different metal electrodes have been plotted against the work function of the corresponding pristine metal surface, Φ.

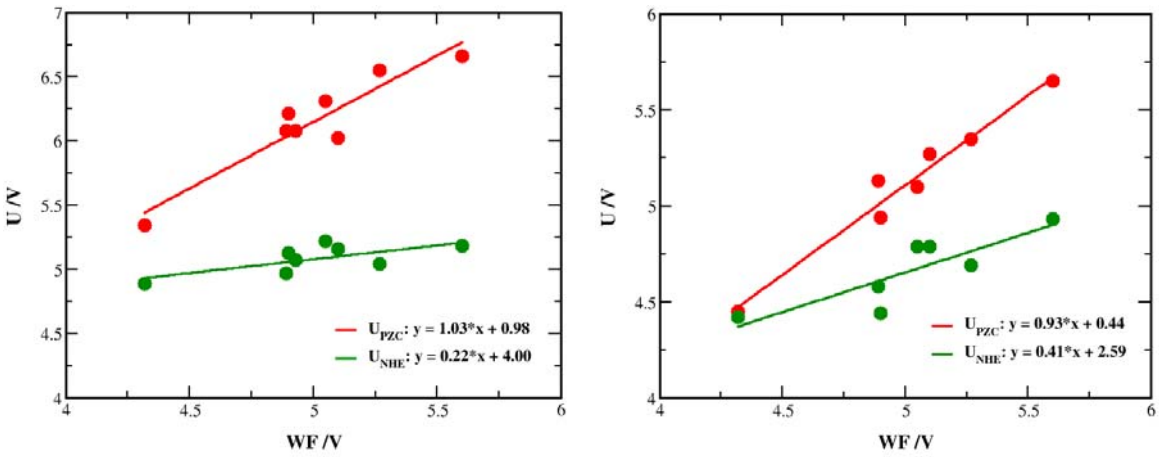

Fig. 5: *Dependence of the absolute potential of zero charge (red) and the potential of the standard hydrogen electrode (green) as a function of the pristine metal work function for a) model 1 and b) model 2.*

As observed, the U_{PZC} varies linearly with the WF with a slope close to 1. In both models, the capacitances (curvatures of the parabolas) across different metals are alike, implying that the chemical potentials (derivative of the parabolas) will be the same in all cases. The shift in G_{int} for different metals observed in Fig. 5a is thus just an artifact of having U_{PZC} as a reference. Moreover, it is clear that the value of the U_{PZC} is dictated by the simulated water structure, making it impossible to make a direct comparison between

experiments and theory. The same one to one correspondence between WF and U_{PZC} has been theoretically argued by Bockris [27] and seen in measurements for different facets of Au and Ag [48]. In general this is only valid as long as the water structure of the interface is fairly constant, which is the case for our artificially constructed water films. In order to get the correct U_{PZC} it is necessary to perform *e.g.* molecular dynamics simulation at room temperature starting from a random water structure.

All the differences pertaining to U_{PZC} should, in principle, be eliminated at SHE conditions (minima in G_{int}), and therefore ideally the slope of the $U_{SHE}(\Phi)$ should be zero. The $U_{SHE}(\Phi)$ slope different from zero, thus reflects the imperfect screening of the water used in the simulation. As can be seen, model 1, with only one but a rather flexible water bilayer that can easily adjust to the electrostatic field, does a much better job at screening than model 2, in which the two bilayers of opposite polarity form a rather rigid water structure. The variations of the ASHEP compared to the experimental reference (4.42-4.44 V) largely stems from lack of cancellation between the dipoles of the individual bilayers. The mean average values for the ASHEP in model 1 and 2 are 5.08 & 4.66 V, respectively. Obviously the latter one falls much closer to the experimental value. This can be appreciated by the fact that model 2 features no net dipole and hence it resembles more the experimental situation where the ASHEP is measured in bulk solution. Naturally, the best option would be to find a water structure that meets both of criteria, that is, perfect charge screening and no net dipole. However, since the internal reference is used the errors made by model 1 and model 2 cancel when two metals or two different potentials are compared. Hence for studying charge transfer reaction we do not expect that the exact water model, capable of screening and solvating the proton, will make any significant difference to the results. We have previously ascertained this point by showing that the energetics of the hydrogen evolution/oxidation reactions are conserved regardless of the interfacial water structure.

4 Conclusions

An absolute potential scale, in density functional theory (DFT) based electrochemistry calculations, is a challenge for two reasons. Firstly, the potential scale is typically estimated by subtracting the experimental value of the ASHEP from the WF of the

electrode placed in an electrode/water/vacuum environment. Commonly, experimental values reported in the literature are not well defined (reported values range from 4.42 to 4.85 V). Secondly, the absolute reference level for the electrons in the calculations is directly dependent on the structure of the water included in the simulations. These problems obvious call for an internal reference for the ASHEP.

In this paper it has been discussed how these discouraging issues can be addressed. First, by reviewing the literature, we identified the most reliable experimental value for the ASHEP. Due to present limitations in computer power it is not practically feasible to emulate bulk water in a large-scale electrochemistry study. Instead, one is usually limited to much less sophisticated water models. Here, two simple, but different, water models have been analyzed in detail and variations caused by insufficient screening and net dipoles have been quantified. Finally, it has been shown how an internal (system dependent) theoretical ASHEP can be deduced for a metal/electrolyte system. By applying such an internal reference, when comparing different electrode materials and potentials, one can avoid most of the errors caused by insufficient charge screening and net dipoles and thus obtain more trustworthy results, despite using a fairly simple description of the water.

Acknowledgements

CAMD is funded by the Lundbeck foundation. The Catalysis for Sustainable Energy initiative is funded by the Danish Ministry of Science, Technology and Innovation. This work was supported by the Danish Center for Scientific Computing. Support from the Danish Council for Technology and Innovation's FTP program and the Strategic Electrochemistry Research Center is acknowledged.

References

1 J. K. Nørskov, J. Rossmeisl, A. Logadottir, L. Lindqvist, J. R. Kitchin, T. Bligaard, H. Jónsson, *J. Phys. Chem. B* **108** (2004) 17886.

2 J. Rossmeisl, J. K. Nørskov, C. D. Taylor, M. J. Janik, M. Neurock, *J. Phys. Chem. B*, **110** (2006) 21833.

3 M. Otani, O. Sugino, *Phys. Rev. B* **73** (2006) 115407.

4 M. Otani and O. Sugino, *Phys. Rev. B* **73** (2006) 115407.

5 J. S. Filhol and M. Neurock, *Angew. Chem., Int. Ed.* **45** (2006) 402.

6 C. D. Taylor, S. A. Wasileski, J.-S. Filhol, M. Neurock, *Phys. Rev B* **73** (2006) 65402.

7 E. Skúlason, G.S. Karlberg, J. Rossmeisl, T. Bligaard, J. Greeley, H. Jónsson, J.K. 340 Nørskov, *Phys. Chem. Chem. Phys.* **9** (2007) 3241.

8 Y. Cai, A. B. Anderson, *J. Phys. Chem. B* **108** (2004) 9829.

9 Y. Cai, A. B. Anderson, J. C. Angus, L. N. Kostadinov, *Electrochem. & Solid-State Lett.*, **8** (2005) E62.

10 J. E. B. Randles, Trans. *Faraday Soc.* **52** (1956) 1973.

11 J. R. Farrell, P. McTigue, *J. Electroanal. Chem.* **139** (1982) 37.

12 **R.** Gomer, G. Tryson, *J. them. Phys* **66** (1977) 4413.

13 W. N. Hansen , D. M. Kolb, *J. Electroanal. Chem.* **100** (1979) 493.

14 E. R. Kötz, H. Neff, K. Müller, *J. Electroanal. Chem.* **215** (1986) 331.

15 J. Schneider, D. Franke, D. M. Kolb, *Surf. Sci.* **198** (1988) 277.

16 W. N. Hansen, G. J. Hansen, *Phys. Rev. A* **36** (1987) 1396.

17 H. Reiss, A. Heller, *J. Phys. Chem.* **89** (1985) 4207.

18 S. Schnur, A. Gross, *N. J. Phys.* **409** (2009) 157.

19 O. Sugino, I. Hamada, M. Otani, Y. Morikawa, T. Ikeshoji, and Y. Okamoto, *Surf. Sci.* **601** (2007) 5237.

20 J. Rossmeisl, E. Skúlason, M. E. Björketun, V. Tripkovic, J. K. Nørskov, *Chem. Phys. Lett.* **466** (2008) 68.

21 E. Skúlason, V. Tripkovic, M. E. Björketun, S. Gu›mundsdóttir, G. Karlberg, J. Rossmeisl, T. Bligaard, H. Jónsson, J. K. Nørskov, *accepted to J. Chem. Phys.*

22 S. Trasatti, *Pure & Appl. Chem.* **58** (1986) 955.

23 S.Trasatti, *Surf. Sci.* **335** (1995) 1.

24 S. Trasatti, *Electrochim. Acta* **36** (1991) 1659.

25 S. Trasatti, E. Lust, Modern Aspect of Electrochemistry, Number 33, edited by Ralph E. White et al., Kluwer Academic/Plenum Publishers, New York, 1999.

26 S. Trasatti, *J. Electroanal. Chem.* **139** (1982) 1.

27 J. O'M Bochris, S. D. Argade, *J. Chem. Phys.* **49** (1968).

28 D. Tsiplakides, C. G. Vayenas, *J. Electrochem. Soc.* **148** (2001) E189.

29 B. Hammer, L. B. Hansen, J. K. Nørskov, *Phys. Rev. B* **59** (1999**)** 7413.

30 H. J. Monkhorst; J. D. Pack, *Phys. Rev. B* **13** (1976) 5188.

31 D. Vanderbilt, *Phys.Rev. B* **41** (1990) 7892.

32 Dacapo pseudopotential code, URL: https.//wiki.fysik.dtu.dk/dacapo, Center for Atomic Scale Materiale Design (CAMD), Technical University of Denmark, Lyngby.

33 Atomic Simulation Environment (ASE), URL: https/wiki.fysik.dtu.dk/ase, Center for Atomic Scale Materiale Design (CAMD), Technical University of Denmark, Lyngby.

34 J. M. Heras, L. Viscido, *Catal. Rev. Sci. Engng* **30** (1988) 281.

35 P. A. Thid, T. E. Madey, *Surf Sci. Rep.* **7** (1987) 211.

36 M. D. Tissandier, K. A. Cowen, W. Y. Feng, E. Gundlach, M. H. Cohen, A. D. Earhart, J. V. Coe, *J. Phys. Chem. A* **102** (1998) 7787.

37 W. R. Fawcett, *Lanqmuir* **24** (2008) 9868.

38 A. A. Isse, A. Gennaro, *J. Phys. Chem. B* **114** (2010) 7894.

39 J. Rossmeisl, E. Skúlason, M. E. Björketun, V. Tripkovic, J. K. Nørskov, *Chem. Phys. Lett.* **466** (2008) 68.

40 C. Clay, S. Haq, A. Hodgson, *Phys. Rev. Lett.* **92** (2004) 46102.

41 C. Clay, S. Haq, A. Hodgson, *Phys. Chem. Lett* **92** (2004) 136103.

42 C. Clay, L. Cummings, A. Hodgson, *Surf. Sci.* **601** (2007) 562.

43 F. T. Wagner, T. E. Moylan, *Surf. Sci.* **191** (1987) 121.

44 H. Ogasawara, B. Brena, D. Nordlund, M. Nyberg, A. Pelmenschikov, L. G. M. Petterson, A. Nilsson, *Phys. Rev. Lett.*, **89** (2002) 276102.

45 G. S. Karlberg, F. E. Olsson, M. Persson, G.Wahnstrom, *J. Chem. Phys.* **119** (2003) 4865.

46 A. Michaelides, P. Hu, *J. Chem. Phys.* **114** (2001) 513.

47 V. Tripkovic, E. Skulason, S. Siahrostami, J. K. Nørskov, J. Rossmeisl, *Electrochim. Acta*, (2010)

48 S. Trasatti, *J. Electroanal. Chem.* **39** (1972) 163.

Paper IV

The oxygen reduction reaction mechanism on Pt(111) from density functional theory calculations

V. Tripković, E. Skúlason, S. Siahrostami, J. K. Nørskov, J. Rossmeisl

Electrochimica Acta, doi:10.1016/j.electacta.2010.02.056

Electrochimica Acta xxx (2010) xxx–xxx

Contents lists available at ScienceDirect

Electrochimica Acta

journal homepage: www.elsevier.com/locate/electacta

The oxygen reduction reaction mechanism on Pt(1 1 1) from density functional theory calculations

Vladimir Tripković[a], Egill Skúlason[a], Samira Siahrostami[a,b], Jens K. Nørskov[a], Jan Rossmeisl[a,*]

[a] Center for Atomic-scale Materials Design (CAMD), Department of Physics, Technical University of Denmark, Kgs. Lyngby 2800, Denmark
[b] Department of Chemistry, College of Sciences, Shiraz University, Shiraz 71454, Iran

ARTICLE INFO

Article history:
Received 7 December 2009
Received in revised form 15 February 2010
Accepted 18 February 2010
Available online xxx

Keywords:
Oxygen reduction reaction
Pt
DFT
Reaction mechanism

ABSTRACT

We study the oxygen reduction reaction (ORR) mechanism on a Pt(1 1 1) surface using density functional theory calculations. We find that at low overpotentials the surface is covered with a half dissociated water layer. We estimate the barrier for proton transfer to this surface and the barrier for proton transport parallel to the surface within the half dissociated water network. We find both barriers to be small. The only potentially dependent step is the proton transfer from water to the half dissociated water layer. We find that ORR proceeds via four direct e^- reductions without significant peroxide formation. We show that the oxygen–oxygen bond breaking is dependent on the local surface environment. The minimum energy pathway is constructed and we confirm that OH removal from the surface determines the overpotential.

1. Introduction

The largest challenge in the proton-exchange membrane fuel cell (PEMFC) catalysis is to reduce the amount of Pt needed at the cathode. The cathode contains 80–90% of the total amount of Pt used in PEMFC. Sluggish kinetics at the cathode accounts for the major part of voltage drop in PEMFCs. This limits state-of-the-art systems to operate at voltages of only ~0.7 V, far from the equilibrium potential of ~1.2 V [1]. To make fuel cell production economically viable, one has to increase the mass activity of Pt by at least factor of four [1].

Deducing a reaction mechanism from the measured kinetics is a tremendously difficult problem [2,3]. In that perspective DFT studies have provided huge molecular level understanding of surface phenomena that are taking place during the ORR. The DFT simulations enabled us to relate the binding energies of all the intermediates in the ORR to the binding energy of oxygen [4] and use that knowledge to construct an activity volcano [5] depending just on that single descriptor. The activity volcano is limited by two rate determining steps; OH removal and OOH formation on the surface [3,6]. Therefore ideally it would be desirable to have weaker OH and stronger OOH binding to the surface. Since one cannot change independently binding energies of OH and OOH, material with the tradeoff of these two limiting regimes will be the best catalyst for this reaction. Pt with an intermediate O binding energy is found to be close to the top of the volcano explaining why it stands out as the best single element catalyst. Higher activities can be reached by slightly tuning the oxygen binding energy by alloying Pt with some other metal [7,8]. However, these previous theoretical studies relied on the binding energies of the most stable intermediates, and it was implicitly assumed that any additional reaction barriers are rather small or essentially potential and metal independent.

The barriers for O_2, OOH and HOOH bond breaking on the pure Pt(1 1 1) surface have been calculated by Nilekar and Mavrikakis in the absence of water and an applied bias [9]. The first charge transfer reaction of the ORR has also been modeled previously by Janik et al. in a water environment at a constant surface charge [10]. This study showed that the barrier for this reaction is very small. The reaction was modeled having water at the surface; however, at the potentials where the ORR takes place, the electrode surface will start to oxidize. Therefore the OH coverage will be substantial and this could significantly affect the results [11].

In the present we study the ORR mechanism at relevant potential, at a realistic surface coverage of OH and in the presence of water. First we calculate the binding energy of hydroxyl as a function of the OH coverage; from this we determine the coverage of OH at potentials of interest to be 1/3 ML. Subsequently we model all ORR intermediates in this H_2O/OH hydrogen bonded network.

2. Method

All the electronic structure calculations have been carried out using density functional theory, using the RPBE functional for

* Corresponding author.
E-mail address: jross@fysik.dtu.dk (J. Rossmeisl).

0013-4686/$ – see front matter © 2010 Elsevier Ltd. All rights reserved.
doi:10.1016/j.electacta.2010.02.056

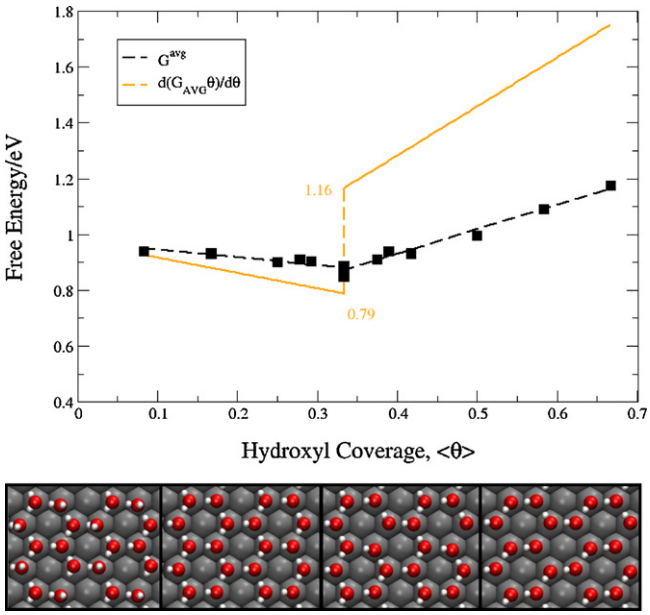

Fig. 1. (a) Average free adsorption energy of hydroxyl species on Pt(1 1 1). Discrete values (black squares) are linearly fitted (black dashed line) from low and high coverage end to 1/3 of hydroxyl coverage. Fits are used to get the differential adsorption energy of OH on the surface (yellow line). Dashed yellow line represents the discontinuity in the differential free energy at 1/3 ML hydroxyl coverage. Differential free energies of hydroxyl at different ends of discontinuity, 0.79 and 1.16 eV are also indicated. (b) Top view of four representative OH coverage structures, at very low hydroxyl coverage (0.08 ML), at different ends of discontinuity (0.33 and 0.42 ML) and at very high hydroxyl coverage (0.79 ML), in the order from left to right, respectively.

exchange and correlation [12]. The optimized RPBE lattice constant of Pt of 4.02 Å was used. The Pt(1 1 1) electrode was represented by periodically repeated 3 layer slabs separated by 12 Å of vacuum. Test with a 5-layer slab gave similar binding energies (within ~0.07 eV per water layer). Various unit cell sizes (3×4), (6×3), (6×4), and (6×6) sampled with $(3 \times 2 \times 1)$, $(2 \times 4 \times 1)$, $(2 \times 3 \times 1)$, and $(2 \times 2 \times 1)$ Monkhorst–Pack k-point sampling grid [13] were used throughout this work. Symmetry has been used to further reduce number of k-points. The dipole correction was used in all cases to decouple the electrostatic interaction between the periodically repeated slabs. The Kohn–Sham equations were solved using a plane wave basis with a plane wave and density cutoff of 26 Ry. Ionic cores are described with Vanderbilt ultrasoft pseudopotentials [14]. A Fermi smearing of 0.1 eV was used and energies were extrapolated to an electronic temperature of 0 K. The two bottom layers of the slab were fixed in their bulk positions, while the top layer together with adsorbates was allowed to relax until the sum of the absolute forces was less than 0.05 eV $Å^{-1}$. Transition states were located using nudged elastic band method [15,16]. In addition to the standard RPBE calculations, we investigated the effect of including van der Waals interaction by performing calculations of the water layer using the vdW-DF functional [17,18]. All calculations were performed using Dacapo [19], GPAW [20] and ASE simulation package [21].

3. Results and discussions

The outline of this section is as follows. First we investigate the half dissociated water layer. We calculate the differential adsorption energy of OH on Pt(1 1 1) surface shown in Fig. 1. We discuss and estimate the barriers for proton transfer from the electrolyte to the OH on the surface and surface proton diffusion, in Figs. 2 and 3, respectively. We illustrate a possible reaction mechanism in Fig. 4

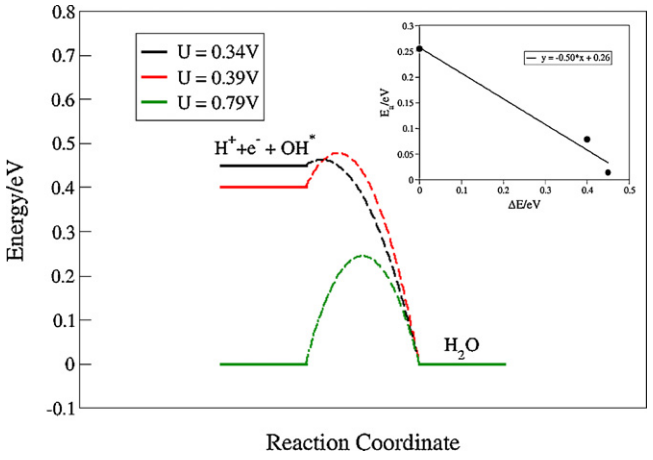

Fig. 2. Potential energy profiles for reducing one OH in the half dissociated water network by proton in the second water layer at three different initial potentials. The potential does not change much during the proton transfer reaction. Inset shows Brønsted–Evans–Polanyi (BEP) relationship for the charge transfer to the surface OH. Transfer coefficient (BEP slope) and the reaction barrier at the equilibrium are 0.5 and 0.26 eV, respectively.

we construct the free energy diagram (FED) of the minimum reaction path taking proton transfer and surface diffusion into account.

3.1. OH coverage

It has been found both experimentally [22,23] and theoretically [22,24,25] that the most stable water structure forms a honeycomb $(\sqrt{3} \times \sqrt{3})$R30 pattern with 2/3 ML water coverage. This water bilayer structure consists of two differently coordinated water molecules; where one is parallel to the surface and the other water molecule has an O–H bond pointing towards/away from the surface. These two structures have the same stability within a few meV [22,26–29]. Water can easily react with oxygen on the surface to form OH maintaining the honeycomb structure [28]. A water phase where every second water molecule has dissociated to OH has been named the half dissociated water structure. This particular water phase was found to be the most stable one up to 160 K under UHV conditions [30]. This stability stems from very strong OH–H_2O hydrogen bond [31,32]. The number of these bonds is maximized in this structure because every OH is bonded to three adjacent water molecules.

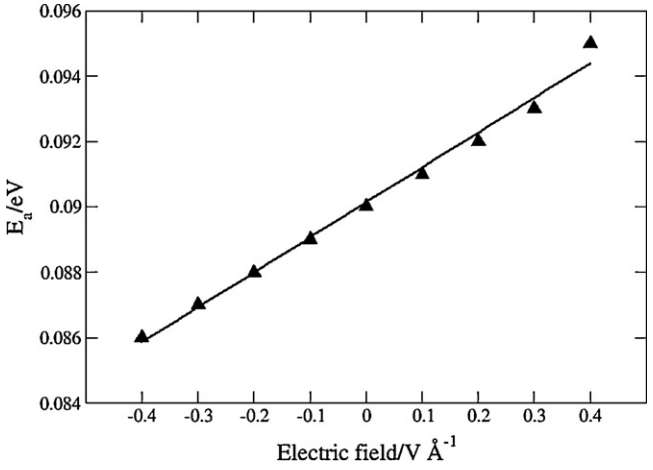

Fig. 3. The transition state energy for proton diffusion within the half dissociated water layer as a function of the applied field. Dipole moment perpendicular to the surface is very small, 0.011 eÅ, indicating that this step is potential independent.

Please cite this article in press as: V. Tripković, et al., The oxygen reduction reaction mechanism on Pt(1 1 1) from density functional theory calculations, Electrochim. Acta (2010), doi:10.1016/j.electacta.2010.02.056

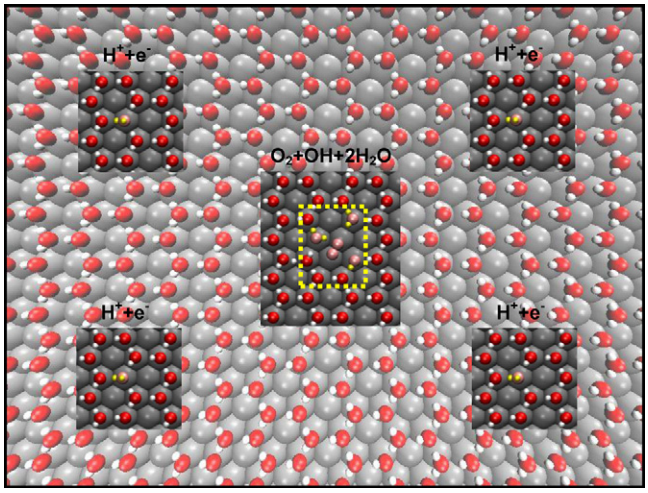

Fig. 4. Schematic illustration of the reaction mechanism. Surface is covered with half dissociated water network (transparent background). Four additional hydrogen atoms indicated (left and right panels). These atoms can easily diffuse to the reaction center (middle panel) where they reduce ORR intermediates. The dashed yellow box in the middle panel represents the simulated unit cell. All the structures are shown embodied in the half dissociated water network.

Under electrochemical conditions, cyclic voltammograms for Pt(1 1 1) show an oxidation peak around 0.8 V vs. reversible hydrogen electrode (RHE) (from simulation point of view there is no difference between the reversible and the standard hydrogen electrode [33]). This peak is believed to be related to the splitting of water into adsorbed OH* and $H^+ + e^-$ [34,3]. It is difficult to get the exact surface structure via *in situ* experiments. However, infrared spectroscopy suggests that the water on Pt(1 1 1) is in an ice-like structure [35]. From DFT simulations of the oxidation peak in cyclic voltammograms, charge seems to be well reproduced by assuming an isotherm with the half dissociated water layer [2,29].

and finally in Figs. 5 and 6

In the next section we will be looking at the three different free energies schemes for OH adsorption; average, integral and differential free energy scheme. The average free energy of OH is defined as the average adsorption energy per number of OHs, n, in the simulated cell. This energy shows the strength of the interaction between the adsorbed OH species. On the other hand, integral free energy is the total OH adsorption energy normalized with the respect to the size of the simulated cell or equivalently number of the surface atoms, N, in the simulation. It is obtained by multiplying the average free energy with the OH coverage. Besides this energy equals the energy stored in a capacitor set up between surface adsorbed water layer and the slab. Differential free adsorption energy is obtained by differentiating the free integral energy with respect to the OH coverage. Differential adsorption energy shows the most stable surface structure at corresponding potential. The relationship between the three different energy schemes is given in Eq. (1).

$$\frac{dG}{N\,d\theta} = \frac{d(G^{avg}\theta)}{d\theta} = \frac{d(G^{int})}{d\theta}, \quad \theta = \frac{n}{N} \tag{1}$$

The average free energy of OH species as a function of coverage is presented in Fig. 1 (black squares). We start by stepwise removing H atoms from the water bilayer. When 1/3 ML of OH coverage is reached, further increase of the OH concentration can only be achieved by taking one of the hydrogen atoms from the water molecules in plane with the surface. This equals to removing one of the hydrogen bonds. 2/3 of OH coverage is reached when one hydrogen atom has been abstracted from all water molecules. We note here that this high OH coverage is unrealistic under electrochemical conditions and that oxide layer will instead build up on the surface at higher potentials [11,36].

Free average energy adsorption profile (dashed black line) is obtained by linearly fitting discrete points from both, low and high coverage end to the coverage of 1/3 ML of hydroxyl. It can be seen from Fig. 1 that OH–OH interaction has a kink in the middle, meaning that the interaction is attractive below 1/3 ML and repulsive above 1/3 ML.

There are two ways in which we can calculate the adsorption energy of OH. We will illustrate this on the example of the integral energy. The first way is to compare the adsorption energies of OH on the surface to the liquid water and hydrogen molecules in the gas phase, whereas water in the bilayer is used as a reference for water molecules. Zero point energy and entropy correction are added to get the free adsorption energy at 300 K ($G = E + ZPE - TS$).

$$E_{OH}^{int} = E\left(\theta OH + \left(\frac{2}{3} - \theta\right) H_2O\right) - E_{slab} - \frac{2}{3}E(H_2O) + \frac{1}{2}\theta E(H_2) - \left(\frac{2}{3} - \theta\right)(E(H_2O*) - E_{slab} - E(H_2O)) \tag{2}$$

Here $E(H_2O^*)$ is the average energy of a water molecule in the water bilayer on the surface.

Another more direct way of calculating the adsorption energy is:

$$E_{OH}^{int} = E\left(\theta OH + \left(\frac{2}{3} - \theta\right) H_2O\right) - E_{slab} + \frac{1}{2}\theta E(H_2) - \frac{2}{3}E(H_2O*) \tag{3}$$

This corresponds to using the water in the bilayer as a reference for OH instead of the liquid water and H_2 in the gas phase. If the water bilayer was in equilibrium with liquid water, Eqs. (2) and (3) would give the same result. The challenge is that in the standard GGA simulations the stability of water in the bilayer is underesti-

Table 1
Dissociation barriers and bond lengths for the most stable oxygen species on Pt(1 1 1) slab coordinated to different number of water molecules. Bond length for O_2 in vacuum from RPBE-DFT calculation is also included for comparison.

	E^{diss}/eV	Bond length/nm
O_2 (g)		0.124
O_2	0.73	0.135
$O_2 + H_2O$	0.67	0.140
$O_2 + 2H_2O$	0.48	0.142
OOH[a] + $2H_2O$	0.37	0.144

[a] In this case OOH is the most stable oxygen species on the surface.

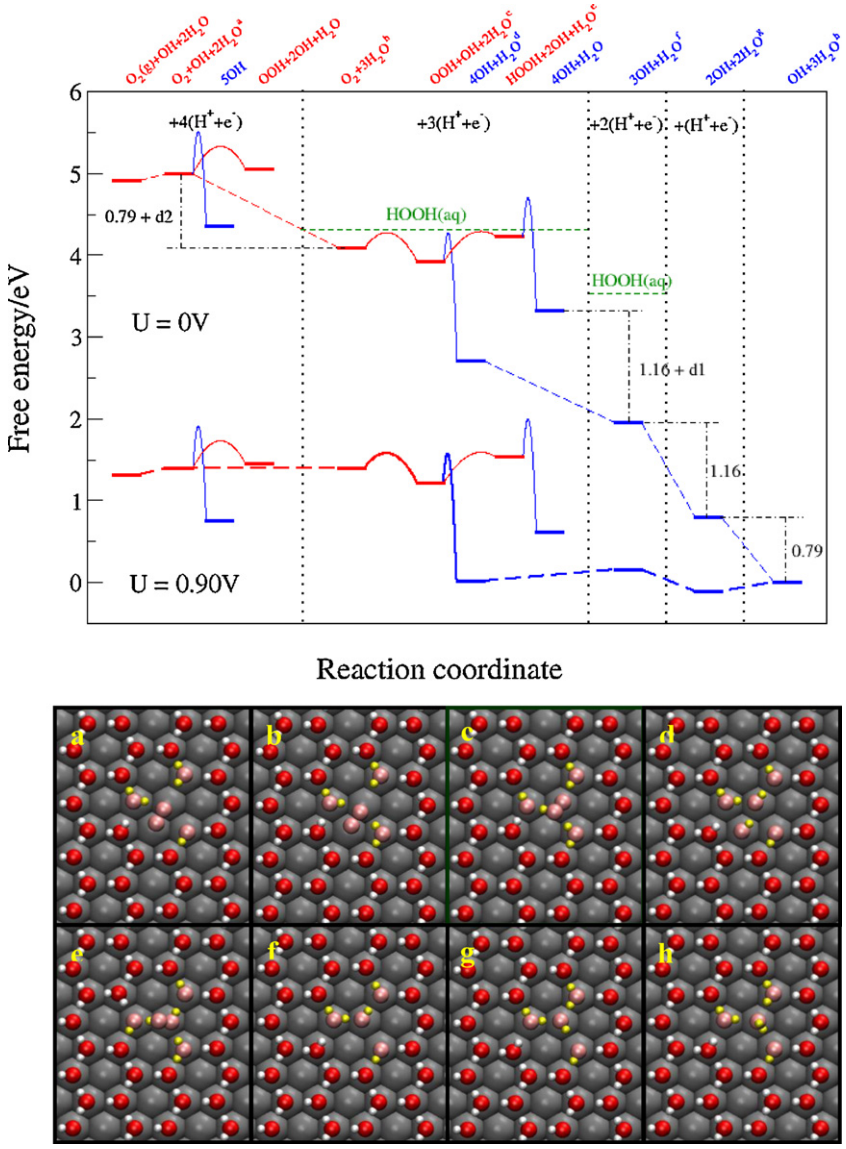

Fig. 5. (a) Free energy diagram for O_2 reduction at two different potentials, 0 (upper) and 0.9 V (lower), respectively. Red color indicates the associated species and the barriers between them. Blue color indicates dissociated species and the barriers for dissociation. Local structures are indicated above the figure panel following the same color code as the species they designate. Labels a–h correspond to the structures in b. Only the species in the reactive center are designated. Other species are left out for the sake of transparency. The thin solid and dashed lines represent the chemical and electrochemical reaction steps. At 0 V peroxide level in aqueous solution after first and second proton transfer is also indicated (green dashed line). Different electrochemical steps are fixed to the values (0.79 eV, 1.16 eV) from Fig. 1 in the way explained in the text. d1 (0.21 eV) and d2 (0.12 eV) represents the effect of (de)stabilization or equivalently energy difference between the structure in the reaction path and the most stable structure with same number of species (one in Fig. 1). Minimum energy path is highlighted at 0.9 V. (b) The most important intermediate structures on the ORR potential energy landscape embodied in the half dissociated water layer network, labeled from a–h. Pt(1 1 1) slab, oxygen and hydrogen atoms are colored in dark gray, red and white, respectively. Oxygen and hydrogen atoms designated in the FED are colored in pink and yellow, respectively.

mated mainly due to lack of van der Waals forces. This means that the potential for water oxidation will also be underestimated. We find that including the van der Waals interactions within the water layer and between the water layer and the surface, stabilize each water molecule with ~0.15 eV compared to the standard RPBE-GGA calculations. This brings the oxidation potential calculated with Eq. (3) close to the potential calculated with Eq. (2). In the following we therefore use first of the two methods for calculating adsorption energies.

Differentiating the integral free energy (see Eq. (1)) we get the differential free energy of the hydroxyl species on the surface (yellow line). The kink in the average free adsorption energy becomes a discontinuity (yellow dashed line) in the differential free adsorption energy.

The differential free energy of OH at different ends of the discontinuity at 1/3 coverage is 0.79 and 1.16 eV, respectively. We conclude from these values that adding/removing $H^+ + e^-$ to/from the half dissociated water differs by 0.37 eV. This is in agreement with previous DFT studies on the OH–H_2O structure [31,32].

We apply the computational standard hydrogen electrode (SHE) [5] to convert the differential free energy scale into an electric potential scale in a similar way as it was done previously for hydrogen adsorption [37].

In that way, Fig. 1 can be interpreted as the potential needed to oxidize the OH–H_2O layer at a given coverage. We will use the differential free energy of hydroxyl at both ends of the discontinuity in Fig. 1 to fix the free energy levels of the different electrochemical steps in the FEDs in Figs. 5 and 6.

Please cite this article in press as: V. Tripković, et al., The oxygen reduction reaction mechanism on Pt(1 1 1) from density functional theory calculations, Electrochim. Acta (2010), doi:10.1016/j.electacta.2010.02.056

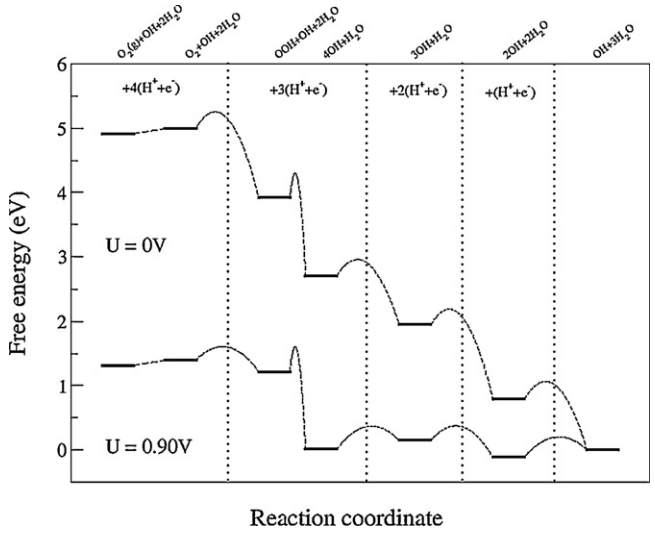

Fig. 6. Simplified free energy diagram for O_2 reduction at 0 V (upper) and 0.9 V (lower) potential. The most stable states in each electrochemical step together with the minimum reaction barrier for splitting the O–O bond are indicated. Electrochemical reduction steps are separated by dashed vertical lines. Barriers for proton transfer to the reaction center in the electrochemical steps (0.26 eV) are indicated with dashed black lines.

3.2. Charge transfer and surface diffusion

Before discussing the ORR mechanism in detail, a few issues regarding proton transfer and surface diffusion will be addressed. The half dissociated water network on the surface can also be viewed as the inner Helmholtz plane in the classical description of the double layer. In this picture the diffuse part or the outer Helmholtz plane of the double layer is set up between a charged water layer and the half dissociated water layer on the surface. Most of the potential drop will take place in the inner Helmholtz plane, because experimental isotherm obtained from integrated CV measurements for Pt(1 1 1) agrees well with the simple binding model of OH on the surface [29]. Therefore surface charge will not be significantly affected by proton concentration in the charged second water layer, opposite to what was found in the hydrogen evolution/oxidation region [38]. In order to mimic proton transfer at high potentials relevant for ORR one has to use very large simulation cells.

We simulate the reduction of the half dissociated water layer in the following approximate way. The largest unit cells we are able to model correspond to 0.79 V (equilibrium potential). In Fig. 2 we present results at three different potentials. For the point at the equilibrium (green line) we find a barrier of 0.26 eV for proton transfer. We note that a previous DFT study also found a low additional barrier for proton transfer to adsorbed oxygen molecule on Pt(1 1 1) surface [10]. Transfer coefficient for this charge transfer reaction is found to be 0.5, and since this is the only step that is potential dependent in the ORR, this will be the overall charge transfer coefficient. This result agrees perfectly with the experimental value of 0.5 [41].

Proton diffusion parallel to the surface occurs readily through interchange of hydrogen bonds within the water network. We get a 0.09 eV barrier for proton diffusion in the dissociated water network. Very low diffusion barriers have also been reported elsewhere [39]. In Fig. 3 we show the influence of an electric field on the transition state energy for the proton diffusion. We found very small changes of 0.01 eV in the activation energy in the large electric field range between −0.4 and +0.4 V Å^{-1}. Therefore we consider proton diffusion as a field and potential-independent step.

We will take the larger of the two barriers (0.26 eV) for the barrier needed to transport proton from the bulk water to the specific site on the surface where ORR takes place. This barrier will be used in the last part of this section to construct simplified FED in Fig. 6.

3.3. Reaction path model

A schematic illustration of the proposed reaction mechanism is shown in Fig. 4. Charge transfer is decoupled from the surface reaction in the following way: (1) a proton is transferred to OH somewhere on the surface where it picks up an electron; (2) the proton can then diffuse independently of the potential to the adsorbed oxygen molecule; and (3) reduce it. This process is repeated four times until the oxygen molecule has been reduced to two water molecules. The potential dependent charge transfer reaction is the same in all four steps with a rather small additional barrier (0.26 eV). We note that direct transfer of a proton to the adsorbed oxygen could also be a possible route, but this would only reduce the barrier relative to what is found in this paper. Since this barrier is already small enough, this will not affect conclusions of this study.

3.4. The free energy diagram

Fig. 5 is constructed from the adsorption energies of different ORR species and the differential free energy of OH. Since ORR is taking place just on specific sites on the surface, we assume that the global OH coverage remains constant. Therefore by locally changing OH coverage as a consequence of ORR, we can just infinitesimally move away from the global surface coverage of 1/3 ML of OH. We analyze the free energy diagram at $U = 0$ V backwards, starting from the last electrochemical step. The difference between the two states in the last electrochemical step is set to 0.79 eV, or the lower value in the discontinuity in Fig. 1. This value corresponds to a subtraction of one H^+ and e^- from H_2O at local OH coverage below 1/3 ML and forming the half dissociated water network, hence infinitesimally increasing the global OH coverage to 1/3 ML. In other words, water dissociation will become feasible at potentials greater than 0.79 V. In the same way are the second and the third electrochemical step set to 1.16 eV; the value at the other end of discontinuity, since we are now removing one $H^+ + e^-$ and hence increasing the OH coverage infinitesimally above 1/3 ML. The fourth electrochemical step is set to 0.79 eV between the two states with the adsorbed oxygen on the surface under different local OH coverage. Again this is because we remove one $H^+ + e^-$ near the adsorbed oxygen molecule where both states are below 1/3 ML of OH coverage. States that we get from our reaction mechanism can have different orientation of adsorbed species on the surface than the most stable structures with the same species. Therefore one also needs to correct for the difference between the most stable structure with certain OH coverage (ones in Fig. 1) and the ones obtained as a product of the reaction mechanism in the FED (d1 and d2 in Fig. 5).

First, we construct the FED at 0 V. We can obtain the FED at any desired potential by shifting the relative positions of all states at $U = 0$ V by the chemical potential of the electrons. We shift the states to 0.9 V potential since this is a potential relevant for ORR and within the potential window where the half dissociated water layer is stable.

The O_2 adsorption will be the first step in the FED. The O_2 level in the gas phase is fixed to a value of 4.92 eV compared to the liquid water and hydrogen in the gas phase. This value corresponds to a maximum work one can get out from the system.

There are two possible reaction paths after initial O_2 adsorption. O_2 can either react with one proton and electron from the surrounding water molecules to form OOH, or dissociate. The relative stability of the O_2 and OOH depends on the local OH coverage.

Please cite this article in press as: V. Tripković, et al., The oxygen reduction reaction mechanism on Pt(1 1 1) from density functional theory calculations, Electrochim. Acta (2010), doi:10.1016/j.electacta.2010.02.056

After proton transfer to the OH in the vicinity of O_2, dissociation becomes more facile. This is related to water at the surface being a stronger proton donor than OH [31,32]. Dissociation barriers and bond lengths depending on the number of hydrogen bonds coordinated to the most stable oxygen species are tabulated in Table 1. For O–O bond scission compared to the most stable intermediate, we get the lowest barrier to be 0.37 eV which is considerably less than 0.73 eV we find on the bare Pt(1 1 1) surface. If we include the electric field correction for transition state for O_2 dissociation at 0.9 V from Ref. [40], barrier will shift upwards by additional 0.06 eV.

OOH species can further react with nearby water molecules to form HOOH. This reaction step is energetically unfavorable which is in agreement with rotating ring disc experiments where only traces of peroxide are present at ORR relevant potentials [41]. The hydrogen peroxide energy level in aqueous solution [42] is also indicated for comparison with the green dashed line in the second and the third panel in Fig. 5. Difference between the two peroxide levels in aqueous solution is 0.79 eV due to the way the FED was constructed.

This analysis confirms our previous established thermodynamically picture that OOH is the most stable reaction intermediate after first reduction step. As a product of O–O bond scission we can either get O or 2OH since the nearest water molecules can donate a hydrogen atom to oxygen to form 2OH. We find very similar reaction energies and activation barriers for these two mechanisms. This is a result of simple scaling relationships that exist between different oxygen species based on the number of bonds each species has to the surface [4,43]. Consequently the difference in the free energy between O and 2OH is independent on material.

The following three consecutive electrochemical steps are simple proton transfer steps. In the final structure there is one more water molecule due to an extra hydrogen atom sitting on top of one OH in the half dissociated water layer. This additional water molecule can be readily replaced by O_2 [44], thus completing the catalytic cycle.

The barrier for breaking the oxygen–oxygen bond is potential independent, which means that it will not show up in comparing activities at different potentials. This is the reason why the analysis based on the intermediates binding gives qualitatively correct polarizations curves [2]. However, the barrier might change when the catalyst is changed, this could affect the previously established volcano curves. We speculate that less reactive catalysts might be predicted too active compared to Pt without explicitly including the kinetics.

The most stable intermediate in each electrochemical step is shown in Fig. 6, a simplified version of Fig. 5. The minimum energy barrier for OOH dissociation is also indicated as well as the barriers for charge transfer between different electrochemical steps. At $U = 0.9$ V from Fig. 6 OOH formation and OH removal step have very similar barriers. We speculate that inclusion of more water (larger unit cells) could slightly stabilize OOH and OH at surface. Any stabilization would reduce the barrier for OOH dissociation and increase the barrier for H_2O formation. This is in agreement with previous theoretical results on Pt(1 1 1) [5], where the rate of OH removal determined the overall ORR activity.

4. Conclusions

In summary we have calculated the reaction path and barriers for ORR on Pt(1 1 1). We would like to highlight that this approach differs from others in that we take explicitly into account the half dissociated water layer on the surface. All ORR intermediates are modeled within this water network, where water is not just accounted for stabilization effect it exerts on surface intermediates, but also it is directly involved in the reaction mechanism. We have constructed differential adsorption energy diagram and we have determined the most stable surface structure at potentials of interest for ORR reduction. We find that there is a discontinuity in the chemical potential at 1/3 ML of OH coverage which corresponds to energy needed for removing one extra hydrogen atom from the half dissociated water layer network. From this we have constructed the FED for O_2 reduction on Pt(1 1 1) at 0.9 V. The results are in agreement with the previously established picture that on Pt(1 1 1), OH reduction is the potential determining step. We find that the most stable species after first proton transfer is OOH with moderately potential-independent dissociation barrier of 0.37 eV. We have also shown that O_2 reduction proceeds via a so-called direct pathway, with negligible amount of peroxide produced in agreement with experimental observation [41]. We showed that there are only small reaction barriers for proton transfer and subsequent surface diffusion. This allowed us to deconvolute the overall reaction into potential dependent charge transfer to the surface and potential-independent proton transfer parallel to the surface. Since the barriers are small we can treat the potential dependent step to be the same for all four electron transfer reactions. We consider surface proton transfer to the ORR intermediates via half dissociated water network. Direct transfer of proton to one of the ORR intermediates could yield smaller barrier, however, since the barriers for the transfer via surface are already small, this will not affect the conclusions of this study.

Acknowledgements

CAMD is funded by the Lundbeck foundation. The Catalysis for Sustainable Energy initiative is funded by the Danish Ministry of Science, Technology and Innovation. This work was supported by the Danish Center for Scientific Computing. Support from the Danish Council for Technology and Innovation's FTP program and the Strategic Electrochemistry Research Center is acknowledged.

References

[1] H.A. Gasteiger, S.S. Kocha, B. Sompalli, F.T. Wagner, Appl. Catal. B: Environ. 56 (2005) 9.
[2] J. Rossmeisl, G.S. Karlberg, T. Jaramillo, J.K. Nørskov, Faraday Discuss. 140 (2008) 337.
[3] J.X. Wang, N.M. Markovic, R.R. Adzic, J. Phys. Chem. B 108 (2004) 4127.
[4] J. Rossmeisl, Á. Logadóttir, J.K. Nørskov, Chem. Phys. 319 (2005) 178.
[5] J.K. Nørskov, J. Rossmeisl, A. Logadottir, L. Lindqvist, J.R. Kitchin, T. Bligaard, H. Jónsson, J. Phys. Chem. B 108 (2004) 17886.
[6] J. Rossmeisl, Z.-W. Qu, H. Zhu, G.-J. Kroes, J.K. Nørskov, J. Electroanal. Chem. 607 (2007) 83.
[7] V.R. Stamenkovic, B.S. Moon, K.J.J. Mayrhofer, P.N. Ross, N.M. Markovic, J. Rossmeisl, J. Greeley, J.K. Nørskov, Angew. Chem. Int. Ed. 45 (2006) 2897.
[8] J. Greeley, I.E.L. Stephens, A.S. Bondarenko, T.P. Johansson, H.A. Hansen, T.F. Jaramillo, J. Rossmeisl, I. Chorkendorff, J.K. Nørskov, Nat. Chem. 1 (2009) 552.
[9] U. Nilekar, M. Mavrikakis, Surf. Sci. 602 (2008) 89.
[10] M.J. Janik, C.D. Taylor, M. Neurock, J. Electrochem. Soc. 156 (2009) 126.
[11] H.A. Hansen, J. Rossmeisl, J.K. Nørskov, Phys. Chem. Chem. Phys. 10 (2008) 3722.
[12] B. Hammer, L.B. Hansen, J.K. Nørskov, Phys. Rev. B 59 (1999) 7413.
[13] H.J. Monkhorst, J.D. Pack, Phys. Rev. B 13 (1976) 5188.
[14] D. Vanderbilt, Phys. Rev. B 41 (1990) 7892.
[15] H. Jónsson, G. Mills, K.W. Jacobsen, in: B.J. Berne, G. Ciccotti, D.F. Coker (Eds.), Classical and Quantum Dynamics in Condensed Phase Simulations, World Scientific, Singapore, 1998.
[16] G. Henkelman, H. Jónsson, J. Chem. Phys. 113 (2000) 9978.
[17] M. Dion, H. Rydberg, E. Schröder, D.C. Langreth, B.I. Lundqvist, Phys. Rev. Lett. 92 (2004) 246401.
[18] Y. Zhang, W. Yang, Phys. Rev. Lett. 80 (1998) 890.
[19] Dacapo pseudopotential code, URL: https://wiki.fysik.dtu.dk/dacapo, Center for Atomic Scale Materiale Design (CAMD), Technical University of Denmark, Lyngby.
[20] J.J. Mortensen, L.B. Hansen, K.W. Jacobsen, Phys. Rev. B 71 (2005) 035109.
[21] Atomic Simulation Environment (ASE), URL: https://wiki.fysik.dtu.dk/ase, Center for Atomic Scale Materiale Design (CAMD), Technical University of Denmark, Lyngby.
[22] H. Ogasawara, B. Brena, D. Nordlund, M. Nyberg, A. Pelmenschikov, L.G.M. Petterson, A. Nilsson, Phys. Rev. Lett. 89 (2002) 276102.
[23] T. Schiros, L.-Å. Näslund, K. Andersson, J. Gyllenpalm, G.S. Karlberg, M. Odelius, H. Ogasawara, L.G.M. Pettersson, A. Nilsson, J. Phys. Chem. C 111 (2007) 15003.

Please cite this article in press as: V. Tripković, et al., The oxygen reduction reaction mechanism on Pt(1 1 1) from density functional theory calculations, Electrochim. Acta (2010), doi:10.1016/j.electacta.2010.02.056

[24] A. Michaelides, P. Hu, J. Chem. Phys. 114 (2001) 1.
[25] P.J. Feibelman, Science 295 (2002) 99.
[26] A. Roudgar, A. Groß, Chem. Phys. Lett. 409 (2005) 157.
[27] S. Schnur, A. Groß, New J. Phys. 11 (2009) 125003.
[28] A. Michaelides, A. Alavi, D.A. King, Phys. Rev. B 64 (2004) 113404.
[29] J. Rossmeisl, J.K. Nørskov, C.D. Taylor, M.J. Janik, M. Neurock, J. Phys. Chem. B 110 (2006) 21833.
[30] C. Clay, S. Haq, A. Hodgson, Phys. Rev. Lett. 92 (2004) 46102.
[31] G.S. Karlberg, G. Wahnström, Phys. Rev. Lett. 92 (2004) 136103.
[32] G.S. Karlberg, G. Wahnström, J. Chem. Phys. 122 (2005) 194705.
[33] G.S. Karlberg, T.F. Jaramillo, E. Skúlason, J. Rossmeisl, T. Bligaard, J.K. Nørskov, Phys. Rev. Lett. 99 (2007) 126101.
[34] N.M. Markovic, H.A. Gasteiger, P.N. Ross, J. Phys. Chem. 99 (1995) 3411.
[35] H. Noguchi, T. Okada, K. Uosaki, Faraday Discuss. 140 (2009) 125.
[36] M. Wakisaka, H. Suzuki, S. Mitsui, H. Uchida, M. Watanabe, J. Phys. Chem. C 112 (2008) 2750.
[37] E. Skúlason, G.S. Karlberg, J. Rossmeisl, T. Bligaard, J. Greeley, H. Jónsson, J.K. Nørskov, Phys. Chem. Chem. Phys. 9 (2007) 3241.
[38] J. Rossmeisl, E. Skúlason, M.E. Björketun, V. Tripkovic, J.K. Nørskov, Chem. Phys. Lett. 466 (2008) 68.
[39] A. Michaelides, P. Hu, J. Am. Chem. Soc. 123 (2001) 4235.
[40] G.S. Karlberg, J. Rossmeisl, J.K. Nørskov, Phys. Chem. Chem. Phys. 9 (2007) 5158.
[41] B.N. Grgur, N.M. Markovic, P.N. Ross, Can. J. Chem. 75 (1997) 1465.
[42] F. Tian, R. Jinnouchi, A.B. Anderson, J. Chem. Phys. 113 (2009) 17484.
[43] F. Abild-Pedersen, J. Greeley, F. Studt, J. Rossmeisl, T.R. Munter, P.G. Moses, E. Skulason, T. Bligaard, J.K. Nørskov, Phys. Rev. Lett. 99 (2007) 016105.
[44] K.Y. Yeh, S.A. Wasileski, M.J. Janik, Phys. Chem. Chem. Phys. 11 (2009) 10108.

Please cite this article in press as: V. Tripković, et al., The oxygen reduction reaction mechanism on Pt(1 1 1) from density functional theory calculations, Electrochim. Acta (2010), doi:10.1016/j.electacta.2010.02.056

Paper V

First principle investigation of zinc-anode dissolution in zinc/air battery

V. Tripković, S. Siahrostami, K. T. Lundgård, K. E. Jensen, H. A. Hansen, J. S. Hummelshøj, J. S. Garðarsson, T. Vegge, J. K. Nørskov, J. Rossmeisl

To be submitted

First principle investigation of zinc-anode dissolution in zinc/air battery

Vladimir Tripković[a], Samira Siahrostami[a,b], Keld T. Lundgård[a], Kristian E. Jensen[a]. Heine A. Hansen[a], Jens S. Hummelshøj[a], Jón S. G. Mýrdal[a,c], Tejs Vegge[c], Jens K. Nørskov[a,d], Jan Rossmeisl[a]*

[a] Center for Atomic-scale Materials Design (CAMD), Department of Physics, Technical University of Denmark, DK-2800 Lyngby, Denmark

[b] Department of Chemistry, College of Sciences, Shiraz University, Shiraz 71454, Iran

[c] Materials Research Division, Risø National Laboratory for Sustainable Energy, Technical University of Denmark, DK--4000 Roskilde, Denmark

[d] Department of Chemical Engineering, Stanford University, Stanford, CA 94305 and Center for Interface Science and Catalysis, SLAC National Accelerator Laboratory, 2575 Sand Hill Rd, Menlo Park, CA 94025, USA

**corresponding author jross@fysik.dtu.dk*

We present a density functional theory investigation of the Zn dissolution (oxidation) on the anode side in the zinc/air battery using a kinked surface to model bulk dissolution of zinc. From the adsorption energies of hydroxyl species and the experimental values for the dissolution potentials, we construct a free energy diagram and find that there is a small overpotential associated with the reaction.

Although the technology originates from 19th century [1], metal/air battery was first put to commercial use in the beginning of the 20th century. It became increasingly popular in the seventies when the first button cells appeared on the market. In recent years, increasing global energy demand along with the depletion of the carbon based natural resources have inspired the pursuit of alternative energy supplies. This has brought battery technology under the spotlight and has encouraged the scientific community to revisit and overcome problems that impeded its large scale utilization.

Metal/air batteries are similar to Fuel Cells (FC); the only difference being that the batteries are energy storage device while the FC is an energy converting device. In the

past, few potential candidates such Li, Ca, Mg, Al, Zn and Fe have been scrutinized as possible energy carriers in batteries. The use of earth abundant metals makes this technology much cheaper than the FC technology. Besides, using oxygen from air as the cathode oxidant, allows the battery to be filled with more anode material, which significantly increases the energy densities of the systems, albeit power densities still remain low. Metal/air cells are characterized by a very flat discharge profile which points to a minute potential loss over time [1].

The zinc/air battery is the only commercialized cell in the metal/air family. Al/air and Li/air cells possess higher energy density than the zinc/air, but they are instable in aqueous and alkaline solutions. For comparison, Al/air cell evolves hydrogen (anode corrosion) in aqueous solution, while Li degrades easily in the presence of trace amounts of water. These problems can be circumvented by using non-aqueous solvents like ionic liquids [2]. Many companies are now trying to develop such batteries. The zinc/air cells are primarily used in hearing aids and other small appliances that demand low currents at long period of time.

The advantage of these cells is that they are cheap, easy to handle and environmentally friendly. On the other hand they feature some significant drawbacks which are responsible for presently very limited extent of this technology. Among these, the most important ones are the anode corrosion, carbonate formation from the CO_2 in the air, which decreases the conductivity of the electrolyte, high sensitivity to temperature and humidity, high self discharge and zinc dendrite formation, where zinc builds unevenly in form of branch-like structures that can short circuit the electrodes and eventually kill the cell [3]. Besides these, a major challenge pertains to make this technology rechargeable with high efficiency. This could be achieved with a bifunctional catalyst capable of performing both Oxygen Reduction Reaction (ORR) during discharge and Oxygen Evolution Reaction (OER) during charging [4]. We have previously shown what are the best catalysts for ORR [5,6] and OER [7,8] among different classes of materials, but the challenge still persists in combining the two [9,10]. Another plausible technical solution is to make a three electrode cell with two cathodes, one for ORR and the other for OER, but this design adds significantly to the size and complexity of the cell [11].

The anode of the zinc/air cell is in the form of zinc paste and in the excess of hydroxyl species, it oxidizes to the zincate ion $[Zn(OH)_4]^{2-}$, while two electrons are released and transferred to the cathode where oxygen is reduced. In solution, the zincate ion spontaneously decays to form ZnO. Non-precious MnO_2 is used for cathode material, while KOH is often chosen as an electrolyte, due to its very good ionic conductance. Half reactions taking place at both electrodes are shown below

Anode:

$$Zn + 4OH^- \rightarrow [Zn(OH)_4]^{2-} + 2e^- \qquad E^\theta = 1.25\ V \qquad (1)$$

$$[Zn(OH)_4]^{2-} \rightarrow ZnO + H_2O + 2OH^- \qquad (2)$$

Cathode:

$$1/2O_2 + 2H_2O + 2e^- \rightarrow 2OH^- \qquad E^\theta = 0.4\ V \qquad (3)$$

Adding these two half reactions and their standard potentials together, gives the overall reaction and the potential of the system.

Overall:

$$Zn + 1/2O_2 \rightarrow ZnO \qquad E^\theta = 1.65V \qquad (4)$$

It is important to note here that the definition of standard potentials implies that reaction is taking place at standard conditions in 1 M solution of each aqueous species. Since one of the aqueous species is OH^- this automatically implies that the potentials in reaction above is given at pH=14. Maximum work that can be extracted from the system is 1.65 eV per electron, albeit the operating voltage is only ~1.30 V [1], due to the kinetic losses related mostly to the ORR at the cathode.

In the present letter we show the free energy diagram (FED) for zinc dissolution at the anode side in zinc/air batteries. This is a continuation of our previous project where we modeled Li/air cell in an *aprotic* solvent [12]. We first present the model used to emulate bulk dissolution of zinc, then we use a simple model to account for a finite bias and finally we show that there is a very small overpotential for this reaction. Although

dissolution processes have been previously successfully studied with DFT [13,14], this is, to the best of our knowledge, the first attempt to model the dissolution of zinc using DFT.

All the electronic structure calculations have been carried out using GPAW program package which is a density functional theory implementation based on the projector-augmented wave (all electron, frozen core approximation) method that uses real-space uniform grids [15]. The grid spacing was set to h = 0.15 Å, as a tradeoff between computational efficiency and accuracy. For description of exchange and correlation the standard GGA-RPBE functional was chosen [16]. The Zn surface was modeled as a kink represented by periodically repeated 6 layer slab separated by approximately 18 Å of vacuum. The two bottom layers were held fixed while the rest was allowed to relax until the sum of the absolute interatomic forces was less than 0.05 eV $Å^{-1}$. The Brillouin zone was sampled by (3x4x1) Monkhorst-Pack grid [17] and symmetry was applied to further reduce the number of k-points. Fermi smearing was set to 0.1 eV and all the energies were extrapolated to the electronic temperature of 0 K. All the calculations were performed in the ASE simulation environment [18].

We start by addressing simple issues regarding lattice constants and the model we assume. The optimized lattice constants of zinc (a=2.66, c=5.37, a/c=2.02) compare well with other theoretical DFT-GGA (a=2.65, c=5.12, a/c=1.93) [19] and experimental (a=2.67, c=4.95, a/c=1.86) [20] values found in the literature. The same agreement holds for the wurtzite structure of $Zn(OH)_2$ (a=4.96, b=5.23, c=8.91) where we compared our data to the only experimental source available (a=4.92, b=5.16, c=8.49) [21]. We have also calculated formation energy of bulk $Zn(OH)_2$ to be 2.35 eV, which is very close to the experimental determined 2.5 eV [22].

We adopted a kinked surface for our model system (see Fig. 1b). There are two reasons for choosing the kink. Firstly, the kink atoms make the strongest bonds (most under coordinated defect sites) to adsorbates and thus they will be the first ones to dissolve. Secondly, when a kink atom is dissolved, it leaves another kink on the surface. Hence, there is no qualitative change in the surface morphology. The difference in energy, before and after the dissolution of the kink atom therefore corresponds to the energy of

one zink atom in the bulk. In this way the bulk dissolution can effectively be emulated by surface dissolution of kink atoms.

We began our study by probing the most stable adsorption sites for hydroxyl species and concluded that the bridge site between the kink and adjacent Zn atom is preferential for the first OH adsorption (cf. Fig. 2). Subsequent OH groups will adsorb on the step, until all the step sites have been covered. In the end, each zinc atom at the step will be bonded to the OH groups. Any additional OH species will bind to the kink atom and pull it out (dissolve) from the surface. This finding clearly demonstrates that the zink anode will dissolve kink atom by kink atom.

In experiments, zink undergoes sequential dissolution to form $[Zn(OH)_4]^{2-}$ ion.

$$Zn + OH^- \rightarrow ZnOH + e^- \quad (5)$$

$$ZnOH + OH^- + e^- \rightarrow Zn(OH)_2 + 2e^- \quad (6)$$

$$Zn(OH)_2 + OH^- \rightarrow [Zn(OH)_3]^- \quad (7)$$

$$[Zn(OH)_3]^- + OH^- \rightarrow [Zn(OH)_4]^{2-} \quad (8)$$

where Zn(OH) and $Zn(OH)_2$ are bulk hydroxides. The equilibrium potential for the formation of the ionic species $[Zn(OH)_3]^-$ and $[Zn(OH)_4]^{2-}$ is 1.15 and 1.25 V, respectively [22]. In our model, the kink atom dissolves after the adsorption of the third hydroxyl group in the same way as $Zn(OH)_2$ dissolves in the excess of OH^- ions (Eq. (7)). We present our results in Fig.1 in the form of a FED. Here, the first and the last two steps in Fig.1 are fixed to the dissolution potentials of zinc forming $[Zn(OH)_3]^-$ and $[Zn(OH)_4]^{2-}$ anions. Herein, we used the experimental values because it is hard to estimate free energy levels of solvated ions within DFT. To get the free energy levels of solid phases Zn(OH) and $Zn(OH)_2$ corresponding to the second and the third step in the FED, we used method outlined elsewhere [5]. Following this method, the total free adsorption energy of OH is given by

$$\Delta G = \Delta E + \Delta ZPE - T\Delta S - 0.059*pH + E_{w,water} \quad (9)$$

We first calculate the OH adsorption energy using water in the liquid and hydrogen in the gas phase as reference states. Then we add the zero point energy (ZPE) and entropy contribution, estimated from the normal mode analysis and thermodynamic tables [23] to be 0.39 eV per OH species at room temperature. Since the pH cannot be explicitly included in the calculations, it is added *a posteriori* by shifting the free energy levels of OH species by –0.059*pH or in our case by -0.83 eV at pH = 14. This is equal to using OH^-(aq) as the reference state instead of H_2O(l). The $E_{w,water}$ is the water induced stabilization energy of OH species. This effect has previously been found to be quite substantial (~0.6 eV) on Pt(111) [5]. In the present analysis we estimated it to be 0.57 eV per OH group. We inferred this value by comparing the free energy level of $[Zn(OH)_3]^-$, when it was moved far away from the surface in the vacuum region and the experimentally determined dissolution potential for $[Zn(OH)_3]^-$.

Resulting FED is shown in Fig. 1 at two potentials U = 0 V and at U = -1.08 V or the lowest potential where all the reaction steps are still downhill in free energy. The FED at U = -1.08 V is obtained by shifting the energy levels at U = 0 V by the chemical potential of the electrons, neU, where n is the number of the electrons involved in the electrochemical reaction [5]. In Fig.1, we have also denoted the formation energy of $Zn(OH)_2$ in the bulk. The small energy difference in the bulk formation energy of $Zn(OH)_2$ obtained from two qualitatively different approaches (bulk and surface calculations) validates our assumed model. The difference between the theoretical equilibrium potential of -1.25 V and -1.08 V is the overpotential (0.17 V) needed to run this reaction. This is close to the experimental observation that the reaction does not feature large overpotential. In Fig. 2, we have made snapshots of the structures in a dissolution cycle. It is clearly seen from snapshots b and f that the surface morphology does not change after dissolution of a kink atom.

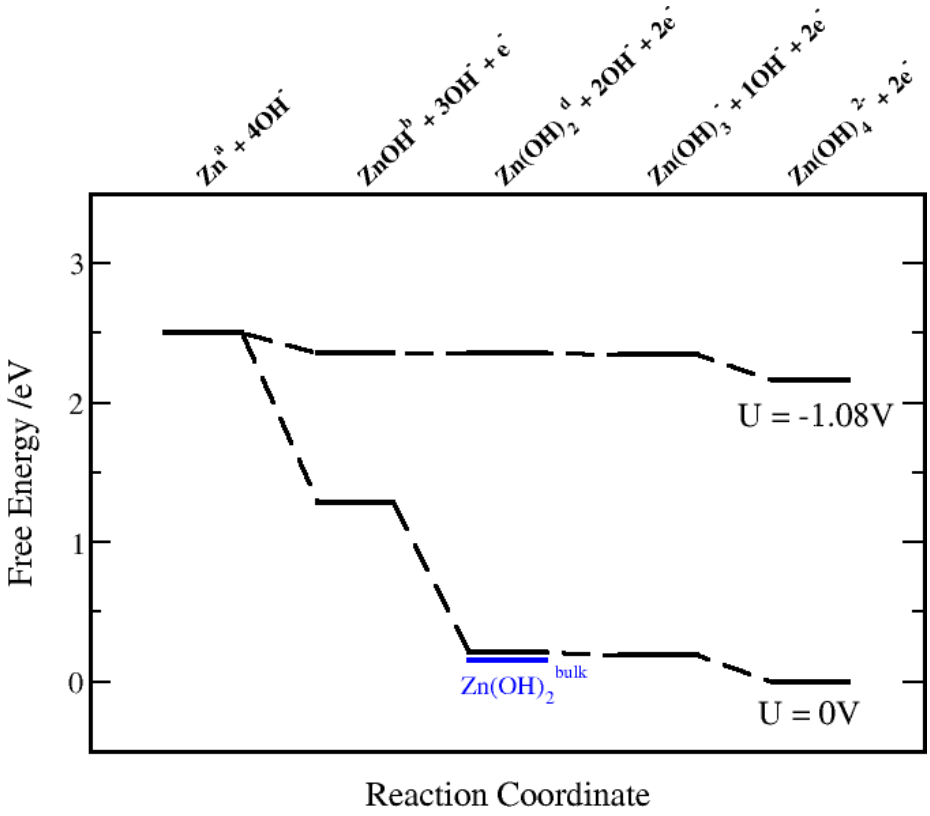

Fig.1: Free energy diagram for Zn dissolution at the anode, shown at two potentials, 0 V and -1.08 V respectively. The $[Zn(OH)_3]^-$ and $[Zn(OH)_4]^{2-}$ levels are fixed to the experimental determined dissolution potentials. The $Zn(OH)_2$ level calculated from the formation energy of the bulk $Zn(OH)_2$ is indicated in blue for comparison. Labels a, b and d correspond to the structures designated below.

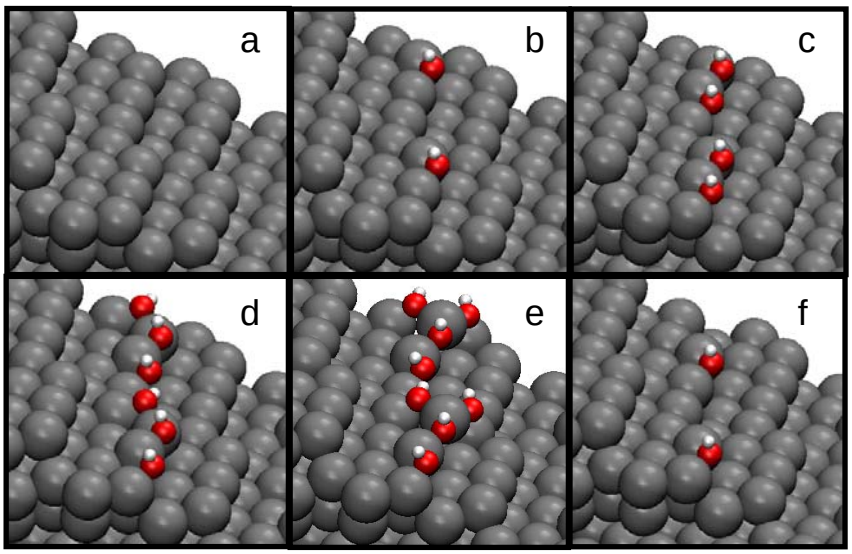

Fig. 2: Snapshot a is a bare Zn kink, while snapshots b-f illustrate steps in one dissolution cycle. The unit cell has been repeated twice in the y direction.

In summary, we have presented a simple analysis of the anode dissolution in the zinc/air battery. The novelty of this approach is that we emulated bulk dissolution by surface adsorption on a Zn kink. From the calculated OH adsorption energies and the dissolution potentials we map out the FED and we show that there is a very small overpotential of 0.17 V related to this reaction. This finding agrees well with the experimental evidence. The close agreement between the two values substantiates the validity of the model and furthermore it demonstrates the versatility of DFT tool in modeling dissolution processes on metal surfaces.

Acknowledgements

CAMD is funded by the Lundbeck foundation. The Catalysis for Sustainable Energy initiative is funded by the Danish Ministry of Science, Technology and Innovation. This work was supported by the Danish Center for Scientific Computing. Support from the Danish Council for Technology and Innovation's FTP program and the Strategic Electrochemistry Research Center is also acknowledged.

References

1 Duracell Technical/OEM primary systems
http://www1.duracell.com/OEM/Primary/Zinc/zinc_air_tech.asp

2 K. M. Abraham, Z. Jiang, *J. Electrochem. Soc.* 143 (1996) 1.

3 P. Sapkota, H. Kim, *J. Ind. & Eng. Chem.* **15** (2009) 445.

4 Y-C. Lu, Z. Xu, H. A. Gasteiger, S. Chen, K. Hamad-Schifferli, Y. Shao-Horn, *J. Am. Chem. Soc. Commun.* (2010).

5 J. K. Nørskov, J. Rossmeisl, A. Logadottir, L. Lindqvist, J. R. Kitchin, T. Bligaard, H. Jónsson, *J. Phys. Chem. B* **108** (2004) 17886.

6 J. Greeley, I. E. L. Stephens, A. S. Bondarenko, T. P. Johansson, H. A. Hansen, T. F. Jaramillo, J. Rossmeisl, I. Chorkendorff, J. K. Nørskov, *Nature Chem.* **1** (2009) 552

7 J. Rossmeisl, Á. Logadóttir, J. K. Nørskov, *Chem. Phys.* **319** (2005) 178.

8 J. Rossmeisl, Z. –W. Qu, H. Zhu, G. -J. Kroes, J. K. Nørskov, *J. Electroanal.Chem.* **607** (2007) 83.

9 K. Kinoshita, Electrochemical Oxygen Technology, John Wiley & Sons Inc., New York, 1992.

10 Y. Gorlin, T. Jaramillo *accepted to J. Am. Chem. Soc.*

11 S. F. Bender, J. W. Cretzmeyer, T. F. Reise in: D.Linden (Ed.) Handbook of Batteries, McGraw-Hill, Inc., New York, 1995, p. 13.1.

12 Hummelshøj J. S., J. Blomquist, S. Datta, T. Vegge, J. Rossmeisl, K. S. Thygesen, A. C. Luntz, K. W. Jacobsen, J. K. Nørskov, *J. Chem. Phys.* **132** (2010) 071101.

13 J. Greeley, J. K. Nørskov, *Electrochim. Acta* **52** (2007) 5829.

14 P. Strasser, S. Koh, J. Greeley, *Phys. Chem. Chem. Phys.* **10** (2008) 3670.

15 J. J. Mortensen, L. B. Hansen, K. W. Jacobsen, *Phys. Rev. B* **71** (2005) 035109.

16 B. Hammer, L. B. Hansen, J. K. Nørskov, *Phys. Rev. B* **59** (1999**)** 7413.

17 H. J. Monkhorst; J. D. Pack, *Phys. Rev. B* **13** (1976) 5188.

18 Atomic Simulation Environment (ASE), URL: https/wiki.fysik.dtu.dk/ase, Center for Atomic Scale Materiale Design (CAMD), Technical University of Denmark, Lyngby.

19 U. Wedig, M. Jansen, B. Paulus, K. Rosciszewski, P Sony, *Phys Rev. B* **75** (2007) 215123.

20 CRC Handbook of Chemistry and Physics, 77th (Ed.), edited by D. Lide (CRC Press, New York, 1996).

21 H. Jacobs, A. Niemann, W. Kockelmann, *Z. Anorg. und Allg. Chem.* **631** (2005) 1247.

22 M. Cai, S-M. Park, *J. Electrochem. Soc.* **143** (1996) 2125.

23 Atkins, P. W. *Physical Chemistry,* 6th ed., Oxford University Press: Oxford, U.K., 1998; pp 485, 925-927, 942.